

Utah State University

DigitalCommons@USU

All Graduate Theses and Dissertations

Graduate Studies

5-2020

Materials Design for High-Performance Organic Redox Flow Batteries and Electrocatalytic Carbon Dioxide and Nitrogen Reduction

Bo Hu

Utah State University

Follow this and additional works at: <https://digitalcommons.usu.edu/etd>



Part of the [Chemistry Commons](#)

Recommended Citation

Hu, Bo, "Materials Design for High-Performance Organic Redox Flow Batteries and Electrocatalytic Carbon Dioxide and Nitrogen Reduction" (2020). *All Graduate Theses and Dissertations*. 7775.

<https://digitalcommons.usu.edu/etd/7775>

This Dissertation is brought to you for free and open access by the Graduate Studies at DigitalCommons@USU. It has been accepted for inclusion in All Graduate Theses and Dissertations by an authorized administrator of DigitalCommons@USU. For more information, please contact digitalcommons@usu.edu.



MATERIALS DESIGN FOR HIGH-PERFORMANCE ORGANIC REDOX FLOW
BATTERIES AND ELECTROCATALYTIC CARBON DIOXIDE
AND NITROGEN REDUCTION

by

Bo Hu

A dissertation submitted in partial fulfillment
of the requirements for the degree

of

DOCTOR OF PHILOSOPHY

in

Chemistry

Approved:

Tianbiao Liu, Ph.D.
Major Professor

Lance C. Seefeldt, Ph.D.
Committee Member

Bradley S. Davidson, Ph.D.
Committee Member

Ryan Jackson, Ph.D.
Committee Member

Bill Doucette, Ph.D.
Committee Member

Richard S. Inouye, Ph.D.
Vice Provost for Graduate Studies

UTAH STATE UNIVERSITY
Logan, Utah

2020

Copyright © Bo Hu 2020

All Rights Reserve

ABSTRACT

Materials Design for High-Performance Organic Redox Flow Batteries and
Electrocatalytic Carbon Dioxide and Nitrogen Reduction

by

Bo Hu, Ph.D. of Science

Utah State University, 2020

Major Professor: Dr. Tianbiao Liu
Department: Chemistry and Biochemistry

Continuous growth in the utilization of renewable but intermittent energy such as solar and wind will accelerate the demand for grid-scale energy storage systems. Redox flow batteries (RFBs) have been intensively studied for large scale energy storage (MW/MWh), which is particularly attractive when integrated with renewable energy sources. In the last decades, researchers are putting more and more efforts on organic redox flow batteries and designing organic redox active materials which are highly soluble, stable, more sustainable, redox potential tunable, and separator compatible. With the desired renewable energy storage, electrocatalysis is a direct approach to synthesis important and valuable industrial products (carbohydrates, ammonia, etc.) from the most common reactants, such as carbon dioxide and nitrogen gas. Nowadays, electrocatalytic CO₂ and N₂ fixation are considered as both appealing processes which could not only contribute to release the pressure from fossil fuel demanding but also reduce the green gas emission.

My dissertation will include my research efforts on mainly two topics:

1. Designing high-performance redox active organic molecules for aqueous and nonaqueous redox flow batteries. I successfully designed and synthesized ferrocene, viologen, (2,2,6,6-Tetramethylpiperidin-1-yl)oxyl (TEMPO) and anthraquinone derivatives, all of which showed excellent solubility, stability, and redox reversibility. In these studies, we conducted a rational molecular design to increase active materials' solubility and improve their chemical and electrochemical stability. Comprehensive UV-Vis, cyclic voltammetry, EPR, NMR, half-cell studies were performed to reveal the chemical decomposition of our redox active materials, which further guided the molecular engineering. In addition, strategies were also developed to utilize multiple electrons of the redox active materials (such as viologen derivatives) to improve batteries' energy density.

2. Electrocatalytic CO₂ fixation based on the enzymatic catalyst and Mo₂N catalyst performance evaluation for N₂ electrocatalytic reduction to ammonia. For CO₂ electrocatalytic reduction, I successfully immobilized nitrogenase MoFe or FeFe protein on glassy carbon electrodes, which displayed efficient catalytic performance for CO₂ reducing to formate. This study stands for a new method to utilized nitrogenase to fulfill valuable product synthesis in the absence of MgATP. N₂ electrocatalytic reduction has been a very hot topic. Various inorganic catalysts have been designed for demonstrating the catalyzed ammonia production from nitrogen gas and water. We choose Mo₂N as a benchmark catalyst to evaluate its catalytic performance for N₂ reduction. However, systematic electrochemical studies and careful ¹⁵N₂ isotope labeling experiment revealed that instead of catalytic N₂ reduction, the ammonia formation is from nitride decomposition.

PUBLIC ABSTRACT

Materials Design for High-Performance Organic Redox Flow Batteries and
Electrocatalytic Carbon Dioxide and Nitrogen Reduction

Bo Hu

Nowadays, the utilization of renewable energy resources such as solar and wind energy has been realized to be a sustainable and environmentally benign strategy to alleviate the world's severe dependency on traditional fossil fuels, and thus enables the environmental recovery and sustainable development of the economy. The massive commercialization of solar and wind energy raises the demands for advanced energy storage technologies, among which the redox flow battery has been recognized as a promising solution due to it is low cost, safe, environmentally benign, and easy to be scaled up. All vanadium redox flow battery stands for the most important system in the market. However, the high price of raw material (V_2O_5), active materials crossover leaded self-discharge, and hazardous electrolyte limit its broad application. Therefore, it is urgent to explore new active materials that are cheaper, more stable and more sustainable. Redox active organic molecules are great candidates to meet those requirements. The metal-free molecules are normally composed of elements of C, H, O, N, etc., which have massive resources from nature. With the rational molecular design, the organic molecules could be very tolerant of side reactions and chemical decomposition. Their electrochemical and physicochemical properties (such as redox potential, solubility and so on) can also be tuned by molecular engineering. My efforts have been putting on design highly water-soluble and stable ferrocene derivative and other metal-free molecules, for example, viologen, (2,2,6,6-Tetramethylpiperidin-1-

yl)oxyl (TEMPO), and anthraquinone derivatives. Their electrochemical properties and battery performance were evaluated with comprehensive techniques. Besides, we systematically studied the chemical decomposition mechanism of these active materials by UV-Vis monitoring, NMR characterization, and half-cell long term cycling. Elucidating the active material decomposition mechanism helps us to improve the molecular structure design for more stable organic redox active materials developing in the future.

Electrocatalysis is a process where electrochemical reactions happen on the surface of the electrodes which deliver or accept electrons. Electrocatalysis could provide another solution for valuable product synthesis with environment protection especially when it is integrated with renewable energy. I have been focusing on electrocatalytic CO₂ and N₂ fixation to synthesis carbohydrate and ammonia in aqueous media. Using CO₂ and water as the reactant, nitrogenase as the catalyst, we electrochemically synthesized formate with high efficiency. I also carefully examined the catalytic activity of Mo₂N for nitrogen reduction reaction (NRR). ¹⁵N₂ isotope labeling experiment revealed that instead of catalytic N₂ reduction, the ammonia formation is from nitride decomposition. The present results raise an urgent alert to the application of other metal nitrides or even nitrogen contained materials for electrocatalytic N₂ reduction reactions.

ACKNOWLEDGMENTS

First of all, I would like to express my sincere gratitude to my main advisor Prof. Tianbiao Liu for his continuous support and patient guidance of my Ph.D. study and research. He keeps encouraging me to perform deep and systematic scientific research, from which I would be benefited in my whole career life. He is also very attentive to my daily life. When I arrived United States, he not only picked me up at the airport but also help me to find temporary accommodation. I really appreciate all the help from Dr. Liu and his family.

I would like to take this chance to thank my Master's degree advisor Prof. Yong Na at Harbin Institute of Technology. When I was studying there, He spent a lot of time to teach me many research techniques personally. He also encouraged me to pursue Ph.D. study in United States. In addition, he provided me a lot of support to help me get through the applications for the Ph.D. study at USU and the scholarship for CSC. Without his help, I could not have the opportunity of studying at USU.

I would like to thank my co-advisor Prof. Lance C. Seefeldt for his support of part of my Ph.D. study and research, many academic suggestions, and the valuable advice of finding a postdoc position. Besides my advisors, I would like to thank other supervisory committee members, Prof. Bradley S. Davidson, Prof. Ryan Jackson, and Prof. Bill Doucette for their valuable encouragement, comments, and suggestions.

I would like to thank my labmates in Liu's group. I would like to thank Dr. Jian Luo for helping me to proofread my dissertation. I also would like to thank Dr. Shuijian He, Dr. Yujing Bi, Camden Debruler, Kevin Nielson, Jared Moss, Maowei Hu, Wenda Wu, and Liping Zhang, for their help during last four years. It is my great pleasure to

work with all of them. I thank Dr. Zhiyong Yang, Dr. Derek Harris for their help on my nitrogenase research in Seefeldt's group.

I would like to thank the China Scholarship Council for the financial supporting of my study and living in the United States. Of course, I also thank the Department of Chemistry and Biochemistry at USU for giving me the opportunity to study here.

I would like to give my special thanks to my family for the support and love - my parents, Guoxiang Hu and Mingzhen Yan; and my sisters Jie Hu and Die Hu. Their love inspire me to face every challenge with courage. I will keep proactive and make myself always be their proud.

At this moment, I would like to say thank you from my deep heart to my beloved girl, Xiaolei Wang, for her love, care, encouragement, understanding, support, and waiting.

CONTENTS

	Page
ABSTRACT.....	iii
PUBLIC ABSTRACT	v
ACKNOWLEDGMENTS	vii
LIST OF TABLES	xi
LIST OF FIGURES	xii
CHAPTER	
I. INTRODUCTION	1
1-1. Background and motivation	1
1-2. Classification for redox flow batteries.....	5
1-3. Important parameters for redox flow batteries' performance and electrocatalysis performance evaluation	7
1-4. Materials design for Aqueous organic redox flow batteries.....	10
1-5. Catalysts for electrocatalytic CO ₂ and N ₂ reduction	12
1-6. Thesis scope.....	14
1-7. References	15
II. (FERROCENYLMETHYL)TRIMETHYLAMMONIUM CHLORIDE AS A STABLE AND HIGHLY SOLUBLE CATHODE MATERIAL FOR AQUEOUS ORGANIC REDOX FLOW BATTERIES.....	20
2-1. Abstract	20
2-2. Introduction	21
2-3. Materials and methods.....	24
2-4. Results and discussion	27
2-5. Conclusion	48
2-6. References	48
III. BOOSTING ENERGY EFFICIENCY AND POWER PERFORMANCE OF NEUTRAL AQUEOUS ORGANIC REDOX FLOW BATTERIES	52
3-1. Abstract	52
3-2. Introduction	52
3-3. Materials and methods.....	55
3-4. Results and discussion	57
3-5. Conclusion	75
3-6. References	76
IV. IMPROVING THE CAPACITY AND STABILITY OF THE VIOLOGEN BASED REDOX FLOW BATTERIES	79

4-1. Abstract	79
4-2. Introduction	80
4-3. Materials and methods	82
4-4. Results and discussion	85
4-5. Conclusion	106
4-6. References	106
V. AMMONIUM FUNCTIONALIZED ANTHRAQUINONE AS AN ANODE MATERIAL FOR NEUTRAL AORFBS	110
5-1. Abstract	110
5-2. Introduction	110
5-3. Materials and methods	113
5-4. Results and discussion	115
5-5. Conclusion	134
5-6. References	135
VI. ELECTROCATALYTIC CARBON DIOXIDE REDUCTION TO FORMATE ON A NITROGENASE MODIFIED BIOELECTRODE	138
6-1. Abstract	138
6-2. Introduction	139
6-3. Materials and methods	141
6-4. Results and discussion	144
6-5. Conclusion	156
6-6. References	156
VII. EVALUATING THE HETEROGENEOUS ELECTROCATALYTIC REDUCTION OF NITROGEN TO AMMONIA BY TETRAGONAL MOLYBDENUM NITRIDE	161
7-1. Abstract	161
7-2. Introduction	161
7-3. Materials and methods	163
7-4. Results and discussion	165
7-5. Conclusion	174
7-6. References	174
APPENDICES	
APPENDICE A. TABLES AND FIGURES	177
APPENDICE B. COPYRIGHTS	183
CURRICULUM VITAE	188

LIST OF TABLES

Table	Page
1-1. Typical CO ₂ and N ₂ reduction reactions and their equilibrium potentials	10
3-1. A summary of the thickness of the DSV, AMV, and ASV membranes and their resistances (R_{hf}) in the NaCl and KCl supporting electrolytes	110
3-2. A comparison of the diffusion (D) and electron transfer rate constants (k^0) of FcNCl and MV in 0.5 M NaCl and KCl supporting electrolytes	113
3-3. A comprehensive comparison of battery resistance (R_{hf}), energy efficiency (EE) and capacity utilization at 60 mA/cm ² , power density, and capacity retention per cycle (200 cycles) of the FcNCl/MV AORFBs using various anion exchange membranes and supporting electrolytes	115
3-4. Energy efficiency (EE) and capacity utilization at 40, 80, and 100 mA/cm ² for 0.5 M (13.4 Ah/L theoretical capacity) FcNCl/MV AORFBs using various anion ion exchange membranes and supporting electrolytes	134
4-1. Electrochemical data of FcN, MV ²⁺ and MV ^{•+} in 1.0 M LiTFSI CH ₃ CN solution	135

LIST OF FIGURES

Figure	Page
1-1. Graphic representation of diverse applications and cell components of redox flow batteries (RFBs)	2
1-2. Schemes of (A) single cell, (B) H-type cell and (C) flow cell for electrocatalytic CO ₂ and N ₂ reduction.....	5
1-3. Classification of redox flow batteries and the common redox active materials applied in aqueous redox flow batteries.	7
1-4. Redox reactions for 4-OH-TEMPO (left), 4-sulfonate-TEMPO (middle), and 4-trimethylammonium-TEMPO (right)	12
2-1. Cyclic voltammograms of FcNCl (red trace), FcN ₂ Br ₂ (purple trace), FcN (black trace), and MV (blue trace). The dashed curve is the cyclic voltammogram of 0.5 M NaCl, labeled with the onset potentials for hydrogen evolution reaction (HER, -1.00 V) and oxygen evolution reaction (OER, 1.50 V)	30
2-2. Cyclic Voltammograms of (A) FcNCl and (C) FcN ₂ Br ₂ at various scan rates from 0.05 V/s to 16 V/s; The plot of i _c and i _a over the square root of scan rates for (B) FcNCl and (D) FcN ₂ Br ₂ (blue trace for oxidation and red trace for reduction). Conditions: 4.0 mM analyte in 0.5 M NaCl electrolyte; glassy carbon working electrode; glassy carbon counter electrode; Ag/AgCl reference electrode	31
2-3. (A) Linear sweep voltammograms of FcNCl (1.0 mM in 0.5 M NaCl); (B) Levich plots of the limiting current vs the square root of rotation rates for FcNCl; (C) The plot of overpotential over the logarithm of kinetic current and the corresponding fitted Tafel plot at 2400 rpm for FcNCl; (D) Linear sweep voltammograms of FcN ₂ Br ₂ (1.0 mM in 0.5 M NaCl); (E) Levich plots of the limiting current vs the square root of rotation rates for FcN ₂ Br ₂ ; (F) The plot of overpotential over the logarithm of kinetic current and the corresponding fitted Tafel plot at 2400 rpm for FcN ₂ Br ₂	33
2-4. Conductivity measurements of (A) FcNCl and (B) MV (C) FcN ₂ Br ₂ from 0.05 M to 1.0 M in NaCl solution at different concentrations, 1.0 M (orange diamond trace), 1.5 M (blue circle trace), and 2.0 M (red triangle trace) at R.T.....	36
2-5. A schematic representation of the FcNCl/MV AORFB and illustrations of discharged and charged states of FcNCl and MV, and cell reactions	37

- 2-6. UV-Vis spectra of FcNCl compound (top) in different states (orange trace for fully charged state and blue trace for fully discharged trace); UV-Vis spectra of MV compound (bottom) in different states (orange trace for fully charged state and blue trace for fully discharged trace); Conditions: for MV 0.1 mM in 2 M NaCl aqueous solution; for FcNCl 1.0 mM in 2.0 M NaCl aqueous solution; All the samples were prepared under nitrogen atmosphere38
- 2-7. Capacity vs cycling numbers from 40 to 100 mA/cm² for the FcNCl/MV AORFB (A) and the FcN₂Br₂/MV AORFB (B). Representative charge and discharge profiles of the FcNCl/MV AORFB (C) and the FcN₂Br₂/MV AORFB (D) from 40 to 100 mA/cm². Plots of averaged coulombic efficiency (blue triangle), energy efficiency (orange circle), and voltage efficiency (green cross) versus current density of the FcNCl/MV AORFB (E) and the FcN₂Br₂/MV AORFB (F). Conditions: catholyte, 0.5 M FcNCl (or FcN₂Br₂) in 2.0 M NaCl aqueous solution; anolyte, 0.5 M MV in 2.0 M NaCl aqueous solution; AMV anion exchange membrane39
- 2-8. (A) Extended 700 cycle testing data of the 0.5 M FcNCl/MV AORFB at 60 mA/cm²: capacity and coulombic efficiency vs cycling numbers (for clarity, data points with an increment of 10 cycles were used for plotting); inset: representative charge and discharge profiles of selected cycles. (B) Extended 500 cycle testing data of the 0.7 M FcNCl/MV AORFB at 60 mA/cm². (C) The representative charge/discharge voltage profiles over time of the 0.5 M FcNCl/MV AORFB at 60 mA/cm² current density41
- 2-9. Polarization and power density curves of the FcNCl/MV AORFB at 0.5 M (red traces) and 0.7 M (blue traces) after full charge using 10 mA/cm²42
- 2-10. Plot of energy efficiency vs cycling numbers for the (A) 0.5 M FcNCl/MV AORFB and (B) 0.7 M FcNCl/MV AORFB at 60 mA/cm²; Nyquist plot of the FcNCl/MV AORFB at (C) 0.5 M and (D) 0.7 M before cycling. Conditions: catholyte, 0.7 M FcNCl in 2.0 M NaCl aqueous solution; anolyte, 0.7 M MV in 2.0 M NaCl aqueous solution; AMV anion exchange membrane43
- 2-11. Comparison of the ¹H NMR spectra of the FcNCl electrolyte (0.5 M in 2.0 NaCl solution) After (top) and before (middle) cycling at the same concentration (diluted to 10 mM in D₂O) under the same conditions. ¹H NMR spectrum of the MV electrolyte after cycling. The proton resonances of the ¹H NMR spectrum of FcNCl after cycling are slightly broadened with a small shift and it is attributed to the presence of a tiny amount of paramagnetic

charged FcNCl (Fe^{3+} oxidation state). The unlabeled large peak at 4.6 ppm in both spectra is assigned to the NMR solvent proton residue, HOD, and H_2O from the electrolyte samples.....	44
2-12. Post-cell CV studies for FcNCl and MV from anode and cathode after 700 cycles indicating no electrolyte crossover; concentration: 4 mM analyte in 0.5 M NaCl aqueous solution; glassy carbon working electrode; glassy carbon counter electrode; Ag/AgCl reference electrode. Each CV only shows redox waves belonged to each individual compound. No redox wave of FcNCl was observed in the CV of MV, and vice versa	45
2-13. (A) Capacity vs. cycle number, (B) energy efficiency vs. cycle number, (C) power density of 0.5 M FcNCl/MV AORFB. Conditions: catholyte, 12 mL 0.5 M FcNCl in 1.5 M NaCl aqueous solution; anolyte, 12 mL 0.5 M MV in 1.5 M NaCl aqueous solution; AMV anion exchange membrane; charging/discharging current density, 60 mA/cm^2	46
2-14. A bar chart comparison of theoretical energy density, demonstrated energy density, and tested cycles labeled with capacity retention per cycle of the FcNCl/MV AORFB and reported representative AORFBs. Chemical abbreviations: 2,6-AQDS, anthraquinon-2,6-disulfonic acid; DHAQ, 2,6-dihydroxyanthraquinone; alloxazine, alloxazine 7/8-carboxylic acid; TEMPTMA, N,N,N,2,2,6,6-heptamethylpiperidinyloxy-4-ammonium chloride.	47
3-1. (A) Nyquist plots of a dummy RFB cell using 2.0 M NaCl without an anion exchange membrane (black trace) and with the DSV (orange trace), AMV (gray trace), and ASV (blue trace) membranes (B) Nyquist plots of AORFB/DSV/NaCl (orange trace), AORFB/AMV/NaCl (gray trace), and AORFB/ASV/NaCl (blue trace); 0.5 M active materials in 2.0 M NaCl.....	59
3-2. (A) Capacity vs. cycle number from 40 to 100 mA/cm^2 of the 0.5 M FcNCl/MV AORFBs with different membranes (see legends) using 2.0 M NaCl supporting electrolyte. (B) Energy efficiency vs. cycle number from 40 to 100 mA/cm^2 of the FcNCl/MV AORFBs with different membranes using 2.0 M NaCl supporting electrolyte. (C) Representative voltage profile vs capacity of the FcNCl/MV AORFBs recorded at 60 mA/cm^2 with various membranes. (D) Polarization and power density curves of the FcNCl/MV AORFBs with different membranes using 2.0 M NaCl supporting electrolyte. Conditions: 0.5 M active materials in 2.0 M supporting electrolyte	60

- 3-3. Conductivity measurement of FcNCl (A) and MV (B) from 0 to 1.0 M in 2.0 M KCl or 2.0 M NaCl solutions at room temperature. (C) Conductivity dependence vs concentration of FcNCl and MV solutions without supporting electrolyte64
- 3-4. Cyclic voltammograms of FcNCl (0.6 V, red trace) and MV (-0.45 V, blue trace) in 0.5 M KCl. The dashed curves are the cyclic voltammograms of FcNCl and MV in 0.5 M NaCl. Conditions: 4 mM FcNCl or MV in 0.5 M KCl or NaCl supporting electrolyte; working electrode, glassy carbon electrode; reference electrode, Ag/AgCl electrode; counter electrode, carbon rod; scan rate, 100 mV/s66
- 3-5. Electrochemical kinetic studies of FcNCl (1.0 mM) and MV (1.0 mM) in 0.5 M KCl. (A) and (E) Linear sweep voltammograms of FcNCl and MV; (B) and (F) Levich plots of the limiting current vs the square root of rotation rates for FcNCl; (C) and (G) Koutechý-Levich plots of FcNCl and MV; (D) and (H) Tafel plots of FcNCl and MV67
- 3-6. (A) Capacity vs. cycle number from 40 to 100 mA/cm² of the FcNCl/MV AORFBs with different membranes (see legends) using 2.0 M KCl supporting electrolyte. (B) Energy efficiency vs. cycle number from 40 to 100 mA/cm² of the FcNCl/MV AORFBs with different membranes using 2.0 M KCl supporting electrolyte. (C) Representative voltage profiles vs capacity of the FcNCl/MV AORFBs recorded at 60 mA/cm² with different membranes. (D) Polarization and power density curves of the FcNCl/MV AORFBs with different membranes using 2.0 M KCl supporting electrolyte. Conditions: 0.5 M active materials in 2.0 M supporting electrolyte69
- 3-7. (A) Nyquist plots of a dummy RFB cell using 2.0 M KCl without an anion exchange membrane (black trace) and with the DSV (orange trace), AMV (gray trace), and ASV (blue trace) membranes. (B) Nyquist plots of AORFB/DSV/KCl (orange trace), AORFB/AMV/KCl (gray trace), and AORFB/ASV/KCl (blue trace); 0.5 M active materials in 2.0 M KCl72
- 3-8. Discharge capacity vs. Cycle number at 60 mA/cm² of FcNCl/MV RFBs with various membranes and supporting electrolytes: (A) NaCl as supporting electrolyte, and (B) KCl as supporting electrolyte73
- 3-9. Plots of energy efficiency vs cycling numbers at 60 mA/cm² for the 0.5 M FcNCl/MV AORFBs using DSV, AMV, and ASV membranes using (A) 2.0 M NaCl and (B) 2.0 M KCl supporting electrolyte73

3-10. Representative voltage profile vs capacity of the FcNCl/MV AORFBs recorded at 40, 80, and 100 mA/cm ² with various membranes using NaCl or KCl supporting electrolyte: (A) 40 mA/cm ² , NaCl; (B) 80 mA/cm ² , NaCl; (C) 100 mA/cm ² , NaCl; (D) 40 mA/cm ² , KCl; (E) 80 mA/cm ² , KCl; (F) 100 mA/cm ² , KCl	74
4-1. Cyclic voltammograms of (NPr) ₂ V (red trace), MV (blue trace), and N ^{Me} -TEMPO (orange trace) in 0.5 M NaCl aqueous solution. Conditions: 4 mM active materials in 0.5 M NaCl; working electrode, glassy carbon electrode; reference electrode, Ag/AgCl electrode; counter electrode, carbon rod; scan rate, 100 mV/s	86
4-2. (A) Schematic representation of viologen/TEMPO anion exchange AORFBs and illustrations of discharged and charged states of viologen anolyte and TEMPO catholyte and cell reactions. (B) Overview of viologen/TEMPO AORFBs reported to date	86
4-3. Battery performance of 0.5 M (NPr) ₂ V/NMe-TEMPO AORFB. (A) Rate performance at different charging/discharging current density. (B) Average coulombic efficiency (CE), voltage efficiency (VE), and energy efficiency (EE) at different charging/discharging current density. (C) Capacity and CE versus cycle number for 500 cycles. Insert is the representative charge/discharge profiles. Battery was cycled at 60 mA/cm ² . (D) Polarization and power density curves of the AORFB at 100% SOC	88
4-4. Battery performance of 0.5 M MV/N ^{Me} -TEMPO AORFB. (A) Rate performance at different charging/discharging current density. (B) Averaged Coulombic efficiency (CE), voltage efficiency (VE) and energy efficiency (EE) at different charging/discharging current density. (C) Capacity and CE versus cycle number for 500 cycles. Inserted is the representative voltage versus capacity profiles. Battery is cycled at 60 mA/cm ² . (D) Polarization curve and power density of the 0.5 M MV/N ^{Me} -TEMPO AORFB	89
4-5. Nyquist plot of the (A) MV/N ^{Me} -TEMPO AORFB and (B) (NPr) ₂ V/N ^{Me} -TEMPO AORFB RFB before cycling	90
4-6. EPR spectra (black) of [MV] ^{•+} (top) and [(NPr) ₂ V] ^{•+} (bottom) and the corresponding spectral simulations (red). The simulation parameters are indicated in the figure	91
4-7. UV-vis spectra of (A) [MV] ^{•+} and (B) [(NPr) ₂ V] ^{•+} in 2 M NaCl aqueous	

solution over 48 hours.....	92
4-8. Proposed favorable dimerization of $[MV]^{+\bullet}$ and unfavorable dimerization of $[(NPr)_2V]^{+\bullet}$. The red double arrows indicate charge repulsion between the pendent ammonium groups	93
4-9. Half-cell studies of $[(NPr)_2V]^{+\bullet}$ and $[MV]^{+\bullet}$ radical cation stability. (A) Capacity vs. cycle number of $MV/MV^{+\bullet}$ half-cell RFB in 200 cycles (Insert: voltage vs. capacity of $MV/[MV^{+\bullet}]$ half-cell RFB of the selected cycles); (B) Capacity vs. cycle number of $(NPr)_2V/[(NPr)_2V]^{+\bullet}$ half-cell RFB in 200 cycles (Insert: voltage vs. capacity of $(NPr)_2V/[(NPr)_2V]^{+\bullet}$ half-cell RFB of the selected cycles). Conditions: 0.5 M active materials in 2 M NaCl, pH value was adjusting to 7 by 10 M NaOH solution	94
4-10. (A) Cyclic voltammogram of a mixture of 1.0 mM FcNTFSI and 1.0 mM MVTFSI. (B) Repeated cyclic voltammetry curves of a 1.0 mM FcNTFSI and 1.0 MVTFSI mixture. Conditions: Glassy carbon as working electrode, Ag/AgNO ₃ as reference electrode, galssy carbon rod as counter electrode, 1.0 M LiTFSI in CH ₃ CN as supporting electrolyte	96
4-11. (A) Linear sweep voltammograms of 1.0 mM FcNTFSI (positive side) and 1.0 mM MVTFSI (negative side) on a rotating glssy carbon electrode in 1.0 M LiTFSI/CH ₃ CN supporting electrolyte; (B) Levich plots of the limiting current vs the square root of rotation rates for FcNTFSI; (C) Levich plots of the limiting current vs the square root of rotation rates for MVTFSI.....	98
4-12. Nicholson's analysis for evaluation of k_0 of FcNTFSI and MVTFSI. (A) CV of FcNTFSI at various scan rates (5, 10, 20, 40, 70, 100, 150, 200, 300, 500, 700, 1000, 1500, 2000, 5000 mV/s). (B) Plot of Ψ versus ΔE_p of the reduction peak and oxidation peak of FcNTFSI. (C) Linear relationship between Ψ and $v^{1/2}$ of FcNTFSI. (D) CV of MVTFSI at various scan rate (5, 10, 20, 40, 70, 100, 150, 200, 300, 500, 700, 1000, 1500, 2000, 5000 mV/s). (E) Plot of Ψ versus ΔE_p of the reduction peak and oxidation peak of the 1 st redox wave of MVTFSI. (F) Linear relationship between Ψ and $v^{1/2}$ of the 1 st reduction/oxidation of MVTFSI.....	99
4-13. Plot of i_c and i_a over the square root of scan rates for FcNTFSI (A) and MVTFSI (B). Conditions: 1.0 mM FcNTFSI, and 1.0 mM MVTFSI mixture. Glassy carbon as working electrode, Ag/AgNO ₃ as reference	

electrode, galssy carbon as counter electrode, 1.0 M LiTFSI in CH ₃ CN as supporting electrolyte	100
4-14. Nyquist plots of the 1 electron utilized FcNTFSI/MVTFSI non-aqueous RFB with mixed electrolyte	102
4-15. Battery performance of one electron utilized FcNTFSI /MVTFSI NAORFB with a mixed electrolyte (0.1 M FcNTFSI and 0.1 M MVTFSI). (A) Voltage versus capacity profile at different charging/discharging current density. (B) Averaged Coulombic efficiency, voltage efficiency and energy efficiency at different charging/discharging current density. (C) Capacity versus cycle number for 100 cycles. Battery is cycled at 30 mA/cm ² . (D) Representative voltage versus capacity profiles	103
4-16. Performance of 2 electron utilized FcNTFSI /MVTFSI NAORFB with mixed electrolyte (0.2 M FcNTFSI and 0.1 M MVTFSI). (A) Voltage versus capacity profile at different charging/discharging current density. (B) Averaged Coulombic efficiency, voltage efficiency and energy efficiency at different charging/discharging current density. (C) Capacity versus cycle number for 100 cycles. Battery is cycled at 30 mA/cm ² . (D) Representative voltage versus capacity profiles	104
4-17. (A) Energy efficiency vs. cycle number of the FcNTFSI (0.1 M)/MVTFSI (0.1 M) NAORFB. (A) Energy efficiency vs. cycle number of the FcNTFSI (0.2 M)/MVTFSI (0.1 M) NAORFB. Current density: 30 mA/cm ²	105
5-1. A comparison of the solubility of AQSSa (yellow), AQSNH ₄ , and AQDSNa ₂ , and AQDS(NH ₄) ₂ . (Inserted scheme: Synthesis of AQDS(NH ₄) ₂) .	116
5-2. (A) ¹ H NMR titration of 50 mM AQDSNa ₂ in D ₂ O with various equivalents of NH ₄ Cl from 1 to 20. Ammonium hydroxide solution was used to adjust the pH value to 7.0. (B) Relationship between ¹ H-NMR chemical shift and the equivalent of ammonium. (C) 2D NMR (COSY) spectrum of 0.1 M AQDS(NH ₄) ₂ in D ₂ O, pH was adjusted to 3 to guarantee the observation of ammonium cation in the spectrum. (D) Schematic hydrogen bonding interactions proposed for AQDS(NH ₄) ₂	118
5-3. ¹³ C NMR of AQDSNa ₂ and AQDS(NH ₄) ₂ in D ₂ O.....	119
5-4. ¹ H NMR titration of 5 mM AQSSa in D ₂ O with 10 and 20 equivalents of	

NH ₄ Cl.....	119
5-5. ¹ H NMR titration of 5 mM sodium 2,4-dimethylbenzenesulfonate in D ₂ O with 10 and 20 equivalents of NH ₄ Cl	120
5-6. ¹ H NMR tests of AQDS(NH ₄) ₂ in D ₂ O at 80 °C for 2 weeks.	120
5-7. (A) Cyclic voltammograms of AQDS(NH ₄) ₂ at various pH conditions. (B) Pourbaix diagram of AQDS(NH ₄) ₂ in 0.5 M NH ₄ I solution. Conditions: 4.0 mM analyte in 0.5 M NH ₄ I electrolyte; scan rate: 100 mV/s; working electrode, glassy carbon electrode; counter electrode, glassy carbon; reference electrode, Ag/AgCl. The pH value was adjusted using ammonium hydroxide solution. FcNCl (-0.60 V vs. NHE at pH 7) was used to calibrate the redox potential.	122
5-8. RDE test: (A) Linear sweep voltammograms of AQDS(NH ₄) ₂ on a glassy carbon rotating disk electrode; (B) Levich plot of the limiting current vs the square root of rotation rates for AQDS(NH ₄) ₂ ; Conditions: 1.0 mM analyte in 0.5 M NH ₄ I electrolyte; scan rate: 5 mV/s; rotation rates from 300 to 2400 rpm; working electrode, glassy carbon rotating disk electrode; counter electrode, glassy carbon; reference electrode, Ag/AgCl. Scan rate study and Nicholson's analysis of AQDS(NH ₄) ₂ : (C) CV of AQDS(NH ₄) ₂ at various scan rates (5, 10, 20, 50, 100, 200, 300, 500, 1000, 2000, 5000 mV/s). (D) The plot of <i>i</i> _c and <i>i</i> _a over the square root of scan rates for AQDS(NH ₄) ₂ (blue trace for oxidative reaction, orange trace for reductive reaction); (E) Plot of Ψ versus 2Δ <i>E</i> _p of AQDS(NH ₄) ₂ . (F) The linear relationship between Ψ and <i>v</i> ^{1/2} of AQDS(NH ₄) ₂	123
5-9. Profile of voltage versus time of the 1 M AQDS(NH ₄) ₂ /NH ₄ I neutral AORFB. Conditions: catholyte, 3 M NH ₄ I solution (18 mL); anolyte, 1 M AQDS(NH ₄) ₂ in 1 M NH ₄ I; current density 40 mA/cm ²	125
5-10. (A) Cyclic voltammogram of 4 mM AQDS(NH ₄) ₂ (in 0.5 M NH ₄ I) and NH ₄ I (in 0.5 M NH ₄ Cl), respectively (pH=7). (B) Schematic representation of the AQDS(NH ₄) ₂ /NH ₄ I neutral AORFB and cell reactions	126
5-11. EIS test of the 0.75 M AQDS(NH ₄) ₂ /I ₂ RFB before and after cycling at 0 SOC.....	127
5-12. (A) Capacity decay of the 0.75 M AQDS(NH ₄) ₂ /NH ₄ I AORFB in the first	

10 cycles due to active material dimerization. After that, the capacity kept stable. (B) Charging/discharging profile for the mixed electrolyte of AQDS(NH ₄) ₂ and (AQDS(NH ₄) ₄). During discharging, the second plateau showed up at 0.2 V, standing for the oxidation of the formed dimer compound in the charging process.....	128
5-13. Battery performance of the 0.75 M AQDS(NH ₄) ₂ /NH ₄ I neutral AORFB. (A) Capacity vs. the cycle number from 40 to 100 mA/cm ² of the battery. 5 cycles' test was conducted for each current density; (B) Voltage versus capacity profile at different charging/discharging current density (Red dash line stands for the theoretical value); (C) Averaged coulombic efficiency, voltage efficiency, and energy efficiency at different charging/discharging current density; (D) Power density of the battery at various state of charge; (E) Capacity versus cycle number for 300 cycles. The battery is cycled at 60 mA/cm ² . Inset: selected representative voltage versus capacity profiles	129
5-14. (A) Representative charging/discharging profile (voltage versus time) of the 0.75 M neutral AQDS(NH ₄) ₂ /I ₂ RFB. (B) Representative charging/discharging profile (voltage versus time) of the 0.75 M neutral AQDS(NH ₄) ₂ /I ₂ RFB	130
5-15. Cyclic voltammetry post analysis of the anolyte of 0.75 M AQDS(NH ₄) ₂ /I ₂ RFB after cycling for 300 cycles.....	131
5-16. ¹ H NMR post analysis of the anolyte of 0.75 M AQDS(NH ₄) ₂ /I ₂ RFB after cycling for 300 cycles.....	132
5-17. Comparison of demonstrated energy densities and capacity retention per month of the selected AQ based AORFBs (Capacity retention lower than 80 % per month was not displayed in the figure)	133
6-1. Schematic showing nitrogenase catalysis with electron transfer from the Fe protein and ATP hydrolysis (left) or from cobaltacene mediated electron catalysis (right) for the MoFe or FeFe proteins catalyzing proton and CO ₂ reduction	141
6-2. Cyclic voltammetry of Cobaltocenium (Cc ⁺) on glassy carbon with and without NaHCO ₃ . Conditions: 0.2 mM Cc ⁺ in 50 mM HEPES buffer solution (PH=7.4)	146

6-3. Schematic of the crosslink reaction among PVA, EDGDE and nitrogenase protein.....	146
6-4. Cyclic voltammetry evaluation of the catalytic performance of Cc^+ mediated FeFe-protein bio-electrode. The grey trace is the CV of Cc^+ on bare glassy carbon electrode. Others CVs were all obtained based on the same FeFe-protein immobilized electrode with the increased $NaHCO_3$ concentration. Conditions: working electrode, MoFe protein modified glassy carbon electrode; reference electrode, saturated calomel electrode (SCE); counter electrode, Platinum wire; supporting electrolyte, 50 mM HEPES buffer (pH=7.4); Cc^+ concentration, 0.4 mM; scan rate, 5 mV/s.....	148
6-4. A. Continuously CV scans of pyrene modified FeFe electrode. (The 4 th , 5 th , 6 th curves are almost overlapped.) B. Cyclic voltammetry of cobaltocenium on bare glassy carbon electrode (solid line) and pyrene modified electrode	149
6-5. Cyclic voltammetry of cobaltocenium mediated electrocatalysis by MoFe protein (top) and FeFe protein (bottom) in the absence (blue traces) and presence of sodium bicarbonate as CO_2 source (red traces). CV traces for a bare glassy carbon electrode under Ar (GC-Ar, black traces) are shown as a control.....	150
6-6. Bulk bioelectrosynthetic reduction of 200 mM $NaHCO_3$ in stirred 50 mM HEPES buffer solution (with 200 mM NaCl and 0.4 mM cobaltocenium) by MoFe (blue trace) and FeFe protein (red trace) bioelectrodes	152
6-7. Percentage of electrons going to different products when driven by Fe protein/ATP (left) or electrocatalysis (right) for the MoFe protein (MoFe) or FeFe protein (FeFe). H_2 is shown in blue, and formate is shown in yellow.....	154
6-8. 1H -NMR of product of bioelectrocatalytic reduction of CO_2 by MoFe electrode	155
6-9. 1H -NMR of product of bioelectrocatalytic reduction of CO_2 by FeFe electrode	155
7-1. XRD pattern of the synthesized Mo_2N . The blue pattern is the standard PDF card for γ - Mo_2N	166
7-2. Top: SEM image elemental mapping of the synthesized γ - Mo_2N . Bottom:	

EDS scanning of Mo and N elements for the selected area, showing homogeneous distribution	167
7-3. (A) LSV curves for γ -Mo ₂ N@Ti electrode in N ₂ and Ar saturated HCl supporting electrolyte (pH=1). Scan rate: 50 mV/s. (B) Chronoamperometric curves for the electrolysis at various controlled potentials with N ₂ as the feeding gas. (C) UV-Vis tests (indophenol-blue assay) for ammonium after electrolysis at various controlled potential. (D) Faradaic efficiency and reaction rate at different potentials	168
7-4. (A) UV-vis measurements of indophenol-blue standard samples with various concentration of NH ₄ Cl. (B) Linear fitting for the absorbance versus NH ₄ Cl concentration. The final standard linear relationship was converted to concentration of ammonia as $y = 0.4431x + 0.0327$ ($R^2 = 0.9989$)	169
7-5. ¹ H NMR spectra of ammonium in the sampled electrolytes after one hour's electrolysis in the presence of saturated ¹⁵ N ₂ and ¹⁴ N ₂ , respectively	170
7-6. Indophenol-blue assay for ammonium after the electrodes were immersed in the different supporting electrolytes (labeled) for 1 hour	171
7-7. Ammonium tests after Mo ₂ N was treated for (A) 2 days and (B) 4 days. (C) Images of the samples treated by various electrolyte for 1 week. Note in (C): Mo ₂ N dissolved in 0.1M NaOH after 1 week	172
7-8. (A) Chronoamperometric curve for the electrolysis at -0.15 V vs. RHE with N ₂ as the feeding gas. (B) UV-Vis tests for the product after 1 hour's and 5 hours' reaction	173

CHAPTER I

INTRODUCTION ^a

1-1. Background and motivation

Redox Flow Batteries

The utilization of renewable energy sources such as solar and wind energy represents a sustainable and environmentally benign strategy to alleviate the world's severe dependency on traditional fossil fuels.¹ It is estimated that 68% of today's electrical energy is supplied from fossil fuels while only 3% from renewable energy technologies.² However, under the pressure of global warming and climate change, more attention and efforts have been focused on renewable energy utilization. For example, global wind power generation capacity is expected to reach 474 GW in the year 2020, about a 5 times increase as compared to 2007.² In order to manage the intermittent and fluctuating nature of solar and wind energy, cost-effective technologies for energy conversion and storage are in urgent need.¹⁻³ Among numerous energy storage technologies, redox flow batteries (RFBs, Figure 1-1) have been recognized as a promising technology to overcome the intermittency of renewable energy and supply reliable electricity to electricity grids with a scale up to MW/MWh.²⁻⁴

Redox flow batteries (RFBs) operate in the general mechanism of a rechargeable battery by using redox active chemicals dissolved in liquid supporting electrolyte

^a Partially adapted with permission from [Hu, B., Luo, J., DeBruler, C., Hu, M., Wu, W., Liu, T. L. (2019). Redox-Active Inorganic Materials for Redox Flow Batteries. In Encyclopedia of Inorganic and Bioinorganic Chemistry]. Copyright 2019. WILEY-VCH Verlag GmbH & Co. KGaA, Weinheim. Reproduced by permission of WILEY-VCH Verlag GmbH & Co. KGaA, Weinheim. <https://onlinelibrary.wiley.com/doi/abs/10.1002/9781119951438.eibc2679>

solutions stored in two reservoirs (Figure 1-1). The redox active liquid electrolytes are termed as anolyte in the anode side and catholyte in the cathode side, respectively. A separator (ion exchange membrane or porous membrane) sandwiched between two electrodes allows the crossover of supporting electrolytes while prohibiting the crossover of active materials. During charge/discharge processes, redox reactions (see Equation 1-1 and 1-2) happen on the surface of the electrode while supporting ions (such as H^+ , Na^+ , and Cl^-) migrate through the ion exchange membrane to balance the charge.

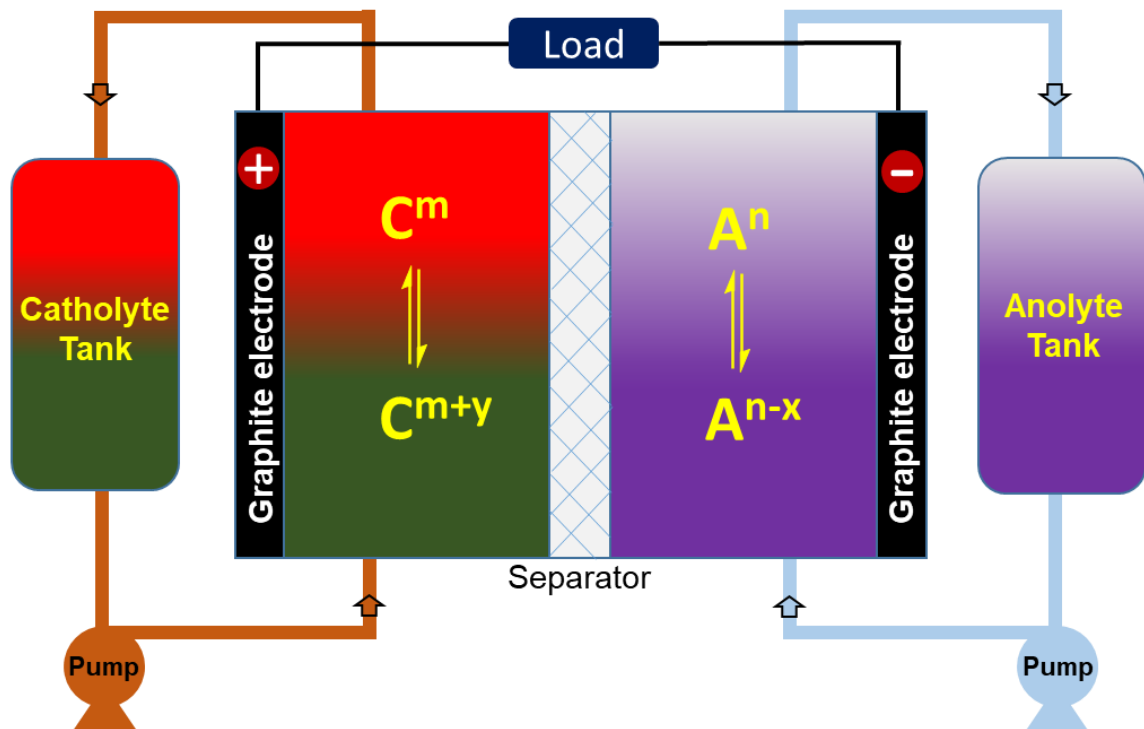
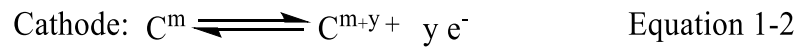


Figure 1-1. Graphic representation of diverse applications and cell components of redox flow batteries (RFBs).

Thereby, a flow battery is able to store or release electrical energy. The unique cell architecture of RFBs empowers a number of attractive technological merits for large-scale energy storage in comparison to traditional static rechargeable batteries. First, RFBs can modulate their energy (the volume of the electrolyte reservoirs) and power (electrode surface area) independently, which makes the power supply more facile to manage.²⁻⁴ Second, RFBs can operate at high current and high power densities due to fast electrochemical kinetics and high conductivities of aqueous supporting electrolytes. Third but not last, RFBs represent a safe energy storage technology by using non-flammable aqueous electrolyte materials. In addition to centralized grid-scale energy storage, RFBs with their technological merits are suitable for relatively small-scale decentralized energy storage applications including residential and commercial power backups, remote micro-grids, charge stations for electric vehicles and fuel productions. It is worth noting that it is also promising to develop high energy density RFBs as direct power sources for electrical vehicles. Redox active material is the core part of the RFB. Therefore, it is of great importance to develop low cost and stable active materials to obtain RFBs' wide application in the future.

Electrocatalytic Carbon Dioxide and Nitrogen Reduction

Extensive consumption of fossil fuels within less than two hundred years has resulted in the truth that the concentration of CO₂ in the atmosphere increased dramatically from 280 ppm at the beginning of the industrial revolution in the 19th century to about 408 ppm in 2018, which has caused serious substantial environmental impacts.⁵ The fact that fossil fuel keeps as the main energy form will still remain for many years. Nowadays, in order to alleviate the pressure from both increasing energy

demanding and more serious climate challenge, heterogeneous electrocatalytic CO₂ reduction is both hot topics toward valuable fuel synthesis in a way that is more energy efficient and environmentally benign. The century-old Haber-Bosch process remains to be the only industrial process to achieve large scale ammonia production more than 150 million tons per year.⁶ Despite its wide application, the Haber-Bosch process is massively energy consuming (ca. 2% of the world's energy supply), heavily fossil fuel dependent (3% - 5% of the world's natural gas production), and greenhouse gas emitting (more than 400 million tons).⁷ The massive energy consumption and CO₂ emitting are mainly from the CH₄ reforming to generate the H₂ feedstock for the next N₂ hydrogenation reaction.⁷ By electrocatalytic N₂ reduction, nitrogen reacts with protons in aqueous electrolytes, thus avoiding the use of H₂ gas as the reactant. Meanwhile, electrocatalytic N₂ reduction could be manipulated at ambient conditions. Therefore, the electrochemical synthesis ammonia is very appealing regarding both energy saving and environment protection.

A three-electrode system can be employed to evaluate the performance of the CO₂ and N₂ electrocatalytic reduction in a single cell, H-type cell, and flow cell as shown in Figure 1-2. The H-type cell for the CO₂ and N₂ reduction could avoid the oxygen influence for the reactions due to the gas impermeable ion exchange membrane sandwiched between the two half-cells. The catalyst was deposited on the surface of glassy carbon or carbon paper and worked as the working electrode. Saturated calomel electrode or Ag/AgCl was applied as the reference electrode. Platinum wire or carbon rod electrode was applied as the counter electrode.

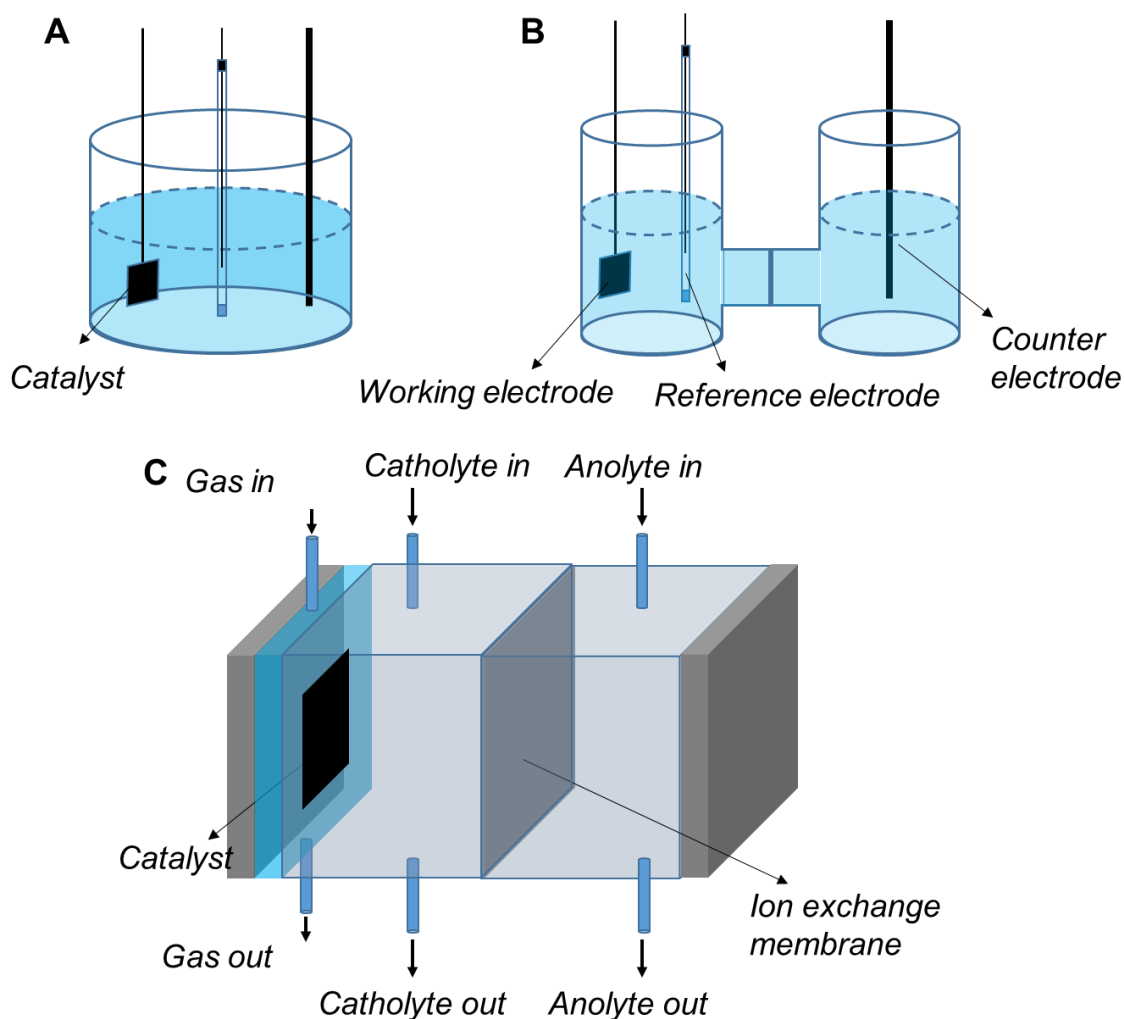


Figure 1-2. Schemes of (A) single cell, (B) H-type cell and (C) flow cell for electrocatalytic CO₂ and N₂ reduction.

1-2. Classification for redox flow batteries

As shown in Figure 1-3, the redox flow batteries can be classified as nonaqueous RFBs (using organic solvent) and aqueous RFBs (using aqueous electrolyte) according to the solvent. Due to the large electrochemical window of organic solvent, the main advantage of the nonaqueous redox flow battery is the high voltage. However, the challenge from the aspect of materials (high cost solvent and supporting electrolyte, active materials crossover) limited their application. Compared to the nonaqueous RFB,

the aqueous RFB delivers lower cell voltage. Nevertheless, the much lower cost, much longer lifetime, and superior safety make it a better choice for practical application. Among the various active materials, a few inorganic systems (Fe-Cr, Zn-Br₂, all-vanadium) have been demonstrated for large scale applications. Since the invention of the all-vanadium redox flow battery (VRFB) at the University of New South Wales, Sydney (Australia) by Skyllas-Kazacos *et al.* in the 1980s, the all-vanadium RFBs have been receiving massive studies and continuous commercialization.⁸ Nevertheless, the capital cost of this RFB system remains too high to enable the broad application at both residential and industrial scale, although it represents the most mature RFB system for large scale energy storage in terms of well-developed battery chemistry and system components. According to the “Energy Storage Technology and Cost Characterization Report” from the Pacific Northwest National Laboratory (PNNL), the price for all vanadium RFBs still remains about \$500 per kW/h, way above the Department of Energy’s target (\$150 per kWh).⁹ Compared to the vanadium source used in VRFB, redox active organic molecules could be cheaper, more sustainable and redox potential tunable, thus draw more and more attention for scientific research. Based on the different pH values applied to various active materials, the AORFBs can be divided into acidic AORFBs, alkaline AORFBs, and pH neutral AORFBs. Anthraquinone (AQDS) and phenazine derivatives were mainly applied to acid or alkaline conditions to guarantee good solubility.²⁵⁻²⁷ Viologen, ferrocene and TEMPO derivatives are only stable at pH neutral conditions, which were intensively studied by our group and others for pH neutral AORFBs application.^{21-24, 30} We also developed a pH neutral AQDS based AORFB by

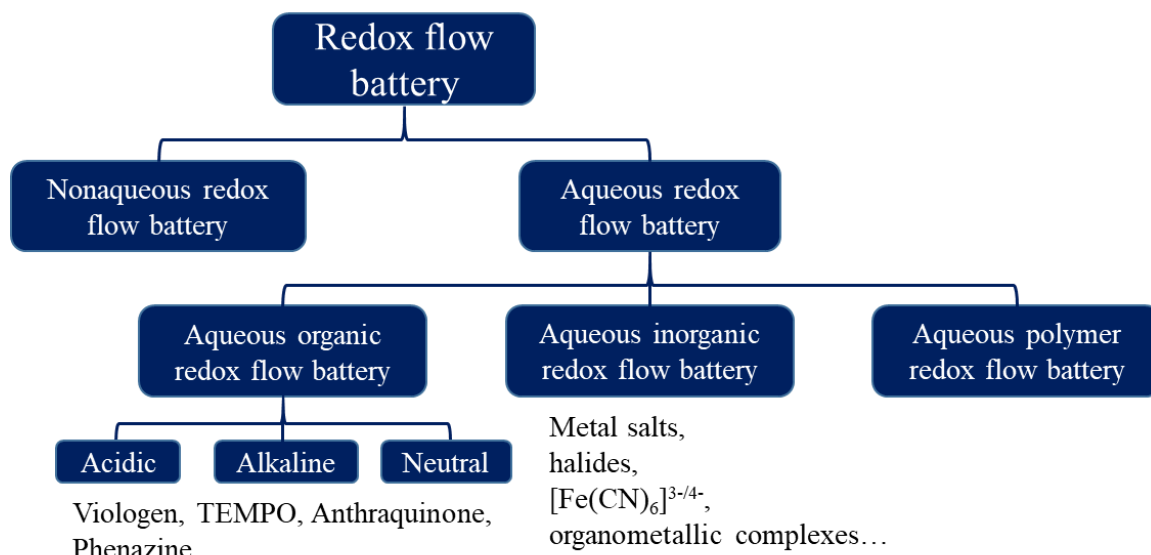


Figure 1-3. Classification of redox flow batteries and the common redox active materials applied in aqueous redox flow batteries.

using the ammonium cation functionalized AQDS derivative which was highly soluble even at pH neutral condition.

1-3. Important parameters for redox flow batteries' performance and electrocatalysis performance evaluation

Important parameters for redox flow batteries

Volumetric energy density as a key parameter for a RFB which stands for the amount of energy that can be stored in the battery per liter electrolyte (Wh/L). The volumetric energy density of a RFB is determined by its cell voltage (V) and charge capacity (Ah/L) as shown in Equation 1-4. Charge capacity (C) is further determined by the concentrations of active materials, and the number of electrons involved in the redox reactions given by Equation 1-3, where n is the number of electrons, F is the faradic constant, c is the concentration of the more soluble electrolyte material between the anolyte and catholyte, μ is the volume factor for the full cell and defined as (1+

$V_{\text{larger}}/V_{\text{smaller}}$ (V_{smaller} is the volume for the less soluble electrolyte and V_{larger} is the volume for the more soluble electrolyte).

$$C = nFc \quad \text{Equation 1-3}$$

$$\text{Energy density} = CV = \frac{nFc}{\mu} V \quad \text{Equation 1-4}$$

The efficiencies of RFBs are manifested by Coulombic efficiency (CE), Voltage efficiency (VE), and energy efficiency (EE) as defined subsequently. Coulombic efficiency (CE) is the ratio between discharge capacity and charge capacity. CE is an important indicator that can reflect active material crossover and irreversible side reactions if it is apparently lower than 100 %.¹⁰ Voltage efficiency (VE) is the ratio between discharge voltage and charge voltage, which reflects the charge/discharge overpotential of the battery. The multiplication of CE and VE gives energy efficiency (EE).

Power density is another important parameter that evaluates the response speed of the RFB systems. It is the product of the output current density and voltage of the battery which is various at different state of charge. For a typical aqueous RFB system, the power density is from about 100 mW/cm² to 1 W/cm², due to the fast redox kinetics, fast mass diffusion, and overall low cell resistance.

Important parameters for electrocatalysis

For electrocatalytic CO₂ and N₂ reduction, the most important parameters are current density and faradaic efficiency (FE). Current density stands for the reaction rate of the catalysis. The most commonly applied current density is geometric current density, i.e. the current density calculated from the overall current divided by electrode geometric surface area. In this case, more porous materials that allow better accessibility of the

substrate to the active sites tend to show higher current density. Therefore, efforts have been made to develop electrocatalyst with larger surface area, such as ultrathin 2D nanosheets,¹¹ nanowires,¹² and single-atom catalysts,^{13,14} to increase the catalytic current density. Meanwhile, cautions have been raised appealing for a more reasonable and scientific way to compare the current density among various catalysts by electrochemical active surface area to avoid overestimating or underestimating for catalytic current density.¹⁵

FE represents the reaction selectivity which can be calculated by Equation 1-5, where $n_{product}$, n_e , F and Q is the amount of product, amount of electron for the reaction, the faradaic constant and total amount of charge, respectively. For CO₂ electrocatalytic reduction, CO was reported as the main product for most of the heterogeneous catalysis where H₂ is the main side product. For N₂ catalytic reduction, the desired product is ammonia. However, the FE for ammonia production is normally lower than 20% due to the strongly competitive hydrogen evolution reaction.

$$FE = \frac{n_{product} n_e F}{Q} \quad \text{Equation 1-5}$$

Turnover number (TON) and turnover frequency (TOF) evaluation for heterogeneous catalysis are more complicated due to unclear numbers of active sites. Therefore, reasonable models are required to estimate the number of the active site for TON and TOF calculation.¹⁵

Overpotential is also important to evaluate the energy efficiency of the reactions. It is calculated as the difference between the onset potential and the thermodynamic

potential. Typical CO₂ and N₂ reduction reactions and their equilibrium potentials were shown in Table 1-1. To avoid the proton concentration influence on these potentials, RHE was commonly applied as the reference, which can be calculated as Equation 1-6.

$$E_{RHE} = E_{NHE} + 0.059pH \quad \text{Equation 1-6}$$

Table 1-1. Typical CO₂ and N₂ reduction reactions and their equilibrium potentials.^{16,17}

Reactions	Equilibrium potential (vs. RHE)
CO ₂ + 2 H ⁺ + 2 e ⁻ → HCOOH	-0.197 V
CO ₂ + 2 H ⁺ + 2 e ⁻ → CO + H ₂ O	-0.117 V
CO ₂ + 4 H ⁺ + 4 e ⁻ → HCHO + H ₂ O	-0.067 V
CO ₂ + 6 H ⁺ + 6 e ⁻ → CH ₃ OH + H ₂ O	0.033 V
CO ₂ + 8 H ⁺ + 8 e ⁻ → CH ₄ + 2 H ₂ O	0.173 V
2 CO ₂ + 12 H ⁺ + 12 e ⁻ → C ₂ H ₄ + 4 H ₂ O	-0.064 V
N ₂ + 2 H ₂ O + 6 H ⁺ + 6 e ⁻ → 2 NH ₄ OH	0.156 V
2H ⁺ + 2e ⁻ → H ₂	0 V

1-4. Materials design for aqueous organic redox flow batteries

As shown in Figure 1-2, Active materials applied in redox flow batteries are very diverse such as redox active metal salt,^{18,19} nonmetal inorganic materials,²⁰ organometallic compounds,²¹⁻²³ organic molecules,²⁴⁻²⁷ and even polymers.²⁸ The satisfactory redox active molecules are required to show the following properties: high solubility in aqueous electrolyte, suitable redox potential, excellent chemically and electrochemically stability, and overall charges containing.

High solubility and suitable redox potential of the molecules enable a high energy density of the battery. For example, in order to compete with the VRFB (25 ~ 35 Wh/L), the active materials of a 1.2 V AORFB need to have a solubility of 1.6 M to 2.2 M at all

states of charge in the supporting electrolyte. For the AORFB with a cell voltage lower than 1 V, the solubility of active materials needs to be at least 1.9 M to achieve an energy density of 25 Wh/L. In order to improve the solubility of active materials, a general idea is improving the interaction between the organic molecules and water molecules, i.e. improving the solvation of the redox active molecules. Strategies have been reported as introducing hydrophilic groups and adding additives to strengthen hydrogen bonding, which both demonstrated substantial solubility boost of various materials.^{21-23,30} However, high concentrated electrolyte always displays very high viscosity which dramatically decreases the electrolyte conductivity and results in poor rate performance, low energy efficiency, and increased external energy consumption from pump operation. This viscosity issue brings in another challenge for the active material design. Therefore, active materials displaying multiple-electron redox property is especially desired for improving the energy density without dramatically increasing materials' concentration.

The stability and charges bearing features are directly relevant to the lifetime of the battery. Specifically, chemical decomposition irreversibly induced charging/discharging capacity decay with the increase of cycle number due to the loss of redox active materials. In aqueous systems, proton and hydroxide involved HER, OER, and nucleophilic attack contributes most to the side reactions. Combined with a deep understanding of the chemical decomposition mechanism, the molecular design could be conducted to avoid these disadvantageous side reactions. The charge-neutral species generated during electrochemical reaction would cross through the ion exchange membrane and lead to cross contamination, which could also irreversibly capacity decay, low coulombic efficiency and loss of the state of charge. Taking 4-OH-TEMPO/MV

system²⁴ as an example, the charge-neutral 4-OH-TEMPO free radical showed crossover through the anion exchange membrane during the charging/discharging process and caused fast capacity decay (Figure 1-4, left). For the 4-sulfonate-TEMPO/Zn RFB,²⁹ although the cathode TEMPO derivative is anion charged, it oxidized oxoammonium product is overall charge-neutral and could also cross through the Nafion-based cation exchange membrane (Figure 1-4, middle). Increasing charges of the TEMPO and maintaining the overall charges at all SOC is an effective strategy to overcome the crossover issue (Figure 1-4 right).³⁰

1-5. Catalysts for electrocatalytic CO₂ and N₂ reduction

In the past few years, electrocatalytic CO₂ and N₂ reduction have been under intensive study. Many efficient catalysts were reported for CO₂ reduction with impressive FE and current density, such as noble metals,³¹⁻³³ non-precious metals,³³ metal oxides,^{34,35} single-atom catalysts^{13,14} and so on. In addition to the inorganic heterogeneous catalysts, some molecular catalyst, such as metal porphyrins and metal phthalocyanines were also applied in both homogeneous and heterogeneous catalysis for CO₂ reduction.³⁷⁻³⁹ In these reactions, CO was reported as the main product for most of the heterogeneous catalysis where H₂ is the main side product. Some materials (such as Bi, Sn, Pb) could catalyze the CO₂ reduction to formate or formic acid.⁴⁰ Copper is the only inorganic

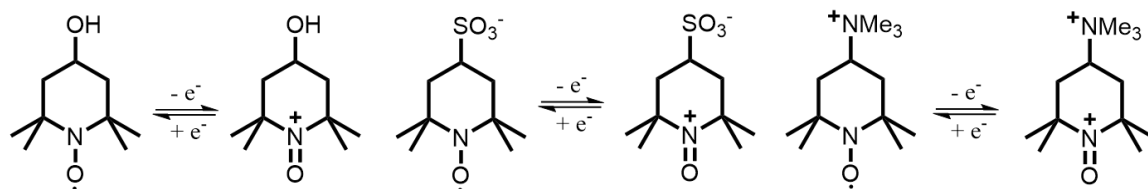


Figure 1-4. Redox reactions for 4-OH-TEMPO (left), 4-sulfonate-TEMPO (middle), and 4-trimethylammonium-TEMPO (right).

catalyst that can catalyze the direct CO₂ reduction to C-C coupling leaded carbon hydrates (C₂H₄, C₂H₅OH, C₃H₇OH, etc.) as the main products, although the selectivity is always difficult to be controlled.⁴¹ By enhancing the hydrophobicity of the surface of the Cu catalyst, a high FE for C₂H₄ was obtained more than 50 %.⁴¹ Nitrogenase is famous for its capability to catalyzed N₂ reduction to ammonia at ambient conditions.

Interestingly, it was found that nitrogenase could also catalyze CO₂ reduction to various products besides N₂ fixation.⁴² The Mo- and V-nitrogenase has also been shown to reduce CO₂ to CH₄ and C₂ and C₃ hydrocarbons. In vivo studies with the Fe-nitrogenase indicate that this enzyme shows the highest CO₂ reduction to CH₄ of the three nitrogenases.⁴³ However, the homogeneous in vivo studies required ATP as the energy source. Applying nitrogenase as an electrocatalyst could bypass the use of ATP and improve the reaction selectivity.

Due to these potential benefits, electrocatalytic N₂ fixation has been under intensive exploration over the last few years and has become a hot topic in catalysis. A number of heterogeneous electrocatalysts have been reported with a various claimed performance for NRR, including noble metals,^{17,44,45} metal oxides,⁴⁶ metal sulfides,⁴⁷ metal nitrides,^{48,49} and metal-free catalysts^{50,51}. In this 6 proton-coupled 6 electron transfer process, the rate determine step for NRR remains unclear although lots of DFT calculations have been conducted. Most of the catalyst design is aiming at improving the nitrogen adsorption on the surface the catalyst. The average performance of the NRR was demonstrated with the FE of < 20% and the yield of ammonia < 50 µg mg_{catalyst}⁻¹ h⁻¹. With such a low reaction rate, any forms of ammonia contamination could bring in an overestimation of the catalyst performance. Besides, strict control experiments are

essential to eliminate contaminations and catalyst decomposition, especially for those nitrogen contained catalysts.

1-6. Thesis scope

In this dissertation, I summarized my work on redox flow batteries and electrocatalysis for CO₂ and N₂ reduction.

In chapter I, a general introduction for redox flow battery mechanism, principals for active materials design, and catalysts for CO₂ and N₂ reduction was presented.

In chapter II, I introduced my research on stable and highly water soluble ferrocene derivatives for neutral AORFB application, which represents the first ferrocene based aqueous electrolyte. By introducing hydrophilic trimethylammonium group in the molecule, the solubility of resulted **FcNCl** was up to 4 M in water while the ferrocene precursor is barely soluble in water.

In chapter III, systematic studies on the separator and supporting electrolyte effect on the FcNCl/MV RFBs were summarized. A general strategy was put forward for improving the energy efficiency and power density of the neutral AORFBs.

In chapter IV, I presented my study on elucidating the radical cation decomposition mechanism for methyl viologen anolyte. UV-Vis spectroscopy and half-cell studies supported the proposed mechanism. Guided by the mechanism, we synthesized (NPr)₂V which displayed performance improvement for the pH neutral AORFBs.

In chapter V, a cation exchange strategy was introduced to improve the solubility of Anthraquinone-2,7-disulfonate salt. The solubility improvement was attributed to the enhanced hydrogen bonding among anthraquinone, ammonium cation, and water

molecules. The mechanism was proved by ^1H NMR titration and 2D NMR (COSY). A 0.75 M AQDS(NH_4)₂/NH₄I was demonstrated with no capacity decay after 300 charging/discharging cycles.

In chapter VI, FeFe-protein and MoFe-protein from nitrogenase were immobilized on the surface of the glassy carbon electrode. The obtained bioelectrodes showed good catalytic activity for CO₂ reduction to formate with an overpotential of only 72 mV. This bio-electrochemical approach for CO₂ reduction bypassed the use of ATP in homogeneous catalysis.

In chapter VII, I presented a careful evaluation of the catalytic activity of Mo₂N for N₂ reduction to ammonia. $^{15}\text{N}_2$ isotope labeling and time-dependent experiments were conducted. The results revealed that ammonium was produced from the chemical decomposition of the nitride catalyst instead of electrocatalytic reduction of N₂ feeding gas.

1-7. References

- (1) Dunn, B.; Kamath, H.; Tarascon, J.-M. *Science* **2011**, *334*, 928.
- (2) Yang, Z.; Zhang, J.; Kintner-Meyer, M. C. W.; Lu, X.; Choi, D.; Lemmon, J. P.; Liu, J. *Chem. Rev.* **2011**, *111*, 3577.
- (3) Soloveichik, G. L. *Chem. Rev.* **2015**, *115*, 11533.
- (4) Wang, W.; Luo, Q.; Li, B.; Wei, X.; Li, L.; Yang, Z. *Adv. Funct. Mater.* **2013**, *23*, 970.
- (5) <https://www.esrl.noaa.gov/gmd/ccgg/trends/index.html> **2018**.
- (6) Nations., F. a. A. O. o. t. U. *World fertilizer trends and outlook to 2020*. **2017**.

- (7) Wang, L.; Xia, M.; Wang, H.; Huang, K.; Qian, C.; Maravelias, C. T.; Ozin, G. A. *Joule* **2018**, 2, 1055.
- (8) Skyllas-Kazacos, M.; Cao, L.; Kazacos, M.; Kausar, N.; Mousa, A. *ChemSusChem* **2016**, 9, 1521.
- (9) PNNL *Energy Storage Technology and Cost Characterization Report*. **2019**.
- (10) Jan, W.; Tino, H.; Tobias, J.; D., H. M.; S., S. U. *Angew. Chem. Int. Ed.* **2017**, 56, 686.
- (11) Han, N.; Wang, Y.; Yang, H.; Deng, J.; Wu, J.; Li, Y.; Li, Y. *Nat. Commun.* **2018**, 9, 1320.
- (12) Zhu, W.; Zhang, Y.-J.; Zhang, H.; Lv, H.; Li, Q.; Michalsky, R.; Peterson, A. A.; Sun, S. *J. Am. Chem. Soc.* **2014**, 136, 16132.
- (13) Zheng, T.; Jiang, K.; Ta, N.; Hu, Y.; Zeng, J.; Liu, J.; Wang, H. *Joule* **2019**, 3, 265.
- (14) Gu, J.; Hsu, C.-S.; Bai, L.; Chen, H. M.; Hu, X. *Science* **2019**, 364, 1091.
- (15) Voiry, D.; Chhowalla, M.; Gogotsi, Y.; Kotov, N. A.; Li, Y.; Penner, R. M.; Schaak, R. E.; Weiss, P. S. *ACS Nano* **2018**, 12, 9635.
- (16) Sun, Z.; Ma, T.; Tao, H.; Fan, Q.; Han, B. *Chem* **2017**, 3, 560.
- (17) Wang, J.; Yu, L.; Hu, L.; Chen, G.; Xin, H.; Feng, X. *Nat. Commun.* **2018**, 9, 1795.
- (18) Li, L.; Kim, S.; Wang, W.; Vijayakumar, M.; Nie, Z.; Chen, B.; Zhang, J.; Xia, G.; Hu, J.; Graff, G.; Liu, J.; Yang, Z. *Adv. Energy Mater.* **2011**, 1, 394.
- (19) Li, B.; Nie, Z. M.; Vijayakumar, M.; Li, G. S.; Liu, J.; Sprenkle, V.; Wang, W. *Nat. Commun.* **2015**, 6, 6303.
- (20) Li, Z.; Weng, G.; Zou, Q.; Cong, G.; Lu, Y.-C. *Nano Energy* **2016**, 30, 283.
- (21) Hu, B.; DeBruler, C.; Rhodes, Z.; Liu, T. L. *J. Am. Chem. Soc.* **2017**, 139, 1207.

- (22) DeBruler, C.; Hu, B.; Moss, J.; Liu, X.; Luo, J.; Sun, Y.; Liu, T. L. *Chem* **2017**.
- (23) Beh, E. S.; De Porcellinis, D.; Gracia, R. L.; Xia, K. T.; Gordon, R. G.; Aziz, M. J. *ACS Energy Lett.* **2017**, 639.
- (24) Liu, T. B.; Wei, X. L.; Nie, Z. M.; Sprenkle, V.; Wang, W. *Adv. Energy Mater.* **2016**, 6.
- (25) Lin, K. X.; Chen, Q.; Gerhardt, M. R.; Tong, L. C.; Kim, S. B.; Eisenach, L.; Valle, A. W.; Hardee, D.; Gordon, R. G.; Aziz, M. J.; Marshak, M. P. *Science* **2015**, 349, 1529.
- (26) Lin, K.; Gómez-Bombarelli, R.; Beh, E. S.; Tong, L.; Chen, Q.; Valle, A.; Aspuru-Guzik, A.; Aziz, M. J.; Gordon, R. G. *Nat. Energy*. **2016**, 1, 16102.
- (27) Huskinson, B.; Marshak, M. P.; Suh, C.; Er, S.; Gerhardt, M. R.; Galvin, C. J.; Chen, X. D.; Aspuru-Guzik, A.; Gordon, R. G.; Aziz, M. J. *Nature* **2014**, 505, 195.
- (28) Janoschka, T.; Martin, N.; Martin, U.; Friebe, C.; Morgenstern, S.; Hiller, H.; Hager, M. D.; Schubert, U. S. *Nature* **2015**, 527, 78.
- (29) Winsberg, J.; Stolze, C.; Schwenke, A.; Muench, S.; Hager, M. D.; Schubert, U. S. *ACS Energy Lett.* **2017**, 2, 411.
- (30) Janoschka, T.; Martin, N.; Hager, M. D.; Schubert, U. S. *Angew. Chem. Int. Ed.* **2016**, 55, 14425.
- (31) Min, X.; Kanan, M. W. *J. Am. Chem. Soc.* **2015**, 137, 4701.
- (32) Kortlever, R.; Peters, I.; Koper, S.; Koper, M. T. M. *ACS Catal.* **2015**, 5, 3916.
- (33) Hori, Y.; Wakebe, H.; Tsukamoto, T.; Koga, O. *Electrochim. Acta* **1994**, 39, 1833.
- (34) Hori, Y.; Takahashi, I.; Koga, O.; Hoshi, N. *J. Mol. Catal. A.* **2003**, 199, 39.

- (35) Ren, D.; Deng, Y.; Handoko, A. D.; Chen, C. S.; Malkhandi, S.; Yeo, B. S. *ACS Catalysis* **2015**, *5*, 2814.
- (36) Sharma, P. P.; Wu, J.; Yadav, R. M.; Liu, M.; Wright, C. J.; Tiwary, C. S.; Yakobson, B. I.; Lou, J.; Ajayan, P. M.; Zhou, X.-D. *Angew. Chem. Int. Ed.* **2015**, *54*, 13701.
- (37) Lieber, C. M.; Lewis, N. S. *J. Am. Chem. Soc.* **1984**, *106*, 5033.
- (38) Costentin, C.; Drouet, S.; Robert, M.; Savéant, J.-M. *Science* **2012**, *338*, 90.
- (39) Shen, J.; Kortlever, R.; Kas, R.; Birdja, Y. Y.; Diaz-Morales, O.; Kwon, Y.; Ledezma-Yanez, I.; Schouten, K. J. P.; Mul, G.; Koper, M. T. M. *Nat Commun.* **2015**, *6*, 8177.
- (40) Birdja, Y. Y.; Pérez-Gallent, E.; Figueiredo, M. C.; Göttle, A. J.; Calle-Vallejo, F.; Koper, M. T. M. *Nat. Energy.* **2019**, *4*, 732.
- (41) Wakerley, D.; Lamaison, S.; Ozanam, F.; Menguy, N.; Mercier, D.; Marcus, P.; Fontecave, M.; Mougél, V. *Nat. Mater.* **2019**, *18*, 1222.
- (42) Yang, Z.-Y.; Moure, V. R.; Dean, D. R.; Seefeldt, L. C. *Proc. Natl. Acad. Sci. U.S.A* **2012**, *109*, 19644.
- (43) Zheng, Y.; Harris, D. F.; Yu, Z.; Fu, Y.; Poudel, S.; Ledbetter, R. N.; Fixen, K. R.; Yang, Z.-Y.; Boyd, E. S.; Lidstrom, M. E.; Seefeldt, L. C.; Harwood, C. S. *Nat. Microbiol.* **2018**, *3*, 281.
- (44) Tao, H.; Choi, C.; Ding, L.-X.; Jiang, Z.; Han, Z.; Jia, M.; Fan, Q.; Gao, Y.; Wang, H.; Robertson, A. W.; Hong, S.; Jung, Y.; Liu, S.; Sun, Z. *Chem* **2019**, *5*, 204.
- (45) Bao, D.; Zhang, Q.; Meng, F.-L.; Zhong, H.-X.; Shi, M.-M.; Zhang, Y.; Yan, J.-M.; Jiang, Q.; Zhang, X.-B. *Adv. Mater.* **2017**, *29*, 1604799.

- (46) Zhang, G.; Ji, Q.; Zhang, K.; Chen, Y.; Li, Z.; Liu, H.; Li, J.; Qu, J. *Nano Energy* **2019**, *59*, 10.
- (47) Zhang, L.; Ji, X.; Ren, X.; Ma, Y.; Shi, X.; Tian, Z.; Asiri, A. M.; Chen, L.; Tang, B.; Sun, X. *Adv. Mater.* **2018**, *30*, 1800191.
- (48) Ren, X.; Cui, G.; Chen, L.; Xie, F.; Wei, Q.; Tian, Z.; Sun, X. *Chem. Commun.* **2018**, *54*, 8474.
- (49) Yang, X.; Nash, J.; Anibal, J.; Dunwell, M.; Kattel, S.; Stavitski, E.; Attenkofer, K.; Chen, J. G.; Yan, Y.; Xu, B. *J. Am. Chem. Soc.* **2018**, *140*, 13387.
- (50) Song, Y.; Johnson, D.; Peng, R.; Hensley, D. K.; Bonnesen, P. V.; Liang, L.; Huang, J.; Yang, F.; Zhang, F.; Qiao, R.; Baddorf, A. P.; Tschaplinski, T. J.; Engle, N. L.; Hatzell, M. C.; Wu, Z.; Cullen, D. A.; Meyer, H. M.; Sumpter, B. G.; Rondinone, A. *J. Sci Adv.* **2018**, *4*, e1700336.
- (51) Qiu, W.; Xie, X.-Y.; Qiu, J.; Fang, W.-H.; Liang, R.; Ren, X.; Ji, X.; Cui, G.; Asiri, A. M.; Cui, G.; Tang, B.; Sun, X. *Nat. Commun.* **2018**, *9*, 3485.

CHAPTER II

(FERROCENYLMETHYL)TRIMETHYLAMMONIUM CHLORIDE AS A STABLE
AND HIGHLY SOLUBLE CATHODE MATERIAL FOR AQUEOUS
ORGANIC REDOX FLOW BATTERIES ^b

2-1. Abstract

Redox flow batteries (RFBs) are a viable technology to store renewable energy in the form of electricity that can be supplied to electricity grids safely and reliably. To address the material based challenges (such as low abundance and high cost of active materials, expensive separators and electrolyte crossover) from traditional inorganic RFBs, we demonstrated a pH neutral aqueous organic redox flow battery (AORFB) technology utilizing a newly designed cathode electrolyte containing highly water-soluble ferrocene molecules. Specifically, water-soluble (ferrocenylmethyl)trimethylammonium chloride (**FcNCl**, 4.0 M in H₂O, 107.2 Ah/L) and *N*¹-ferrocenylmethyl-*N*¹, *N*¹, *N*², *N*², *N*²-pentamethylpropane-1,2-diammonium dibromide, (**FcN₂Br₂**, 3.1 M in H₂O, 83.1 Ah/L) were synthesized through structural decoration of hydrophobic ferrocene with synergetic hydrophilic functionalities including ammonium cation groups and halide anions. When paired with methyl viologen (MV) as an anolyte, the resulted FcNCl/MV and FcN₂Br₂/MV AORFBs displayed excellent performance in noncorrosive pH neutral NaCl supporting electrolytes. Notably, the FcNCl/MV AORFB

^b Adapted with permission from [Hu, B.; DeBruler C., Rhodes, Z.; Liu, T. L. *J. Am. Chem. Soc.*, **2017**, 139, 1207]. Copyright 2017. ACS Publications. Reproduced by permission of ACS Publications, <https://pubs.acs.org/doi/abs/10.1021/jacs.6b10984>.

exhibited unprecedented long cycling performance, 700 cycles at 60 mA/cm² with 99.99% capacity retention per cycle. To further improve the batteries' energy efficiency and power density to meet fast charge/discharge responses in the application of large scale electrochemical energy storage. We conducted a systematic study on the effects of ion exchange membranes and supporting electrolytes on the resistance and electrochemical performance of the FcNCl/MV AORFB. With an optimized combination of the membrane and the supporting electrolyte, unprecedented energy efficiency and power density were achieved at 85% at 40 mA/cm² or 79% at 60 mA/cm² and 122.7 mW/cm² for the neutral AORFB (0.5 M active materials). The present results emphasize the importance of minimizing battery resistance, and also further advance the promise of neutral AORFBs for sustainable and green energy storage of renewable energy.

2-2. Introduction

The increasing worldwide energy demand necessitates large scale and efficient utilization of renewable energy, such as solar, wind, and hydroelectric power.¹ Simultaneously, the utilization of renewable energy can address environmental challenges instigated by the production and burning of fossil fuels. However, the intermittence and fluctuating nature of these renewable energy resources have to be mitigated using effective energy storage solutions.¹⁻³ Redox flow batteries (RFBs) have been recognized as a viable technology for large-scale energy storage (up to MW/MWh) by government agencies, industrial partners, and research institutions.²⁻⁶ Compared to static rechargeable batteries (e.g. lead acid batteries and Li ion batteries), several technical merits enable RFBs to be well-suited for the integration of renewable energy and balancing electricity grids: high power input and output, decoupled energy and

power, safety features, and scalability (up to MW/MWh). Traditional inorganic RFBs, including vanadium RFBs and Zn-Br₂ RFBs, have evolved as relatively established technologies. However, their extensive applications for large scale energy storage suffer from several major techno-economical drawbacks, expensive and resource-limited active materials (vanadium RFBs), corrosive and hazardous electrolytes in both RFBs, low current performance (Zn-Br₂ RFBs due to Zn dendrite formation), electrolyte crossover, and expensive system costs, such as the Nafion membrane used in both RFBs. Thus, there is an urgent call to develop low cost and safe RFB technologies to meet burgeoning energy storage demands.

To address the challenges encountered by existing inorganic RFBs, we and others have proposed aqueous organic RFBs (AORFBs) employing sustainable and abundant redox-active organic molecules as a new generation of RFBs for green energy storage.⁷⁻¹⁴ In addition to the general features of RFBs discussed above, AORFBs have several outstanding advantages for large scale energy storage: 1) using organic redox-active materials consisting of earth-abundant elements is a sustainable practice, and they are also synthetically tunable to gain high oxidation/reduction redox potentials and high solubility, thus high energy density RFBs; 2) utilization of non-flammable aqueous electrolytes offers safety benefits; 3) aqueous electrolytes consisting water and simple inorganic supporting electrolytes such as NaCl, KOH, are inexpensive; 4) high-conductivity aqueous electrolytes and well-developed selective ion conductive membranes for aqueous electrolytes allow high power operation while achieving high energy efficiency. Specifically, we have been focusing on developing neutral aqueous organic RFBs for safe and low cost large-scale and residential energy storage using

sustainable, non-corrosive and non-flammable aqueous redox-active electrolytes and low cost ion exchange membranes.¹² Several groups including us have made significant progress in the emerging AORBF technology in the last few years, such as high power acid/alkaline AORBFs,^{7-11,14} and high voltage and low cost pH neutral AORBFs.^{12,13,15} Meanwhile, progress has also been made in developing non-aqueous organic RFBs (NAORFBs).¹⁶⁻²³

However, in spite of the rapid advances, most of the reported AORFBs and NAORFBs only displayed limited cycling performance (typically not more than 100 cycles), which is primarily attributed to the electrochemical and chemical instability of electrolyte materials. In addition, most of the reported AORFBs still have lower energy densities than the state of the art vanadium RFBs (41.8 Wh/L), which is limited by either catholyte or anolyte. We believe that these limitations can be mitigated by designing robust and high capacity redox active electrolyte materials.

Herein we introduce a stable cycling AORFB technology named ferrocene/MV AORFBs (Figure 1). This redox flow battery technology is constructed on newly designed catholyte containing a highly water-soluble redox-active ferrocene compound, (ferrocenylmethyl)trimethylammonium chloride (**FcNCl**, 107.2 Ah/L) or *N*¹-ferrocenylmethyl-*N*¹, *N*¹, *N*², *N*², *N*²-pentamethylpropane-1,2-diammonium dibromide, (**FcN₂Br₂**, 83.1 Ah/L), along with methyl viologen (MV) anolyte, a neutral NaCl supporting electrolyte, and a low cost anion exchange membrane. This is the first application of ferrocene compounds in AORFBs. These ferrocene/MV AORFBs are characterized by high theoretical energy density (up to 52.4 Wh/L), and excellent cycling performance from 40 mA/cm² to 100 mA/cm². Particularly, the FcNCl/MV AORFB

exhibited unprecedented cycling performance (700 cycles at 60 mA/cm² with 99.99% capacity retention per cycle. The presented results highlight the great promise of AORFBs for energy storage applications. Thereafter, we systematically studied the roles of electrolytes and separators played on the energy efficiency and power output of the FcNCl/MV AORFB. By utilizing more conductive supporting electrolyte and membrane, the batteries' energy efficiency and power density were boosted to 79% at 60 mA/cm² and 122.7 mW/cm², respectively.

2-3. Materials and methods

Materials

(Ferrocenylmethyl)dimethylamine was purchased from TCI chemicals. Methyl chloride (1 M in t-butylether) and (3-bromopropyl)trimethylammonium bromide were purchased from Sigma Aldrich. Methyl viologen was purchased from Acros Organics. All the chemicals were stored in an Argon glove box and used directly. All the solvents (CH₃CN, DMSO, diethyl ether) were purchase from fisher chemicals. Deionized water was obtained from a MilliporeSigma Milli-DI Water Purification System and purged overnight using N₂ before use. All experimental operations were conducted under N₂ atmosphere. SelemionTM ion exchange membranes were purchased from ASAHI GLASS CO., LTD, Japan. All ion exchange membranes were soaked in 0.5 M NaCl solution overnight before use.

Characterization

NMR studies were conducted using a Bruker 500 MHz NMR spectrometer. UV-Vis data were collected using an Ocean Optics spectrometer. Elemental analysis was

done at Atlantic Microlab. The conductivity of the electrolyte solutions was measured using a Mettler Toledo conductivity meter at R.T.

Materials synthesis

Synthesis of **FcNCl**: A 250 mL Schlenk flask was degassed with N₂ and maintained under N₂. (ferrocenylmethyl)dimethylamine (20 g, 82.3 mmol) and methyl chloride (1 M in t-butylether, 82.3 mL for 82.3 mmol, used 90 mL) were combined in 50 mL CH₃CN in the 250 mL flask. The reaction mixture was stirred at R.T. overnight. The red-orange precipitate was formed and collected by filtration. 100 mL of ether was added to the supernatant solution to precipitate a second crop of the product. The combined product was washed twice with 40 mL of ether and dried under vacuum. The product is hygroscopic and stored in a dry desiccator. The yield was ca. 95% (23.0 g). ¹H NMR (D₂O, 300 MHz): δ (in p.p.m.), 2.91 (s, 9 H), 4.24 (s, 5 H), 4.35 (s, 2H), 4.39 (s, 2H), 4.47 (d, 2H). Anal. calcd for C₁₄H₂₀NClFe·0.5 H₂O: C 55.53, H 6.94, N 4.63; found C 55.26, H 7.05, N 4.61.

Synthesis of **FcN₂Br₂**: **FcN₂Br₂** was synthesized from (ferrocenylmethyl)dimethylamine (3.4 g, 14 mmol) and (3-bromopropyl)trimethylammonium bromide (3.8 g, 14.5 mmol) in 10 mL DMSO in a procedure similar as **FcNCl**. The yield was 90.1 % (6.2 g). ¹H NMR (D₂O) δ (in p.p.m.), 2.25 (m, 2 H), 2.94 (s, 6 H), 3.12 (s, 9 H), 3.19 (t, 2 H), 3.31 (t, 2 H), 4.26 (s, 5 H), 4.42 (d, 2 H), 4.46 (s, 2 H), 4.48 (s, 2H).

Solubility tests

The solubility of **FcNCl**, **FcN₂Br₂**, **FcN**, and MV was measured in water by preparing a 1.0 mL super-saturated solution in a 5.0 mL graduated cylinder. Similar

solubility tests in water were conducted for ferrocenecarboxylic acid, 1-1'-ferrocenedicarboxylic acid, ferrocenecarboxylic acid, and 1,1'-ferrocenedimethanol.

Electrochemical cyclic voltammetry studies

All electrochemical cyclic voltammetry (CV) experiments were carried out in 0.5 M NaCl electrolyte solutions. Cyclic voltammetry experiments were performed with a Gamry 1000E potentiostat. All potentials were referenced to NHE according to the known $MV^{2+/1+}$ redox couple (-0.45 V vs NHE). The working electrode (1 mm PEEK-encased glassy carbon, Cypress Systems EE040) was polished using Al_2O_3 (BAS CF-1050, dried at 150 °C under vacuum) suspended in deionized H_2O , then rinsed with deionized H_2O and dried with airflow. The reference electrode consisted of a silver wire coated with a layer of AgCl and suspended in a solution of 0.5 M NaCl electrolyte. A glassy carbon rod (Structure Probe, Inc.) was used as the counter electrode. Before each measurement, the electrolyte was purged by nitrogen gas for 5 minutes.

Electrochemical linear sweeping voltammetry studies:

All linear sweeping voltammetry (LSV) studies were conducted using a Gamry 1000E potentiostat in a three-electrode configuration, a glassy carbon disk working electrode (5 mm Teflon encased glassy carbon disk, Pine Research Instrumentation) along with a glassy carbon counter electrode and a Ag/AgCl reference electrode as used in CV studies. All potentials were referenced to NHE according to the known $MV^{2+/1+}$ redox couple (-0.45 V vs NHE). Before data collection, the disk electrode was prepared using the procedure described in the CV studies. The electrode was then rotated from 300 to 2400 rpm with increments of 300 rpm, which was controlled by a Pine MSR rotator

system. LSV scans were recorded at a rate of 5 mV/s from 0.3 V to 0.8 V vs NHE. At each rotation rate, the LSV was recorded three times to ensure repeatability.

Flow cell tests

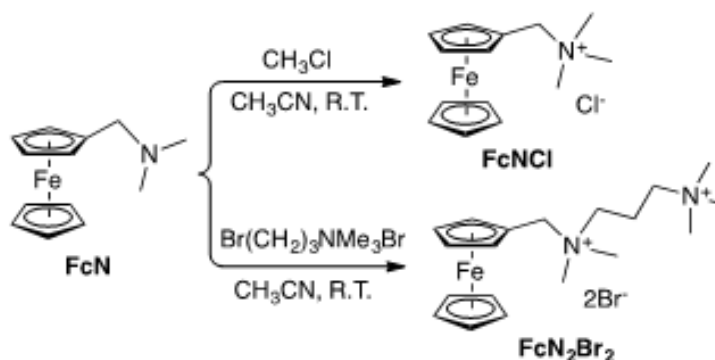
The flow cells for the FcNCl/MV AORFB and the FcN₂Br₂/MV AORFB were constructed with two carbon electrolyte chambers, two graphite felt electrodes (SGL Carbon Group, Germany) and a piece of anion exchange membrane (AMV, 120 μ m thickness, pore size < 10 Å, Selemion, Japan) sandwiched between graphite felts, and two copper current collectors. Each carbon chamber was connected with an electrolyte reservoir using a piece of Viton tubing. The electrolyte reservoir is home designed and is a 10 mL glass tube (2 cm inner diameter). The active area of the cell was 10 cm². A Masterflex[®] L/S[®] peristaltic pump (Cole-Parmer, Vernon Hills, IL) was used to press the Viton tubing to circulate the electrolytes through the electrodes at a flow rate of 60 mL/min. In each reservoir, the balanced flow cell employed 11-13 mL of the NaCl electrolytes containing 0.5 or 0.7 M active materials. Both reservoirs were purged with nitrogen to remove O₂ and then sealed before cell cycling. The flow cell was galvanostatically charged/discharged at R.T. on a battery tester (Land Instruments) in the voltage range of 1.5 – 0.1 V at current densities ranging from 40 to 100 mA/cm². The polarization curve and electrochemical impedance spectra were recorded using a Gamry 1000E potentiostat. The discharged and charged states of **FcNCl** and **MV** were measured using UV-Vis spectroscopy. Post cell studies of the FcNCl/MV AORFB using ¹H NMR and CV were conducted for both electrolytes at the end of the cell tests.

2-4. Results and discussion

Molecular design of FcNCl and FcN₂Br₂

Because of their reversible $\text{Fe}^{3+/2+}$ redox couple and thermal stability, the 1973 Nobel Prize-winning organometallic complex, ferrocene, and its derivatives have been utilized in a wide array of applications in chemistry and materials science since their discovery in the 1950s.²⁴⁻²⁶ In addition, the synthesis of ferrocene derivatives has been well developed, involving low-cost starting materials based on earth-abundant elements: C, H, N, O, and Fe. Thus, they are sustainable and can be low cost in large-scale production. However, most of the known ferrocene compounds are aliphatic or hydrophobic, i.e. only soluble in organic solvents. Thus, ferrocene compounds have been only applied as the cathode in a couple of semi-flow²¹ or static liquid²⁷ Li/ferrocene non-aqueous batteries. We rationalized that ferrocene compounds functionalized with hydrophilic groups could be water-soluble and demonstrate superior performance in aqueous RFBs. Obviously, we first screened commercially available ferrocene compounds functionalized with hydrophilic functional groups (ferrocenecarboxylic acid, 1,1'-ferrocenedicarboxylic acid, ferrocenecarboxylic acid, and 1,1'-ferrocenedimethanol). However, these ferrocene derivatives are only slightly soluble in water, < 100 mM, therefore, not suitable for applications in aqueous RFBs. We found that (ferrocenylmethyl)trialkylammonium iodides exhibited solubility in aqueous solutions,^{28,29} although (ferrocenylmethyl)dimethylethylammonium bis(trifluoro-methane) sulfonimide (TFSI, a hydrophobic anion) applied in the nonaqueous Li/ferrocene RFB was reported nearly insoluble in water.²¹ To apply the (ferrocenylmethyl)trialkylammonium redox-active moiety for ARFBs using selective Cl^- anion transfer mechanism, we are particularly interested in the (ferrocenylmethyl)trialkylammonium chloride redox-active species. In addition, compared to I^- (+ 0.55 V vs. NHE), Cl^- counter ion has a much higher oxidation

potential (+1.40 V vs. NHE) and will not interfere with the $\text{Fe}^{3+/2+}$ redox couple of (ferroc-enylmethyl)trialkylammonium moiety. Following the synthesis of (ferrocenylmethyl)tri-alkylammonium iodides, we prepared (ferrocenylmethyl)trimethylammonium chloride (**FcNCl**) through direct alkylation of (ferrocenylmethyl)dimethylamine (**FcN**) with CH_3Cl . Simply mixing of (ferrocenylmethyl)dimethylamine with CH_3Cl in CH_3CN at room temperature (R.T.) resulted in the formation of red-orange **FcNCl** precipitates with a 95% isolated yield (Scheme 2-1). The one-step N-alkylation reaction is quite straightforward and was demonstrated at 20 g scale. **FcNCl** was fully characterized by ^1H NMR, UV-VIS, and elementary analysis to establish its identity and purity. **FcNCl** is surprisingly highly soluble in H_2O with solubility ca. 4.0 M, corresponding to a capacity 107.2 Ah/L, a desired characteristic for RFB applications. Even in 2.0 M NaCl, the solubility of **FcNCl** was recorded at 3.0 M (80.4 Ah/L). The high-water solubility of **FcNCl** stimulated us to synthesize N^1 -ferrocenylmethyl- N^1 , N^1 , N^2 , N^2 , N^2 -pentamethylpropane-1,2-diammonium dibromide, **FcN₂Br₂** (Scheme 1), featured with two pendant ammonium groups. **FcN₂Br₂** exhibits a solubility of 3.1 M (83.1 Ah/L) in water, and 2.0 M (53.6 Ah/L) in 2.0 M NaCl.



Scheme 2-1. The synthesis of **FcNCl** and **FcN₂Br₂**

In contrast, pristine ferrocene (Cp_2Fe) and the precursor, (ferrocenylmethyl)dimethylamine, are insoluble or barely soluble in water. In addition, as stated above, (ferrocenylmethyl)dimethylethylammonium TFSI is also insoluble in water.²¹ It is believed that such high solubility of **FcNCl** and **FcN₂Br₂** is credited to the synergetic effects of their hydrophilic pendant ammonium functionality and halide counter ion.

CV studies of **FcNCl** and **FcN₂Br₂**

Cyclic voltammetry studies revealed a reversible $\text{Fe}^{3+/2+}$ redox couple at 0.61 V vs NHE for both **FcNCl** and **FcN₂Br₂** (Figure 2-1), indicating that the two ammonium substituents have nearly identical electronic influences on the ferrocene moiety. The pendent electron-withdrawing ammonium group of both compounds positively shifts the $\text{Fe}^{3+/2+}$ redox potential by 210 mV compared to the **FcN** precursor (+ 0.40 V vs NHE).

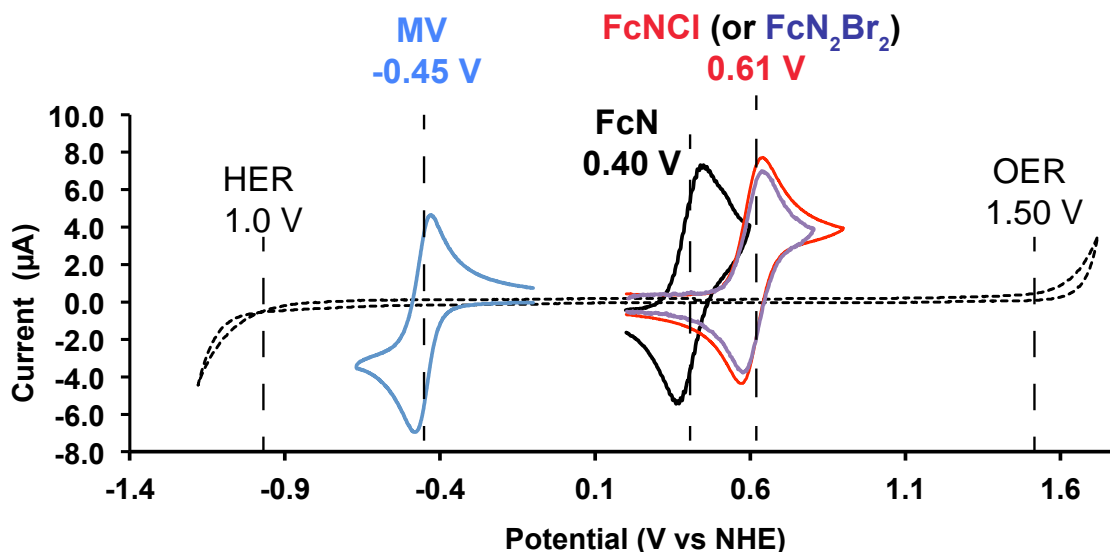


Figure 2-1. Cyclic voltammograms of **FcNCl** (red trace), **FcN₂Br₂** (purple trace), **FcN** (black trace), and **MV** (blue trace). The dashed curve is the cyclic voltammogram of 0.5 M NaCl, labeled with the onset potentials for hydrogen evolution reaction (HER, -1.00 V) and oxygen evolution reaction (OER, 1.50 V).

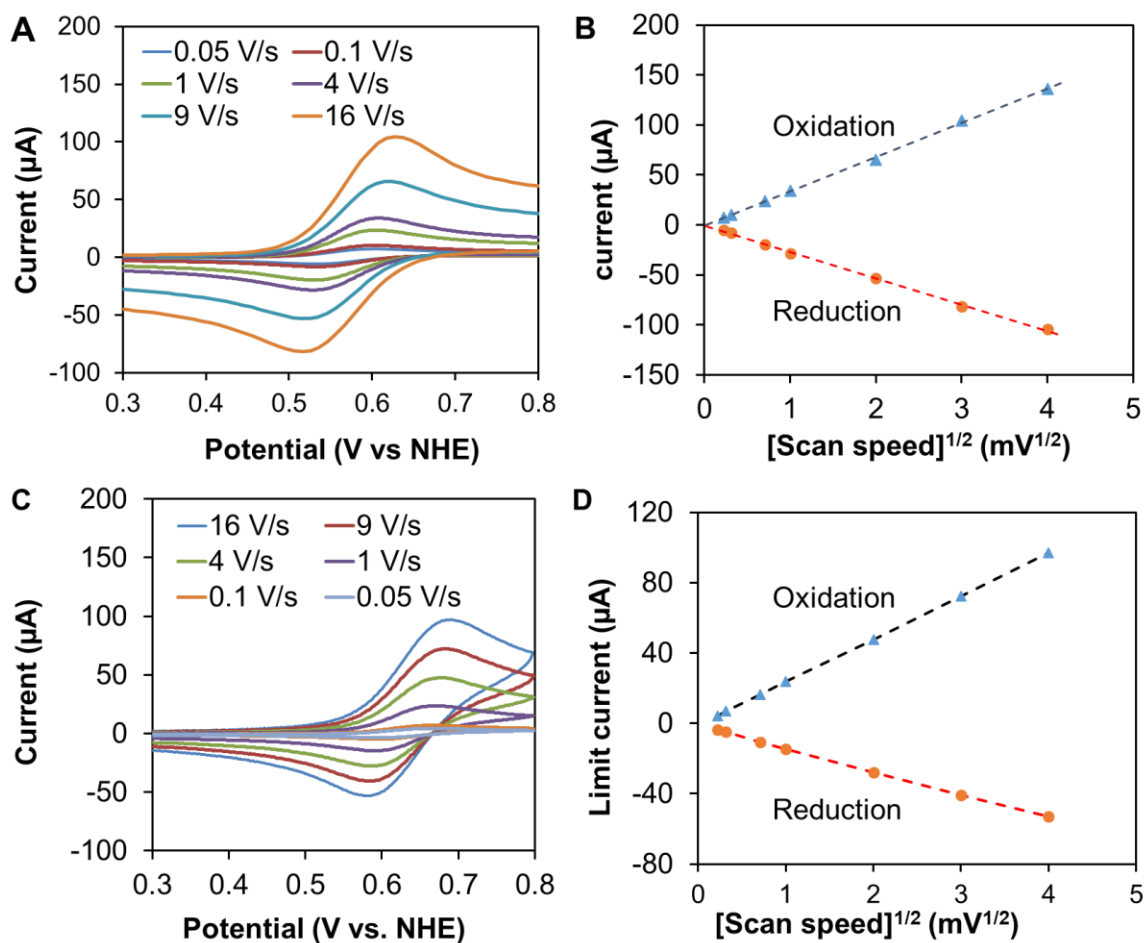


Figure 2-2. Cyclic Voltammograms of (A) **FcNCl** and (C) **FcN₂Br₂** at various scan rates from 0.05 V/s to 16 V/s; The plot of i_c and i_a over the square root of scan rates for **FcNCl** and (D) **FcN₂Br₂** (blue trace for oxidation and red trace for reduction). Conditions: 4.0 mM analyte in 0.5 M NaCl electrolyte; glassy carbon working electrode; glassy carbon counter electrode; Ag/AgCl reference electrode.

Considering the high capacities of these functionalized ferrocene compounds, their oxidation potentials are positive enough for AORFB applications. Profited from the large overpotential of hydrogen evolution reaction (HER) and oxygen evolution reaction on the carbon electrode, all redox reaction happened within the water's electrochemical window (Figure 2-1, dash trace), indicating OER and HER side reactions are not thermodynamically accessible within the cycling voltage window of the **FcNCl/MV**

AORFB. Scan rate dependence studies of **FcNCl** and **FcN₂Br₂** (Figure 2-2) demonstrated linear relationships between the peak oxidation/reduction current and the square root of the scan rate, indicating that their reversible oxidation/reduction processes are both diffusion controlled.

RDE studies of FcNCl and FcN₂Br₂

To further understand the electrochemical kinetics of **FcNCl** and **FcN₂Br₂**, they were studied by linear sweep voltammetry (LSV) using a glassy carbon rotation disc electrode. The limiting currents (i.e. the mass transport-limited current intensity) were taken at 0.7 V vs NHE for **FcNCl** and plotted over the square root of the rotation rate (rad/s). The data were fitted to yield a straight Levich plot, with the slope defined by the Levich equation (Equation 2-1), where $n = 1$ for one-electron process, Faraday's constant $F = 96485$ C/mol, electrode area $A = 0.785$ cm², **FcNCl** concentration $C_0 = 1.0$ mM, D is diffusion coefficient, kinematic viscosity $\nu = 0.009$ cm²/s for 0.5 M NaCl solution. A plot of overpotential versus $\log_{10}(i_k)$ was constructed for the LSV data collected at 2400 rpm for **FcNCl** where i_k is the kinetic current for the oxidation of **FcNCl**. The x-intercept of the fitted Tafel plot gives the log of the exchange current i_0 , which equals to FAC_0k_0 (Equation 2-2), and gives electron transfer rate constant k_0 . The similar tests were performed for **FcN₂Br₂**.

$$\text{Levich plot slope} = 0.62nFAC_0D^{\frac{2}{3}}\nu^{\frac{1}{6}} \quad (\text{Equation 2-1})$$

$$i_0 = FAC_0k_0 \quad (\text{Equation 2-2})$$

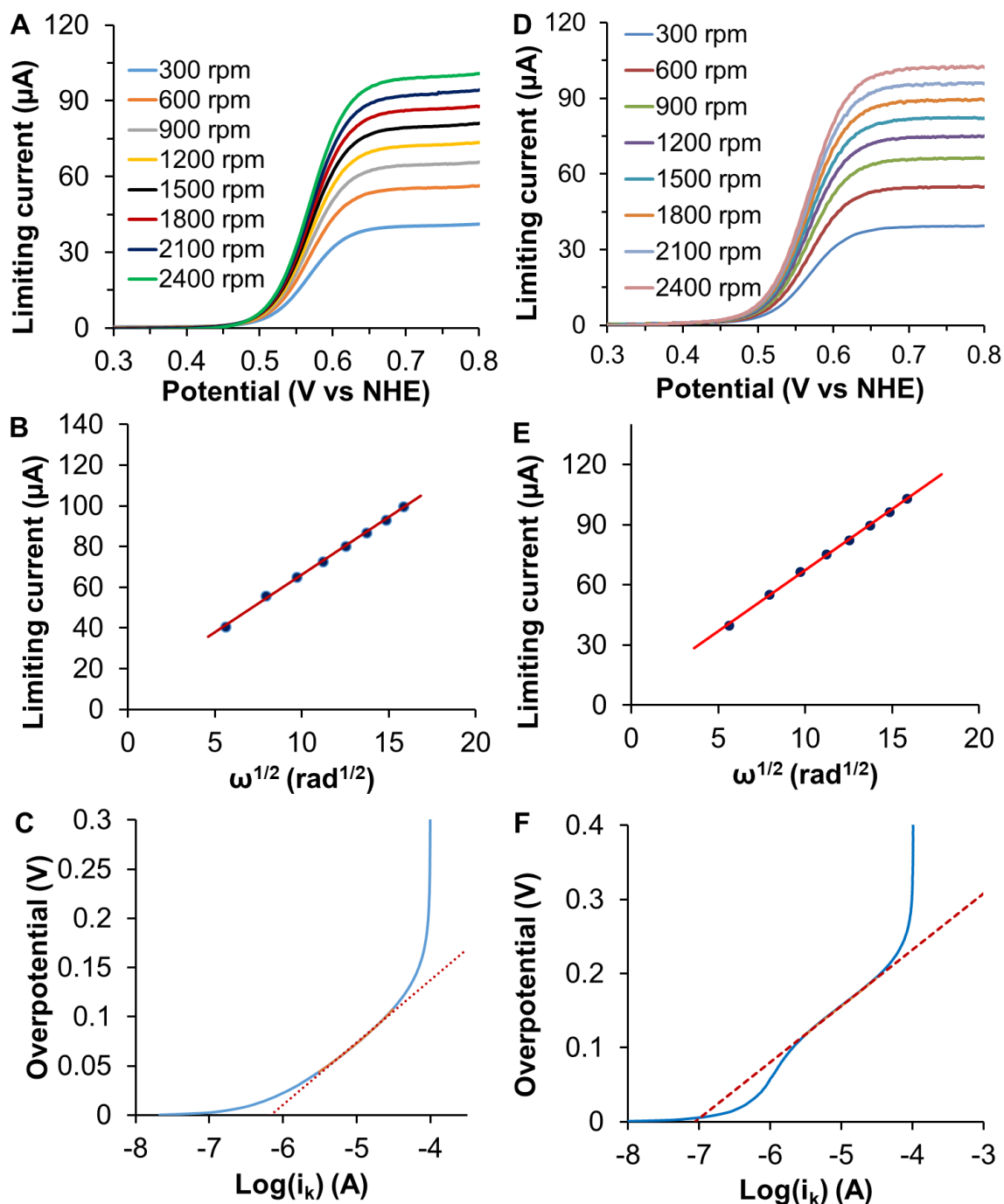


Figure 2-3. (A) Linear sweep voltammograms of **FcNCl** (1.0 mM in 0.5 M NaCl); (B) Levich plots of the limiting current vs the square root of rotation rates for **FcNCl**; (C) The plot of overpotential over the logarithm of kinetic current and the corresponding fitted Tafel plot at 2400 rpm for **FcNCl**; (D) Linear sweep voltammograms of **FcN₂Br₂** (1.0 mM in 0.5 M NaCl); (E) Levich plots of the limiting current vs the square root of

rotation rates for **FcN₂Br₂**; (F) The plot of overpotential over the logarithm of kinetic current and the corresponding fitted Tafel plot at 2400 rpm for **FcN₂Br₂**.

The results are presented in Figure 2-3. The rotation speed was increased from 300 rpm to 2400 rpm to gain different mass-transport limited current with a scan rate at 5 mV/s. The diffusion coefficient of **FcNCl** was calculated to be 3.74×10^{-6} cm²/s from the slope of the Levich plot using Levich equation (Equation 1-1). Subsequently, a plot of oxidation overpotential over the logarithm of the kinetic current (Figure 2-3, A-C) at 2400 rpm was constructed to determine the rate constant for the charge transfer process for the oxidation of **FcNCl**. The Tafel equation (Equation 1-2) is applicable over 45 mV overpotential and the fitted Tafel plot (shown as the blue dotted line in Figure 3C) yielded a rate constant of 3.66×10^{-5} cm/s for **FcNCl**. These same analyses (Figure 2-3, D-F) yielded a diffusion constant of 3.64×10^{-6} cm²/s and an electron transfer rate constant of 4.60×10^{-6} cm/s for **FcN₂Br₂**. The large electron transfer rate and diffusion constant can contribute to reducing polarization overpotential due to the charge transfer and mass transport resistances. The electron-transfer rate and diffusion constants of **FcNCl** and **FcN₂Br₂** are greater than most of inorganic species³⁰ and as good as reported redox active organic molecules applied in ARFBs.^{9,11,14} Thus, the fast electrochemical kinetic results further indicate that **FcNCl** and **FcN₂Br₂** are suitable candidates for AORFBs.

Flow cell performance

Paired with methyl viologen (MV, -0.45 V vs NHE, 3.5 M solubility in water), an established anolyte material for AORFBs, the resulting **FcNCl**/MV and **FcN₂Br₂**/MV AORFB can deliver 1.05 V cell voltage (Figure 2-1). Together with their high charge capacities in 2.0 M NaCl, **FcNCl**/MV and **FcN₂Br₂**/MV AORFBs possess theoretical

energy densities of 45.5 Wh/L and 35.8 Wh/L, respectively (calculated using Equation 3 given in the experimental section). The energy density of the **FcNCl**/MV AORFB is the highest known to-date for AORFBs and higher than state of the art vanadium ARFBs (41.8 Wh/L) and relatively less than Zn-Br₂ RFBs (ca. 65 Wh/L).^{3,31,32}

Electrolyte conductivity directly affects batteries' overall resistance, thus plays an important role in RFBs' rate performance, energy efficiency and power output. Therefore, before the RFB testing, we systematically examined electrolyte conductivity with various concentrations of active materials and supporting electrolyte (NaCl). As shown in Figure 2-4, conductivity of both catholyte and anolyte continuous changed with the increase of active materials and supporting electrolyte. Overall, the higher concentration of supporting electrolyte contributed to higher electrolyte conductivity. 2 M NaCl supporting electrolyte could provide the highest conductivity of catholyte and anolyte up to 160 ms/cm and 173 ms/cm, respectively. At each NaCl concentration, with active materials' concentration increase electrolyte conductivity increased at the beginning and then decreased. This is resulted from both ion concentration increase and electrolyte viscosity increase. As indicated by the conductivity measurements, 0.5 M concentration of the electrolytes in 2.0 M NaCl could give optimal energy efficiency in terms of overall electrolyte conductivity (135 ms/cm² for **FcNCl** and 175 ms/cm² for **MV**). Thus, the flow cell study was conducted at 0.5 M for both active materials in 2.0 M NaCl electrolyte (corresponding to 7.0 Wh/L energy density) at 20 °C. At the same condition, **FcNCl** and **FcN₂Br₂** showed a similar conductivity.

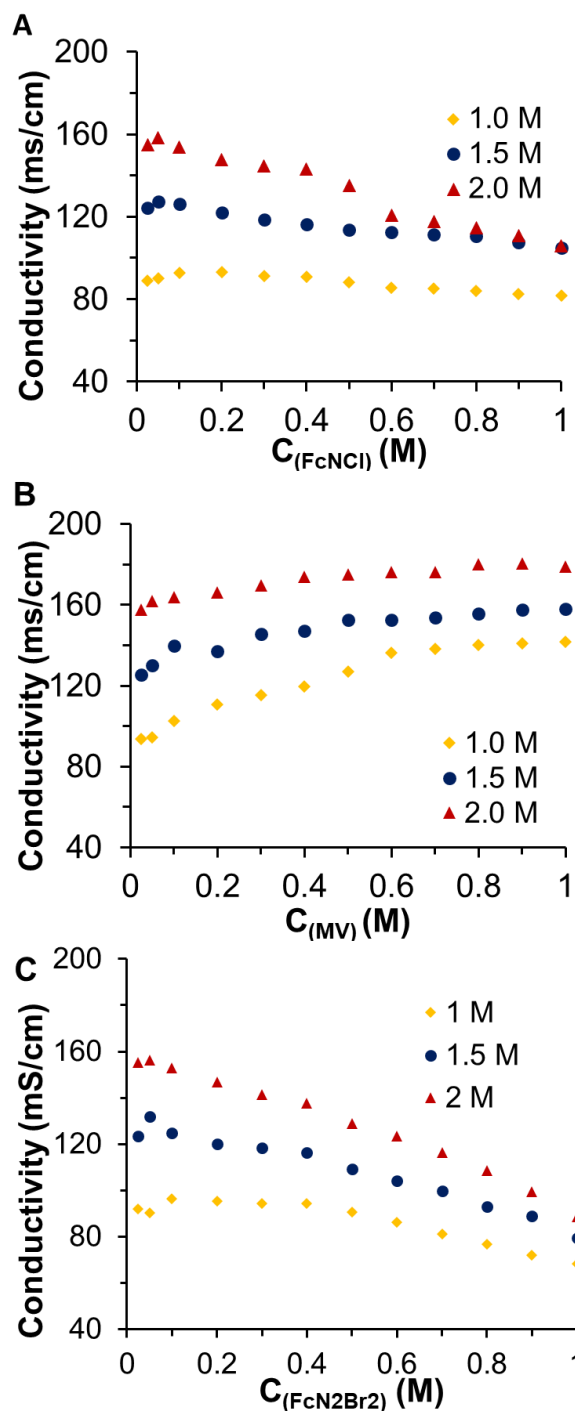


Figure 2-4. Conductivity measurements of (A) FcNCl and (B) MV (C) FcN_2Br_2 from 0.05 M to 1.0 M in NaCl solution at different concentrations, 1.0 M (orange diamond trace), 1.5 M (blue circle trace), and 2.0 M (red triangle trace) at R.T.

The FcNCl/MV AORFB cell design is outlined in Figure 2-5. Because of the cation nature of the redox-active moieties of **FcNCl** and **MV**, a piece of anion exchange membrane (AEM, Selemin, Japan) was employed, that is ca. 1/5 the cost of typical Nafion membrane. It is expected that the AEM incorporated with pendant ammonium cation functionality only permits selective Cl^- transport while suppressing the crossover of the active catholyte and anolyte materials.

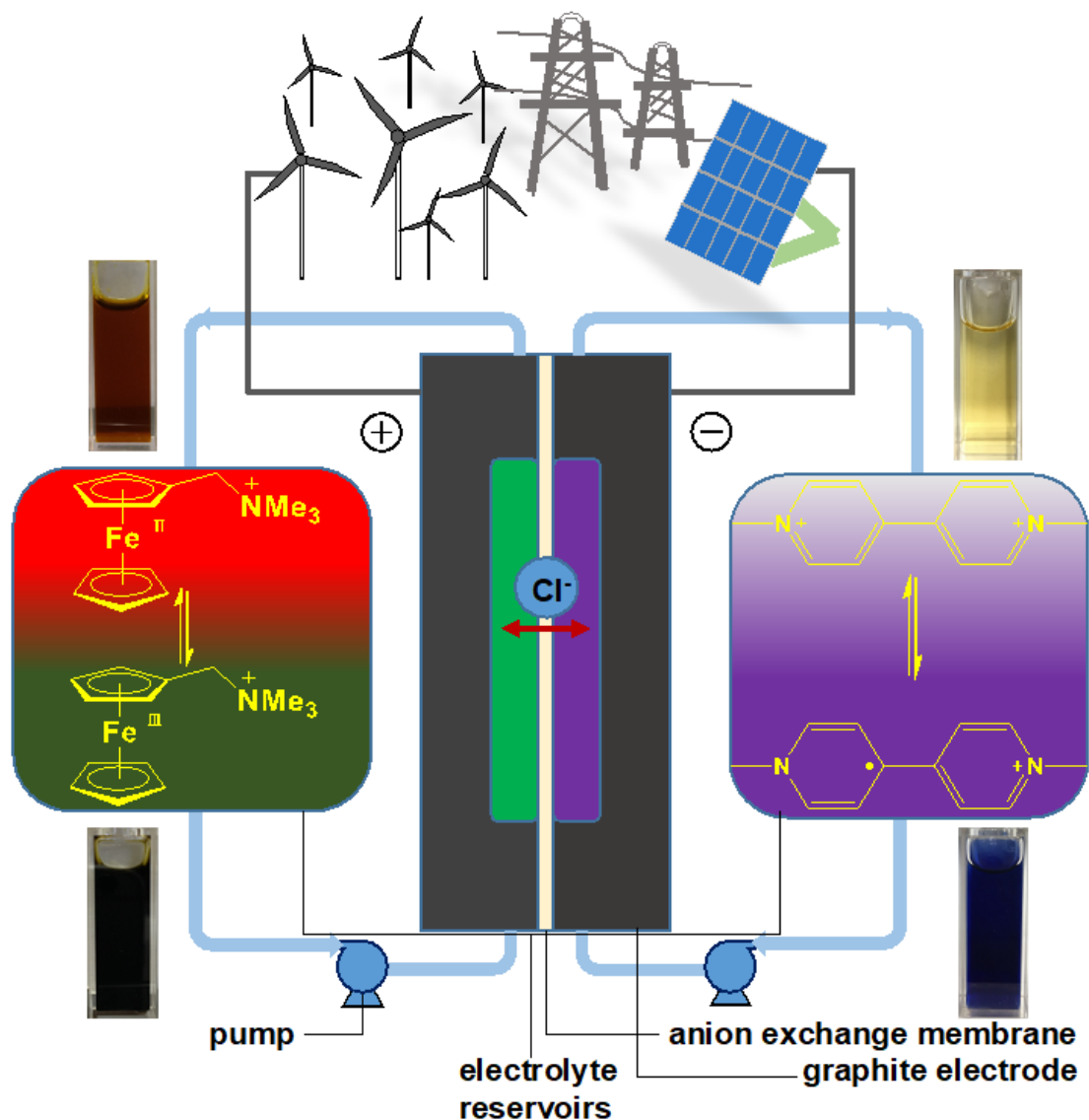


Figure 2-5. A schematic representation of the **FcNCl/MV** AORFB and illustrations of discharged and charged states of **FcNCl** and **MV**, and cell reactions.

The current rate performance was investigated from 40 mA/cm² to 100 mA/cm² with an increment of 20 mA/cm². For each current density, 6 charge and discharge cycles were tested with cutoff voltages at 1.5 V for the charging process and 0.1 V for the discharge process. Upon charging, both electrolyte solutions underwent immediate color changes, from red-orange to deep green for **FcNCl**, and from colorless to deep purple for **MV** (see Figure 2-5). The observed color changes were consistent with the UV-Vis spectrum of **FcNCl** and **MV** in their charged and discharged states (Figure 2-6). **FcNCl**, in its discharged state, exhibits absorbance at 440 nm, and its charged state, **FcNCl**₂, shows major absorption at 630 nm. The discharged state (**MV**²⁺) of **MV** has no absorption in the visible region while its charged state (**MV**⁺) exhibits strong waves at 400 nm and 600 nm.

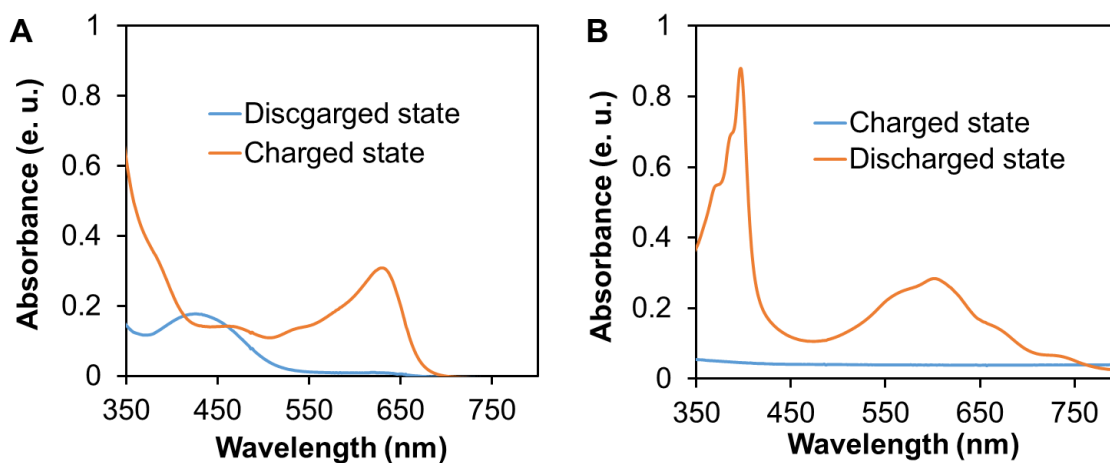


Figure 2-6. UV-Vis spectra of **FcNCl** compound (top) in different states (orange trace for fully charged state and blue trace for fully discharged trace); UV-Vis spectra of **MV** compound (bottom) in different states (orange trace for fully charged state and blue trace for fully discharged trace); Conditions: for **MV** 0.1 mM in 2 M NaCl aqueous solution; for **FcNCl** 1.0 mM in 2.0 M NaCl aqueous solution; All the samples were prepared under nitrogen atmosphere.

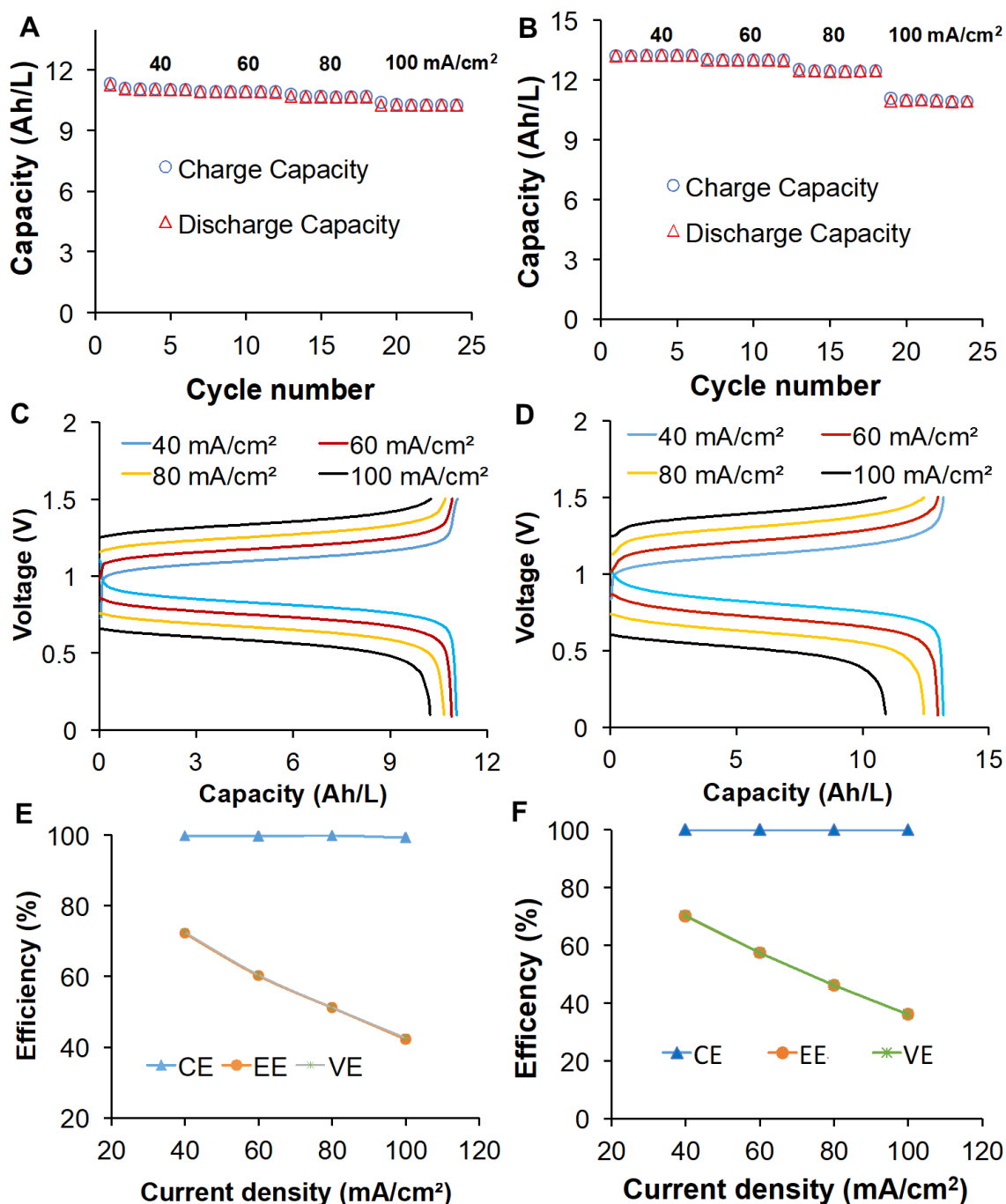


Figure 2-7. Capacity vs cycling numbers from 40 to 100 mA/cm² for the FcNCl/MV AORFB (A) and the FcN₂Br₂/MV AORFB (B). Representative charge and discharge profiles of the FcNCl/MV AORFB (C) and the FcN₂Br₂/MV AORFB (D) from 40 to 100 mA/cm². Plots of averaged coulombic efficiency (blue triangle), energy efficiency (orange circle), and voltage efficiency (green cross) versus current density of the FcNCl/MV AORFB (E) and the FcN₂Br₂/MV AORFB (F). Conditions: catholyte, 0.5 M

FcNCl (or **FcN₂Br₂**) in 2.0 M NaCl aqueous solution; anolyte, 0.5 M **MV** in 2.0 M NaCl aqueous solution; AMV anion exchange membrane.

Representative charge/discharge profiles are displayed in Figure 5A. With the increase of the current density, the cell capacity keeps decreasing, mainly due to increased overpotential and reduced charge/discharge time at higher current densities. At 40 mA/cm², averaged charge and discharge voltage occurred at 1.12 V and 0.82 V. At 100 mA/cm², the averaged cell voltages for charge and discharge were observed at 1.32 V and 0.61 V. The trend of coulombic efficiency and energy efficiency are outlined in Figure 2-7. Coulombic efficiency stayed above 99% for all current densities while energy efficiency decreased from 72% for 40 mA/cm² to 43% for 100 mA/cm² due to increased ohmic energy loss. Stable capacity retention was observed for continuous 24 cycles at four current densities. The current rate performance of the neutral FcNCl/MV AORFB is comparable with acidic vanadium RFBs and outperforms Zn-halide RFBs. To further validate the cycling performance of the FcNCl/MV ARFB at 0.5 M, the long time cycling was examined at 60 mA/cm² (Figure 2-8A), which showed a high energy efficiency, 61%. The 0.5 M cell tested at 60 mA/cm² delivered rather stable capacity retention. After 700 cycles tested in 12 days, capacity still remained above 90.3%. The charge/discharge voltage profiles over time are provided in the supporting information (Figure 2-8C). On average, the capacity retention was ca. 99.99% for a single charge/discharge cycle. The robust cycling performance is credited to the excellent electrochemical and thermal stability of both active materials. For the same long cycling cell, the polarization curve was recorded at a full charge state using a small current density, 10 mA/cm². The resulting power density curve revealed a peak power density

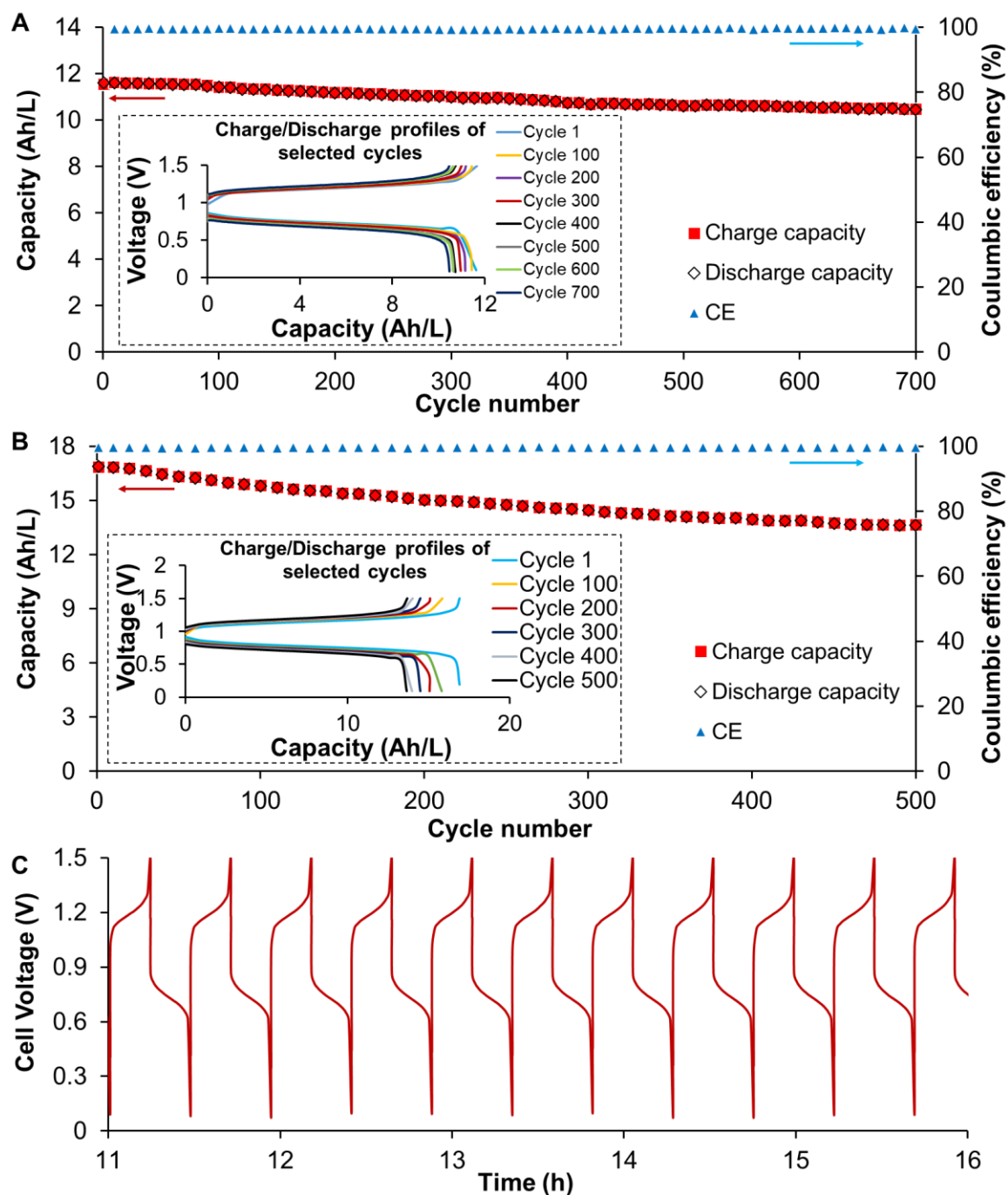


Figure 2-8. (A) Extended 700 cycle testing data of the 0.5 M FcNCl/MV AORFB at 60 mA/cm²: capacity and coulombic efficiency vs cycling numbers (for clarity, data points with an increment of 10 cycles were used for plotting); inset: representative charge and discharge profiles of selected cycles. (B) Extended 500 cycle testing data of the 0.7 M FcNCl/MV AORFB at 60 mA/cm². (C) The representative charge/discharge voltage profiles overtime of the 0.5 M FcNCl/MV AORFB at 60 mA/cm² current density.

output at 85 mW/cm^2 (Figure 2-9, red trace). The averaged energy efficiency stayed ca. 60% with small fluctuations over 700 cycles (Figure 2-10A). To demonstrate higher energy density performance, a flow cell was tested at 0.7 M (9.9 Wh/L energy density) with stable capacity retention at 81% after 500 cycles in 11 days (Figure 2-8B). The 0.7 M cell even delivered increased energy efficiency at 65% at 60 mA/cm^2 (Figure 2-10B) which is due to the decreased high-frequency area specific resistance R_{hf} from the EIS measurements (Figure 2-10C and D). Correspondingly, an increased peak power density was measured at 125 mW/cm^2 (Figure 2-9, blue trace), which is in the same order of peak power density outputs observed for acidic and alkaline AORFBs. The outstanding current and power performance highlights the practical potential of the FcNCl/MV AORFB to provide quick response to energy demands in the coupled electricity grid.

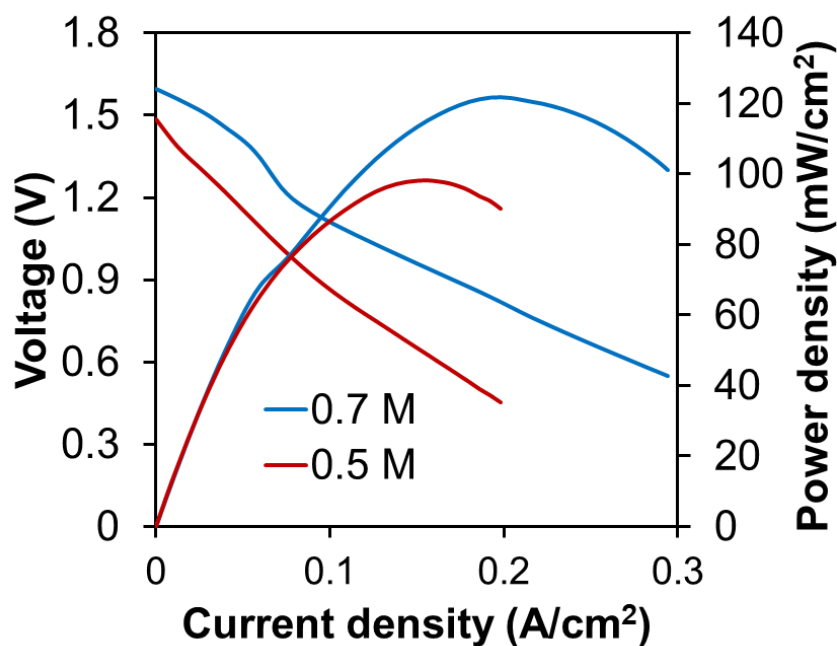


Figure 2-9. Polarization and power density curves of the FcNCl/MV AORFB at 0.5 M (red traces) and 0.7 M (blue traces) after full charge using 10 mA/cm^2 .

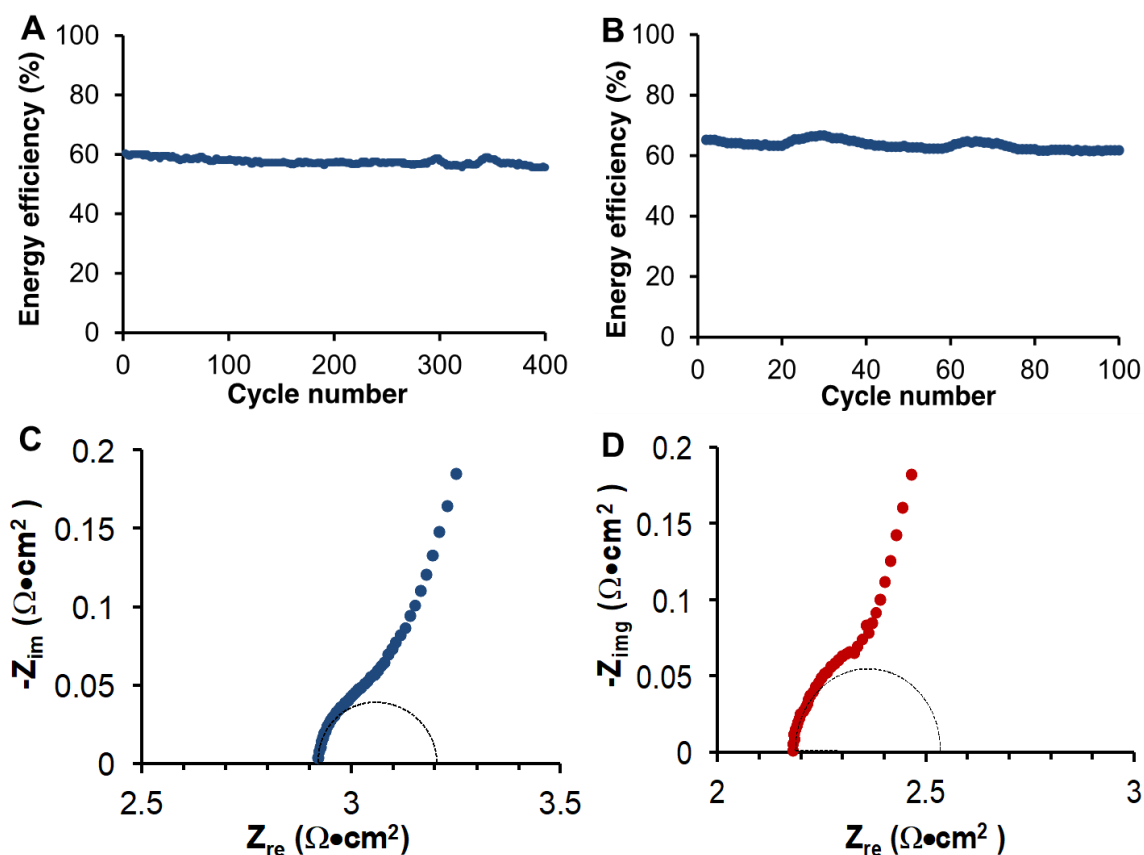


Figure 2-10. Plot of energy efficiency vs cycling numbers for the (A) 0.5 M **FcNCl**/MV AORFB and (B) 0.7 M **FcNCl**/MV AORFB at 60 mA/cm²; Nyquist plot of the **FcNCl**/MV AORFB at (C) 0.5 M and (D) 0.7 M before cycling. Conditions: catholyte, 0.7 M **FcNCl** in 2.0 M NaCl aqueous solution; anolyte, 0.7 M **MV** in 2.0 M NaCl aqueous solution; AMV anion exchange membrane.

Post-cell analysis for the 0.5 M cell after 700 cycles was conducted using cyclic voltammetry and ¹H NMR (Figure 2-11 and 2-12). Both CV and ¹H NMR studies indicated there was no chemical degradation for both catholyte and anolyte. Also, the post-analysis studies indicated there was no crossover between catholyte and anolyte as no **FcNCl** was detected in the ¹H NMR spectrum and CV of MV, and *vice versa*, highlighting the excellent compatibility of both catholyte and anolyte with the AEM membrane. Identical results were obtained for the 0.7 M cell.

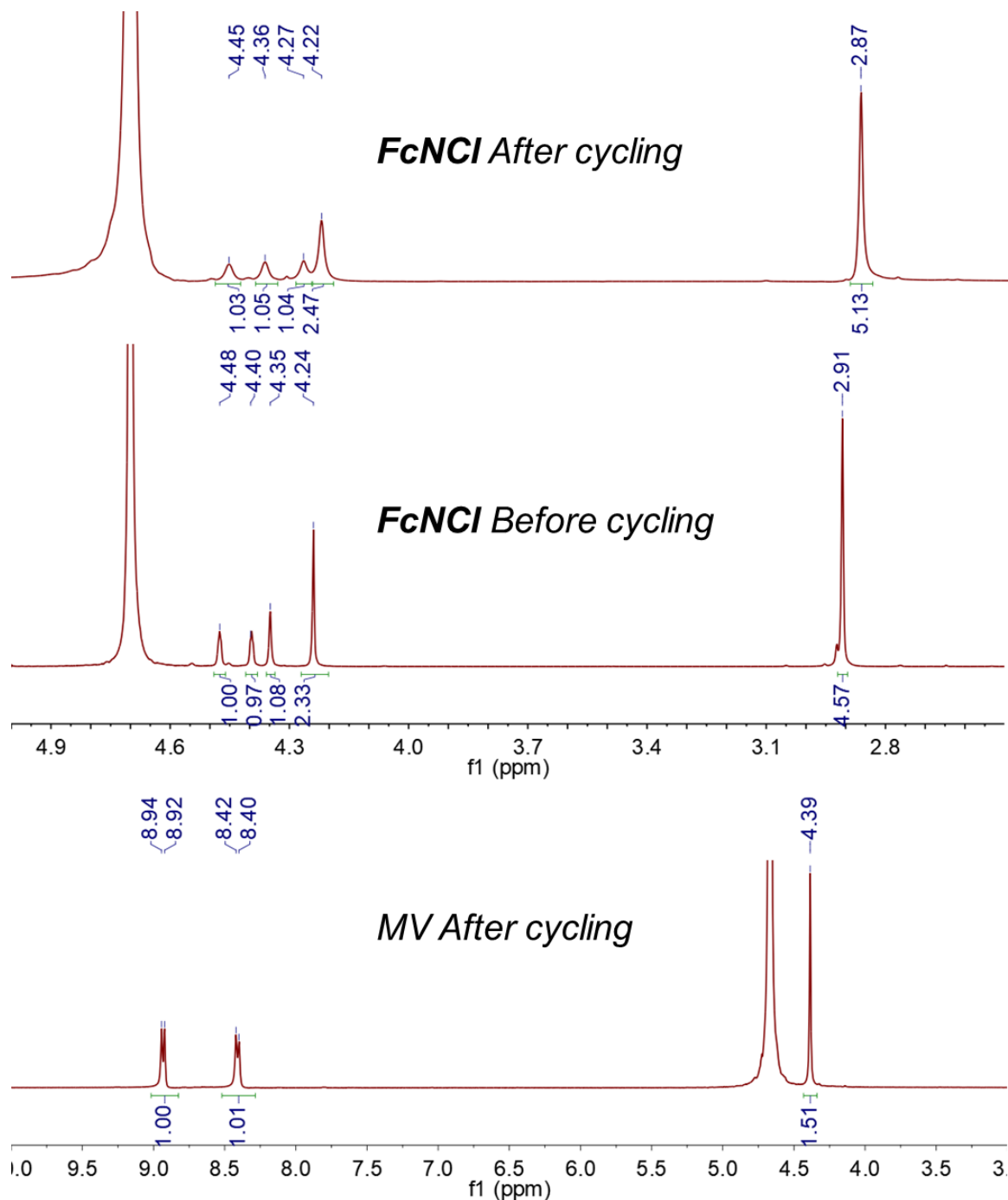


Figure 2-11. Comparison of the ^1H NMR spectra of the **FcNCl** electrolyte (0.5 M in 2.0 NaCl solution) After (top) and before (middle) cycling at the same concentration (diluted to 10 mM in D_2O) under the same conditions. ^1H NMR spectrum of the MV electrolyte after cycling. The proton resonances of the ^1H NMR spectrum of **FcNCl** after cycling are slightly broadened with a small shift and it is attributed to the presence of a tiny amount of paramagnetic charged **FcNCl** (Fe^{3+} oxidation state).

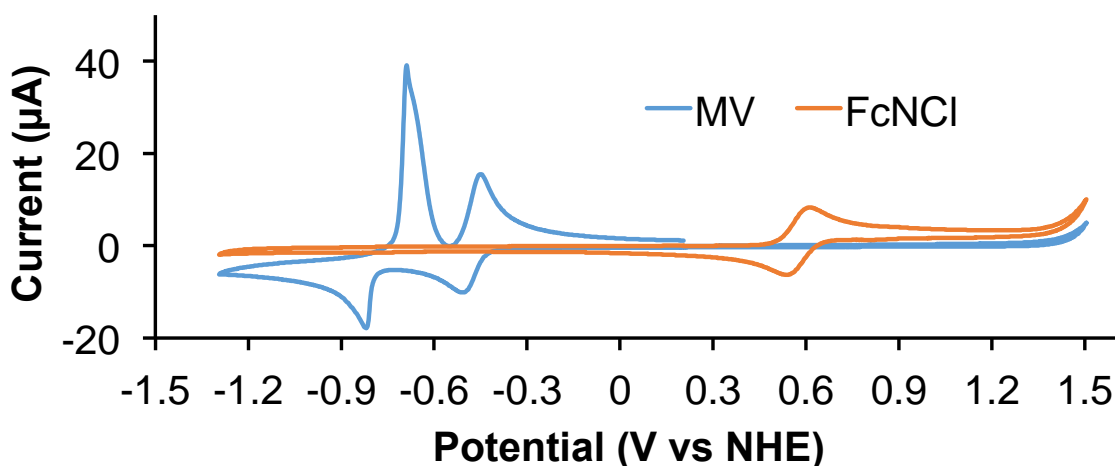


Figure 2-12. Post-cell CV studies for **FcNCl** and MV from anode and cathode after 700 cycles indicating no electrolyte crossover; concentration: 4 mM analyte in 0.5 M NaCl aqueous solution; glassy carbon working electrode; glassy carbon counter electrode; Ag/AgCl reference electrode. Each CV only shows redox waves belonged to each individual compound. No redox wave of **FcNCl** was observed in the CV of MV, and vice versa.

Temperature dependent performance of FcNCl/MV AORFB

Due to the different regions and weather that the RFBs might be applied to, it is crucial to examine the batteries' performance at various temperatures. For AORFBs, it is more important to study the batteries' performance at elevated temperatures because of the limited temperature window and nonflammable advantage of the aqueous system. We examined the 0.5 M FcNCl/MV AORFB's performance at 4 different temperatures (10 °C, 20 °C, 40 °C, 50 °C). The battery was cycled at each temperature for 5 cycles, when the charging/discharging capacity, energy efficiency and power density data were collected (shown in Figure 2-13). With the increased temperature, all the mentioned battery performance parameters showed improvement. Energy efficiency increased from 40 % at 10 °C to 62 % at 50 °C. Power density also showed the same trend of boost. Notably, at 50 °C the battery could reach a capacity utilization up to 99 %, and even at 10 °C the

battery still delivered more than 67 % of the theoretical capacity. All these performance improvements could be attributed to the accelerated mass diffusion and charge transfer at elevated temperatures due to decreased electrolyte viscosity and faster redox reactions.

Figure 2-14 provides a comparison of energy density (theoretical and demonstrated) and demonstrated cycles (labeled with cycling stability) of the FcNCl/MV

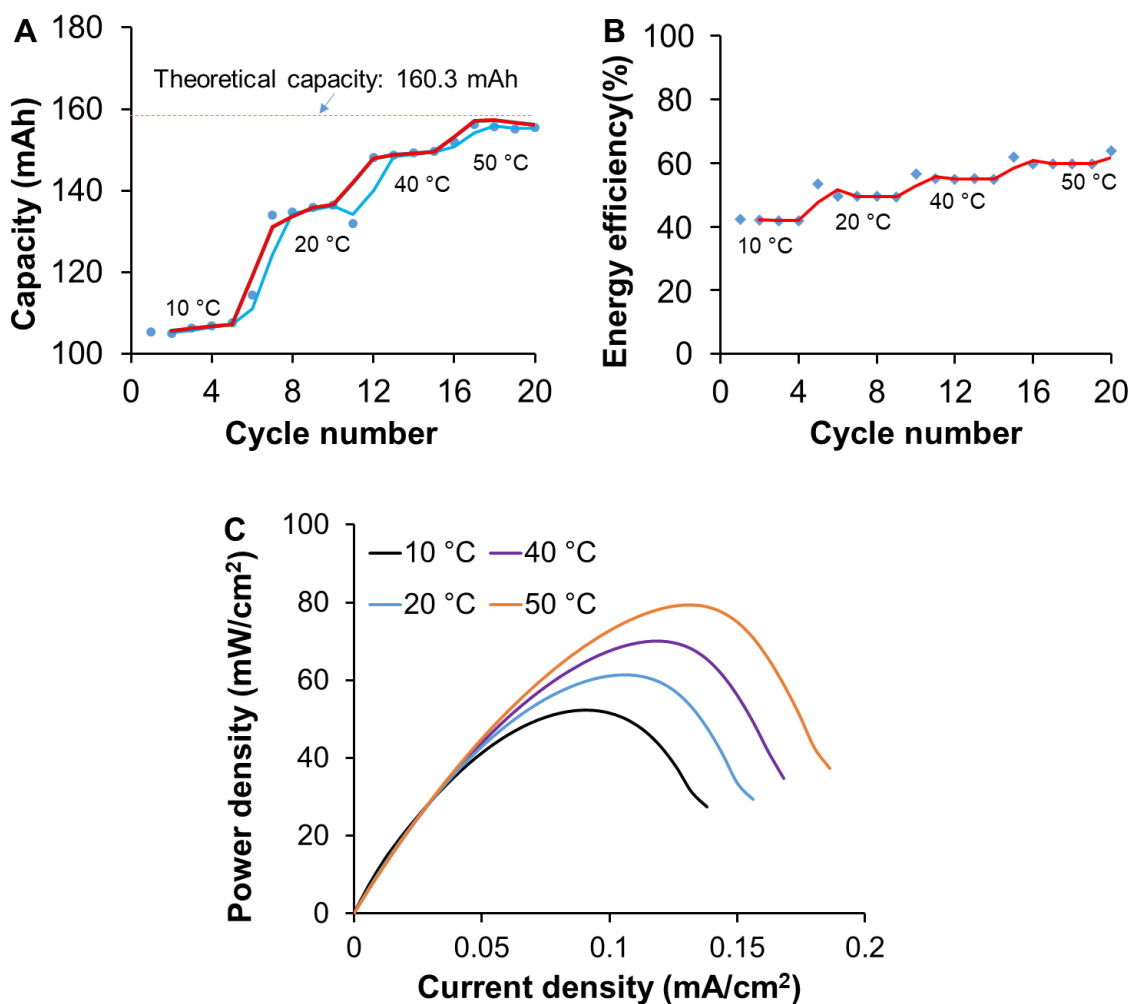


Figure 2-13. Temperature dependent studies of FcNCl/MV AORFBs. (A) Capacity vs. cycle number, (B) energy efficiency vs. cycle number, (C) power density of 0.5 M FcNCl/MV AORFB. Conditions: catholyte, 12 mL 0.5 M FcNCl in 1.5 M NaCl aqueous solution; anolyte, 12 mL 0.5 M MV in 1.5 M NaCl aqueous solution; AMV anion exchange membrane; charging/discharging current density, 60 mA/cm².

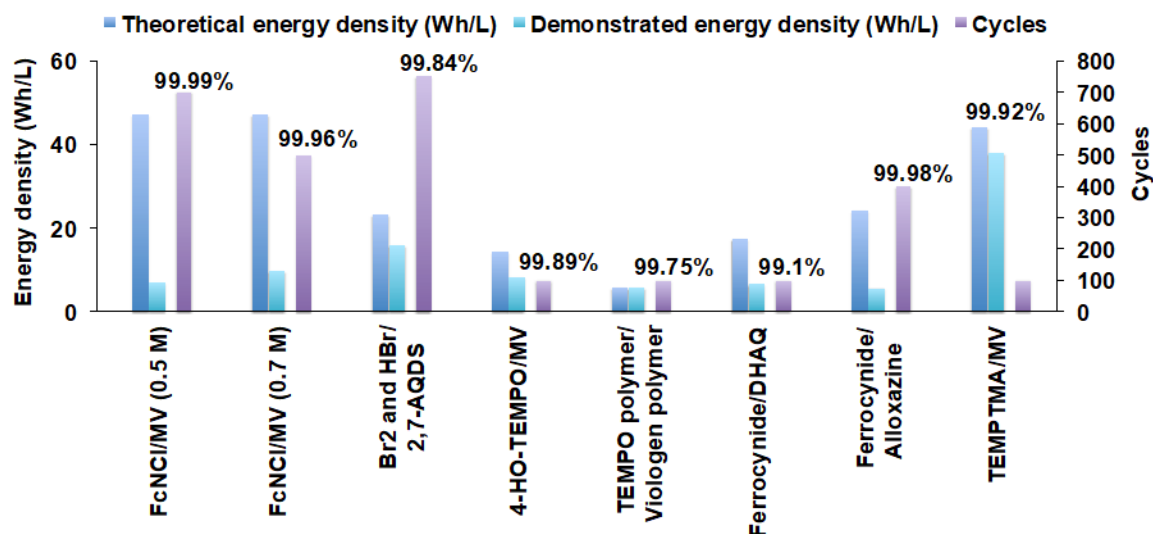


Figure 2-14. A bar chart comparison of theoretical energy density, demonstrated energy density, and tested cycles labeled with capacity retention per cycle of the FcNCI/MV AORFB and reported representative AORFBs. Chemical abbreviations: 2,6-AQDS, anthraquinone-2,6-disulfonic acid; DHAQ, 2,6-dihydroxyanthraquinone; alloxazine, alloxazine 7/8-carboxylic acid; TEMPTMA, N,N,N,2,2,6,6-heptamethylpiperidinyloxy-4-ammonium chloride.

AORFB and representative AORFBs reported to date.^{11-14,33} It is worth noting that the redox potentials of both active materials, **FcNCI** (or **FcN₂Br₂**) and **MV**, are bracketed within the water splitting voltage window (Figure 2, 1.5 V vs NHE for O₂ evolution reaction, [OER], and -1.0 V vs NHE for H₂ evolution reaction, [HER]), indicating that the OER and HER side reactions are not accessible within the cycling voltage window of the FcNCI/MV AORFB. Because of large overpotential of the OER and the HER on the carbon electrode, the observed water splitting window, 2.5 V, is much wider than the standard thermodynamic free energy for water splitting, 1.23 V. The 2.5 V water splitting window allows developing high voltage AORFBs. Voltage modulation can be achieved by synthetic tuning of redox potentials of organic materials, and is expected to further

enhance energy density of AORFB. Regarding **FcNCl** and **FcN₂Br₂**, the second cyclopentadienide ligand can be also modified by an electron-withdrawing group to further increase the oxidation potential of the Fe^{3+/2+} couple. The synthesis of new water-soluble ferrocene molecules is an ongoing effort in our research group.

2-5. Conclusion

In summary, we have developed a new AORFB technology employing sustainable and tunable active electrolyte materials based on earth-abundant elements: C, H, N, and Fe. The synthesis of the new **FcNCl** and **FcN₂Br₂** cathode materials is convenient and scalable using commercial precursors and their performance can be further improved through structural modification. Together with inexpensive, non-corrosive and non-flammable NaCl supporting electrolyte and low cost AEM membrane, the present high energy density and long cycling AORFB technology is economically attractive and environmentally friendly. In a broad sense, this work highlights the great potential of rationally designed redox-active organic molecules to construct low cost, safe and high performance AORFBs by overcoming technical constraints of traditional inorganic ARFBs, such as resource limits, corrosive electrolytes, and expensive membrane.

2-7. Reference

- (1) Dunn, B.; Kamath, H.; Tarascon, J.-M. *Science* **2011**, *334*, 928.
- (2) Yang, Z.; Zhang, J.; Kintner-Meyer, M. C. W.; Lu, X.; Choi, D.; Lemmon, J. P.; Liu, J. *Chem. Rev.* **2011**, *111*, 3577.
- (3) Soloveichik, G. L. *Chem. Rev.* **2015**, *115*, 11533.
- (4) Darling, R. M.; Gallagher, K. G.; Kowalski, J. A.; Ha, S.; Brushett, F. R. *Energy Environ. Sci.* **2014**, *7*, 3459.

- (5) *ARPA-E GRIDS Program Overview*, <https://arpa-e.energy.gov/?q=arpa-e-programs/grids>; DOE Office of ARPR-E, 2011.
- (6) *Program Planning Document on Energy Storage*, <http://energy.gov/oe/downloads/energy-storage-program-planning-document-2011>; DOE Office of Electricity Delivery&Energy Reliability, 2011.
- (7) Xu, Y.; Wen, Y.; Cheng, J.; Yanga, Y.; Xie, Z.; Cao, G. In *World Non-Grid-Connected Wind Power and Energy Conference, 2009. WNWEC 2009 IEEE*: Nanjing, China, 2009, p 1.
- (8) Xu, Y.; Wen, Y.-H.; Cheng, J.; Cao, G.-P.; Yang, Y.-S. *Electrochim. Acta* **2010**, *55*, 715.
- (9) Huskinson, B.; Marshak, M. P.; Suh, C.; Er, S.; Gerhardt, M. R.; Galvin, C. J.; Chen, X.; Aspuru-Guzik, A.; Gordon, R. G.; Aziz, M. J. *Nature* **2014**, *505*, 195.
- (10) Yang, B.; Hooper-Burkhardt, L.; Wang, F.; Surya Prakash, G. K.; Narayanan, S. *R. J. Electrochem. Soc.* **2014**, *161*, A1371.
- (11) Lin, K.; Chen, Q.; Gerhardt, M. R.; Tong, L.; Kim, S. B.; Eisenach, L.; Valle, A. W.; Hardee, D.; Gordon, R. G.; Aziz, M. J.; Marshak, M. P. *Science* **2015**, *349*, 1529.
- (12) Liu, T.; Wei, X.; Nie, Z.; Sprenkle, V.; Wang, W. *Adv. Energy Mater.* **2016**, *6*, 1501449.
- (13) Janoschka, T.; Martin, N.; Martin, U.; Friebe, C.; Morgenstern, S.; Hiller, H.; Hager, M. D.; Schubert, U. S. *Nature* **2015**, *527*, 78.
- (14) Lin, K.; Gómez-Bombarelli, R.; Beh, E. S.; Tong, L.; Chen, Q.; Valle, A.; Aspuru-Guzik, A.; Aziz, M. J.; Gordon, R. G. *Nat. Energy* **2016**, *1*, 16102.

- (15) Janoschka, T.; Martin, N.; Hager, M. D.; Schubert, U. S. *Angew. Chem. Int. Ed.* **2016**, *55*, 14427.
- (16) Wei, X.; Xu, W.; Vijayakumar, M.; Cosimbescu, L.; Liu, T.; Sprenkle, V.; Wang, W. *Adv. Mater.* **2014**, *26*, 7649.
- (17) Wei, X.; Xu, W.; Huang, J.; Zhang, L.; Walter, E.; Lawrence, C.; Vijayakumar, M.; Henderson, W. A.; Liu, T.; Cosimbescu, L.; Li, B.; Sprenkle, V.; Wang, W. *Angew. Chem. Int. Ed.* **2015**, *54*, 8684.
- (18) Duan, W.; Vemuri, R. S.; Milshtein, J. D.; Laramie, S.; Dmello, R. D.; Huang, J.; Zhang, L.; Hu, D.; Vijayakumar, M.; Wang, W.; Liu, J.; Darling, R. M.; Thompson, L.; Smith, K.; Moore, J. S.; Brushett, F. R.; Wei, X. *J. Mater. Chem. A* **2016**, *4*, 5448.
- (19) Nagarjuna, G.; Hui, J.; Cheng, K. J.; Lichtenstein, T.; Shen, M.; Moore, J. S.; Rodríguez-López, J. *J. Am. Chem. Soc.* **2014**, *136*, 16309.
- (20) Huang, Q.; Yang, J.; Ng, C. B.; Jia, C.; Wang, Q. *Energy Environ. Sci.* **2016**, *9*, 917.
- (21) Zhao, Y.; Ding, Y.; Song, J.; Li, G.; Dong, G.; Goodenough, J. B.; Yu, G. *Angew. Chem. Int. Ed.* **2014**, *53*, 11036.
- (22) Ding, Y.; Yu, G. *Angew. Chem. Int. Ed.* **2016**, online.
- (23) Brushett, F. R.; Vaughey, J. T.; Jansen, A. N. *Adv. Energy Mater.* **2012**, *2*, 1390.
- (24) Kealy, T. J.; Pauson, P. L. *Nature* **1951**, *168*, 1039.
- (25) Wilkinson, G.; Rosenblum, M.; Whiting, M. C.; Woodward, R. B. *J. Am. Chem. Soc.* **1952**, *74*, 2125.
- (26) E. O. Fischer, W. P. *Z. Naturforsch.* **1952**, *B7*, 377.

- (27) Wei, X.; Cosimbescu, L.; Xu, W.; Hu, J. Z.; Vijayakumar, M.; Feng, J.; Hu, M. Y.; Deng, X.; Xiao, J.; Liu, J.; Sprenkle, V.; Wang, W. *Adv. Energy Mater.* **2015**, *5*, 1400678.
- (28) Lindsay, J. K.; Hauser, C. R. *J. Org. Chem.* **1957**, *22*, 355.
- (29) Nielson, R. M.; Hupp, J. T. *Inorg. Chem.* **1996**, *35*, 1402.
- (30) Shah, A. A.; Watt-Smith, M. J.; Walsh, F. C. *Electrochim. Acta* **2008**, *53*, 8087.
- (31) Leung, P.; Li, X.; Ponce de Leon, C.; Berlouis, L.; Low, C. T. J.; Walsh, F. C. *RSC Adv.* **2012**, *2*, 10125.
- (32) Li, L.; Kim, S.; Wang, W.; Vijayakumar, M.; Nie, Z.; Chen, B.; Zhang, J.; Xia, G.; Hu, J.; Graff, G.; Liu, J.; Yang, Z. *Adv. Energy Mater.* **2011**, *1*, 394.
- (33) Huskinson, B.; Marshak, M. P.; Gerhardt, M. R.; Aziz, M. J. *ECS Trans.* **2014**, *61*, 27.

CHAPTER III. BOOSTING ENERGY EFFICIENCY AND POWER PERFORMANCE OF NEUTRAL AQUEOUS ORGANIC REDOX FLOW BATTERIES ^c

3-1. Abstract

Neutral aqueous organic redox flow batteries (AORFBs) have stood out as a promising RFB technology for sustainable and safe energy storage. It is critical to improving their energy efficiency and power density to meet fast charge/discharge responses in the application of large scale electrochemical energy storage. Herein we show a systematic study on the effects of ion exchange membranes and supporting electrolytes on the resistance and electrochemical performance of a neutral AORFB, the FcNCl/MV AORFB, where FcNCl is (ferrocenylmethyl)trimethylammonium chloride and MV is methyl viologen dichloride. Electrochemical impedance spectroscopic studies revealed that the membrane and the supporting electrolyte are the primary and secondary components accountable for the resistance and charge/discharge overpotential of the neutral AORFB. With an optimized combination of the membrane and the supporting electrolyte, unprecedented energy efficiency and power density were achieved at 85% at 40 mA/cm² or 79% at 60 mA/cm² and 122.7 mW/cm² for the neutral AORFB. The present results emphasize the importance of minimizing battery resistance, and also further advance the promise of neutral AORFBs for sustainable and green energy storage of renewable energy.

3-2. Introduction

^c Adapted with permission from [Hu, B.; Seefeldt, C., DeBruler C.; Liu, T. L. *J. Mater. Chem. A*, **2017**, 5, 22137]. Copyright 2017. Royal Society of Chemistry. Reproduced by permission of Royal Society of Chemistry. <https://pubs.rsc.org/en/content/articlelanding/2017/ta/c7ta06573f#!divAbstract>.

In the advent of a transition from fossil fuels to renewable energy, redox flow batteries (RFBs) have aroused increasing attention for massive storage of renewable solar and wind energy.^{1,2} Compared to static rechargeable batteries, several technical merits highlight RFBs as a more suitable choice to mitigate the intermittency of renewable energy and store it as reliable electricity. The technical merits of RFBs include decoupled energy and power, high current and high power performance, scalability, commercially available ion exchange membranes, and non-flammable and low cost aqueous supporting electrolytes. In order to achieve economical and environmentally benign electrochemical energy storage using RFBs, there has been a transition from redox inorganic materials to sustainable and tunable redox organic molecules as active materials in RFBs.^{3,4} Both aqueous organic redox flow batteries (AORFBs) and non-aqueous redox flow batteries (NAORFBs) have emerged as promising alternatives to traditional aqueous inorganic RFBs (AIRFBs).⁵⁻²⁶ In addition to the sustainability and tunability of organic active materials, AORFBs preserve the aforementioned technical strengths of traditional AIRFBs and hold a great promise for technical implementation.¹⁵ Acidic, alkaline, and neutral AORFBs using a variety of redox active organic molecules/polymers have been rapidly developed in recent years.^{5, 7-10, 12-15, 21, 24, 27, 28} Particularly, we have contributed to the development of neutral AORFBs employing water-soluble viologen (anolyte), TEMPO (catholyte), and ferrocene (catholyte) molecules.^{8, 15, 29, 30}

Thus far, neutral AORFBs employing viologen anolytes and ammonium functionalized ferrocene catholytes have demonstrated a rather stable flow battery performance up to 700 cycles.^{15, 21} However, neutral AORFB^{8, 14, 15} are relatively less energy efficient and less powerful than acidic and alkaline AORFBs and AIRFBs.^{10, 12, 24}

For large scale energy storage, energy efficient and high power RFBs are desired to provide fast charge/discharge responses.^{1, 2} Thus, it is critical to improving energy efficiency and power performance of neutral AORFBs. In chapter II, a highly stable neutral FcNCl/MV AORFB was introduced with 99.99% capacity retention per cycle for 700 cycles, 60% energy efficiency at 60 mA/cm², where FcNCl is (ferrocenylmethyl)trimethylammonium chloride and MV is methyl viologen dichloride.¹⁵ Despite the high energy density that this neutral system could achieve, its power output capability is inferior to most of the acidic and alkaline based AORFBs. For example, the traditional all vanadium RFBs with acid as supporting electrolyte which could deliver energy efficiency (current density: 100 mA/cm²) up to 80%, which is twice of the FcNCl/MV battery at the same current density.³¹ The power density of VRFBs is also several times of the pH neutral FcNCl/MV RFB.³² This is mainly attributed to the lower conductivity of the neutral electrolyte. For practical large scale energy storage, energy efficient and high power RFBs are desired to provide fast charge/discharge responses. Thus, it is critical to improve energy efficiency and power performance of neutral AORFBs. Herein, through the case studies of the neutral FcNCl/MV AORFB, for the first time, we demonstrate a strategy of optimizing two fundamental material components, ion exchange membrane and supporting electrolyte, to reduce the battery resistance and boost the energy efficiency and power performance of neutral AORFBs. With an optimal membrane and an optimal supporting electrolyte, the 0.5 M neutral FcNCl/MV AORFB achieved unprecedented energy efficiency of 85% at 40 mA/cm² (or 79% at 60 mA/cm², 67.1 % at 100 mA/cm²) which is very close to the commercialized all VRFBs. An optimized power density was demonstrated as high as 122.7 mW/cm² for a

0.7 M battery. It is anticipated that the optimization approach can be extended to other AORFBs.

3-3. Materials and methods

Materials

FcNCl was synthesized as introduced in Chapter II. Methyl viologen was purchased from Acros Organics. All the solvents (CH_3CN , DMF, CH_2Cl_2 , diethyl ether) were purchase from fisher chemicals. Deionized water was obtained from a MilliporeSigma Milli-DI Water Purification System and purged overnight using N_2 before use. All experimental operations were conducted under a N_2 atmosphere. SelemionTM ion exchange membranes were purchased from ASAHI GLASS CO., LTD, Japan. The ion exchange membranes were soaked in 0.5 M NaCl aqueous solution overnight before use.

Characterization

NMR studies were conducted using a Bruker 500 MHz NMR spectrometer. Elemental analysis was done at Atlantic Microlab. The conductivity of the electrolyte solutions was measured using a Mettler Toledo conductivity meter at R.T.

Electrochemical cyclic voltammetry studies

All electrochemical cyclic voltammetry (CV) experiments were carried out in 0.5 M NaCl electrolyte solutions. Cyclic voltammetry experiments were performed with a Gamry 1000E potentiostat. All potentials were referenced to NHE according to the known $\text{MV}^{2+/1+}$ redox couple (-0.45 V vs NHE)³³. The working electrode (1 mm PEEK-encased glassy carbon, Cypress Systems EE040) was polished using Al_2O_3 (BAS CF-1050, dried at 150°C under vacuum) suspended in deionized H_2O , then rinsed with

deionized H₂O and dried with air flow. The reference electrode consisted of a silver wire coated with a layer of AgCl and suspended in a solution of 0.5 M NaCl electrolyte. A glassy carbon rod (Structure Probe, Inc.) was used as the counter electrode. Before each measurement, the electrolyte was purged by nitrogen gas for 5 minutes.

Electrochemical linear sweeping voltammetry studies

All linear sweeping voltammetry (LSV) studies were conducted using a Gamry 1000E potentiostat in a three-electrode configuration, a glassy carbon disk working electrode (5 mm Teflon encased glassy carbon disk, Pine Research Instrumentation) along with a glassy carbon counter electrode and a Ag/AgCl reference electrode as used in CV studies. All potentials were referenced to NHE according to the known MV^{2+/1+} redox couple (-0.45 V vs NHE). Before data collection, the disk electrode was prepared using the procedure described in the CV studies. The electrode was then rotated from 300 to 2400 rpm with increments of 300 rpm, which was controlled by a Pine MSR rotator system. LSV scans were recorded at a rate of 5 mV/s from 0.3 V to 0.8 V vs NHE. At each rotation rate, the LSVs were recorded three times to ensure repeatability. The diffusion coefficients were calculated by Levich equation (Equation 2-1). The Electron transfer rate constants were calculated by Koutechý-Levich equation as follows:

$$\frac{1}{i_l} = \frac{1}{i_k} + \frac{1}{0.62nFAD^{2/3}\nu^{-1/6}C} \omega^{-1/2} \quad (\text{Equation 3-1})$$

Electrochemical impedance measurements

EIS data were collected using a Gamry 5000E potentiostat. For the ion exchange membrane resistance measurements, several dummy cells were assembled with and without ion exchange membranes. Then, EIS experiments were conducted. The

membrane resistance was calculated by Equation 3-2. Full cell EIS tests were done as introduced in Chapter II.

$$R_{\text{membrane}} = R_{hf, \text{ with membrane}} - R_{hf, \text{ without membrane}} \quad (\text{Equation 3-2})$$

Flow cell tests

The FcNCl/MV AORFBs were constructed with two carbon electrolyte chambers, two graphite felt electrodes (SGL Carbon Group, Germany) and a piece of anion exchange membrane (SelemionTM, Japan) sandwiched between graphite felts, and two copper current collectors. Each carbon chamber was connected with an electrolyte reservoir using a piece of Viton tubing. The electrolyte reservoir is home designed and is a 10 mL glass tube (2 cm inner diameter). The active area of the cell was 10 cm². A Masterflex[®] L/S[®] peristaltic pump (Cole-Parmer, Vernon Hills, IL) was used to press the Viton tubing to circulate the electrolytes through the electrodes at a flow rate of 60 mL/min. In each reservoir, the balanced flow cell employed 12 mL of the NaCl electrolytes containing 0.5 M active materials. Both reservoirs were purged with nitrogen to remove O₂ and then sealed before cell cycling. The flow cell was galvanostatically charged/discharged at R.T. on a battery tester (Land Instruments) in the voltage range of 1.5 – 0.1 V at current densities ranging from 40 to 100 mA/cm². The polarization curves were collected using a Gamry 5000E potentiostat.

3-4. Results and discussion

Membrane resistance measurements

The ion exchange membrane and the supporting electrolyte are two fundamental materials in charge of charge transfer inside a redox flow battery, and thus have significant impacts on energy efficiency and power density of redox flow batteries. To

understand how the anion exchange membrane and the supporting electrolyte affect the battery performance of the FcNCl/MV AORFB, we have investigated these two factors systematically. It is expected that the optimization of the conductivities of the membrane and the supporting electrolyte can reduce the battery resistance and boost the energy efficiency and power density of the AORFB. We first studied how the anion exchange membrane and NaCl electrolyte affect the battery resistance through electrochemical impedance spectroscopic (EIS) studies. The membrane resistance was determined in a dummy cell using 2.0 M NaCl supporting electrolyte without the FcNCl and MV active materials. The Nyquist plot of the first dummy cell with the AMV membrane (Figure 3-1A, gray trace) revealed a high-frequency area resistance (R_{hf}) of $3.48 \Omega \cdot \text{cm}^2$. The second dummy cell without the membrane gave an R_{hf} value of $0.68 \Omega \cdot \text{cm}^2$ that represents the resistance of 2.0 M NaCl supporting electrolyte. The membrane resistance was calculated as $2.80 \Omega \cdot \text{cm}^2$, the difference of $3.5 \Omega \cdot \text{cm}^2$ and $0.7 \Omega \cdot \text{cm}^2$. The Nyquist plot (Figure 3-1B, grey trace) of the 0.5 M FcNCl/MV **AORFB/AMV/NaCl** using 2.0 M NaCl supporting electrolyte was recorded to get an R_{hf} as $3.99 \Omega \cdot \text{cm}^2$ that consists of the resistances of the AMV membrane (thickness, 110 μm) and the NaCl supporting electrolyte. The observed difference between the R_{hf} values of the 0.5 M FcNCl/MV AORFB and the dummy cell is attributed to the influence of the dissolved active materials. It is clear that the AMV membrane is the primary component of the resistance of the battery. Inspired by the above results, we envisaged that using a more conductive membrane would lower the battery resistance significantly to enhance its electrochemical performance including energy efficiency and power density. Thus, we conducted a similar EIS study with another thinner Selemion anion exchange membrane (Selemion

DSV membrane, thickness 90 μm). The resistance (R_{hf}) of the thinner DSV membrane was measured as $1.13 \Omega\cdot\text{cm}^2$ (Figure 2A, orange trace), more than 60 % smaller than that of the AMV membrane ($1.67 \Omega\cdot\text{cm}^2$).

Battery performance test with NaCl supporting electrolyte with various anion exchange membranes

In order to study how the membrane resistance affects the electrochemical performance of the FcNCl/MV AORFB, we did a comparative study of these two membranes in a 0.5 M FcNCl/MV AORFB. The electrochemical performance of 0.5 M FcNCl/MV AORFBs using the AMV and DSV membranes (called **AORFB/AMV/NaCl** and **AORFB/DSV/NaCl**, respectively) was collected at various current densities from 40 to 100 mA/cm^2 with an increment of 20 mA/cm^2 (Figure 2-14). For each current density, 7 charge and discharge cycles were tested with cutoff voltages at 1.5 V for the charging process and 0.1 V for the discharge process. Both **AORFB/DSV/NaCl** and

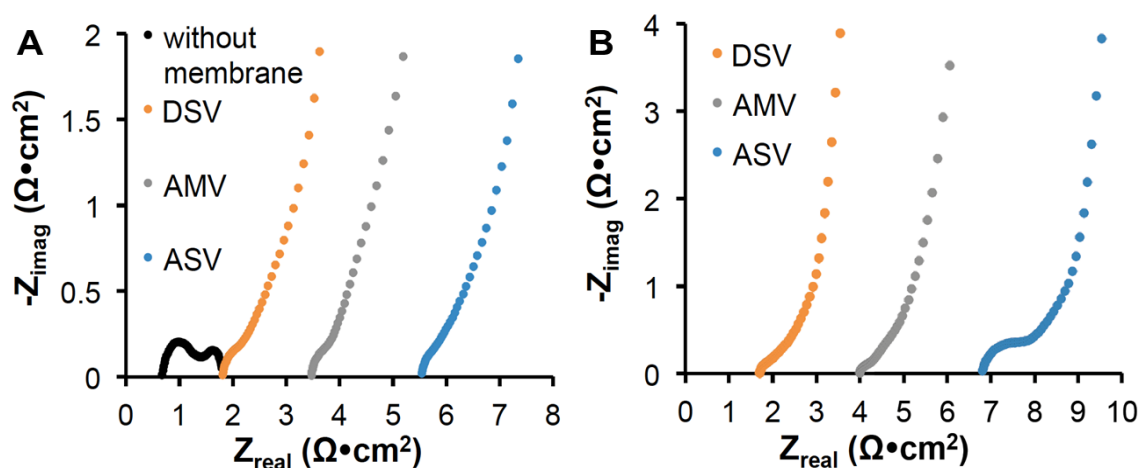


Figure 3-1. (A) Nyquist plots of a dummy RFB cell using 2.0 M NaCl without an anion exchange membrane (black trace) and with the DSV (orange trace), AMV (gray trace), and ASV (blue trace) membranes (B) Nyquist plots of **AORFB/DSV/NaCl** (orange trace), **AORFB/AMV/NaCl** (gray trace), and **AORFB/ASV/NaCl** (blue trace); 0.5 M active materials in 2.0 M NaCl.

AORFB/AMV/NaCl batteries displayed good capacity retention (13.4 Ah/L theoretical capacity) from 40 mA/cm² (> 11.6 Ah/L or 89% capacity utilization) to 100 mA/cm² (> 11.1 Ah/L or 84% capacity utilization).

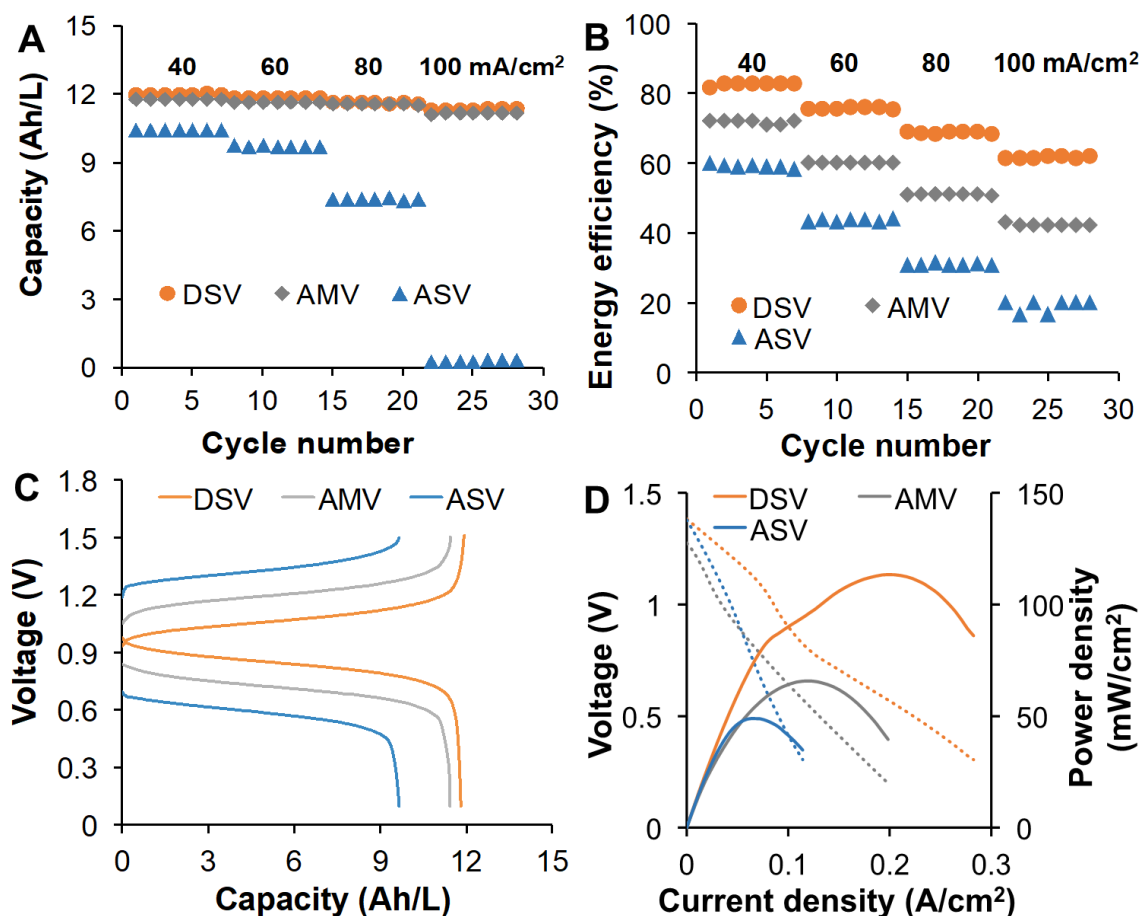


Figure 3-2. (A) Capacity vs. cycle number from 40 to 100 mA/cm² of the 0.5 M FcNCl/MV AORFBs with different membranes (see legends) using 2.0 M NaCl supporting electrolyte. (B) Energy efficiency vs. cycle number from 40 to 100 mA/cm² of the FcNCl/MV AORFBs with different membranes using 2.0 M NaCl supporting electrolyte. (C) Representative voltage profile vs capacity of the FcNCl/MV AORFBs recorded at 60 mA/cm² with various membranes. (D) Polarization and power density curves of the FcNCl/MV AORFBs with different membranes using 2.0 M NaCl supporting electrolyte. Conditions: 0.5 M active materials in 2.0 M supporting electrolyte.

AORFB/DSV/NaCl showed a slightly higher capacity utilization out of 13.4 Ah/L theoretical capacity than **AORFB/AMV/NaCl**, e.g. at 60 mA/cm², 11.9 Ah/L for the DSV membrane (Figure 3-2A, orange trace) and 11.6 Ah/L for the AMV membrane (Figure 3-2A, gray trace). As shown in Figure 3-2B, **AORFB/DSV/NaCl** (orange trace) is clearly more energy efficient than **AORFB/AMV/NaCl** (gray trace) at 4 four tested current densities. For example, at 60 mA/cm², **AORFB/DSV/NaCl** delivered an energy efficiency of 76%, 16% higher than that of **AORFB/AMV/NaCl**, 60% energy efficiency. Representative charge/discharge voltage profiles versus capacity at 60 mA/cm² were given in Figure 3-2C (gray and orange traces). In line with the observed energy efficiencies, for **AORFB/DSV/NaCl**, the averaged charge/discharge voltage tested at 60 mA/cm² appeared at 0.97/0.86 V while observed at 1.05/0.84 V for the AMV membrane. The smaller charge/discharge overpotential observed for **AORFB/DSV/NaCl** is benefitted from its lower membrane resistance. As the Coulombic efficiencies of both batteries are nearly 100%, the voltage efficiency (ca. 76%) of **AORFB/DSV/NaCl** is higher than that of **AORFB/DSV/NaCl**, ca. 60%. Polarization curves were collected for both batteries to compare their power density. **AORFB/DSV/NaCl** was able to deliver a peak power density of 113.3 mW/cm² at ca. 200 mA/cm² (Figure 3-2D, orange trace). **AORFB/AMV/NaCl** delivered a peak power density of 65.7 mW/cm² at 114 mA/cm² (Figure 3-2D, gray trace), much smaller than that of the former battery.

The present data established a number of benefits using a more conductive or less resistant anion exchange membrane including improved capacity utilization, energy efficiency, and power density. To further confirm the effects of membrane on the battery performance, we continued to study a thicker membrane (Selemin ASV membrane,

thickness 120 μm). The resistance (R_{hf}) of the ASV membrane was measured as 4.86 $\Omega\cdot\text{cm}^2$ (Figure 3-1A, blue trace). The properties of these membranes are summarized in Table 3-1. Indeed, as seen in Figure 3-2, **AORFB/ASV/NaCl** exhibited lower capacity utilization, lower energy efficiency, and a lower power density than the former two batteries using the DSV and AMV membranes. At 60 mA/cm^2 , **AORFB/ASV/NaCl** delivered energy efficiency of 44% and capacity utilization of 9.7 Ah/L, only 72.4% out of the theoretical capacity, 13.4 Ah/L. The rate performance of **AORFB/ASV/NaCl** was much poorer than the other two batteries. At 100 mA/cm^2 , the battery barely could be cycled with very low capacity utilization. The peak power density was measured as only 48.6 mW/cm^2 . To gain an in-depth understanding of the battery performance, EIS tests were conducted with the two batteries using the DSV and ASV membranes under the fully discharged state to give their battery resistance (R_{hf}) as 1.70 and 6.81 $\Omega\cdot\text{cm}^2$, respectively (Figure 3-1B, orange trace and blue trace). Consistent with **AORFB/AMV/NaCl**, the major resistant component of **AORFB/DSV/NaCl** and **AORFB/ASV/NaCl** is attributed to their membrane resistance, 1.11 and 4.86 $\Omega\cdot\text{cm}^2$ respectively. All three batteries showed a small charge transfer resistance ($< 1.00 \Omega\cdot\text{cm}^2$), which is benefited from the fast charge transfer of the active materials, FcNCl and MV. It is clear that in the order of DSV, AMV and, ASV, the battery resistance increased as the membrane resistance enlarges. Similarly, the observed charge/discharge overpotential (Figure 3-2C) for these AORFBs also increased with the increase of the membrane resistance.

Conductivity measurements of NaCl and KCl based electrolyte

Compared to the membrane resistance, the resistance of the supporting electrolyte ($0.68 \Omega \cdot \text{cm}^2$) is much smaller. However, it could not be neglected. Different cations and anions display very different ionic equivalent conductivity and mobility in water. Specifically, the proton has an ionic equivalent conductivity and mobility of $350 \text{ S}/(\text{cm} \cdot \text{eq})$ and $0.362 \text{ cm}^2/(\text{V} \cdot \text{S})$, which are both several times higher than those of Na^+ .³⁴

In the electrolyte of a RFB, electron transfer and counter ion diffusion happen simultaneously redox reactions, where ions (anions or cations) exchange through the membrane is much slower than electron transfer, thus plays the role of the rate determining step of the reactions. Therefore, the higher ionic equivalent conductivity and mobility are in favor of the lower electrolyte resistance and faster redox reaction, which provides the reason why acidic and alkaline AORFBs normally could be more efficient and powerful than neutral AORFBs. According to this theory, power and efficiency could also be improved for neutral AORFBs, such as the FcNCl/MV battery, if a more conductive supporting electrolyte is used. We found that at the same concentrations, the conductivity of KCl aqueous solution could be 36% higher than NaCl aqueous solution (e.g. $187.0 \text{ mS}/\text{cm}$ for 2.0 M KCl vs $138.1 \text{ mS}/\text{cm}$ for 2.0 M NaCl). The same as NaCl, KCl is inexpensive, safe and environmentally benign, and thus is also a good choice of supporting electrolytes for neutral AORFBs. For both anolyte and catholyte, NaCl and KCl supporting electrolytes provided almost identical tendency of conductivity (as shown in Figure 3-3). At 0.5 M active materials in 2.0 M NaCl solution, optimal conductivity can be obtained for the FcNCl/MV AORFB, $135.6 \text{ mS}/\text{cm}$ for FcNCl and $175.2 \text{ mS}/\text{cm}$ for MV giving an averaged conductivity of $155.2 \text{ mS}/\text{cm}$. Similarly, at 0.5 M active materials in 2.0 M KCl solution, the averaged conductivity of FcNCl and MV is optimal,

168.1 mS/cm for FcNCl and 207.1 mS/cm for MV giving an averaged conductivity of 187.6 mS/cm. FcNCl and MV in KCl supporting electrolytes were on average 25% more conductive than in NaCl supporting electrolytes. In addition, it should be noticed that the supporting electrolytes could greatly improve the conductivity of the FcNCl catholyte and also enhance the conductivity of the MV anolyte (Figure 3-3), which is clearly beneficial to the battery conductivity. The FcNCl anolyte without a supporting electrolyte

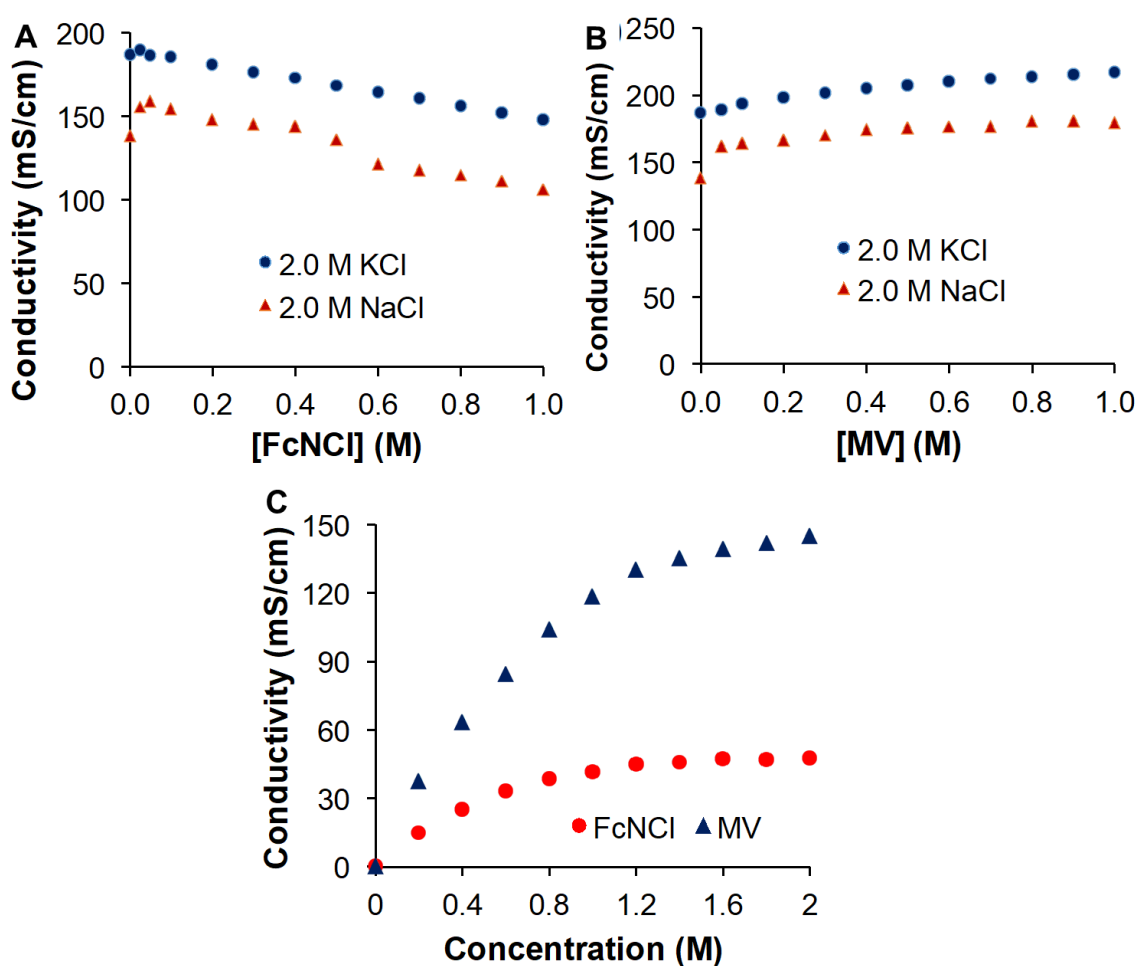


Figure 3-3. Conductivity measurement of FcNCl (A) and MV (B) from 0 to 1.0 M in 2.0 M KCl or 2.0 M NaCl solutions at room temperature. (C) Conductivity dependence vs concentration of FcNCl and MV solutions without supporting electrolyte.

Table 3-1. A summary of the thickness of the DSV, AMV, and ASV membranes and their resistances (R_{hf}) in the NaCl and KCl supporting electrolytes.

Membranes	Thickness (μm)	Area resistance (R_{hf} , $\Omega\cdot\text{cm}^2$)	
		In 2.0 M NaCl	In 2.0 M KCl
DSV	90	1.13	1.07
AMV	110	2.80	2.75
ASV	120	4.86	4.54

only exhibited an optimal conductivity up to 47.7 mS/cm around 1.8 M while the MV anolyte by itself gave an optimal conductivity of 145 mS/cm around 2.0 M but still much lower than that in the presence of supporting electrolyte (Figure 3-3B and C).

Electrochemical studies of active materials in NaCl and KCl supporting electrolyte

Electrochemical studies were conducted to examine how the supporting electrolyte affects the electrochemical behaviors of the active materials, FcNCl and MV. Cyclic voltammetry studies revealed that both FcNCl (0.6 V vs NHE) and MV (-0.45 V vs. NHE) have almost identical redox potentials and current in NaCl and KCl supporting electrolytes (Figure 3-4), indicating that the different cation barely affected the redox activity and reversibility of both FcNCl and MV.

To understand whether the supporting electrolyte affects the electrochemical kinetics of the active materials, linear sweep voltammetry (LSV) tests were conducted using a glassy carbon rotation disc electrode from 300 rpm to 2400 rpm at a scan rate of 5 mV/s (Figure 3-5A and E). The diffusion coefficients of FcNCl and MV in 0.5 m KCl were calculated as 3.40×10^{-6} and $4.42 \times 10^{-6} \text{ cm}^2/\text{s}$ from the slope of their Levich plots (Figure 3-5B and F) using Levich equation (Equation 1-1). For the overpotential from 10

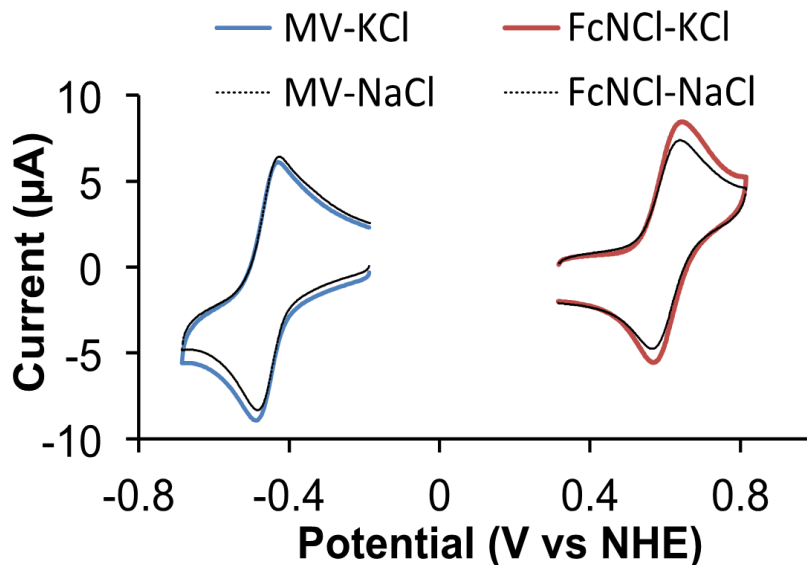
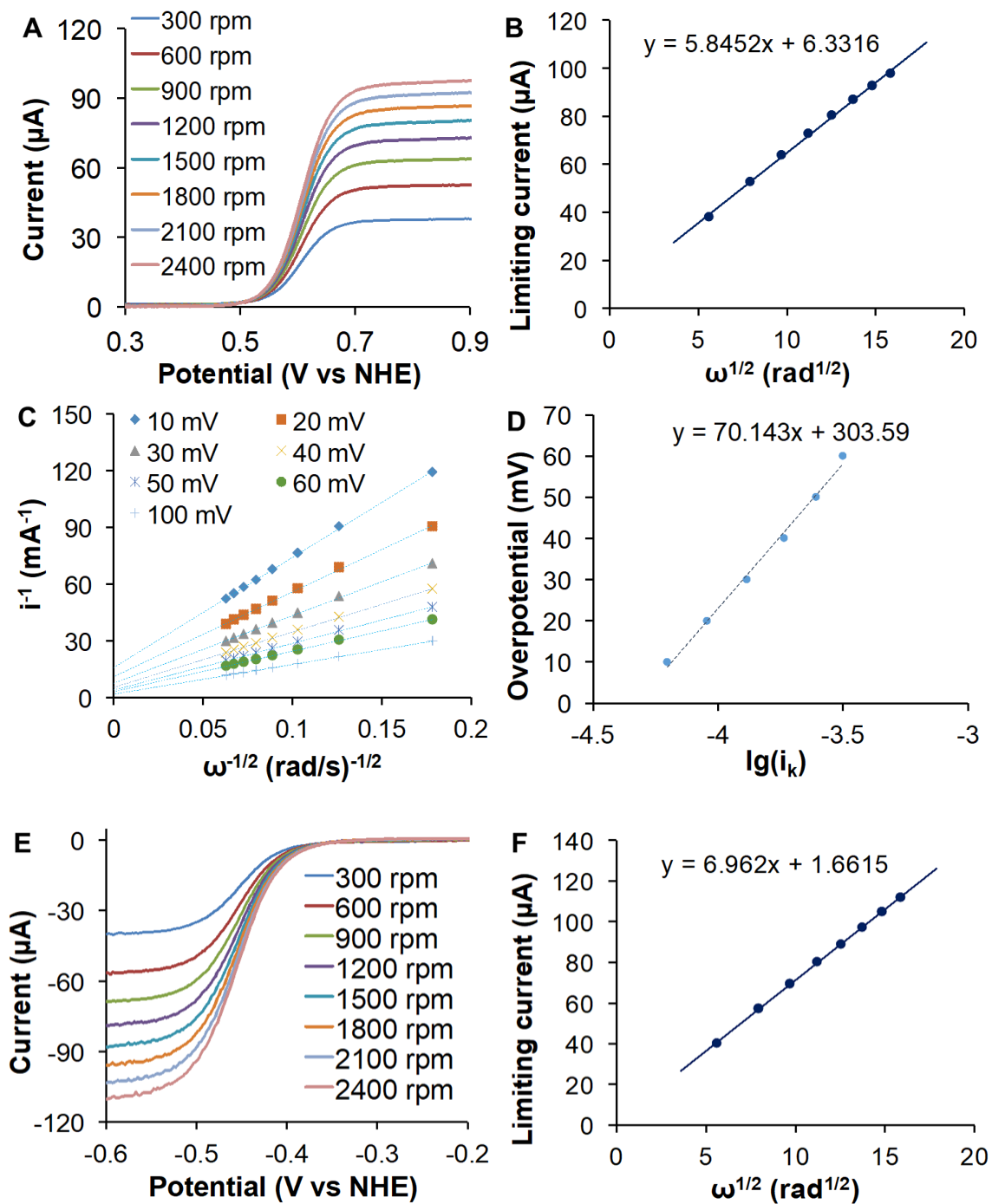


Figure 3-4. Cyclic voltammograms of FcNCl (0.6 V, red trace) and MV (-0.45 V, blue trace) in 0.5 M KCl. The dashed curves are the cyclic voltammograms of FcNCl and MV in 0.5 M NaCl. Conditions: 4 mM FcNCl or MV in 0.5 M KCl or NaCl supporting electrolyte; working electrode, glassy carbon electrode; reference electrode, Ag/AgCl electrode; counter electrode, carbon rod; scan rate, 100 mV/s.

to 100 mV for the reduction of MV and the oxidation of FcNCl, the corresponding Koutechý-Levich plots (Figure 3-5C and G) were constructed to yield a kinetic current that is independent of mass transport according to the Koutechý-Levich equation (Equation 3-1). Different from Chapter II, here we applied Koutechý-Levich method to overcome the diffusion limitation of the RDE tests due to the limited rotating speed, thus obtained a more accurate evaluation of the electron transfer rate constants for FcNCl and MV. Then for each compound, a Tafel plot was developed using the overpotential over the logarithm of the derived ideal kinetic current (Figure 3-5D and H). The exchange currents were yielded by extrapolating the corresponding Tafel plot to the x-axis, 4.79×10^{-5} mA/cm² for FcNCl and 5.84×10^{-5} mA/cm² for MV, respectively.



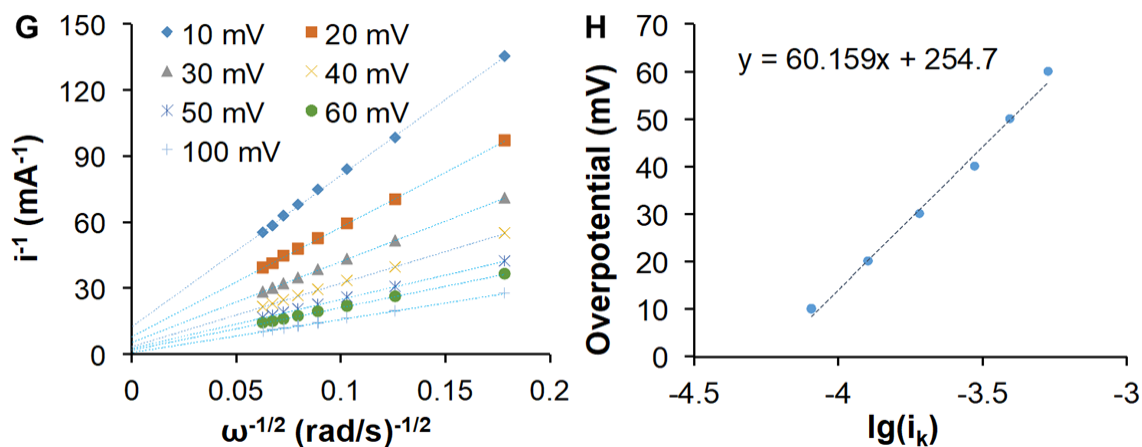


Figure 3-5. Electrochemical kinetic studies of FcNCl (1.0 mM) and MV (1.0 mM) in 0.5 M KCl. (A) and (E) Linear sweep voltammograms of FcNCl and MV; (B) and (F) Levich plots of the limiting current vs the square root of rotation rates for FcNCl; (C) and (G) Koutechý-Levich plots of FcNCl and MV; (D) and (H) Tafel plots of FcNCl and MV.

Through Koutechý-Levich analysis (Equation 3-1), the electron transfer rate constant of FcNCl and MV in KCl was calculated as 2.48×10^{-3} cm/s for FcNCl and 3.08×10^{-3} cm/s for MV, respectively. As summarized in Table 3-2, both FcNCl and MV in the KCl supporting electrolyte exhibited a fast electron transfer rate constant than in the NaCl supporting electrolyte. The enhanced electron transfer rate constants can reduce the charge transfer resistances of both compounds at the electrode surface, and thus improve energy efficiency and power performance in a redox flow battery.

Table 3-2. A comparison of the diffusion (D) and electron transfer rate constants (k^0) of FcNCl and MV in 0.5 M NaCl and KCl supporting electrolytes. a. Diffusion constants of FcNCl and MV were cited from ref. 16 and 9, respectively. Electron transfer rate constants (k^0) of FcNCl and MV were recalculated using the data from ref. 16 and 9 using the Koutechý-Levich treatment.

Compounds	In 0.5 M NaCl ^a		In 0.5 M KCl	
	D (cm^2/s)	k^0 (cm/s)	D (cm^2/s)	k^0 (cm/s)
FcNCl	3.74×10^{-6}	7.99×10^{-4}	3.40×10^{-6}	2.48×10^{-3}
MV	2.57×10^{-5}	5.18×10^{-3}	4.42×10^{-6}	3.08×10^{-3}

Battery performance test with KCl supporting electrolyte with various anion exchange membranes

Subsequently, three FcNCl/MV AORFBs in 2.0 M KCl, **AORFB/DSV/KCl**, **AORFB/AMV/NaCl**, and **AORFB/ASV/KCl**, were assembled with three membranes to study their battery performance. Their battery data were presented in Figure 3-6.

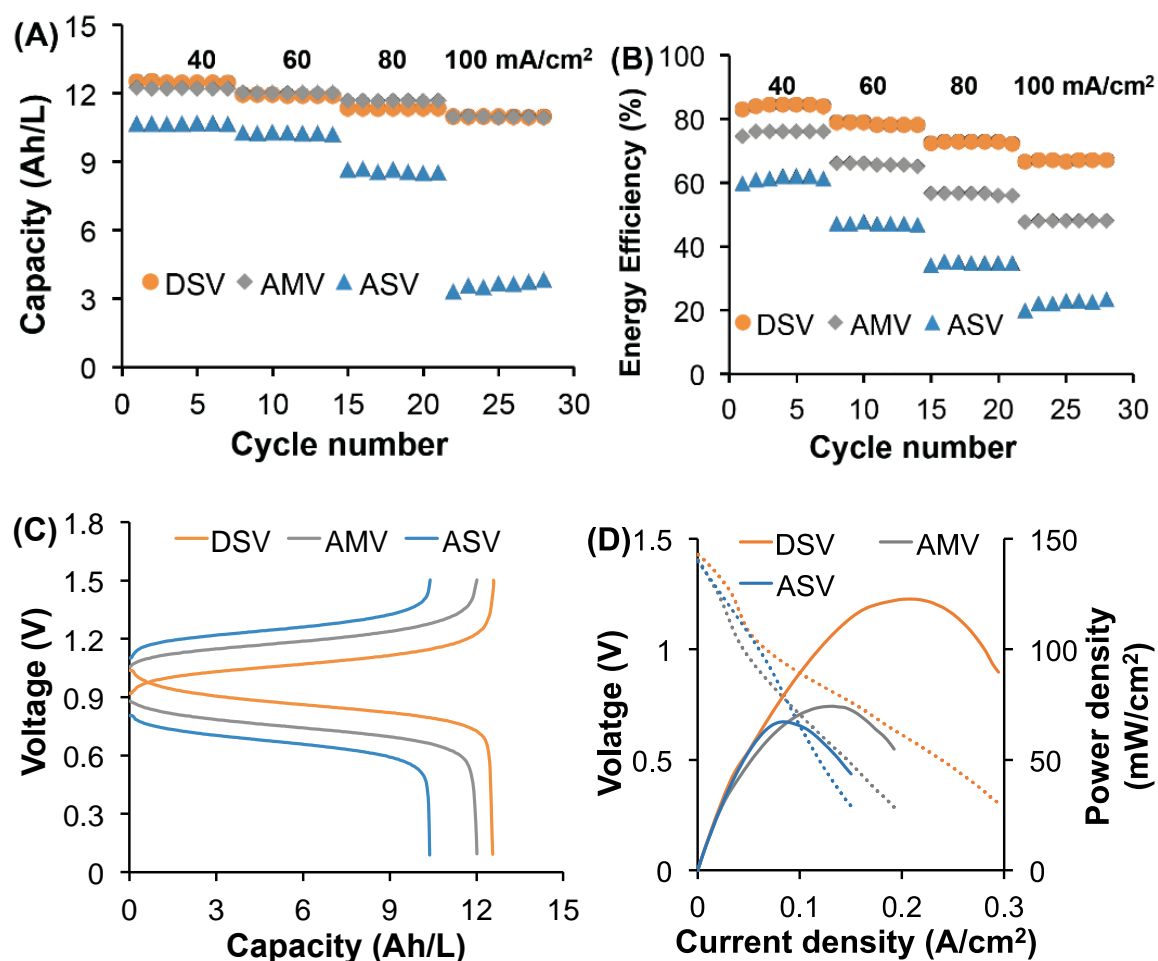


Figure 3-6. (A) Capacity vs. cycle number from 40 to 100 mA/cm² of the **FcNCl/MV** AORFBs with different membranes (see legends) using 2.0 M KCl supporting electrolyte. (B) Energy efficiency vs. cycle number from 40 to 100 mA/cm² of the **FcNCl/MV** AORFBs with different membranes using 2.0 M KCl supporting electrolyte. (C) Representative voltage profiles vs capacity of the **FcNCl/MV** AORFBs recorded at 60 mA/cm² with different membranes. (D) Polarization and power density curves of the

FcNCl/MV AORFBs with different membranes using 2.0 M KCl supporting electrolyte. Conditions: 0.5 M active materials in 2.0 M supporting electrolyte.

Each of three AORFB/KCl batteries exhibited improved battery performance regarding energy efficiency, capacity utilization, charge/discharge overpotential, and power density compared to the corresponding AORFB in NaCl. A comprehensive comparison of electrochemical performance regarding energy efficiency and capacity utilization at 60 mA/cm², and power densities of these AORFBs in KCl and NaCl were given in Table 3-3 below. Taking **AORFB/DSV/KCl** for example, the battery delivered higher energy efficiency (79%, Figure 5A orange trace) and capacity utilization (12.2 Ah/L out of theoretical 13.4 Ah/L, 89.5%, Figure 5B orange trace) at 60 mA/cm², and power density (122.7 mW/cm², Figure 5D orange trace) than those of **AORFB/DSV/NaCl**, specifically, 76% energy efficiency, 11.9 (88.1% Ah/L) capacity utilization, and 113.3 mW/cm². At 40 mA/cm², **AORFB/DSV/KCl** even achieved 85% energy efficiency (Figure 5B orange trace and Table 3-3). Within the series, like the AORFBs using NaCl, an AORFB/KCl using a thinner membrane delivered higher energy efficiency, higher capacity utilization, and a higher power density.

In a dummy cell, the resistance of 2.0 M KCl was recorded as 0.51 $\Omega\cdot\text{cm}^2$ (Figure 3-7A, black dot trace) versus 0.68 $\Omega\cdot\text{cm}^2$ for 2.0 M NaCl, which is consistent with their relative conductivities. In 2.0 M KCl, the R_{hf} values of the DSV, AMV, and ASV membranes were measured as 1.07, 2.75, and 4.54 $\Omega\cdot\text{cm}^2$, slightly lower than those in 2.0 M NaCl. Consistent with the higher conductivities of the FcNCl catholyte and the MV anolyte in 2.0 M KCl, each of **AORFB/DSV/KCl**, **AORFB/AMV/KCl**, and **AORFB/ASV/KCl** showed a reduced R_{hf} resistance, 1.60, 3.46, and 5.87 $\Omega\cdot\text{cm}^2$, respectively (Figure 3-7B and Table 3-3) than that of the corresponding battery using

Table 3-3. A comprehensive comparison of battery resistance (R_{hf}), energy efficiency (EE) and capacity utilization at 60 mA/cm², power density, and capacity retention per cycle (200 cycles) of the **FcNCl/MV** AORFBs using various anion exchange membranes and supporting electrolytes.

AORFBs	R_{hf} ($\Omega \cdot \text{cm}^2$)	EE (%)	Capacity utilization (Ah/L)	Power density (mW/cm ²)	Capacity retention per cycle (%)
DSV/NaCl	1.70	76	11.9 (88.1%)	113.3	99.964
AMV/NaCl	3.99	60	11.6 (86.5%)	65.7	99.988
ASV/NaCl	6.81	44	9.7 (72.4%)	48.6	99.993
DSV/KCl	1.60	79	12.2 (89.5%)	122.7	99.955
AMV/KCl	3.46	66	12.5 (92.3%)	74.1	99.971
ASV/KCl	5.87	48	10.7 (76.9%)	67.2	99.961

NaCl supporting electrolyte. Again, the membrane resistance is the major component for these batteries using KCl supporting electrolyte. Clearly, the improved battery performance of the AORFBs/KCl than the AORFBs/NaCl is attributed to the higher electrolyte conductivities or lower electrolyte resistances in KCl than in NaCl.

Cycling performance of the FcNCl/MV AORFBs at 0.5 M for six combinations of supporting electrolytes and anion exchange membranes was further validated by long cycling tests (200 cycles) at 60 mA/cm² (Figure 3-8A and B). All these batteries demonstrated coulombic efficiency above 99.9% and capacity retention above 99.95% per cycle (Table 3-3) through all cycles. Interestingly, the battery with ASV membrane in NaCl supporting electrolyte showed the best cycling stability (99.993% capacity retention per cycle) compared to the AMV (99.988% capacity retention per cycle) and DSV

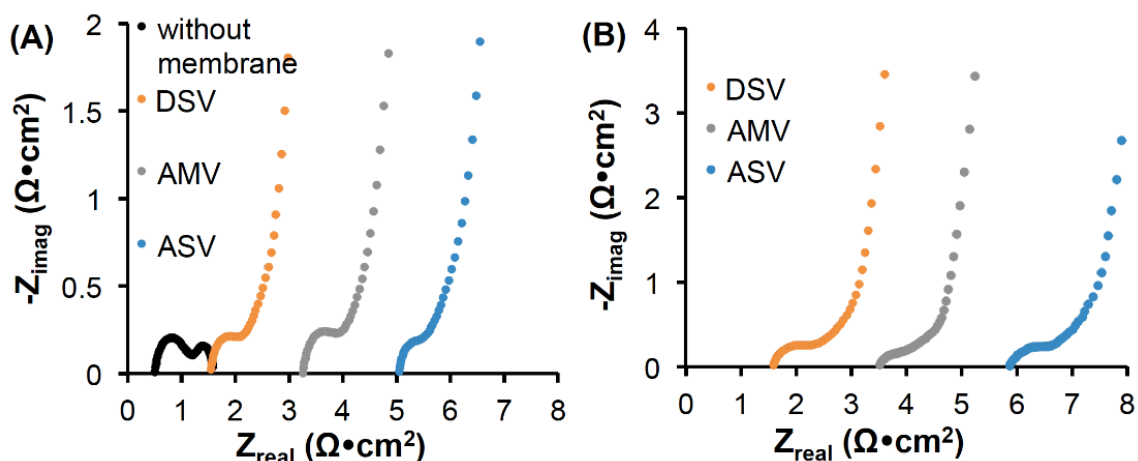


Figure 3-7. (A) Nyquist plots of a dummy RFB cell using 2.0 M KCl without an anion exchange membrane (black trace) and with the DSV (orange trace), AMV (gray trace), and ASV (blue trace) membranes. (B) Nyquist plots of **AORFB/DSV/KCl** (orange trace), **AORFB/AMV/KCl** (gray trace), and **AORFB/ASV/KCl** (blue trace); 0.5 M active materials in 2.0 M KCl.

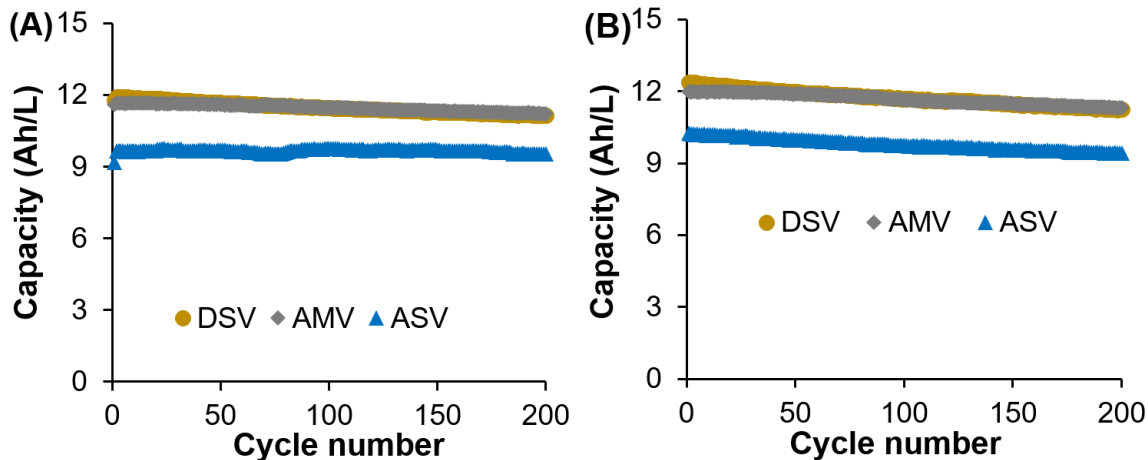


Figure 3-8. Discharge capacity vs. Cycle number at 60 mA/cm² of **FcNCl/MV** RFBs with various membranes and supporting electrolytes: (A) NaCl as supporting electrolyte, and (B) KCl as supporting electrolyte.

membranes (99.964% capacity retention per cycle). A similar trend regarding capacity retention was observed in KCl supporting electrolyte (see Table 3-3). Energy efficiencies

for 200 cycles of these batteries were shown in Figure 3-9. With more conductive electrolyte KCl, batteries' rate performance and was also improved remarkably (shown in Figure 3-10 and Table 3-4). In terms of overall electrochemical performance (rate capability, energy efficiency, coulombic efficiency, power density, cell voltage, and cycling stability), these FcNCl/MV batteries with various combinations of supporting electrolyte and membranes are among the best performing AORFBs reported to date.^{5, 7-10, 12-15, 21, 27}

Particularly, the energy efficiency and power densities of the FcNCl/MV AORFBs using DSV are in the ballpark of acidic/alkaline AORFBs.^{10, 12, 28} In terms of energy efficiency and power density, it is recommended to use a more ion conductive membrane thus a lower resistance for AORFB applications.

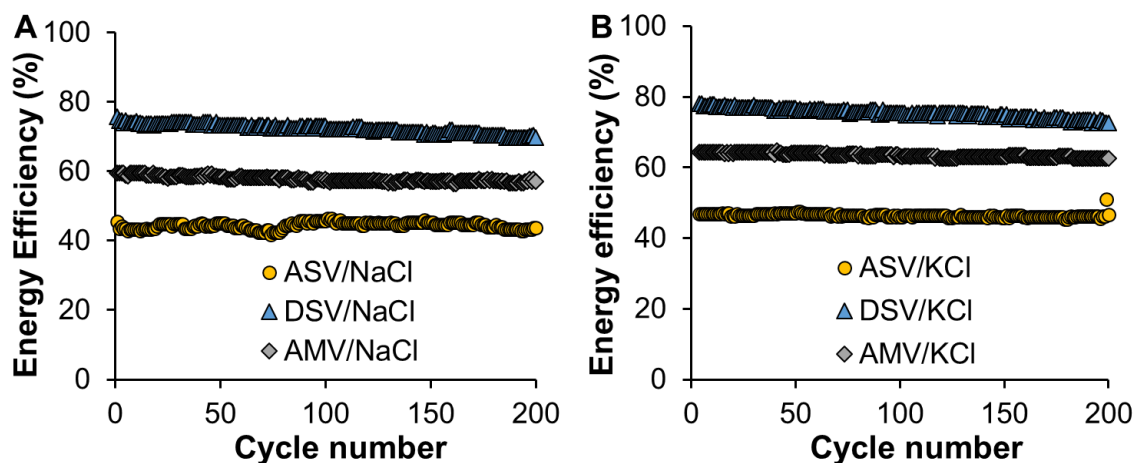


Figure 3-9. Plots of energy efficiency vs cycling numbers at 60 mA/cm² for the 0.5 M FcNCl/MV AORFBs using DSV, AMV, and ASV membranes using (A) 2.0 M NaCl and (B) 2.0 M KCl supporting electrolyte;

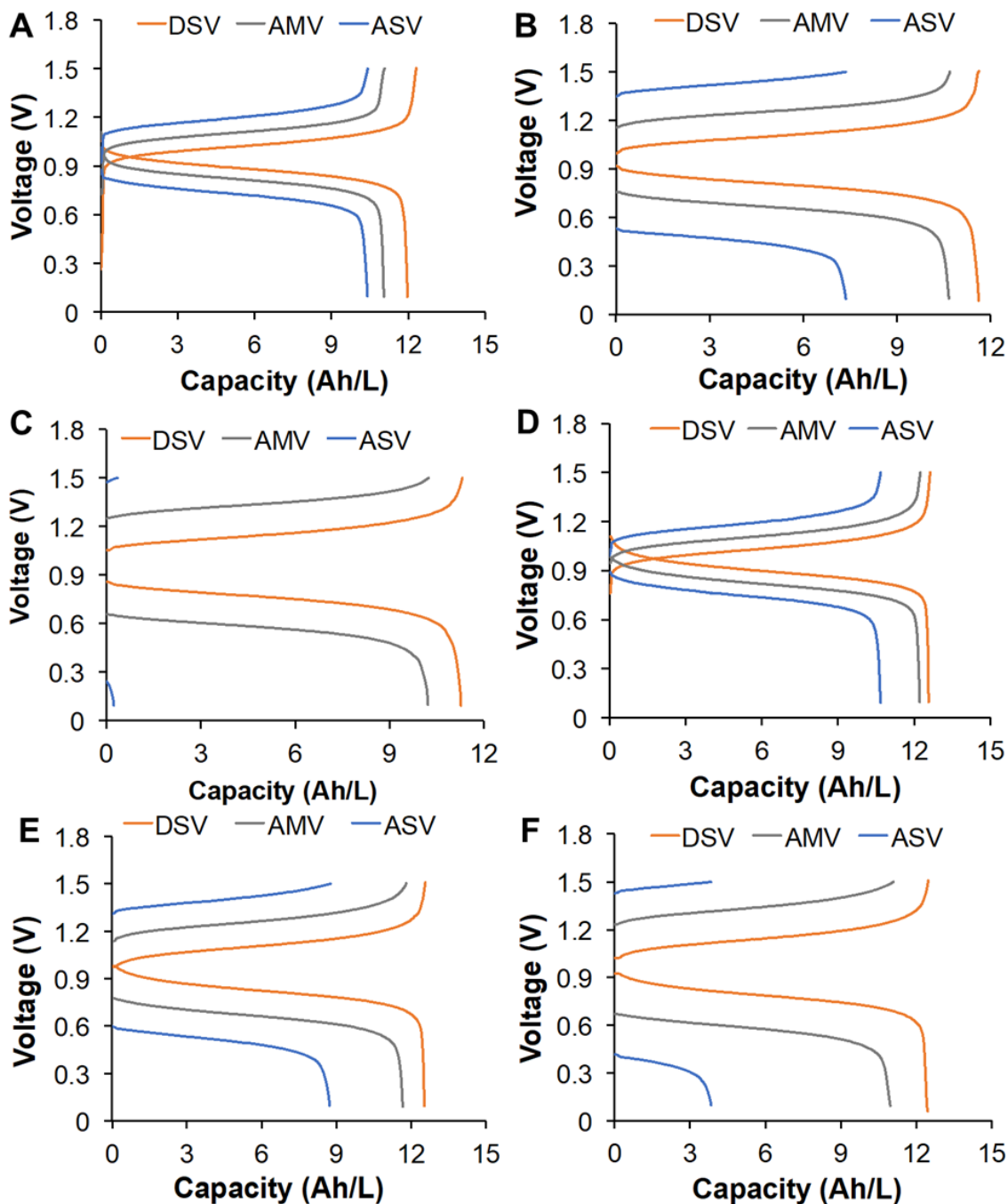


Figure 3-10. Representative voltage profile vs capacity of the **FcNCl/MV** AORFBs recorded at 40, 80, and 100 mA/cm² with various membranes using NaCl or KCl supporting electrolyte: (A) 40 mA/cm², NaCl; (B) 80 mA/cm², NaCl; (C) 100 mA/cm², NaCl; (D) 40 mA/cm², KCl; (E) 80 mA/cm², KCl; (F) 100 mA/cm², KCl.

Table 3-4. Energy efficiency (EE) and capacity utilization at 40, 80, and 100 mA/cm² for 0.5 M (13.4 Ah/L theoretical capacity) FcNCl/MV AORFBs using various anion ion exchange membranes and supporting electrolytes.

AORFBs	40 mA/cm ²		80 mA/cm ²		100 mA/cm ²	
	EE (%)	Capacity utilization (Ah/L)	EE (%)	Capacity utilization (Ah/L)	EE (%)	Capacity utilization (Ah/L)
DSV/NaCl	82.7	11.8	70.0	11.6	61.9	11.31
AMV/NaCl	72.1	11.6	51.1	11.5	42.2	11.13
ASV/NaCl	58.9	9.7	31.0	7.4	20.0	0.3
DSV/KCl	85.0	12.0	72.8	11.7	67.1	11.7
AMV/KCl	76.0	12.5	56.5	11.3	47.9	11.7
ASV/KCl	62.1	10.3	34.9	8.7	23.1	3.8

3-5. Conclusion

EIS studies revealed the battery resistance of the FCNCl/MV AORFB is primarily dominated by the anion exchange membrane. The thinnest DSV membrane with the lowest area resistance presented the best current dependent performance, energy efficiency, capacity utilization, and power density. KCl supporting electrolyte showed a higher conductivity than NaCl and resulted in the further improvement of the battery performance. In addition, the supporting electrolyte affects electrochemical kinetics including the diffusion constant and the electron transfer rate constant of the active materials. Our study emphasizes that battery resistance is an important factor that determines the charge/discharge overpotential, energy efficiency, and power density performance of the FCNCl/MV AORFB. The present strategy of optimizing membrane and supporting electrolyte yielded unprecedented energy efficiency and power density for neutral AORFBs and can be applied to other organic redox flow batteries. The results

further advance the potential of neutral AORFBs for sustainable and green energy storage of renewable energy.

3-6. References

- (1) Z. Yang, J. Zhang, M. C. W. Kintner-Meyer, X. Lu, D. Choi, J. P. Lemmon and J. Liu, *Chem. Rev.*, 2011, **111**, 3577-3613.
- (2) G. L. Soloveichik, *Chem. Rev.*, 2015, **115**, 11533-11558.
- (3) J. Winsberg, T. Hagemann, T. Janoschka, M. D. Hager and U. S. Schubert, *Angew. Chem. Int. Ed.*, 2016, **56**, 686-711.
- (4) P. Leung, A. A. Shah, L. Sanz, C. Flox, J. R. Morante, Q. Xu, M. R. Mohamed, C. Ponce de León and F. C. Walsh, *J. Power Sources*, 2017, **360**, 243-283.
- (5) Y. Xu, Y.-H. Wen, J. Cheng, G.-P. Cao and Y.-S. Yang, *Electrochim. Acta*, 2010, **55**, 715-720.
- (6) F. R. Brushett, J. T. Vaughey and A. N. Jansen, *Adv. Energy Mater.*, 2012, **2**, 1390-1396.
- (7) B. Huskinson, M. P. Marshak, C. Suh, S. Er, M. R. Gerhardt, C. J. Galvin, X. Chen, A. Aspuru-Guzik, R. G. Gordon and M. J. Aziz, *Nature*, 2014, **505**, 195-198.
- (8) T. Liu, X. Wei, Z. Nie, V. Sprenkle and W. Wang, *Adv. Energy Mater.*, 2016, **6**, 1501449.
- (9) B. Yang, L. Hoober-Burkhardt, F. Wang, G. K. Surya Prakash and S. R. Narayanan, *J. Electrochem. Soc.*, 2014, **161**, A1371-A1380.
- (10) K. Lin, R. Gómez-Bombarelli, E. S. Beh, L. Tong, Q. Chen, A. Valle, A. Aspuru-Guzik, M. J. Aziz and R. G. Gordon, *Nat. Energy*, 2016, **1**, 16102.
- (11) Y. Ding and G. Yu, *Angew. Chem. Int. Ed.*, 2016, **55**, 4772-4776.

- (12) K. Lin, Q. Chen, M. R. Gerhardt, L. Tong, S. B. Kim, L. Eisenach, A. W. Valle, D. Hardee, R. G. Gordon, M. J. Aziz and M. P. Marshak, *Science*, 2015, **349**, 1529-1532.
- (13) T. Janoschka, N. Martin, U. Martin, C. Friebe, S. Morgenstern, H. Hiller, M. D. Hager and U. S. Schubert, *Nature*, 2015, **527**, 78-81.
- (14) T. Janoschka, N. Martin, M. D. Hager and U. S. Schubert, *Angew. Chem. Int. Ed.*, 2016, **55**, 14427-14430.
- (15) B. Hu, C. DeBruler, Z. Rhodes and T. L. Liu, *J. Am. Chem. Soc.*, 2017, **139**, 1207-1214.
- (16) X. Wei, W. Xu, M. Vijayakumar, L. Cosimbescu, T. Liu, V. Sprenkle and W. Wang, *Adv. Mater.*, 2014, **26**, 7649-7653.
- (17) X. Wei, W. Xu, J. Huang, L. Zhang, E. Walter, C. Lawrence, M. Vijayakumar, W. A. Henderson, T. Liu, L. Cosimbescu, B. Li, V. Sprenkle and W. Wang, *Angew. Chem. Int. Ed.*, 2015, **54**, 8684-8687.
- (18) J. Huang, L. Cheng, R. S. Assary, P. Wang, Z. Xue, A. K. Burrell, L. A. Curtiss and L. Zhang, *Adv. Energy Mater.*, 2015, **5**, 1401782.
- (19) C. S. Sevov, D. P. Hickey, M. E. Cook, S. G. Robinson, S. Barnett, S. D. Minteer, M. S. Sigman and M. S. Sanford, *J. Am. Chem. Soc.*, 2017, **139**, 2924-2927.
- (20) C. S. Sevov, S. K. Samaroo and M. S. Sanford, *Adv. Energy Mater.*, 2017, **7**, n/a-n/a.
- (21) E. S. Beh, D. De Porcellinis, R. L. Gracia, K. T. Xia, R. G. Gordon and M. J. Aziz, *ACS Energy Letters*, 2017, **2**, 639-644.
- (22) J. R. McKone, F. J. DiSalvo and H. D. Abruna, *J. Mater. Chem. A*, 2017, **5**, 5362-5372.
- (23) G. Cong, Y. Zhou, Z. Li and Y.-C. Lu, *ACS Energy Letters*, 2017, **2**, 869-875.

- (24) K. Gong, F. Xu, J. B. Grunewald, X. Ma, Y. Zhao, S. Gu and Y. Yan, *ACS Energy Letters*, 2016, **1**, 89-93.
- (25) Z. Li, S. Li, S. Liu, K. Huang, D. Fang, F. Wang and S. Peng, *Electrochem. Solid-State Lett.*, 2011, **14**, A171-A173.
- (26) P. K. Leung, T. Martin, A. A. Shah, M. A. Anderson and J. Palma, *Chem. Commun.*, 2016, **52**, 14270-14273.
- (27) Y. Xu, Y. Wen, J. Cheng, Y. Yanga, Z. Xie and G. Cao, presented in part at the World Non-Grid-Connected Wind Power and Energy Conference, 2009. WNWEC 2009 Nanjing, China, September, 2009.
- (28) A. Orita, M. G. Verde, M. Sakai and Y. S. Meng, *Nat Commun* 2016, **7**, 13230.
- (29) T. Liu, B. Li, X. Wei, Z. Nie, V. Sprenkle and W. Wang, *USA Patent Application, US20160308233A1*, 2015.
- (30) T. Liu, B. Hu and C. Debruler, *USA Provisional Patent Application*, 2016.
- (31) Li, L.; Kim, S.; Wang, W.; Vijayakumar, M.; Nie, Z.; Chen, B.; Zhang, J.; Xia, G.; Hu, J.; Graff, G.; Liu, J.; Yang, Z. *Adv. Energy Mater.* **2011**, *1*, 394.
- (32) Skyllas-Kazacos, M.; Cao, L.; Kazacos, M.; Kausar, N.; Mousa, A. *ChemSusChem*, **2016**, *9*, 1521.
- (33) C. L. Bird and A. T. Kuhn, *Chem. Soc. Rev.*, 1981, *10*, 49.
- (34) Laidler K. J.; Meiser J. H. *Physical Chemistry*, **1982**. ISBN 0-8053-5682-7.

CHAPTER IV. IMPROVING THE CAPACITY AND STABILITY OF THE VIOLOGEN BASED REDOX FLOW BATTERIES ^d

4-1. Abstract

In this chapter, a viologen derivative 1,1'-bis[3-(trimethylammonio)propyl]-4,4'-bipyridinium tetrachloride ((**NPr**)₂**V**), bearing two pendant ammonium groups, was firstly designed and proved to be more stable than MV at the one-electron reduced state by UV-Vis spectra. Paired with 4-trimethylammonium-TEMPO chloride (N^{Me}-TEMPO) as catholyte, a high voltage (1.38 V) total organic aqueous redox flow battery was demonstrated. The high radical stability of [(**NPr**)₂**V**]^{•+} enabled the flow battery achieving 97.48 % capacity retention for 500 cycles and a power density of 128.2 mW/cm². UV-Vis was also applied to monitor the radical stability in aqueous solution. Then, we proposed a possible radical cation degradation mechanism which was further proved by gas chromatography. In order to avoid the dimer induced radical cation decomposition, we proposed to utilize MV into the nonaqueous system. By a straightforward anion exchange from Cl⁻ to bis(trifluoromethane)sulfonamide (TFSI⁻), the synthesized **MV(TFSI)**₂ showed two reversible redox processes in the organic solvent, indicating the feasibility of utilizing both electrons to double the batteries capacity. Paired with a ferrocene derivative (Ferrocenylmethyl)trimethylammonium

^d Adapted with permission from [Hu, B.; Tang, Y.; Luo, J.; Grove, G.; Guo, Y.; Liu, T. L. *Chem. Commun.* **2018**, 54, 6871]. Copyright 2018. Royal Society of Chemistry. Reproduced by permission of Royal Society of Chemistry. <https://pubs.rsc.org/en/content/articlelanding/2018/cc/c8cc02336k/unauth#!divAbstract>. Adapted with permission from [Hu, B.; Liu, T. L. *J. Energy Chem.* **2018**, 27, 1326]. Copyright 2018 Elsevier Inc. Reproduced by permission of Elsevier Inc., <https://www.sciencedirect.com/science/article/pii/S2095495617311403?via%3Dihub>.

bis(trifluoromethanesulfonyl)imide, **FcNTFSI**, as catholyte, the **MVTFS/FcNTFSI** nonaqueous organic redox flow battery (NOARFB) can take advantage of either one electron or two-electron storage of the methyl viologen moiety and provide theoretical energy density of 24.9 Wh/L.

4-2. Introduction

Recently, aqueous organic redox flow batteries (AORFBs) have experienced rapid research development under acidic,^{1,2} pH neutral,³⁻¹² and alkaline conditions^{13, 14} employing redox active molecules including viologen, ferrocene, quinone, (2,2,6,6-Tetramethylpiperidin-1-yl)oxyl (TEMPO) and pyrazine derivatives. In addition to reserving general technical merits of RFBs, redox active organic materials confer two major technical and economic advantages over redox active inorganic salts,¹⁶⁻¹⁸ including synthetic tunability to achieve high battery performance (such as high solubility, optimal redox potentials, and membrane compatibility), and no resource limitation using earth-abundant elements such as H, C, O, and N. In addition, redox active molecules for nonaqueous redox flow batteries (NAORFBs) have also been under enthusiastic exploration.^{18, 22-30} Viologen molecules are highly attractive anolyte materials due to its high solubility in water, low cost, synthetic tunability, fast electrochemical kinetics, and excellent chemical stability under pH neutral conditions.^{3-8, 10-12}

Thus far, viologen based neutral AORFBs has demonstrated the most robust cycling performance,^{5-8, 12} representing the state of the art organic redox flow batteries. In 2015, we reported a 1.2 V methyl viologen(MV)/4-HO-TEMPO total organic redox flow battery using Cl⁻ charge transfer mechanism.⁴ In 2016, Schubert et al. advanced the anion exchange MV/TEMPO AORFB using 4-trimethylammonium-TEMPO chloride (NMe-

TEMPO) as catholyte which is more stable and less crossover than 4-HO-TEMPO.⁶ Herein, a 1.38 V highly stable viologen/TEMPO AORFB using 1,1'-bis[3-(trimethylammonio)propyl]-4,4'-bipyridinium tetrachloride, ((NPr)₂V) as anolyte and 4-trimethylammonium-TEMPO chloride (N^{Me}-TEMPO) as catholyte was reported with outstanding cycling stability, 97.48% total capacity retention or 99.995% capacity retention per cycle for 500 cycles at 60 mA/cm² and a high power density of 128.2 mW/cm² at pH neutral conditions, representing the most stable total organic aqueous redox flow battery known to date. (NPr)₂V was recently reported as anolyte in two viologen/ferrocene AORFBs studies by us⁸ and Aziz⁷ et al. Both studies revealed that (NPr)₂V with its positively charged ammonium pendant arms manifested an improved cycling stability than MV and 1-(trimethylammonio)propyl]-1'-methyl-4,4'-bipyridinium tribromide, ((NPr)(Me)V).^{7,8} It is believed that the charged state, [(NPr)₂V]⁺ is more stable than [MV]⁺ by avoiding a dimerization degradation process. We envisioned that (NPr)₂V could also further improve the electrochemical performance of previously reported high voltage viologen/TEMPO AORFBs. To validate the hypothesis, we conducted side by side half-cell study the two viologen radical cations as well as full RFB tests using (NPr)₂V and MV as anolyte and N^{Me}-TEMPO as catholyte.

In order to avoid the dimerization process, two strategies were applied:

1. Developing viologen derivatives with longer and more sterically hindered pendant ammonium side groups to make the dimerization thermodynamically unfavorable.
 2. Applying the viologen in a nonaqueous electrolyte where the radical cation dimer could not be generated.
- For strategy 1, we found (trimethylammonio)butyl groups contributed most to avoiding the dimer formation. Full RFB testing further proved its superior

stability in aqueous neutral electrolyte. For strategy 2, we introduced methyl viologen bis(trifluoromethane)sulfonamide, **MVTFSI**, as the anode material for a NORFB application. It is notable that **MVTFSI** was found to display two reversible redox events in a nonaqueous supporting electrolyte. Paired with (Ferrocenylmethyl)trimethylammonium bis(trifluoromethanesulfonyl)imide, **FcNTFSI**, as catholyte, the **MVTFSI/FcNTFSI** NOARFB could take advantage of two-electron storage of the methyl viologen moiety and provide a theoretical energy density of 24.9 Wh/L. The demonstrated NOARFBs displayed excellent cycling performance, including up to a 63.3 % energy efficiency at 40 mA/cm², and more than 88% total capacity retention after 100 cycles.

4-3. Materials and methods

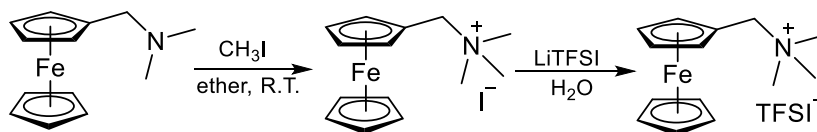
Materials

2,2,6,6-Tetramethyloxy-4-aminopiperidine was purchased from Ark Pharm fine chemicals. Methyl iodide, 4,4'-bipyridine, (3-bromopropyl)trimethylammonium bromide, chloroacetic acid, and Amberlite[®] IRA-900 chloride form anion exchange resin were received from Sigma Aldrich. (Ferrocenylmethyl)dimethylamine and Lithium bis(trifluoromethanesulfonyl)imide (LiTFSI) were purchased from TCI chemicals. All the chemicals were used as received without further treatment. Deionized water was obtained from a MilliporeSigma Milli-DI Water Purification System and purged overnight using N₂ before use. All experimental operations were conducted under a N₂ atmosphere. Selemion[™] ion exchange membranes were purchased from ASAHI GLASS CO., LTD, Japan. The ion exchange membranes were soaked in 0.5 M NaCl aqueous solution overnight before use. Microporous separators were obtained from Daramic[®], US

Synthesis of active materials

Synthesis of N^{Me} -TEMPO, $(N^{\text{Pr}})_2V$, MV: All these materials were synthesized according to literature.

Synthesis of **FcNTFSI**: (Ferrocenylmethyl)dimethylamine (7.29 g, 30 mmol) was dissolved in 50 mL diethyl ether. To this solution, methyl iodide (5.7 g, 40 mmol) was added dropwise at room temperature. Then the mixture was stirred for 2 hours. The orange precipitate was filtered and washed twice with 20 mL diethyl ether. After the yellow powder was dried under vacuum, it was dissolved in 200 mL deionized water. 10 mL LiTFSI (8.61 g, 30 mmol) aqueous solution was added and stirred for half an hour. The generated orange precipitate was filtered and washed with 200 mL deionized water. Dried under vacuum at 70 °C, the product was collected as an orange powder (15.3 g, 94.8%). $^1\text{H-NMR}$ (500 MHz, Acetone- d_6): δ (in p.p.m.), 3.21 (s, 9H), 4.27 (s, 5H), 4.44 (s, 2H), 4.62 (s, 2H), 4.68 (d, 2H). Anal. calcd for $\text{C}_{16}\text{H}_{20}\text{N}_2\text{O}_4\text{F}_6\text{S}_2$: C 36.07, H 3.82, N 5.35; found C 35.61, H 4.05, N 5.26.



Synthesis of **MVTFSI**: Methyl viologen dichloride (MVC_2) was synthesis according to reported procedure. MVC_2 (10 g, 38.8 mmol) was dissolved in 100 mL deionized water. 10 mL LiTFSI (12 g, 4 mmol) aqueous solution was added and stirred for half an hour. The generated white precipitate was filtered and washed with 200 mL

deionized water. Dried under vacuum at 70 °C, the product was collected as a white fine powder (28.6 g, 98.9%). ^1H -NMR (500 MHz, Acetone- d^6): δ (in p.p.m.) 4.76 (s, 6H), 8.86 (d, 4H), 9.41 (d, 4H). (Figure S2) Anal. calcd for $\text{C}_{16}\text{H}_{14}\text{N}_4\text{O}_8\text{F}_{12}\text{S}_4$: C 25.74, H 1.89, N 7.50; found C 25.37, H 1.75, N 7.26.

Synthesis of **(NPr)₂V**: **(NPr)₂V** was synthesis according to reported procedure.⁸

Synthesis of **[(NPr)₂V]^{•+}** and **[MV]^{•+}**: Both radicals were prepared in the same manner (described for **[(NPr)₂V]^{•+}** following). In an Argon or N₂ glovebox (<0.5 ppm O₂), **(NPr)₂V** (9.8 mg, 0.03 mmol) was dissolved in 3.0 mL degassed DI water in a 10 mL vial, and then Zn powder (4.0 mg, 0.06 mmol) was added into the solution. The reaction solution was monitored by UV-Vis to determine the completion of the reaction. After filtering the excess Zn powder, the obtained 10 mM solution was used for other studies.

All the ^1H NMR spectra were shown in appendix section.

Radical tests by UV-Vis

For monitoring the stability, in the Argon-filled glovebox, a 0.1 mM radical solution (**[(NPr)₂V]^{•+}** or **[MV]^{•+}**) in 2.0 M NaCl solution was prepared. The solution was added into quartz cuvettes sealed with a Teflon septum. UV-vis spectra were collected every 48 hours to monitor the degradation of the radicals by an Ocean Optical UV-vis spectrometer.

EPR test

Two EPR samples were prepared using the following procedure: All steps were performed in a N₂ glovebox (<0.5 ppm O₂). DI H₂O used during the sample preparation was degassed to remove O₂ prior to the experiments. 22.8 mg MV or **(NPr)₂V** was

dissolved in 0.887 ml DI H₂O, then 3.1 mg fine Zn powder was mixed with the anolyte solution. After mixing, 0.2 ml of the solution was transferred and further diluted with an additional 0.2 ml of DI H₂O to reach the final volume of 0.4 ml. This final solution was transferred into an EPR tube and frozen in liquid nitrogen. X-band EPR spectra were measured on a Bruker Elexsys E-500 spectrometer equipped with an Oxford ESP-910 cryostat. The detailed measurement conditions are temperature 17 K, microwave power 2 μ W, modulation amplitude 0.05 mT, modulation frequency 100 kHz, microwave frequency 9.64 GHz. The EPR spectra simulation was performed by SpinCount program. Each spectrum can be fitted with an isotropic g ($g_x = g_y = g_z$) value. g strain (σ_g , the distribution of g values) was used to account for the broadness of the linewidth.

Other methods

Material characterization, electrochemical CV and LSV studies, and flow cell tests were conducted using similar methods as introduced as in Chapter II and III.

4-4. Results and discussion

Viologen/N^{Me}-TEMPO AORFBs

According to the CV of (NPr)₂V (-0.38 V vs NHE), MV (-0.45 V vs NHE), and N^{Me}-TEMPO (1.0 V vs NHE) in the NaCl supporting electrolyte (Figure 4-1), the (NPr)₂V/N^{Me}-TEMPO and MV/N^{Me}-TEMPO have an open circuit cell potential of 1.38 and 1.45 V, respectively. To be consistent with our previous studies, 0.5 M viologen compound in 2.0 M NaCl and 0.5 M N^{Me}-TEMPO in 2.0 M NaCl aqueous solutions were employed as catholyte and anolyte in flow battery studies. A 0.5 M (NPr)₂V/N^{Me}-TEMPO AORFB was first examined in a flow battery using a piece of Selemion AMV anion exchange membrane in an Argon filled glovebox (< 1.0 ppm O₂) (Figure 4-2).

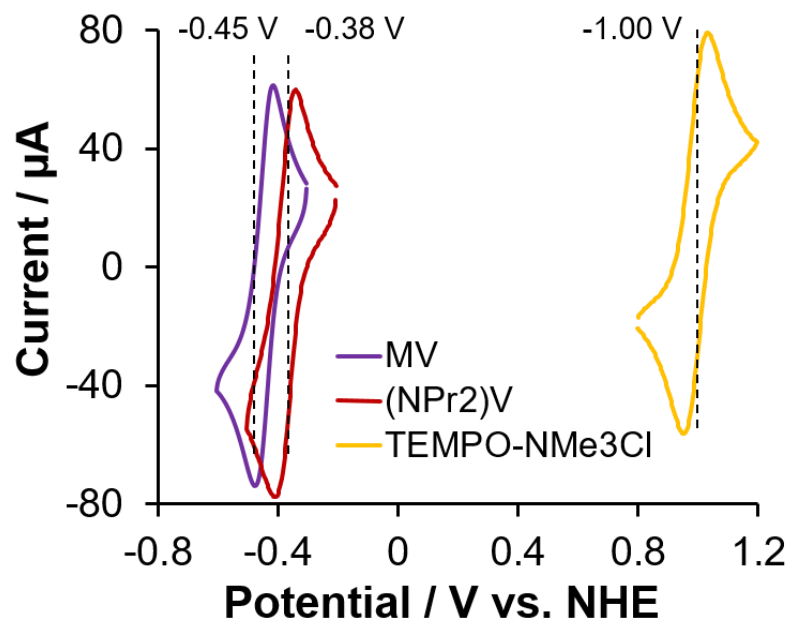


Figure 4-1. Cyclic voltammograms of (NPr)₂V (red trace), MV (blue trace), and N^{Me}-TEMPO (orange trace) in 0.5 M NaCl aqueous solution. Conditions: 4 mM active materials in 0.5 M NaCl; working electrode, glassy carbon electrode; reference electrode, Ag/AgCl electrode; counter electrode, carbon rod; scan rate, 100 mV/s.

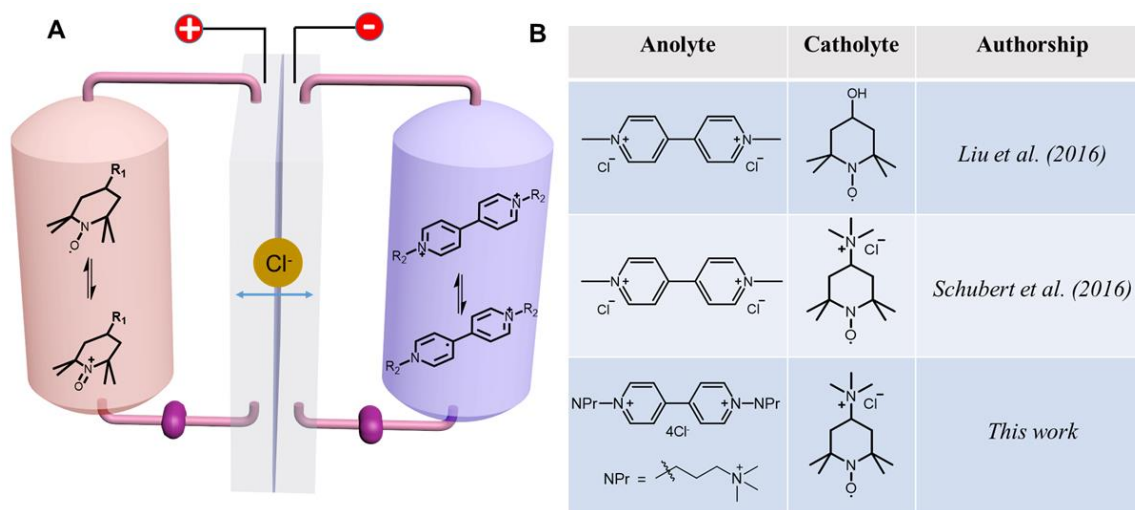


Figure 4-2. (A) Schematic representation of viologen/TEMPO anion exchange AORFBs and illustrations of discharged and charged states of viologen anolyte and TEMPO catholyte and cell reactions. (B) Overview of viologen/TEMPO AORFBs reported to date.

The charging and discharging cutting-off voltages were set to 1.7 V and 0.3 V, respectively. To explore the current rate performance, the (NPr)₂V/N^{Me}-TEMPO AORFB was first cycled at different current densities from 20 mA/cm² to 80 mA/cm² with an increment of 20 mA/cm² as shown in Figure 4-3A. At each current density, Coulombic efficiency was maintained above 99%. The observed energy efficiency (Figure 4-3B, orange plot) decreased when a larger current density was applied due to the increased cell overpotential, which is in line with the trend of voltage efficiency change (Figure 4-3B, gray plot). The battery delivered an energy efficiency of 57.1 % at 60 mA/cm² which is comparable with the reported neutral viologen AORFBs. To explore the long term cycling stability, then the (NPr)₂V/N^{Me}-TEMPO AORFB was tested for extended 500 cycles at 60 mA/cm². The flow battery delivered excellent cycling stability by retaining 97.48 % total capacity after 500 cycles, corresponding to 99.995 % capacity retention per cycle (Figure 4-3C), representing the most stable total organic redox flow battery known to date. In addition, the (NPr)₂V/N^{Me}-TEMPO AORFB was also proved to be very powerful, which is benefited from its high cell voltage. A polarization test at 100% state of charge revealed a peak power density of 128.2 mW/cm² at pH neutral conditions (Figure 4-3D). Under the same testing conditions, a 0.5 M MV/N^{Me}-TEMPO AORFB was also comprehensively studied for its rate performance, cycling stability, and power performance (Figure 4-4).

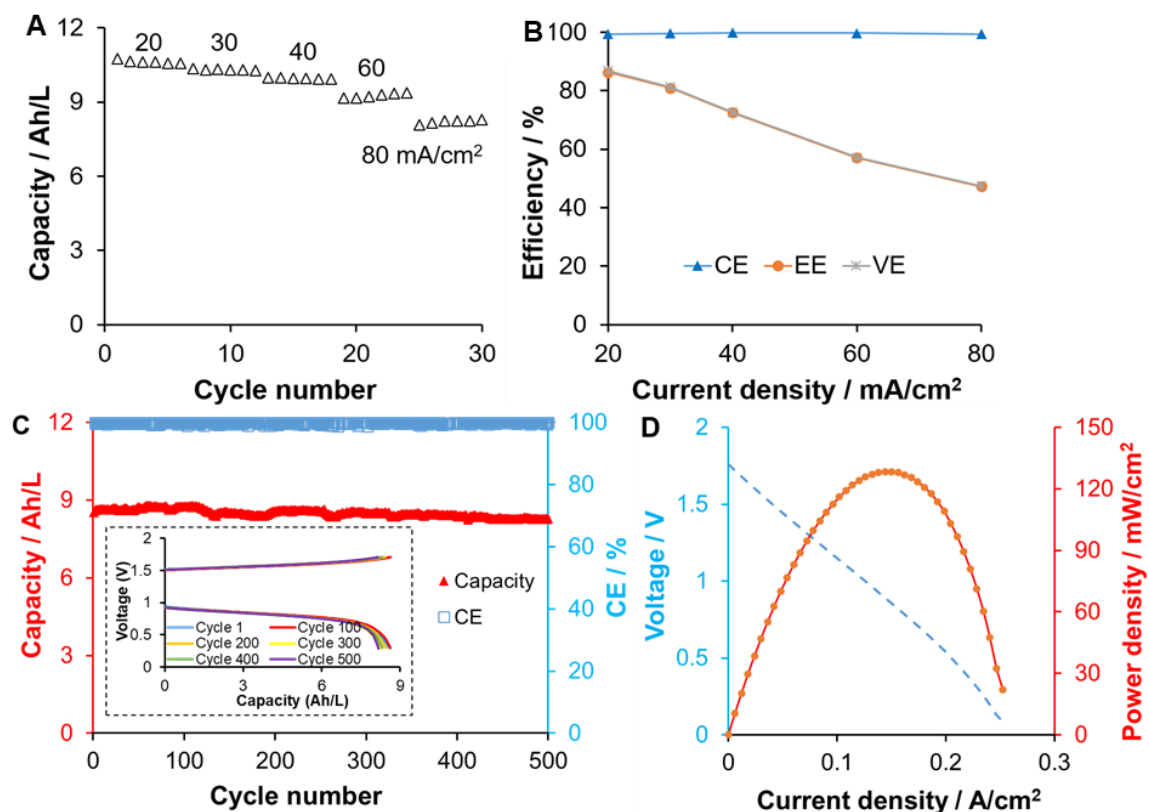


Figure 4-3. Battery performance of 0.5 M (NPr)₂V/NMe-TEMPO AORFB. (A) Rate performance at different charging/discharging current density. (B) Average coulombic efficiency (CE), voltage efficiency (VE), and energy efficiency (EE) at different charging/discharging current density. (C) Capacity and CE versus cycle number for 500 cycles. Insert is the representative charge/discharge profile. The battery was cycled at 60 mA/cm². (D) Polarization and power density curves of the AORFB at 100% SOC.

Compared to the (NPr)₂V/N^{Me}-TEMPO AORFB, the MV/N^{Me}-TEMPO AORFB demonstrated a slightly better rate and power performance, specifically, exhibiting an energy efficiency of 61.3 % at 60 mA/cm² and a peak power density of 134.0 mW/cm² at 100% SOC. Electrochemical impedance spectroscopy (Figure 4-5) revealed a high frequency area specific resistance (R_{hf}) of 4.33 $\Omega \cdot \text{cm}^2$ for the MV/N^{Me}-TEMPO AORFB which is slightly smaller than that of the (NPr)₂V/N^{Me}-TEMPO battery AORFB (4.48 $\Omega \cdot \text{cm}^2$) (Fig. 4-5). The different ohmic resistances of two AORFBs are mainly attributed

to the lower ionic conductivity of the (NPr)₂V anolyte (152.2 mS/cm) than the MV anolyte (175.2 mS/cm). However, the long term cycling stability of the MV/N^{Me}-TEMPO AORFB is apparently inferior to that of the (NPr)₂V/N^{Me}-TEMPO AORFB (97.48 % total capacity or 99.995 % capacity retention per cycle). After 500 cycles at 60 mA/cm², the MV/N^{Me}-TEMPO AORFB retained 91.21 % total capacity which is equivalent to 99.982 % capacity retention per cycle (Fig. 4-4).

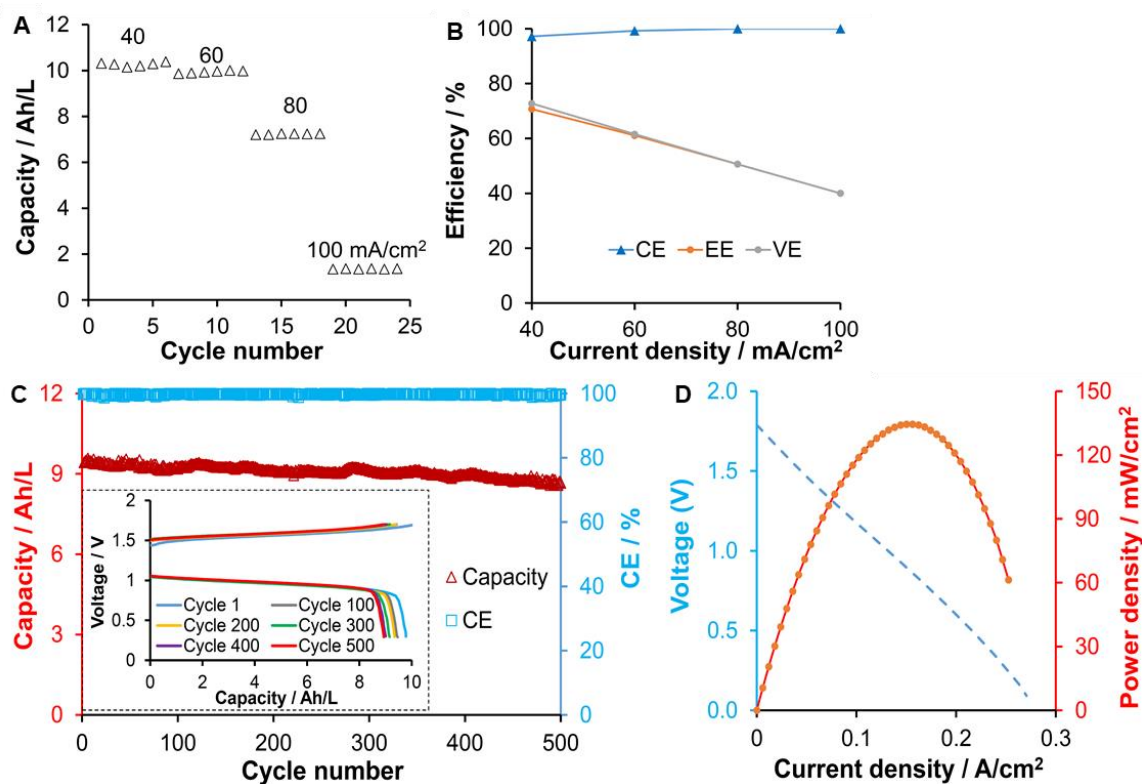


Figure 4-4. Battery performance of 0.5 M MV/N^{Me}-TEMPO AORFB. (A) Rate performance at different charging/discharging current density. (B) Averaged Coulombic efficiency (CE), voltage efficiency (VE) and energy efficiency (EE) at different charging/discharging current density. (C) Capacity and CE versus cycle number for 500 cycles. Inserted is the representative voltage versus capacity profile. The battery is cycled at 60 mA/cm². (D) Polarization curve and power density of the 0.5 M MV/N^{Me}-TEMPO AORFB.

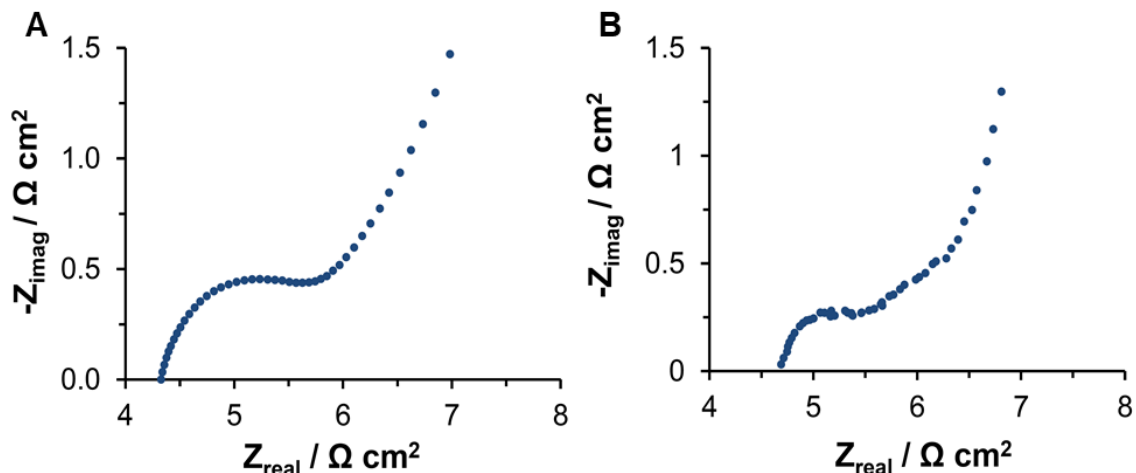


Figure 4-5. Nyquist plot of the (A) MV/N^{Me}-TEMPO AORFB and (B) (NPr)₂V/N^{Me}-TEMPO AORFB RFB before cycling.

[(NPr)₂V]^{•+} and [MV]^{•+} radical cation stability study by UV-Vis

As mentioned above, we believe that the more stable charged state, [(NPr)₂V]^{•+}, than [MV]^{•+} contributes the observed improved cycling stability of the (NPr)₂V/N^{Me}-TEMPO AORFB. To confirm the hypothesis, we isolated [(NPr)₂V]^{•+} and [MV]^{•+} and compared their stability in aqueous solution by UV-Vis spectroscopy. To mitigate oxygen induced degradation of viologen radicals, all operations were conducted in an Argon glovebox (< 1.0 ppm O₂). [(NPr)₂V]^{•+} and [MV]^{•+} were prepared by the chemical reduction of (NPr)₂V and MV using zinc powder. The radical nature of deep purple [(NPr)₂V]^{•+} and [MV]^{•+} was confirmed by EPR spectroscopy (Figure 4-6). Isotropic EPR signals, indicative of an S = ½ spin state, were observed at g = 2.003 and 2.004 for [MV]^{•+} and [(NPr)₂V]^{•+}, respectively.

The radical stability of [(NPr)₂V]^{•+} and [MV]^{•+} (0.1 mM in 2.0 M NaCl) was monitored by UV-vis absorption spectroscopy every 2 hours (Figure. 4-7). Main absorption peaks were observed at 608 nm for [MV]^{•+} and 605 nm for

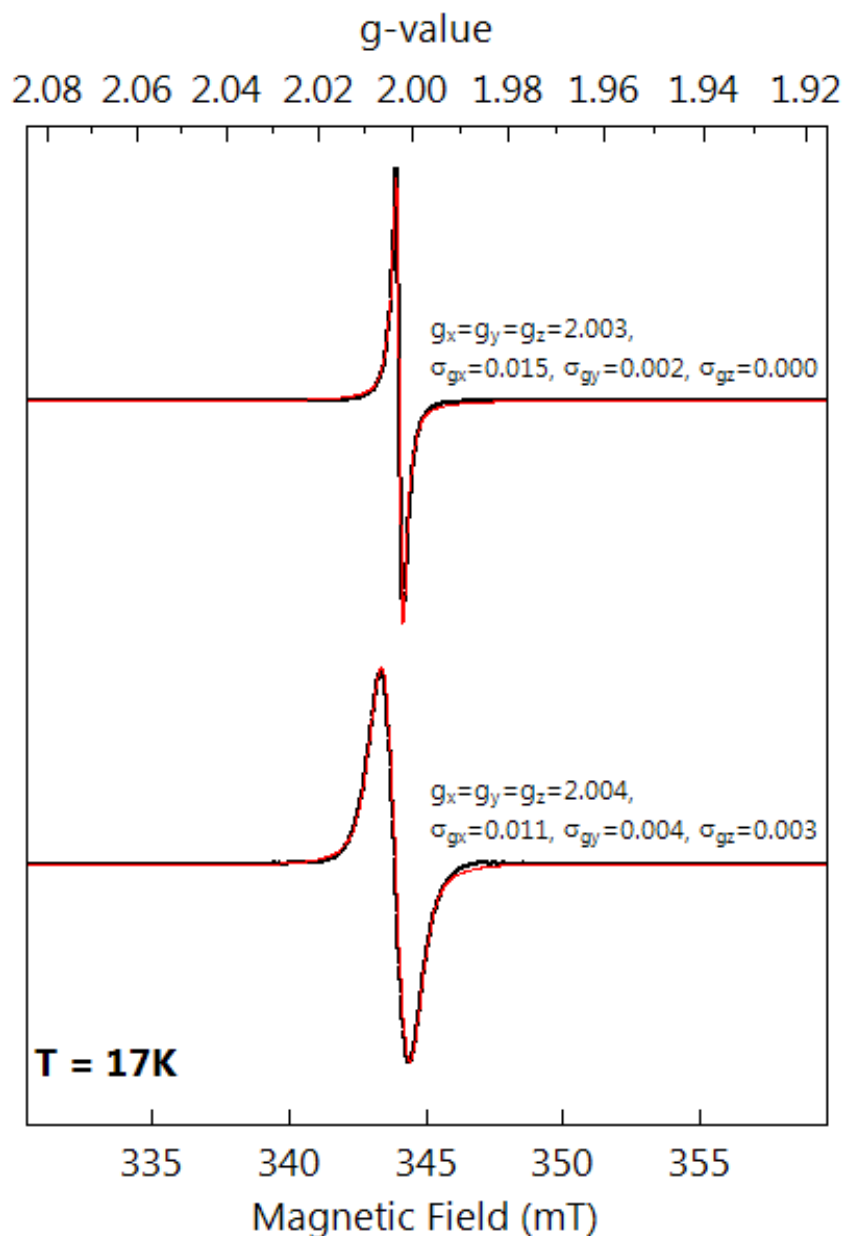


Figure 4-6. EPR spectra (black) of $[\text{MV}]^{+•}$ (top) and $[(\text{NPr})_2\text{V}]^{+•}$ (bottom) and the corresponding spectral simulations (red). The simulation parameters are indicated in the figure.

$[(\text{NPr})_2\text{V}]^{+•}$, which indicates that the introduction of pendant ammonium groups only slightly affects the electronic structure of the pyridinium moiety. This is also in line with the small difference between the reduction potential between $(\text{NPr})_2\text{V}$ and MV (Figure 4-

1). Over 48 hour continuous measurements, the absorption of $[\text{MV}]^{+\bullet}$ showed slow decay. For $[(\text{NPr})_2\text{V}]^{+\bullet}$, almost no absorption decrease was observed. These results are not only consistent with the above battery results and also provide direct experimental evidence for the better radical stability of $[(\text{NPr})_2\text{V}]^{+\bullet}$ than $[\text{MV}]^{+\bullet}$ in aqueous NaCl supporting electrolyte.

It was previously proposed that viologen radicals can undergo a dimerization degradation process (see $[\text{MV}]^{+\bullet}$ in Figure. 4-8). Compared to $[\text{MV}]^{+\bullet}$, the observed exceptional stability of $[(\text{NPr})_2\text{V}]^{+\bullet}$ is interpreted as the mitigated dimerization due to the increased charge repulsion by two additional positively charged propyl ammonium pendant arms, which are lack for $[\text{MV}]^{+\bullet}$. In the case of the dimerization of two $[\text{MV}]^{+\bullet}$, it was possible that the subsequent step is a disproportionation reaction to generate one equivalent $[\text{MV}]^{2+}$ and one equivalent $[\text{MV}]^0$, respectively. Neutral $[\text{MV}]^0$ is insoluble and can precipitate out.

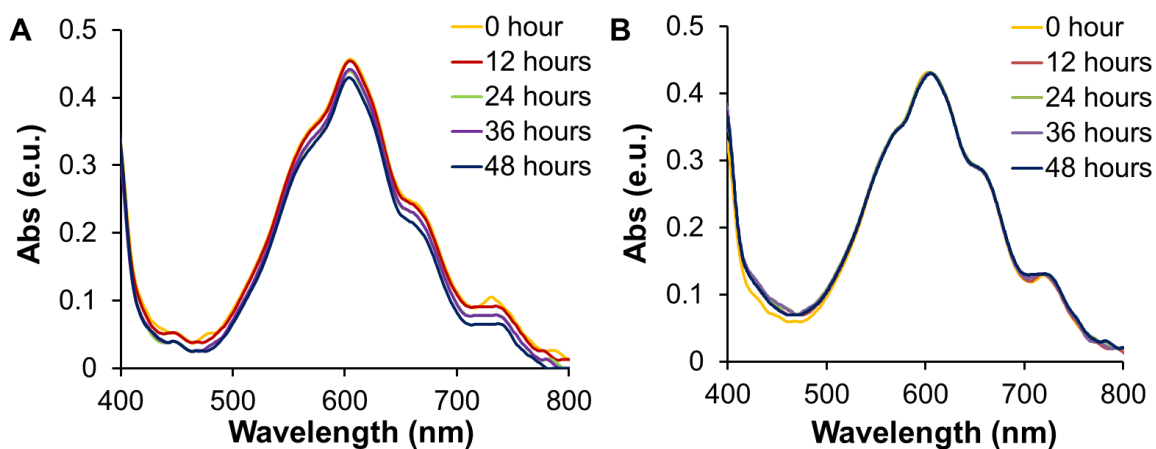


Figure 4-7. UV-vis spectra of (A) $[\text{MV}]^{+\bullet}$ and (B) $[(\text{NPr})_2\text{V}]^{+\bullet}$ in 2 M NaCl aqueous solution over 48 hours.

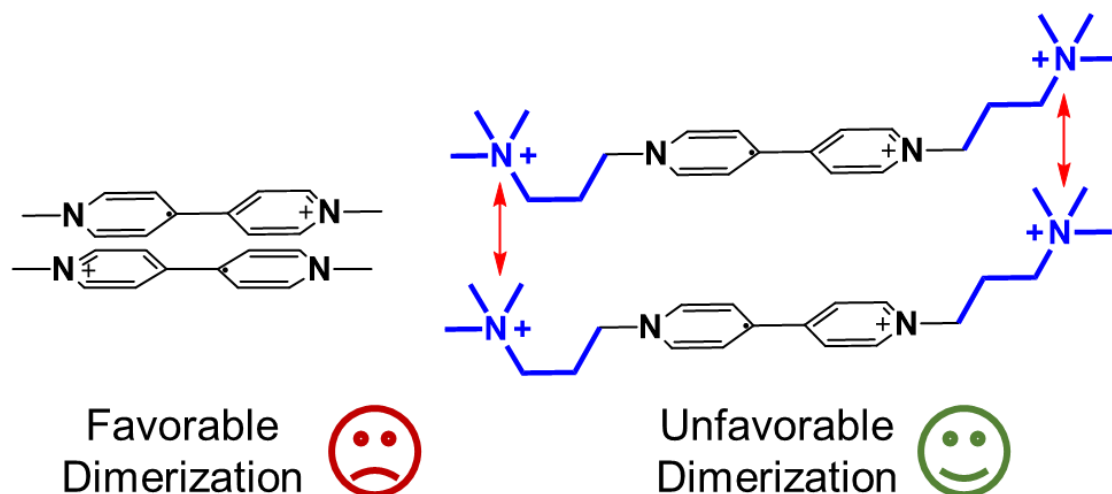


Figure 4-8. Proposed favorable dimerization of $[\text{MV}]^{+\bullet}$ and unfavorable dimerization of $[(\text{NPr})_2\text{V}]^{+\bullet}$. The red double arrows indicate charge repulsion between the pendant ammonium groups.

In terms of thermodynamics, $[\text{MV}]^0$ may reduce protons to form H_2 even at pH neutral conditions ($[\text{MV}]^{+/0}$ at -0.72 V vs NHE and H^+/H_2 at -0.45 V vs NHE).

$[(\text{NPr})_2\text{V}]^{+\bullet}$ and $[\text{MV}]^{+\bullet}$ radical cation stability study by half-cell tests

Half-cell study is a concept to utilize the two different oxidation states of the same redox active materials as anode and cathode material as shown in Figure 4-9. When the resulted 0 V flow cell is cycled, the capacity retention could be used to separately study the material's electrochemical stability without any influence from other redox active materials. In our experiments, 0.5 M viologen radical cation in 2 M NaCl electrolyte was prepared as catholyte. 0.5 M viologen dication in 2 M NaCl electrolyte was prepared as anolyte. The pH value of the electrolyte was adjusting to 7 by 10 M NaOH solution. Thereafter, a flow battery was assembled following the general procedure mentioned in previous chapters. To cycling the simulated battery, the cutting-off voltages were set as

0.4 V for the charging process and -0.4 V for the discharging process. The charging/discharging current density was set as 60 mA/cm². As shown in Figure 4-9, after 200 cycles, the (NPr)₂V/(NPr)₂V⁺⁺ half-cell RFB showed no capacity decay, much more stable than the MV/MV⁺⁺ half-cell RFB (4.56% capacity decay after 200 cycles). The results further proved the better stability of [(NPr)₂V]⁺⁺ than [MV]⁺⁺.

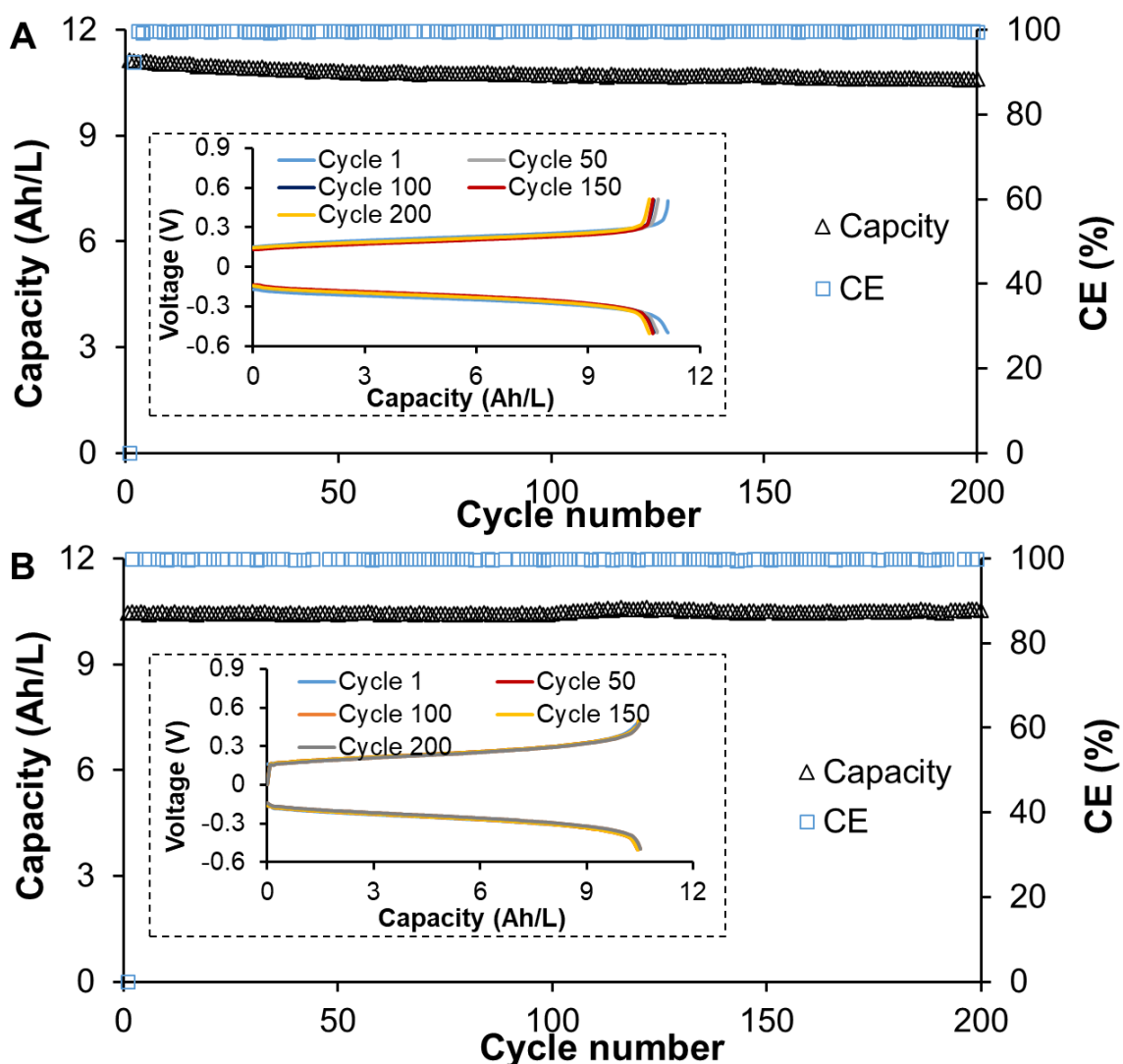


Figure 4-9. Half-cell studies of [(NPr)₂V]⁺⁺ and [MV]⁺⁺ radical cation stability. (A) Capacity vs. cycle number of MV/MV⁺⁺ half-cell RFB in 200 cycles (Insert: voltage vs. capacity of MV/[MV⁺⁺] half-cell RFB of the selected cycles); (B) Capacity vs. cycle

number of $(\text{NPr})_2\text{V}/[(\text{NPr})_2\text{V}]^{++}$ half-cell RFB in 200 cycles (Insert: voltage vs. capacity of $(\text{NPr})_2\text{V}/[(\text{NPr})_2\text{V}]^{++}$ half-cell RFB of the selected cycles). Conditions: 0.5 M active materials in 2 M NaCl, pH value was adjusting to 7 by 10 M NaOH solution.

MVTFSI/FcNTFSI NORFB for avoiding radical dimer and achieving double electron utilization and

It was reported that the viologen radical cation dimers could be only observed in aqueous solutions.³² The dimer formation in the nonaqueous solvent is less common and thermodynamically favorable. Moreover, the proton involved side reactions can be avoided in the organic solvent, especially in the aprotic solvent. Therefore, we believed MV could be more stable in NORFB as proton and dimer caused MV^{++} decomposition would no longer take place. Moreover, we hypothesized that the insolubility of the non-polar two-electron reduced species, MV^0 , in aqueous solutions could be totally upturned in nonaqueous solutions, and thus can achieve the two-electron utilization of **MV** in NAORFBs. Following our previous studies on FcNCl/MV AORFBs, ion exchange reactions were first conducted to replace Cl^- of FcNCl and MVCl_2 with TFSI to enable **FcNTFSI** and **MVTFSI** soluble in organic solvents. The obtained **FcNTFSI** and **MVTFSI** exhibited solubility in CH_3CN as 1.2 M and 0.98 M, respectively.

Cyclic voltammetry (CV) experiments were conducted to determine the redox potential and reversibility of both active materials a nonaqueous supporting electrolyte. As expected, in 1.0 M LiTFSI in CH_3CN , **MVTFSI** displays two reversible redox events (Figure 4-10A) corresponding to redox pair $\text{MV}^{2+}/\text{MV}^{•+}$ (-0.79 V vs. $\text{Fc}^{+/0}$) and $[\text{MV}]^{•+}/[\text{MV}]^0$ (-1.20 V vs. $\text{Fc}^{+/0}$). Owing to the excellent redox reversibility of the ferrocene moiety and the electron withdrawing effect of ammonium function groups, **FcNTFSI** shows a well-defined reversible wave with $E_{1/2}$ of +0.27 vs. $\text{Fc}^{+/0}$. Then,

repeated CV scanning was run for 200 cycles. The almost overlapped traces reveal very good electrochemical stability for both compounds under CV conditions (Figure 4-11B).

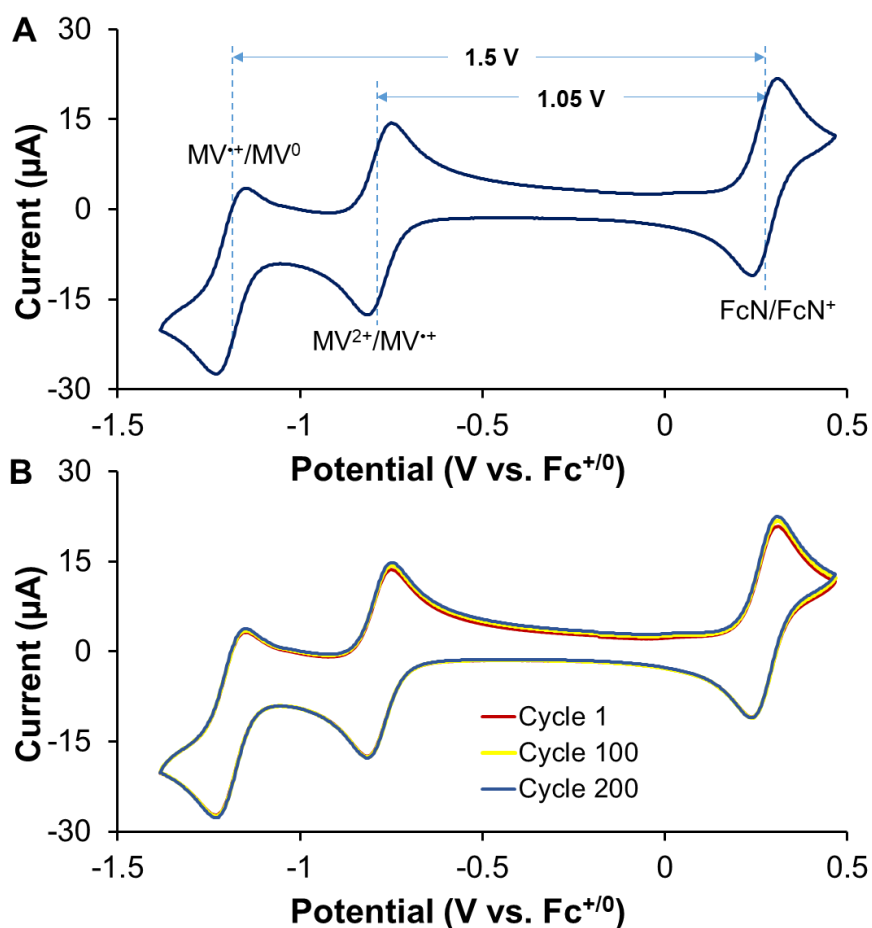


Figure 4-10. (A) Cyclic voltammogram of a mixture of 1.0 mM **FcNTFSI** and 1.0 mM **MVTF SI**. (B) Repeated cyclic voltammetry curves of a 1.0 mM **FcNTFSI** and 1.0 **MVTF SI** mixture. Conditions: Glassy carbon as the working electrode, Ag/AgNO₃ as reference electrode, glassy carbon rod as the counter electrode, 1.0 M LiTFSI in CH₃CN as supporting electrolyte.

RDE and Nicholson's analysis for MVTF SI and FcNTFSI

To further understand the electrochemical kinetics of both compounds, linear sweep voltammetry (LSV) studies were carried out using a glassy carbon rotating

electrode. As shown in Figure 4-11, rotating speed was increased from 300 rpm to 2400 rpm to obtain different mass transport limiting current (i_L). Two successive plateaus were observed for the two reductions of **MVTFSI**. It is noteworthy that limiting the current of the second reduction ($i_{L,2nd}$) of **MVTFSI** should be calculated by using the observed net limiting current of the second plateau to subtract the limiting current of the 1st reduction ($i_{L,1st}$). From the slope of Levich plots of **FcNTFSI** and **MVTFSI** (Figure 4-11), the diffusion coefficients were calculated to be $7.12 \times 10^{-6} \text{ cm}^2/\text{s}$ for **FcNTFSI**, and $7.54 \times 10^{-6} \text{ cm}^2/\text{s}$, and $5.59 \times 10^{-6} \text{ cm}^2/\text{s}$ the 1st reduction of **MVTFSI** and the 2nd reduction of **MVTFSI**, respectively.

As shown in Figure 4-12, CV experiments were conducted at different scan rates from 5 mV/s to 5 V/s. The linear relationship between peak current and the square root of the scan rate ($v^{1/2}$) revealed all the redox processes are diffusion controlled (Figure 4-13). Then Nicholson's analysis of scan rate dependent cyclic CV data was applied to determine electron transfer rate constants (k^0). Compared to Koutechý-Levich analysis, the Nicholson's method is more accurate for fast electron transfer rate constant estimation. The Ψ values can be calculated by an established fitting equation (Equation 4-1) where peak potential separation (ΔE_p) is the only variable parameter. Then k^0 can be calculated by the slope of the linear relationship between Ψ value and reciprocal of the square root of scan rate ($v^{1/2}$) in the range from 5 to 500 mV/s according to Equation 4-2.

$$\Psi = \frac{-0.6288 + 0.0021n\Delta E_p}{1 - 0.017n\Delta E_p} \quad (\text{Equation 4-1})$$

$$\Psi = k^0 \left(\frac{\pi D n F}{RT} \right)^{\frac{1}{2}} v^{-\frac{1}{2}} \quad (\text{Equation 4-2})$$

k^0 is the electron transfer rate constant, ΔE_p is the peak potential separation calculated by $(E_{\text{oxidation}} - E_{\text{reduction}})$ at different scan rates. For the second redox process of **MV** ($\text{MV}^{+}/\text{MV}^0$), all the ΔE_p at different scan rates was found to be 75 mV. Therefore, 75 mV was directly applied to calculate the Ψ value and. The electron transfer rate constants were estimated to be 0.32 cm/s for **FcNTFSI**, and 0.15 cm/s and 1.0 cm/s the 1st electron of **MVTFSI** and the 2nd electron of **MVTFSI**, respectively.

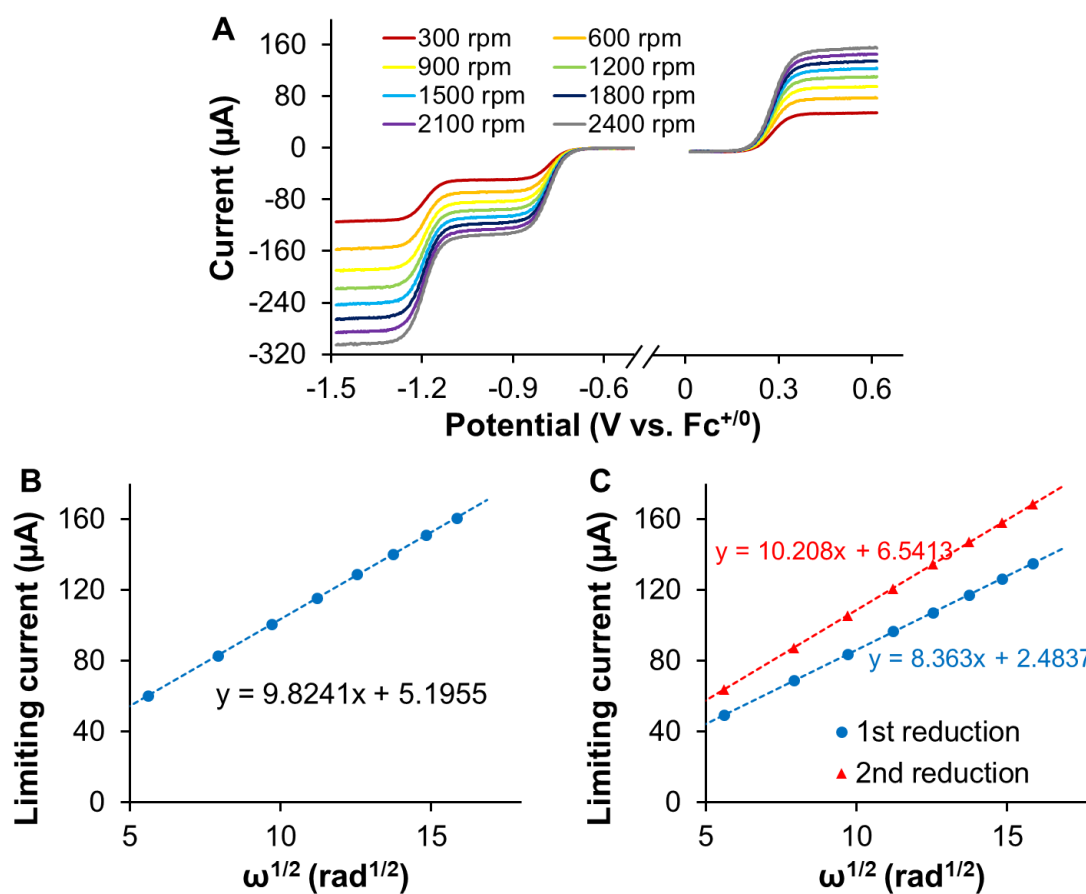


Figure 4-11. (A) Linear sweep voltammograms of 1.0 mM **FcNTFSI** (positive side) and 1.0 mM **MVTFSI** (negative side) on a rotating glassy carbon electrode in 1.0 M LiTFSI/CH₃CN supporting electrolyte; (B) Levich plots of the limiting current vs the square root of rotation rates for **FcNTFSI**; (C) Levich plots of the limiting current vs the square root of rotation rates for **MVTFSI**.

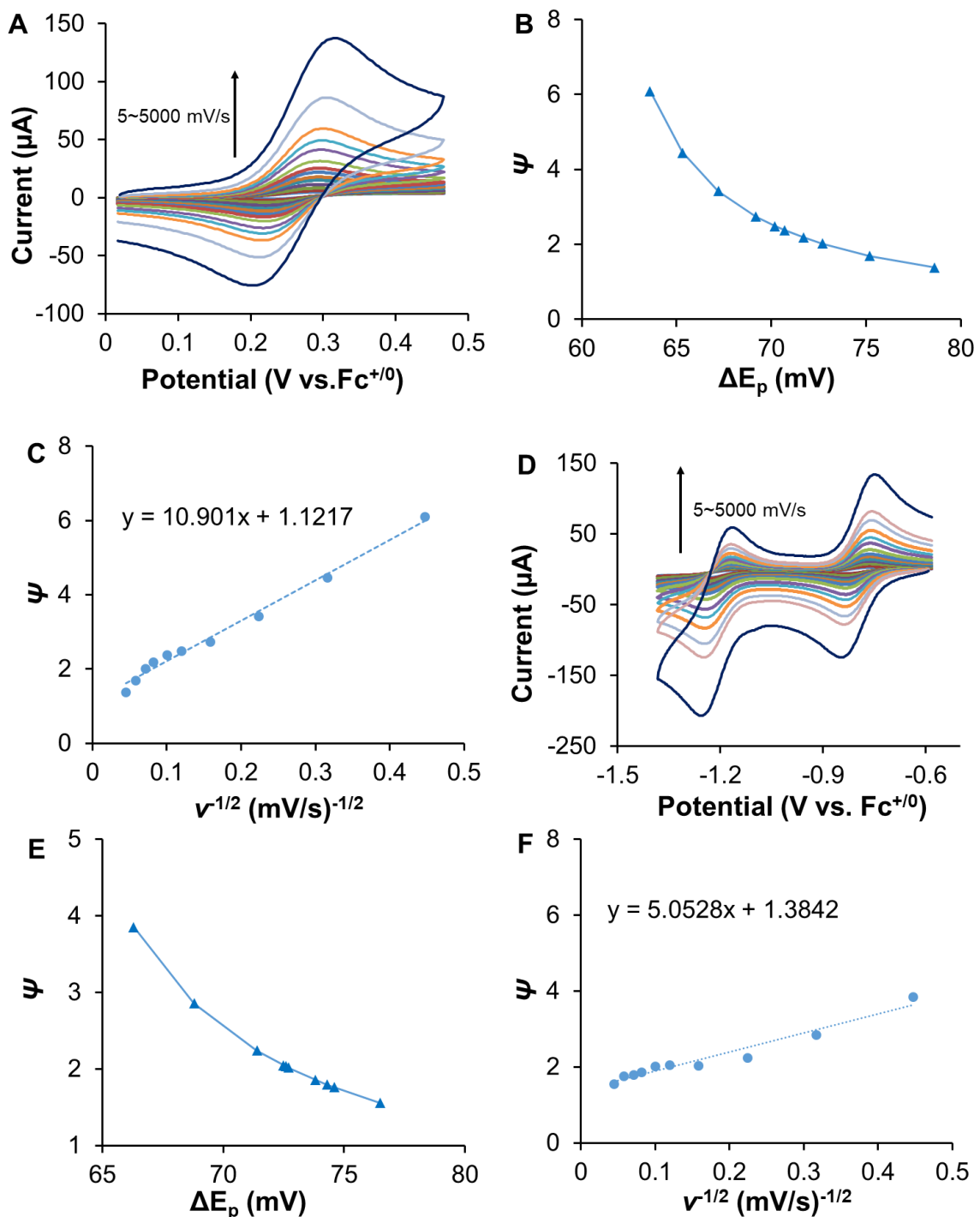


Figure 4-12. Nicholson's analysis for the evaluation of k_0 of **FcNTFSI** and **MVTF SI**. (A) CV of **FcNTFSI** at various scan rates (5, 10, 20, 40, 70, 100, 150, 200, 300, 500, 700, 1000, 1500, 2000, 5000 mV/s). (B) The plot of Ψ versus ΔE_p of the reduction peak and oxidation peak of **FcNTFSI**. (C) The linear relationship between Ψ and $\nu^{1/2}$ of **FcNTFSI**. (D) CV of **MVTF SI** at various scan rate (5, 10, 20, 40, 70, 100, 150, 200, 300, 500, 700, 1000, 1500, 2000, 5000 mV/s). (E) The plot of Ψ versus ΔE_p of the reduction peak and

oxidation peak of the 1st redox wave of **MVTFSI**. (F) The linear relationship between Ψ and $\nu^{1/2}$ of the 1st reduction/oxidation of **MVTFSI**.

Table 4-1. Electrochemical data of **FcN**, **MV²⁺** and **MV^{•+}** in 1.0 M LiTFSI CH₃CN solution

Active species	FcN	MV²⁺	MV^{•+}
$E_{1/2}$ (V vs. Fc ^{+/0})	+0.27	-0.79	-1.2
D (cm ² /s)	7.12×10^{-6}	7.54×10^{-6}	5.59×10^{-6}
k^0 (cm/s)	0.32	0.15	1.0

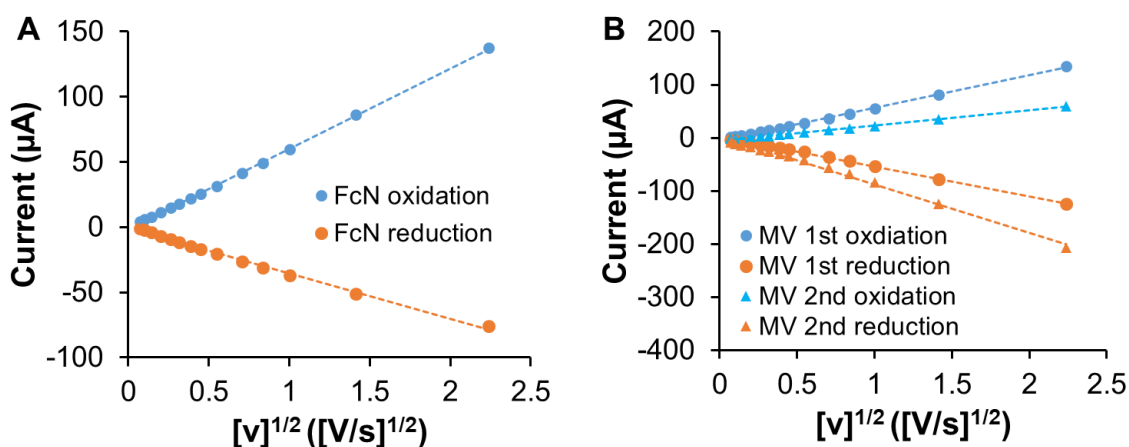


Figure 4-13. The plot of i_c and i_a over the square root of scan rates for **FcNTFSI** (A) and **MVTFSI** (B). Conditions: 1.0 mM FcNTFSI, and 1.0 mM MVTF SI mixture. Glassy carbon as the working electrode, Ag/AgNO₃ as the reference electrode, glassy carbon as the counter electrode, 1.0 M LiTFSI in CH₃CN as supporting electrolyte.

One electron utilized MVTF SI/FcNTFSI NORFB

It has been commonly observed that active materials crossover in NAORFBs can cause battery self-discharge and active species imbalance between anode and cathode due to the lack of selective ion exchange membranes in nonaqueous solutions, hence leading to undesired capacity decay.³¹ To minimize the crossover, using mixed anolyte and catholyte can help to minimize diffusion controlled transportation through a non-ion selective porous separator. In our battery tests, a Daramic 175 porous membrane was

used. The separator has a high ionic conductivity but low ion selectivity due to its large pore size. 1.0 M LiTFSI in CH₃CN solution was used as supporting electrolyte due to its high ionic conductivity up to 34 S/cm that is in favor of high current density operation and high energy efficiency. First, we examined the battery performance only utilizing the first electron storage of **MVTFSI**. 0.1 M **FcNTFSI** and 0.1 M **MVTFSI** were dissolved in 1.0 M LiTFSI CH₃CN solution and used as both anolyte and catholyte for the 1.05 V **MVTFSI/FcNTFSI** symmetric NAORFB. Before charging the battery, electrochemical impedance spectroscopy (EIS) was applied to test the resistance of the flow cell. A high-frequency area specific resistance was measured to be 3.33 $\Omega \text{ cm}^2$ as shown in Figure 4-14, which is comparable to our previous FcNCl/MV aqueous redox flow batteries.¹⁵ Whereafter, the charging cutting-off voltage was set to 1.5 V to avoid the 2nd reduction of **MVTFSI**. The discharging cutting-off voltage was set to 0.1 V. The **MVTFSI/FcNTFSI** NAORFB was cycled at different current densities from 10 mA/cm² to 40 mA/cm² with an increment of 10 mA/cm² as shown in Figure 4-15A. The battery showed a good rate performance. At 30 mA/cm², it still can utilize 78.4 % of the theoretic capacity (2.10 Ah/L out of 2.68 Ah/L). Due to the active material crossover, when the battery was run at a current density as low as 10 mA/cm², the charge capacity even outstepped the theoretic capacity. With the increase of the current density, coulombic efficiency increased for 82.8 % at 10 mA/cm² to 95.2 % at 40 mA/cm² (Figure 4-15B, blue trace). This can be explained by the fact that the crossover of active materials was slowed down when the battery was run at higher current densities. The observed energy efficiency (Figure 4-15B, gray trace) decreased when a larger current density was applied due to the increased cell overpotential, which is in line with the trend of voltage efficiency change (Figure 4-

16B, orange trace). The battery displayed outstanding energy efficiencies as high as 63.3 % at 40 mA/cm². Agreeing with the EIS result, this value is comparable with neutral viologen AORFBs. For the purpose of achieving high capacity utilization and high energy efficiency, 30 mA/cm² was applied to extended 100 cycle studies. At this current density, the battery delivered an energy density of 2.20 Wh/L. The battery also showed excellent cycling stability regarding both capacity retention and Coulombic efficiency. Within 100 cycles the battery retained 91.8 % total capacity, corresponding to 99.92 % capacity retention per cycle (Figure 4-15C). Impressive energy efficiency was achieved and kept stable above 73 % (Figure 4-17). Compared to the corresponding FcNCl/MV AORFB, the present **MVTFSI/FcNTFSI** NAORFB demonstrated inferior capacity retention and capacity utilization, which is ascribed to the lower chemical stability and crossover of the active materials.

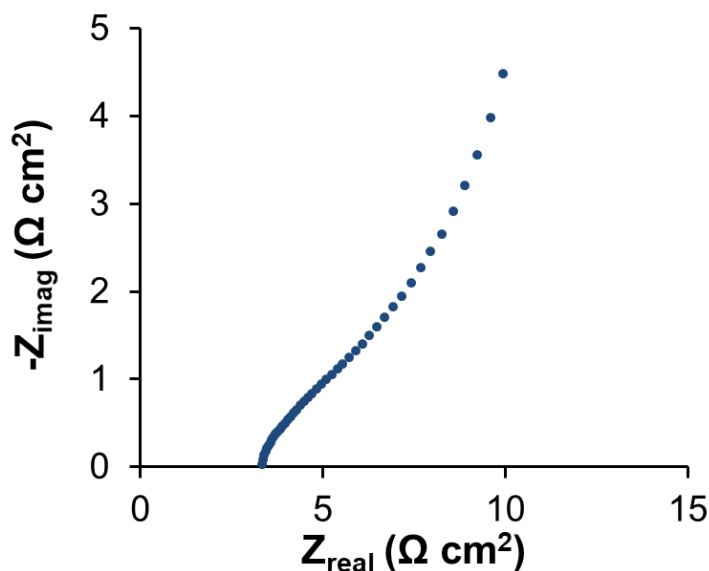


Figure 4-14. Nyquist plots of the 1 electron utilized FcNTFSI/MVTFSI non-aqueous RFB with mixed electrolyte.

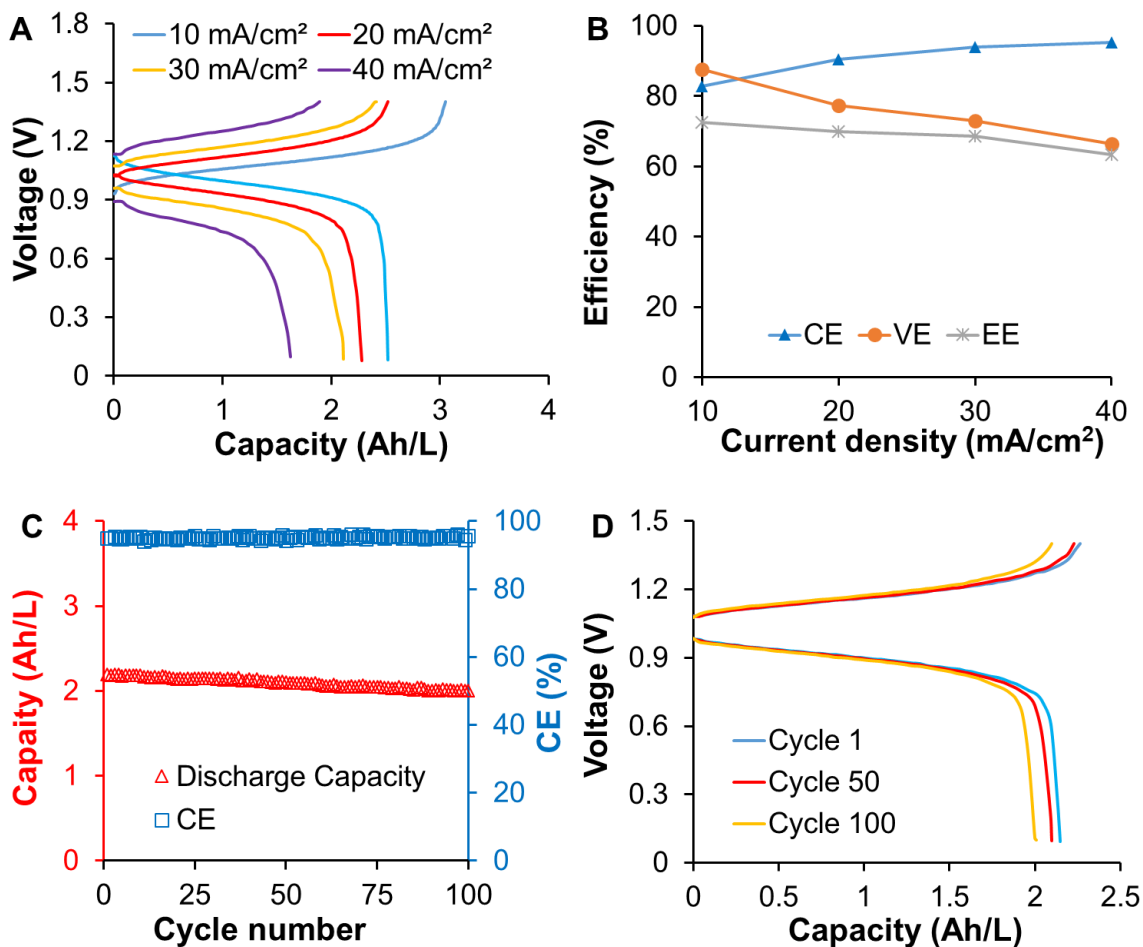


Figure. 4-15. Battery performance of one electron utilized **FcNTFSI/MVTFSI** NAORFB with a mixed electrolyte (0.1 M **FcNTFSI** and 0.1 M **MVTFSI**). (A) Voltage versus capacity profile at different charging/discharging current density. (B) Averaged Coulombic efficiency, voltage efficiency, and energy efficiency at different charging/discharging current density. (C) Capacity versus cycle number for 100 cycles. The battery is cycled at 30 mA/cm². (D) Representative voltage versus capacity profiles.

Two electron utilized MVTFSI/FcNTFSI NORFB

Subsequently, we demonstrated the two-electron utilization of **MVTFSI** to enable the 1.5 V **MVTFSI/FcNTFSI** NAORFB by using a mixed electrolyte of 0.2 M **FcNTFSI** and 0.1 M **MVTFSI**. The cutting-off voltage was set to 1.85 V for charging to achieve the second reduction of **MVTFSI**. The discharging voltage was kept at 0.1 V.

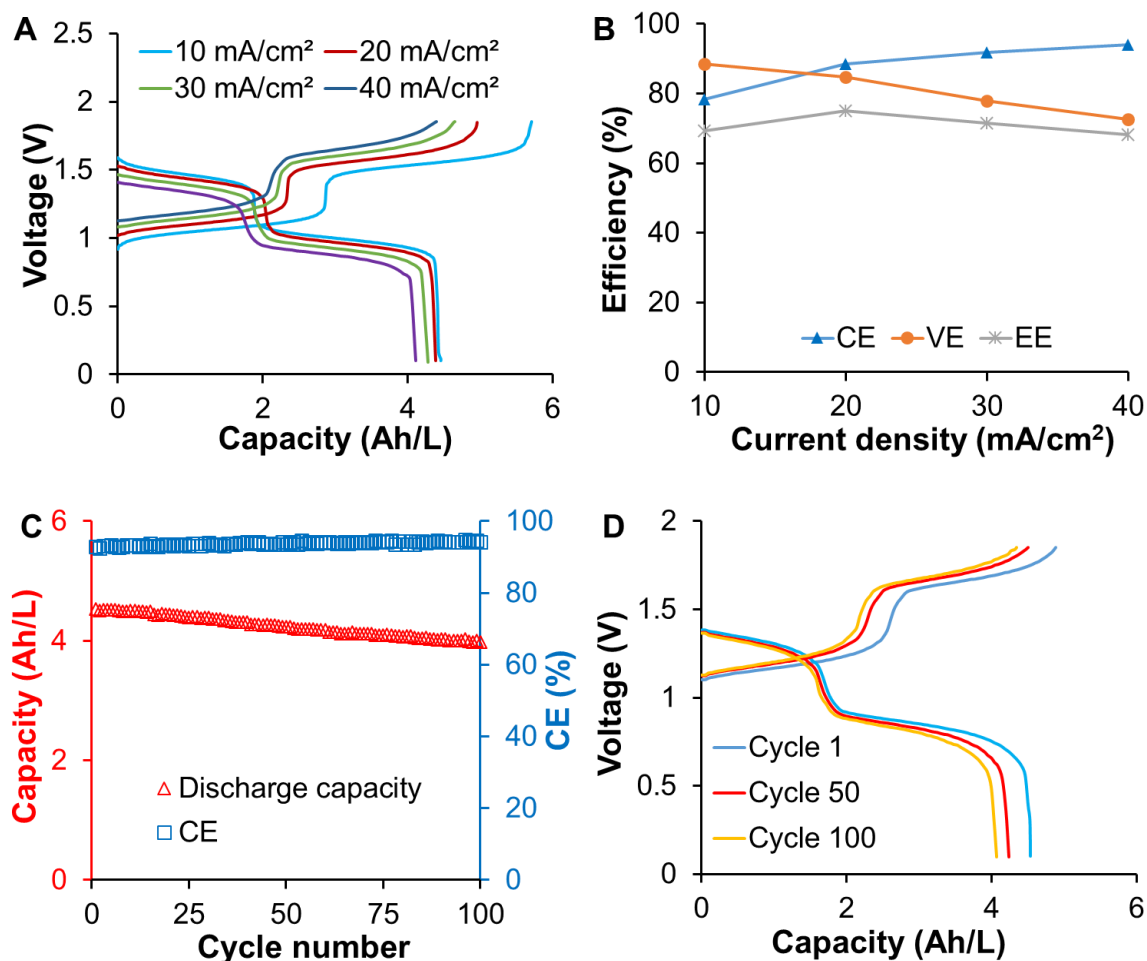


Figure 4-16. Performance of 2 electron utilized **FcNTFSI/MVTFSI** NAORFB with mixed electrolyte (0.2 M **FcNTFSI** and 0.1 M **MVTFSI**). (A) Voltage versus capacity profile at different charging/discharging current density. (B) Averaged Coulombic efficiency, voltage efficiency, and energy efficiency at different charging/discharging current density. (C) Capacity versus cycle number for 100 cycles. The battery is cycled at 30 mA/cm². (D) Representative voltage versus capacity profiles.

As shown in Figure 4-17A, two well-defined charging/discharging plateaus were obtained corresponding to the two redox reactions, **MV²⁺/MV^{•+}** and **MV^{•+}/MV⁰**, respectively. The **MVTFSI/FcNTFSI** NAORFB was first tested at different current densities from 10 mA/cm² to 40 mA/cm². Compared to 1 electron utilized battery, the 2 electrons utilized battery displayed doubled capacity and better rate performance at various current densities. With the increase of current density, discharged capacity just

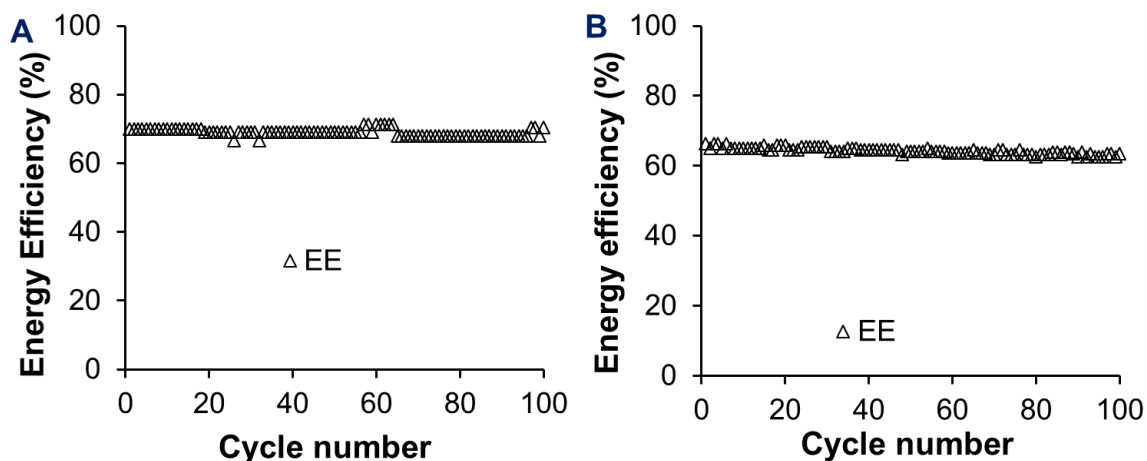


Figure 4-17. (A) Energy efficiency vs. cycle number of the **FcNTFSI** (0.1 M)/**MVTFSI** (0.1 M) NAORFB. (A) Energy efficiency vs. cycle number of the **FcNTFSI** (0.2 M)/**MVTFSI** (0.1 M) NAORFB. Current density: 30 mA/cm².

showed a slightly decrease from 4.38 Ah/L at 10 mA/cm² to 4.10 Ah/L at 40 mA/cm².

The same trends for efficiency changes were shown as the 1 electron utilized battery (Figure 4-16B). Then the battery was cycled at 30 mA/cm². At this current density, energy density was achieved as high as 5.66 Wh/L which is more than 2.5 times the 1 electron utilized battery (2.20 Wh/L), which thanks to the doubled capacity and the increased voltage of 1.5 V (Figure 4-11). The two-electron utilized flow battery exhibited a stable energy efficiency of 71.4 % in 100 cycles which is comparable with the one-electron utilized battery (Figure 4-17). Stable capacity retention (88.3%) was also achieved for these two-electron utilized batteries as shown in Figure 4-16C and 4-16D. The possible reason for the observed capacity decay could be due to the electrolyte imbalance caused by crossover during battery cycling as well as a small amount of chemical degradation. In order to minimize the crossover of active materials, we need to develop more advanced ion selective separators or design redox active macromolecules which are difficult to cross the separator.

4-5. Conclusion

In conclusion, a highly stable high voltage (NPr)₂V/N^{Me}-TEMPO AORFB was developed, and the flow battery demonstrated capacity retention of 99.995% per cycle and power density of 128 mW/cm², representing the most stable total organic redox flow battery known to date. An overview of aqueous organic RFBs to date was shown in Appendix Table 1. UV-Vis spectroscopic and half-cell studies confirmed that the outstanding cycling stability of the (NPr)₂V/N^{Me}-TEMPO AORFB is attributed to the exceptional radical stability of (NPr)₂V^{•+}. In order to avoid radical dimerization and proton involved side reactions, stable **FcNTFSI/MVTFSI** NAORFBs were also demonstrated. By simply changing the counter anion, we also solved the solubility problem of the insoluble MV⁰ redox state observed in aqueous solutions. Thereby, two-electron utilization of methyl viologen was achieved in the **FcNTFSI/MVTFSI** NAORFBs which contributed to the energy density increase of more than 2.5 times. The present study not only the importance of the molecular engineering strategy to improve active materials' stability and solubility but also advances the state of the art of RFBs for sustainable and green energy storage of renewable energy.

4-6. Reference

- (1) Yang, B.; Hooper-Burkhardt, L.; Wang, F.; Surya Prakash, G. K.; Narayanan, S. R. *J. Electrochem. Soc.* **2014**, *161*, A1371.
- (2) Huskinson, B.; Marshak, M. P.; Suh, C.; Er, S.; Gerhardt, M. R.; Galvin, C. J.; Chen, X.; Aspuru-Guzik, A.; Gordon, R. G.; Aziz, M. J. *Nature* **2014**, *505*, 195.
- (3) Janoschka, T.; Martin, N.; Martin, U.; Friebe, C.; Morgenstern, S.; Hiller, H.; Hager, M. D.; Schubert, U. S. *Nature* **2015**, *527*, 78.

- (4) Liu, T.; Wei, X.; Nie, Z.; Sprenkle, V.; Wang, W. *Adv. Energy Mater.* **2016**, *6*, 1501449.
- (5) Hu, B.; DeBruler, C.; Rhodes, Z.; Liu, T. L. *Journal of the American Chemical Society* **2017**, *139*, 1207.
- (6) Janoschka, T.; Martin, N.; Hager, M. D.; Schubert, U. S. *Angew. Chem. Int. Ed.* **2016**, *55*, 14427.
- (7) Beh, E. S.; De Porcellinis, D.; Gracia, R. L.; Xia, K. T.; Gordon, R. G.; Aziz, M. J. *ACS Energy Lett.* **2017**, *2*, 639.
- (8) DeBruler, C.; Hu, B.; Moss, J.; Liu, X.; Luo, J.; Sun, Y.; Liu, T. L. *Chem* **2017**, *3*, 1.
- (9) Luo, J.; Sam, A.; Hu, B.; DeBruler, C.; Wei, X.; Wang, W.; Liu, T. L. *Nano Energy* **2017**, *42*, 215.
- (10) Hu, B.; Seefeldt, C.; DeBruler, C.; Liu, T. *J. Mater. Chem. A* **2017**, *5*, 22137.
- (11) Luo, J.; Hu, B.; Debruler, C.; Liu, T. L. *Angew. Chem. Int. Ed.* **2018**, *57*, 231.
- (12) DeBruler, C.; Hu, B.; Moss, J.; Luo, J.; Liu, T. L. *ACS Energy Lett.* **2018**, 663.
- (13) Lin, K.; Chen, Q.; Gerhardt, M. R.; Tong, L.; Kim, S. B.; Eisenach, L.; Valle, A. W.; Hardee, D.; Gordon, R. G.; Aziz, M. J.; Marshak, M. P. *Science* **2015**, *349*, 1529.
- (14) Yang, Z.; Tong, L.; Tabor, D. P.; Beh, E. S.; Goulet, M.-A.; De Porcellinis, D.; Aspuru-Guzik, A.; Gordon, R. G.; Aziz, M. J. *Adv. Energy Mater.* **2018**, *8*, 1702056.
- (15) Winsberg, J.; Hagemann, T.; Janoschka, T.; Hager, M. D.; Schubert, U. S. *Angew. Chem. Int. Ed.* **2016**, *56*, 686.
- (16) Leung, P.; Shah, A. A.; Sanz, L.; Flox, C.; Morante, J. R.; Xu, Q.; Mohamed, M. R.; Ponce de León, C.; Walsh, F. C. *J. Power Sources* **2017**, *360*, 243.

- (17) Wei, X.; Pan, W.; Duan, W.; Hollas, A.; Yang, Z.; Li, B.; Nie, Z.; Liu, J.; Reed, D.; Wang, W.; Sprenkle, V. *ACS Energy Lett.* **2017**, 2187.
- (18) Ding, Y.; Zhang, C.; Zhang, L.; Zhou, Y.; Yu, G. *Chem. Soc. Rev.* **2017**, 47, 69.
- (19) Yang, Z.; Zhang, J.; Kintner-Meyer, M. C. W.; Lu, X.; Choi, D.; Lemmon, J. P.; Liu, J. *Chem. Rev.* **2011**, 111, 3577.
- (20) Soloveichik, G. L. *Chem. Rev.* **2015**, 115, 11533.
- (21) Wang, W.; Luo, Q.; Li, B.; Wei, X.; Li, L.; Yang, Z. *Adv. Funct. Mater.* **2013**, 23, 970.
- (22) Huang, J.; Cheng, L.; Assary, R. S.; Wang, P.; Xue, Z.; Burrell, A. K.; Curtiss, L. A.; Zhang, L. *Adv. Energy Mater.* **2015**, 5, 1401782.
- (23) Zhou, M.; Huang, Q.; Pham Truong, T. N.; Ghilane, J.; Zhu, Y. G.; Jia, C.; Yan, R.; Fan, L.; Randriamahazaka, H.; Wang, Q. *Chem* **2017**, 3, 1036.
- (24) Ding, Y.; Zhao, Y.; Li, Y.; Goodenough, J. B.; Yu, G. *Energy Environ. Sci.* **2017**, 10, 491.
- (25) Wei, X.; Xu, W.; Huang, J.; Zhang, L.; Walter, E.; Lawrence, C.; Vijayakumar, M.; Henderson, W. A.; Liu, T.; Cosimbescu, L.; Li, B.; Sprenkle, V.; Wang, W. *Angew. Chem. Int. Ed.* **2015**, 54, 8684.
- (26) Wei, X.; Xu, W.; Vijayakumar, M.; Cosimbescu, L.; Liu, T.; Sprenkle, V.; Wang, W. *Adv. Mater.* **2014**, 26, 7649.
- (27) Wei, X.; Duan, W.; Huang, J.; Zhang, L.; Li, B.; Reed, D.; Xu, W.; Sprenkle, V.; Wang, W. *ACS Energy Lett.* **2016**, 1, 705.
- (28) Sevov, C. S.; Hickey, D. P.; Cook, M. E.; Robinson, S. G.; Barnett, S.; Minteer, S. D.; Sigman, M. S.; Sanford, M. S. *J. Am. Chem. Soc.* **2017**, 139, 2924.

- (29) Yang, C.; Nikiforidis, G.; Park, J. Y.; Choi, J.; Luo, Y.; Zhang, L.; Wang, S.-C.; Chan, Y.-T.; Lim, J.; Hou, Z.; Baik, M.-H.; Lee, Y.; Byon, H. R. *Adv. Energy Mater.* **2018**, 8, 1702897..
- (30) Hu, B.; Liu, T. L. *J. Energy Chem.* **2018**, 27, 1326.
- (31) Duan, W.; Huang, J.; Kowalski, J. A.; Shkrob, I. A.; Vijayakumar, M.; Walter, E.; Pan, B.; Yang, Z.; Milshtein, J. D.; Li, B.; Liao, C.; Zhang, Z.; Wang, W.; Liu, J.; Moore, J. S.; Brushett, F. R.; Zhang, L.; Wei, X. *ACS Energy Lett.* **2017**, 2, 1156.
- (32) Kosower, E. M.; Cotter, J. L. *J. Am. Chem. Soc.* **1964**, 86, 5524.

CHAPTER V

AMMONIUM FUNCTIONALIZED ANTHRAQUINONE AS AN ANODE
MATERIAL FOR NEUTRAL AORFBS ^e**5-1. Abstract**

9,10 -anthraquinone-2,7-disulfonic acid (AQDSH₂) as a benchmark anolyte material has been frequently applied in acidic aqueous organic redox flow batteries (AORFBs). However, the chemical stability issue of AQDSH₂ at acidic conditions and the corrosion nature of strong acid supporting electrolyte bring a big roadblock for its practical application. A feasible strategy to overcome these issues is migrating to pH neutral conditions and employing the soluble salts of AQDSH₂. Herein, we report the 9,10-anthraquinone-2,7-disulfonic diammonium salt (**AQDS(NH₄)₂**) as the anode material for pH neutral AORFBs with a solubility of 1.9 M in water, which is more than 3 times of the sodium salt. Paired with NH₄I catholyte, the resulting neutral AORFB could deliver a theoretic energy density of up to 40 Wh/L. A 0.75 M battery (an energy density of 12.5 Wh/L) displayed outstanding stable cycling stability for 300 cycles. The present **AQDS(NH₄)₂** flow battery chemistry opens a new pass way to apply anthraquinone in developing low cost and benign pH neutral flow batteries for scalable energy storage.

5-2. Introduction

Nowadays, the utilization of renewable energy resources such as solar and wind

^e Adapted with permission from [Hu, B.; Luo, J.; Hu, M.; Yuan B. Liu, T. L. *Angew. Chem. Int. Ed.*, **2019**, 58, 2]. Copyright 2019. WILEY-VCH Verlag GmbH & Co. KGaA, Weinheim. Reproduced by permission of WILEY-VCH Verlag GmbH & Co. KGaA, Weinheim. <https://onlinelibrary.wiley.com/doi/full/10.1002/anie.201907934>

energy has been realized to be a sustainable and environmentally benign strategy to alleviate the world's severe dependency on traditional fossil fuels, and thus enables the environmental recovery and sustainable development of the economy.¹ In order to manage the intermittent and fluctuating nature of solar and wind energy, cost-effective technologies for energy conversion and storage are in urgent need.¹⁻⁵ Among the numerous energy storage technologies, redox flow batteries (RFBs) have been recognized as a promising technology to overcome the intermittency of renewable energy and supply reliable continuing electricity to electricity grids with a scale up to MW/MWh.^{1-3,5} The unique cell design of RFBs empowers a number of attractive technical merits for large-scale energy storage in comparison to traditional static rechargeable batteries, such as excellent scalability, unique energy/power decoupled capability, high current operation, high power output and so on.^{2,3,5} As one of the most advanced RFB technologies, the vanadium redox flow battery (VRFB) has received the most commercializing attempts. Nevertheless, its wide adoption is still limited by the high active material cost, low earth abundance for vanadium and strong acidic hazardous electrolyte.^{6,7} To overcome these technical challenges, we and other groups have developed aqueous organic RFBs (AORFBs) and nonaqueous organic RFBs (NAORFBs) employing more sustainable and abundant redox active organic molecules, such as viologen,⁸⁻¹⁵ metallocene,^{9,10,16-18} Pyridium,¹⁹ quinone,^{7,20-23} (2,2,6,6-Tetramethylpiperidin-1-yl)oxyl (TEMPO)^{11,13,14,24} and pyrazine²⁵⁻²⁷ derivatives. Among the various redox active molecules, viologen and anthraquinone (AQ) have been extensively studied as anolytes in AORFBs.

Among the various redox active molecules, viologen and anthraquinone (AQ) have been extensively studied as anolytes in AORFBs. So far viologen based pH neutral

AORFBs have demonstrated most stable cycling performance as the pH neutral condition suppresses side reactions for active species caused by protons and hydroxides at acidic and alkaline conditions. However, AQ molecules have been primarily studied in acidic or alkaline AORFBs and subject to chemical degradation at either acidic or alkaline conditions. First, side reactions under acidic conditions (such as bromination and acid catalyzed reactions) lead to capacity decay.²⁸ Second, the redox potential of AQ molecules such as AQDSH₂ positively shifts to + 0.21 V vs. SHE in acidic electrolytes, dramatically limiting the open circuit voltage for the whole battery. Third but not the last, acidic supporting electrolytes and bromine based catholyte are highly corrosive and hazardous. Other anthraquinone derivatives have also been studied in alkaline AORFBs but still suffer chemical degradation,^{22,29} a major cause for capacity decay, low solubility and high cost. Deteriorative impacts of acidic or alkaline conditions are also applied to catholyte molecules. For example, K₄Fe(CN)₆ as the most common cathode material in alkaline AORFBs is not chemically stable at alkaline conditions as recently examined in a half-cell flow battery study.³¹

Thus, we have become promoted to investigate AQ molecules at pH neutral conditions to address these technical issues observed in AQ based acidic and alkaline AORFBs and achieve improved cycling performance. 9,10-anthraquinone-2,7-disulfonic acid (AQDSH₂) represents one of the most inexpensive AQ anolyte candidates and was first applied in strongly acidic AORFBs. Intuitively, the sodium salt of sulfonated anthraquinone derivatives of AQDSH₂ is the first class of candidates to be investigated. 9,10-anthraquinone-2-sulfonic acid sodium salt (AQSN_a) and 9,10-anthraquinone-2,7-disulfonic acid disodium salt (AQDSNa₂) maintain many merits of the acid compound

(e.g. extraordinary stability, fast redox kinetics, and widespread commercial availability). However, we found both AQSDNa and AQSDNa₂ have much lower solubility in water at pH 7 (less than 30 mM for AQSDNa and 0.58 M for AQSDNa₂ in water) which limits the capacity and energy density of these AQ molecule based pH neutral AORFBs. Only a very few studies have been reported in improving their solubility for neutral AORFBs application. One example is employing ethylene glycol as additives to increase the solubility of AQSDNa₂. Recently, an ethylene oxide functionalized AQ demonstrated high solubility at pH neutral conditions but is not chemically stable.³³ Herein, we report the synthesis, spectroscopic, and electrochemical studies of a highly soluble ammonium cation functionalized AQ molecule, **AQDS(NH₄)₂** (1.9 M in H₂O, and 1.3 M in 1.0 M NH₄I). An **AQDS(NH₄)₂/NH₄I** pH neutral AORFB with an energy density of 12.5 Wh/L delivered very stable cycling performance in a pH neutral AORFB for 300 cycles and outstanding energy efficiency of 72.3% at 60 mA/cm².

5-3. Materials and methods

Materials

Anthraquinone-2,7-disulfonic acid disodium salt was purchased from TCI chemicals. All the chemicals were stored in an Argon glove box and used directly. Ammonium hydroxide (30 % solution) was purchased from Fisher chemicals. Deionized water was obtained from a MilliporeSigma Milli-DI Water Purification System and purged overnight using N₂ before use. All experimental operations were conducted under N₂ atmosphere. NafionTM 115 membranes were purchased from FuelCellStore, TX. The Nafion membranes were boiled in 1 M H₂SO₄ solution for 2 hours, 30 % H₂O₂ solution

for 2 hours, and then immersed in 0.5 M NH_4I aqueous solution overnight. The membranes are rinsed with DI water before use.

Characterization

NMR studies were conducted using a Bruker 500 MHz NMR spectrometer. UV-Vis data were collected using an Ocean Optics spectrometer. Elemental analysis was done at Atlantic Microlab. The conductivity of the electrolyte solutions was measured using a Mettler Toledo conductivity meter at R.T.

Materials synthesis

Synthesis of **AQDS(NH_4)₂**: 9,10-Anthraquinone-2,6-disulfonic acid disodium salt (20.0 g, 48.5 mmol) was dissolved in 100 mL deionized water and flushed over a cation exchange column with Amberlite cation exchange resin (IR-120 hydrogen form). The obtained 9,10-Anthraquinone-2,6-disulfonic acid solution was cooled down by an ice bath. Then 10 mL 30% ammonium hydroxide was added to convert the acid to ammonium salt. After the water was removed by a rotary evaporator, the wet solid residue was dried in a vacuum oven at 70 °C overnight. The final product was collected as dark brown solid (19.1 g, 98.5 %). ^1H -NMR (500 MHz, D_2O): δ =8.29 (d, 2H), 8.02 (dd, 2H), 7.94 (d, 2H). Anal. Calcd for $\text{C}_{14}\text{H}_{14}\text{O}_8\text{N}_2\text{S}_2$: C, 41.76; H, 3.48; N, 6.96. Found C, 42.03; H, 3.51; N, 6.28.

Synthesis of **AQDS NH_4** : 9,10-Anthraquinone-2-disulfonic acid sodium salt (3.0 g, 9.7 mmol) and 30 mL Amberlite cation exchange resin (IR-120 hydrogen form) were add in 50 mL deionized water. The mixture was stirred overnight when all anthraquinone was dissolved. Then the mixture was filtered and the filtrate was flushed over a cation exchange column with Amberlite cation exchange resin (IR-120 hydrogen form) again.

The following steps are the same as **AQDS(NH₄)₂** synthesis. The product was obtained as light yellow powder with a yield of 98 %. ¹H-NMR (500 MHz, D₂O): δ =8.23 (s, 1H), 8.04 (m, 2H), 7.87 (m, 2H) , 7.65 (m, 2H). Anal. Calcd for C₁₄H₁₁O₅NS: C, 55.08; H, 3.63; N, 4.59. Found C, 55.31; H, 3.94; N, 4.57.

Solubility tests

The solubility of **AQDS(NH₄)₂** and **AQDSNa₂** was measured in water and 1 M NH₄I by a UV-vis spectrometer. 1 mL super-saturated solution in a 5 mL graduated cylinder was prepared. The up layer clear solution was diluted by 1000 times. Then the UV-Vis spectrum was collected. Solubility data were calculated by using a prepared standard curve.

Other methods

Electrochemical studies and flow cell tests were conducted using similar methods as introduced in Chapter IV.

5-4. Results and discussion

The solubility of AQDS(NH₄)₂ and AQSNa₂

Our group reported a molecular engineering study of ferricyanide and ferrocyanide catholyte for pH neutral AORFB applications using a straightforward strategy of cation modulation. The newly designed neutral (NH₄)₃Fe(CN)₆ and (NH₄)₄Fe(CN)₆ catholyte manifest much higher solubility than their sodium and potassium salt and retain comparable chemical stability. Inspired by the ammonium cation effect to improve the solubility of ferricyanide and ferrocyanide compounds, we adopted the same strategy to AQSNa and AQDSNa₂ salts. By replacing the counter cation Na⁺ with NH₄⁺, a solubility increase and chemical stability maintainability were

anticipated. The desired anthraquinone sulfonic acid ammonium salts, **AQSNH₄** and **AQDS(NH₄)₂**, were synthesized by a straightforward two-step route with high yields (Figure 5-1). The synthesis of **AQDS(NH₄)₂** was demonstrated a scale of 20 g with an excellent yield. UV-Vis measurements were conducted to determine the solubility of **AQSNH₄** and **AQDS(NH₄)₂**. In agreement with our expectation, both ammonia salts showed much higher solubility compared to their sodium form (Figure 5-1). **AQSNH₄** can be dissolved in water up to 0.15 M while the **AQSNa** is barely soluble (less than 30 mM). Surprisingly, **AQDS(NH₄)₂** displayed a remarkable solubility of 1.9 M in water which is more than 3 times of that of **AQDSNa₂** (0.58 M in water). Even in 1.0 M **NH₄I** supporting electrolyte, the solubility still can reach 1.3 M. To the best of our knowledge, this is one of the most water-soluble anthraquinone derivatives at the pH neutral condition.

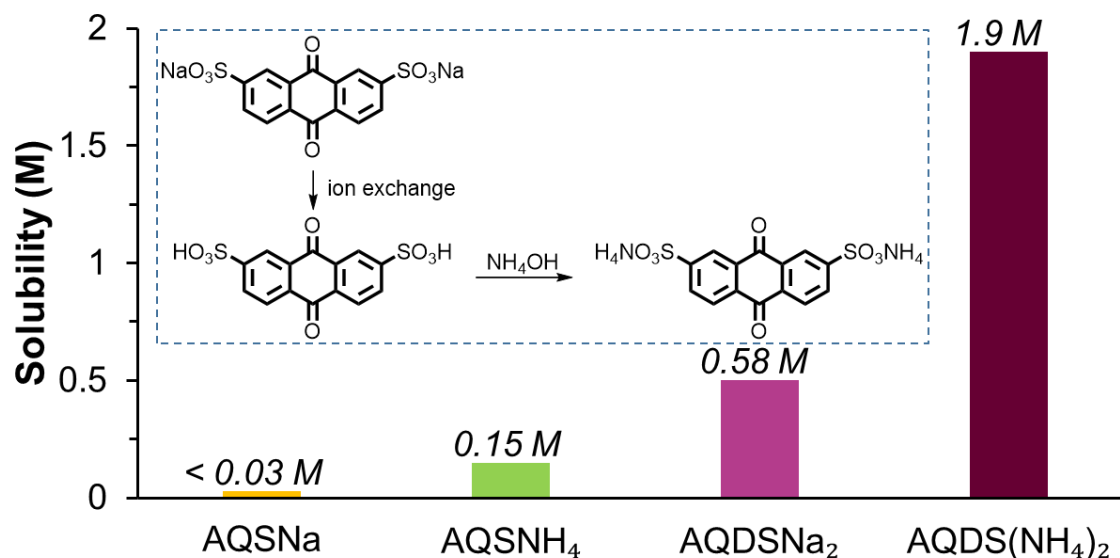


Figure 5-1. A comparison of the solubility of AQSNa (yellow), **AQSNH₄**, and AQDSNa₂, and **AQDS(NH₄)₂**. (Inserted scheme: Synthesis of **AQDS(NH₄)₂**)

NMR studied for AQDS(NH₄)₂ and AQSNH₄

We hypothesized that the boosted solubility was attributed to two reasons. On the one hand, the hydrophilic property of ammonium cation facilitates the dissolving of the salt in water as reported in our previous work.¹² On the other hand, hydrogen bonds formed among NH₄⁺ cation and AQDS anion is believed to enhance the solvation of AQDS anions in water, thus improving its solubility. In order to obtain the evidence for these hydrogen-bonding interactions, Nuclear magnetic resonance (NMR) titration studies of AQDSNa₂ were performed with the addition of NH₄Cl as the ammonium source (Figure 5-2A). The pH value of each NMR sample was adjusted to 7.0 to avoid the possible chemical shift drift due to pH change. As a result of the NH₄Cl titration, a marked upfield shift of the ¹H-NMR signals of AQDS²⁻ moiety was observed. Protons, H_a and H_c, experienced relative large chemical shift while the proton H_b, far from the carbonyl oxygen atoms, displayed the smallest signal shift (-0.0102 ppm/equiv. NH₄Cl). The observations indicate the hydrogen bonding interactions between the carbonyl oxygen atom and NH₄⁺ cations (Figure 5-2D). This is in line with the ¹³C NMR signal upfield shift of AQDS(NH₄)₂ compared to AQDSNa₂ (see Figure 5-3). Specifically, the ¹³C resonances of carbon atoms at positions 9 and 10 showed upfield shift while other carbons barely had any changes. In the 2D NMR (COSY) spectrum (Figure 5-2C), the strong interaction between the proton of ammonium and the protons of AQDS was also observed and highlighted by the blue dash rectangles in Figure 5-2C, providing another strong evidence for the formation of hydrogen-bonds. In addition, a control experiment was conducted by titrating sodium 2,4-dimethylbenzenesulfonate with NH₄Cl (Figure 5-5). In this case, no chemical shift was observed with the NH₄⁺ concentration increase, further proving that the hydrogen bonds form on the carbonyl oxygen atoms other than

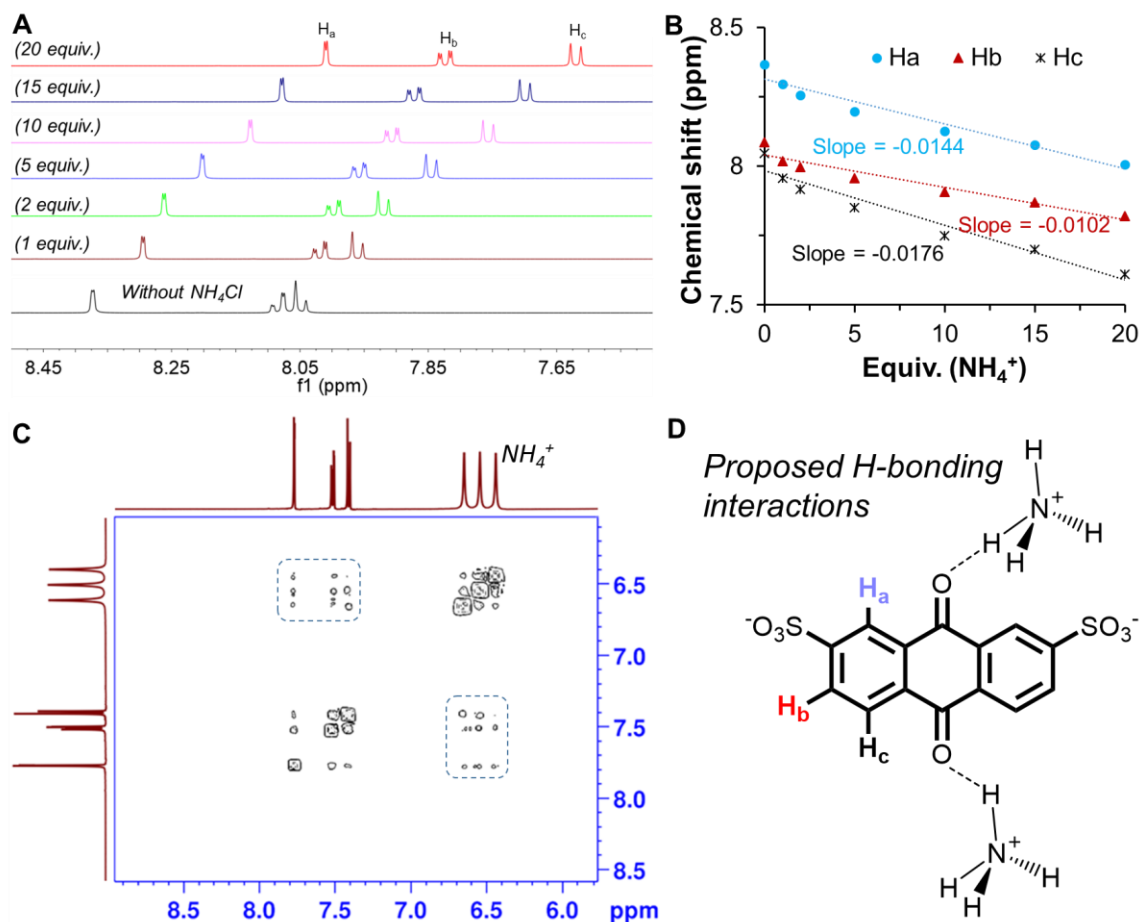


Figure 5-2. (A) ¹H NMR titration of 50 mM AQDSNa₂ in D₂O with various equivalents of NH₄Cl from 1 to 20. Ammonium hydroxide solution was used to adjust the pH value to 7.0. (B) Relationship between ¹H-NMR chemical shift and the equivalent of ammonium. (C) 2D NMR (COSY) spectrum of 0.1 M AQDS(NH₄)₂ in D₂O, pH was adjusted to 3 to guarantee the observation of ammonium cation in the spectrum. (D) Schematic hydrogen bonding interactions proposed for AQDS(NH₄)₂.

sulfonate oxygen atoms. A similar trend was also observed for AQDSNa by the same NH₄Cl titration (Figure 5-4). The synthesized AQDS(NH₄)₂ was proved to be not only highly soluble in water but also chemically stable even at an elevated temperature and pH neutral conditions. During two weeks, the treatment of an NMR sample of AQDS(NH₄)₂ in D₂O at 80 °C, ¹H NMR studies indicated no chemical decomposition (Figure 5-6), the desired chemical characteristic for flow battery applications.

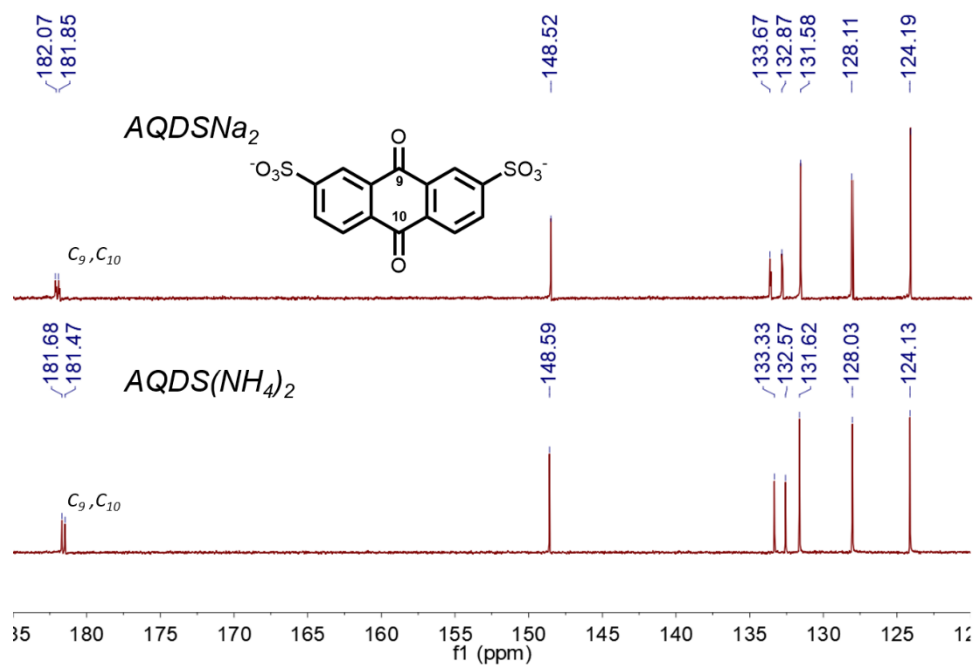


Figure 5-3. ^{13}C NMR of AQDSNa₂ and AQDS(NH₄)₂ in D₂O.

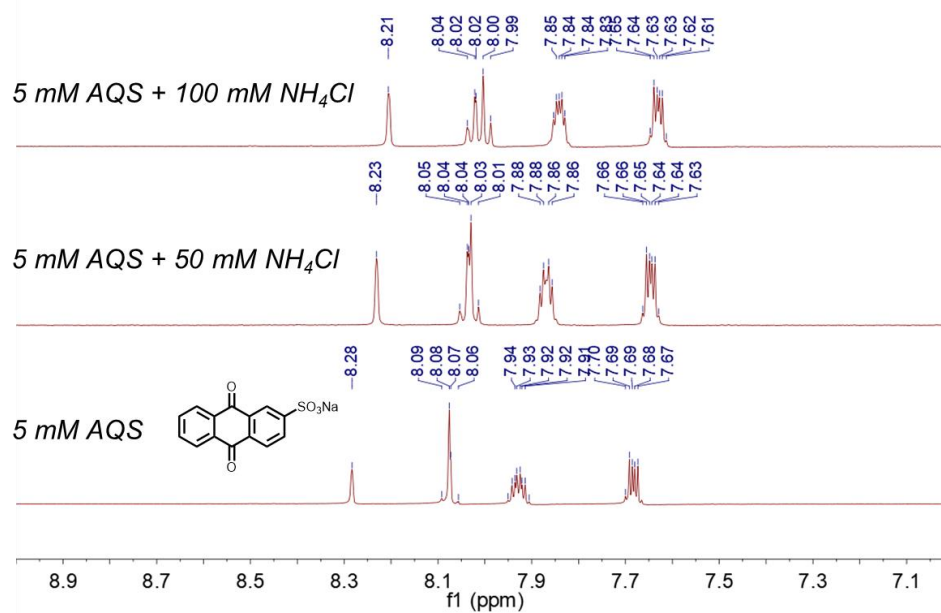


Figure 5-4. ^1H NMR titration of 5 mM AQSNa in D₂O with 10 and 20 equivalents of NH₄Cl.

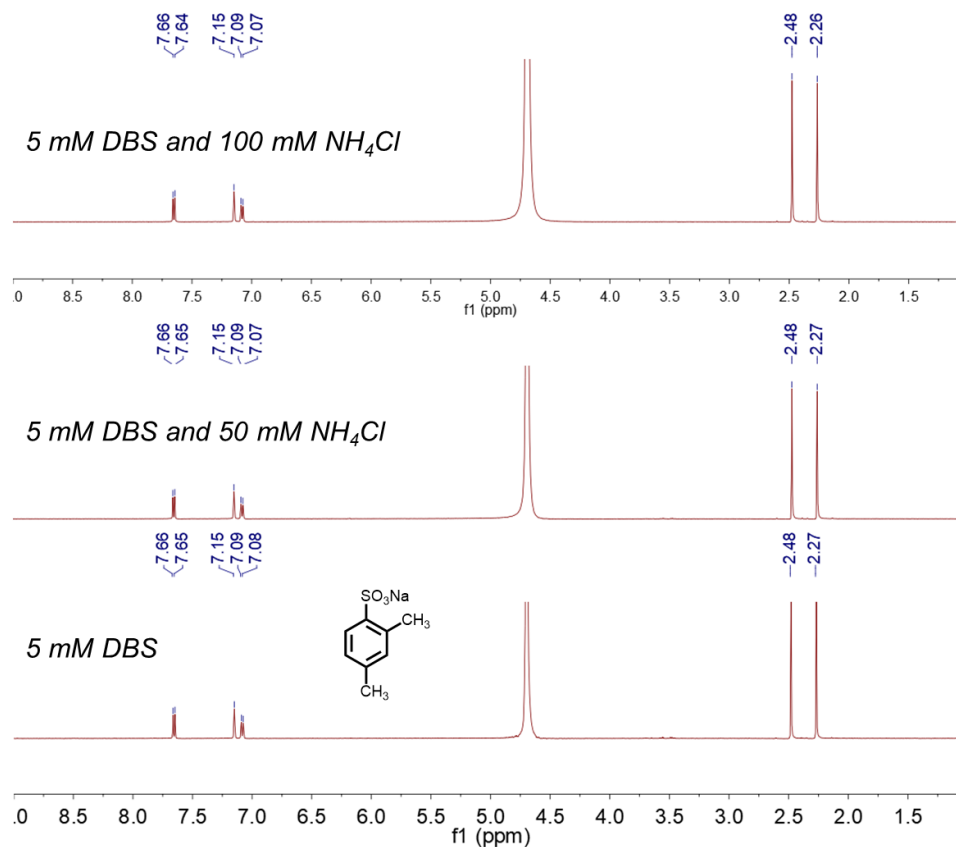


Figure 5-5. ^1H NMR titration of 5 mM sodium 2,4-dimethylbenzenesulfonate in D_2O with 10 and 20 equivalents of NH_4Cl .

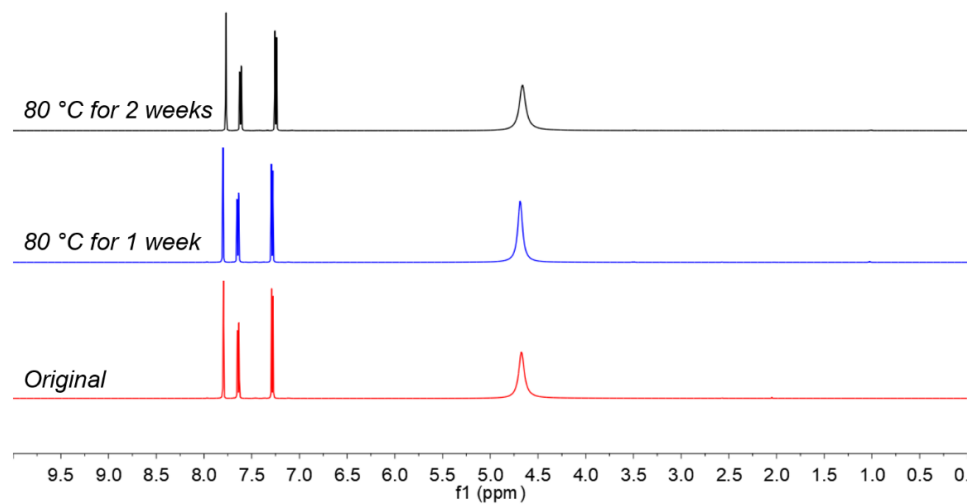
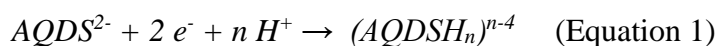


Figure 5-6. ^1H NMR tests of $\text{AQDS}(\text{NH}_4)_2$ in D_2O at 80°C for 2 weeks.

Electrochemical studies for AQDS(NH₄)₂

The ensuing studies were directed on the electrochemical behaviors of **AQDS(NH₄)₂**. Cyclic voltammetry studies revealed a pair of reversible redox peaks at -0.20 V vs NHE in 0.5 M NH₄I electrolyte at pH 7 (Figure 5-7A), which is ca. 410 mV more negative than that of AQDSH₂ at acidic conditions. The thermodynamic potentials of proton-coupled electron transfer (PCET) redox reactions of anthraquinone molecules are well known to be pH dependent, especially in the near neutral region (pH 3-9).²⁰ The general electrochemical reaction of AQDS²⁻ is shown in Equation 1, where two electrons were transferred while various numbers ($0 \leq n \leq 2$) of protons might be coupled at different pH values. The Pourbaix diagram of **AQDS(NH₄)₂** (Figure 5-7B) was generated by measuring its redox potential at different pH values. To our surprise, the redox potential of **AQDS(NH₄)₂** kept nearly unchanged from pH 4 to 7, revealing the two-electron processes without being coupled by protons in this pH region. This phenomenon is attributed to the H-bonding interactions between ammonium cations and the carbonyl oxygen atoms of the AQDS anion. From pH 7 to 10, the redox potential linearly shifted to being more negative with a slope of -30 mV/pH ((Figure 5-7B). By using the Nernst equation, we can establish a relationship between the redox potential and the number of protons and electrons involved in the electrochemical reactions. Equation 2 showed the derivation of the Nernst equation for the reaction displayed in Equation 1, where $z = 2$ in this case (two-electron process).



$$E = E^0 - \frac{RT}{zF} \ln \frac{1}{[H^+]^n} = E^0 - \frac{0.059n}{z} pH \quad (\text{Equation 2})$$

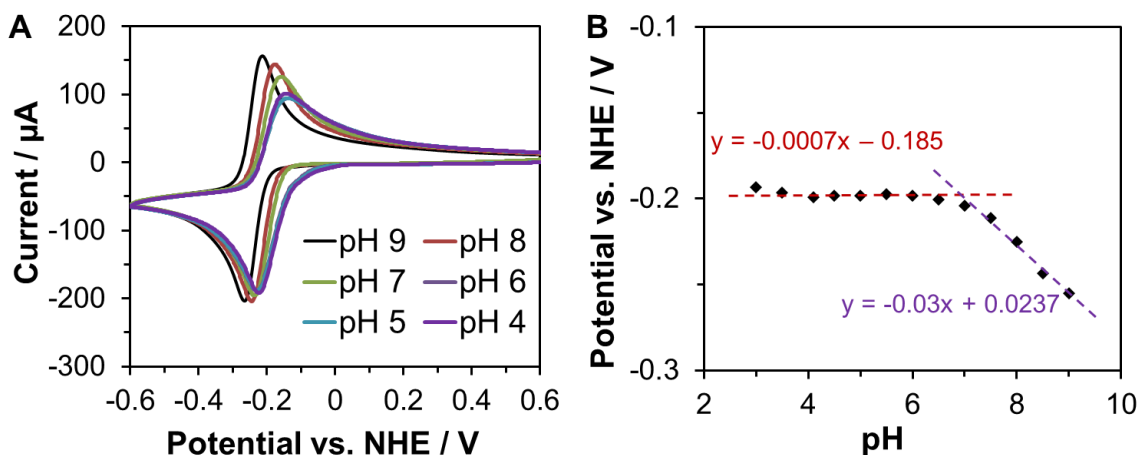


Figure 5-7. (A) Cyclic voltammograms of **AQDS(NH₄)₂** at various pH conditions. (B) Pourbaix diagram of **AQDS(NH₄)₂** in 0.5 M NH₄I solution. Conditions: 4.0 mM analyte in 0.5 M NH₄I electrolyte; scan rate: 100 mV/s; working electrode, glassy carbon electrode; counter electrode, glassy carbon; reference electrode, Ag/AgCl. The pH value was adjusted using ammonium hydroxide solution. FcNCl (-0.60 V vs. NHE at pH 7) was used to calibrate the redox potential.

According to Equation 2 where n was calculated as $(30 \text{ mV} \times 2)/0.059 \text{ V} = 1.02$, the redox chemistry of **AQDS(NH₄)₂** in the region of pH 7 - 10 was assigned as a single proton-coupled 2 electron process. Meanwhile, peak to peak separation decreased with the increase of pH value as shown in Figure 5-7A, indicating gradually improved redox kinetics. Electrochemical kinetics studies of **AQDS(NH₄)₂** were conducted by rotating disk electrode measurements and Nicolson's analysis which have been introduced in the previous chapters. The Levich study and Nicolson measurements revealed the fast electrochemical kinetics of **AQDS(NH₄)₂** at pH 7 with a diffusion coefficient and an electron transfer rate constant of $4.55 \times 10^{-6} \text{ cm}^2/\text{s}$ and 0.077 cm/s , respectively. Besides, scan rate dependent studies of **AQDS(NH₄)₂** (Figure 5-8D) also demonstrated that its reversible reduction/oxidation reactions are both diffusion controlled processes.

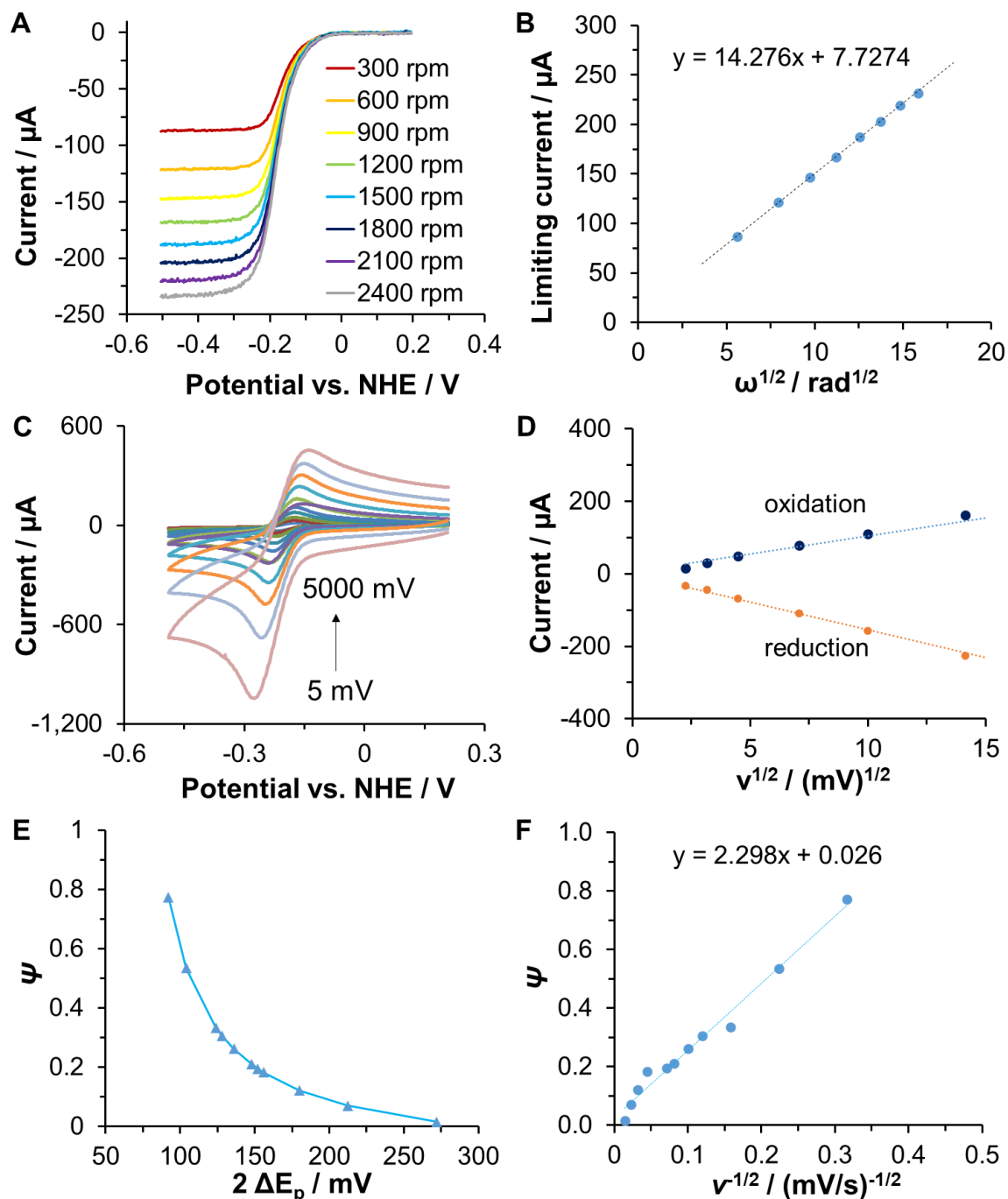


Figure 5-8. RDE test: (A) Linear sweep voltammograms of $\text{AQDS}(\text{NH}_4)_2$ on a glassy carbon rotating disk electrode; (B) Levich plot of the limiting current vs the square root of rotation rates for $\text{AQDS}(\text{NH}_4)_2$; Conditions: 1.0 mM analyte in 0.5 M NH_4I electrolyte; scan rate: 5 mV/s; rotation rates from 300 to 2400 rpm; working electrode, glassy carbon rotating disk electrode; counter electrode, glassy carbon; reference electrode, Ag/AgCl. Scan rate study and Nicholson's analysis of $\text{AQDS}(\text{NH}_4)_2$: (C) CV of $\text{AQDS}(\text{NH}_4)_2$ at various scan rates (5, 10, 20, 50, 100, 200, 300, 500, 1000, 2000,

5000 mV/s). (D) The plot of i_c and i_a over the square root of scan rates for **AQDS(NH₄)₂** (blue trace for oxidative reaction, orange trace for reductive reaction); (E) Plot of Ψ versus $2\Delta E_p$ of **AQDS(NH₄)₂**. (F) The linear relationship between Ψ and $v^{1/2}$ of **AQDS(NH₄)₂**.

AQDS(NH₄)₂/NH₄I neutral AORFB demonstration

For the full AORFB demonstration, NH₄I was selected as the cathode material due to its ammonium cation, excellent stability, and high solubility (ca. 10 M in water). The resulted **AQDS(NH₄)₂/NH₄I** combination predicts a theoretical cell voltage of 0.865 V (Figure 5-10A). Considering the high solubility of **AQDS(NH₄)₂** and the two electron redox process, the **AQDS(NH₄)₂/NH₄I** AORFB could deliver a theoretical energy density as high as 44 Wh/L for the full battery (30 Wh/L when 1 M NH₄I supporting electrolyte is used). We first examined 1 M **AQDS(NH₄)₂/NH₄I** AORFB which could reach an energy density of more than 18.5 Wh/L, very close to the commercialized all vanadium RFBs (25~35 Wh/L). However, during the charging process, it was noticed that the reduced state of **AQDS(NH₄)₂** was not as soluble as **AQDS(NH₄)₂**. The hydroquinone precipitate formed and caused the failure of charging and discharging which could be realized in the charging/discharging profile of the 1 M battery with unsmooth charging/discharging curves (Figure 5-9). The solubility of the two-electron reduced **AQDS(NH₄)₂** was revealed as 0.8 M in 0.5 M NH₄I aqueous solution.

After optimizing the condition, we systematically evaluated the cycling performance of the **AQDS(NH₄)₂/NH₄I** AORFB at 0.75 M (1.5 M e⁻, a charge capacity of 40.2 Ah/L and an energy density of 12.5 Wh/L). The cell design is outlined in Figure 5-10B, where a piece of Nafion 115 membrane was employed as the separator to allow the exchange of ammonium cation and avoid the crossover of anionic redox active species including AQDS²⁻, I⁻, and I₃⁻. 0.5 M NH₄I was added into anode as supporting electrolyte

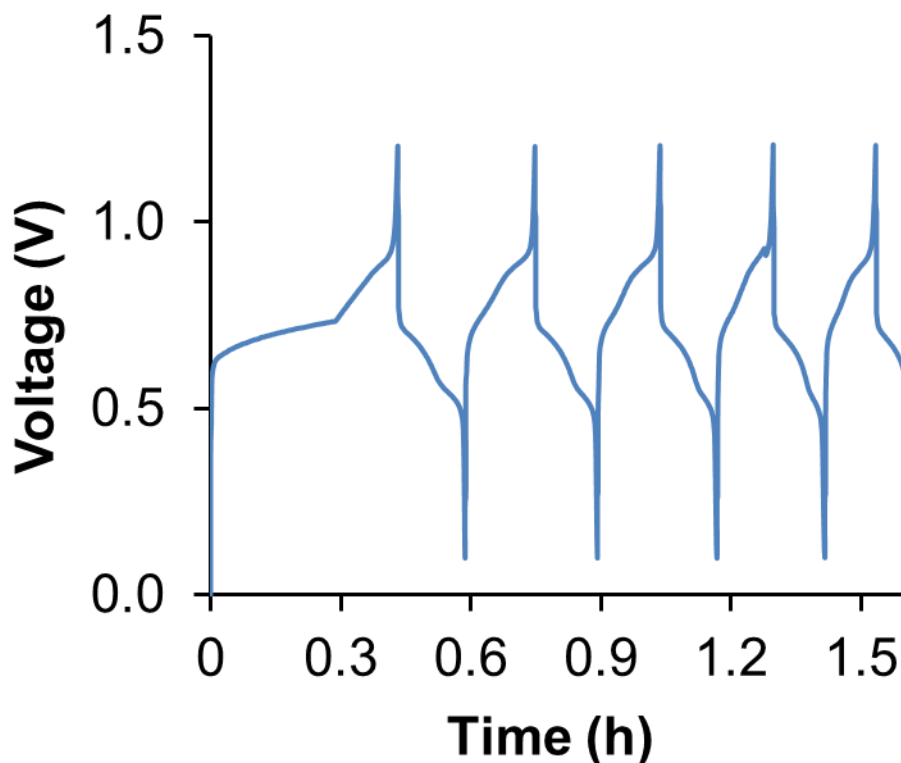


Figure 5-9. Profile of voltage versus time of the 1 M AQDS(NH₄)₂/NH₄I neutral AORFB. Conditions: catholyte, 3 M NH₄I solution (18 mL); anolyte, 1 M AQDS(NH₄)₂ in 1 M NH₄I; current density 40 mA/cm².

to improve electrolyte conductivity. Up to 5 equivalent NH₄I (compared to AQDS(NH₄)₂) was used in the cathode side to ensure the reliable evaluation of the limiting AQDS(NH₄)₂ anolyte side while enabling the fully I₂ complexing to generate soluble I₃⁻. Electrochemical impedance spectroscopy (EIS) revealed a high-frequency area specific resistance (R_{hf}) of the battery as low as 1.44 $\Omega \cdot \text{cm}^2$ (Figure 5-11).

The current rate performance was investigated from 40 mA/cm² to 100 mA/cm² with an increment of 20 mA/cm². For each current density, 5 charge and discharge cycles were tested with cutoff voltages at 1.2 V for the charging process and 0.2 V for the discharging process. In our AQDS(NH₄)₂/NH₄I AORFB cycling experiments, we noticed the low coulombic efficiency (CE) and capacity retention during first several cycles

Figure 5-10. (A) Cyclic voltammogram of 4 mM **AQDS(NH₄)₂** (in 0.5 M NH₄I) and NH₄I (in 0.5 M NH₄Cl), respectively (pH=7). (B) Schematic representation of the **AQDS(NH₄)₂**/NH₄I neutral AORFB and cell reactions.

(Figure 5-12A) which is owing to the intermolecular dimerization between **AQDS(NH₄)₂** and its reduced species (**AQDS(NH₄)₄**). It was reported that **AQDSH₂** and its reduced species could form a dimer compound which cannot be utilized in the discharging process, thus hindering the full utilization of the active materials.³⁴ To support the hypothesis, in a mixed electrolyte of **AQDS(NH₄)₂** and (**AQDS(NH₄)₄**), there was an additional oxidation observed at 0.2 V, assigned to the oxidation of the **AQDS(NH₄)₂/AQDS(NH₄)₄** dimer (Figure 5-12B), whose exact structure remains to be elucidated. In the future, it is possible to avoid dimerization using additives or structural modifications.

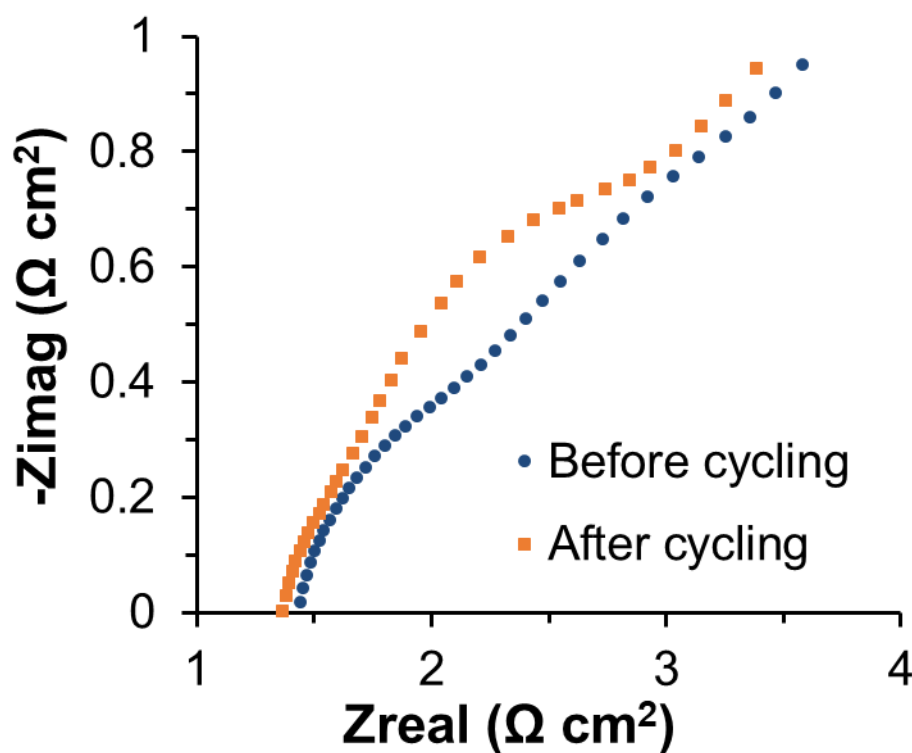


Figure 5-11. EIS test of the 0.75 M **AQDS(NH₄)₂/I₂** RFB before and after cycling at 0 SOC.

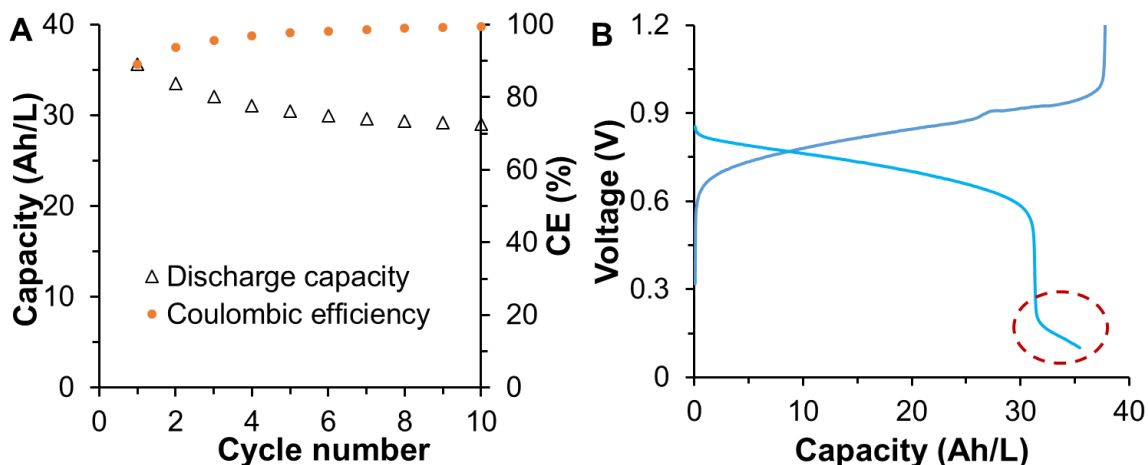


Figure 5-12. (A) Capacity decay of the 0.75 M $\text{AQDS}(\text{NH}_4)_2/\text{NH}_4\text{I}$ AORFB in the first 10 cycles due to active material dimerization. After that, the capacity kept stable. (B) Charging/discharging profile for the mixed electrolyte of $\text{AQDS}(\text{NH}_4)_2$ and $(\text{AQDS}(\text{NH}_4)_4)$. During discharging, the second plateau showed up at 0.2 V, standing for the oxidation of the formed dimer compound in the charging process.

As a result, the battery was firstly cycled at a current density of 40 mA/cm^2 until the CE reached 99 % to avoid the inaccuracy of the rate performance evaluation due to the dimmer formation. Thereafter, the current rate dependent cycling was conducted. Overall, $\text{AQDS}(\text{NH}_4)_2/\text{NH}_4\text{I}$ AORFB exhibited an excellent rate performance. As shown in Figure 5-13A, 5 stable cycles were demonstrated at each current density without capacity decay. At 40 mA/cm^2 , the battery presented a capacity utilization of 76.4 % (30.7 Ah/L out of 40.2 Ah/L), which decreased to 72.3 % when the current density was increased to 60 mA/cm^2 (Figure 5-13B) due to increased charging/discharging overpotential. Benefitted from low cell resistance, the battery exhibits an impressive energy efficiency of up to 81.7 % at 40 mA/cm^2 and 70.6 % at 60 mA/cm^2 (Figure 5-13C), standing for the most energy efficient neutral AORFBs to date. In addition, a high power density of 91.5 mW/cm^2 was recorded at 100 % SOC (Figure 5-13D), which could

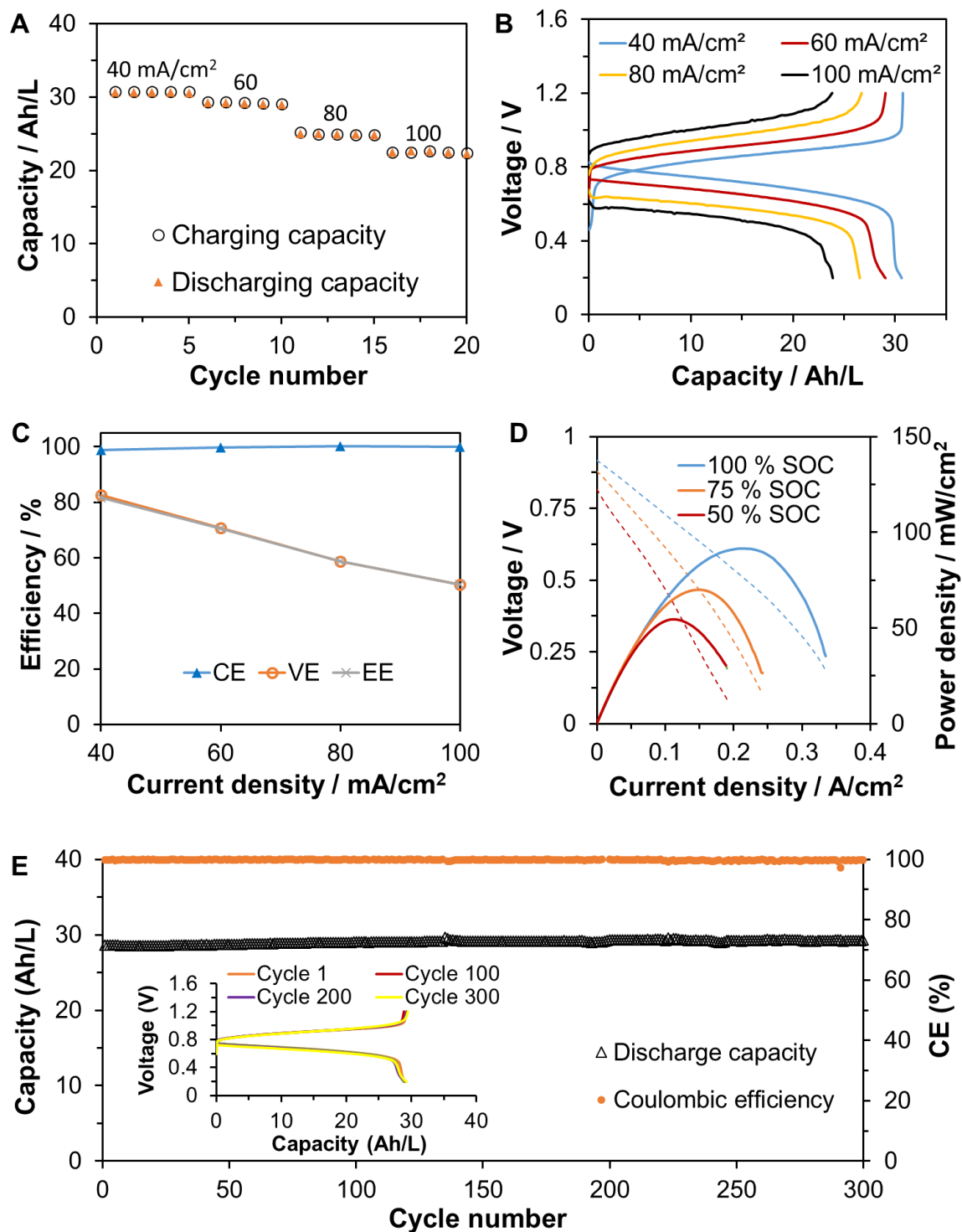


Figure 5-13. Battery performance of the 0.75 M AQDS(NH₄)₂/NH₄I neutral AORFB. (A) Capacity vs. the cycle number from 40 to 100 mA/cm² of the battery. 5 cycles' test was conducted for each current density; (B) Voltage versus capacity profile at different charging/discharging current density (Red dash line stands for the theoretical value); (C) Averaged coulombic efficiency, voltage efficiency, and energy efficiency at different

charging/discharging current density; (D) Power density of the battery at various state of charge; (E) Capacity versus cycle number for 300 cycles. The battery is cycled at 60 mA/cm². Inset: selected representative voltage versus capacity profiles.

be further optimized by applying more conductive ion exchange membranes and supporting electrolytes. Long-term cycling was examined at 60 mA/cm² to further validate the cycling stability of the **AQDS(NH₄)₂/NH₄I** AORFB (Figure 5-13E), which was first cycled at 40 mA/cm² for a few cycles to stabilize the dimerization process. The smooth charging/discharging curves indicated that no precipitate was generated (Figure 5-14A). The battery delivered rather stable capacity retention as no capacity decay was detected after 300 cycles (ca. 15 days) and represent the most stable AQ based AORFBs. Judging from the well-overlapped charging/discharging profile (Figure 5-12E and Figure 5-14A), the charging/discharging overpotential stay the same during the cycles from 10 to 300, which suggested no ohmic loss and good chemical compatibility with the membrane and other cell components. This is also in line with the almost identical R_{hf}

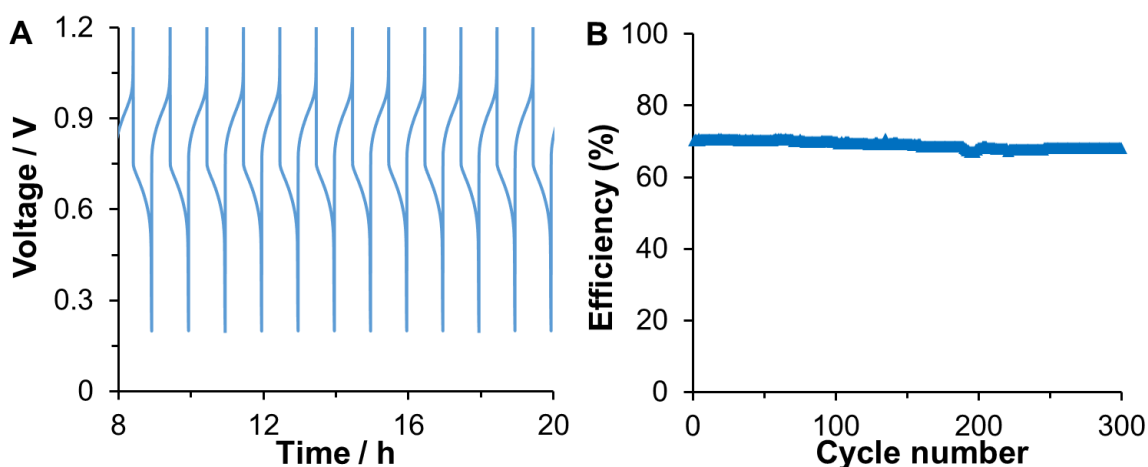


Figure 5-14. (A) Representative charging/discharging profile (voltage versus time) of the 0.75 M neutral **AQDS(NH₄)₂/I₂** RFB. (B) Representative charging/discharging profile (voltage versus time) of the 0.75 M neutral **AQDS(NH₄)₂/I₂** RFB.

from the EIS measurements before and after cycling (Figure 5-11). The energy efficiency maintained about 70 % during cycling (Figure 5-14B).

Post analysis of $\text{AQDS}(\text{NH}_4)_2/\text{I}_2$ neutral AORFB.

Post-cell analysis for the 0.75 M $\text{AQDS}(\text{NH}_4)_2/\text{NH}_4\text{I}$ AORFB after 300 cycles were conducted using cyclic voltammetry, ^1H NMR (Figure 5-15 and 5-16). Both CV and ^1H NMR studies indicated there was no chemical degradation for $\text{AQDS}(\text{NH}_4)_2$. In stark contrast, even at the 0.1 M concentration, an $\text{AQDSNa}_2/\text{NaI}$ AORFB could not be cycled because of the rapid precipitate formation of the charged state, AQDSNa_4 , further highlighting the unique role of the NH_4^+ cations for $\text{AQDS}(\text{NH}_4)_2$.

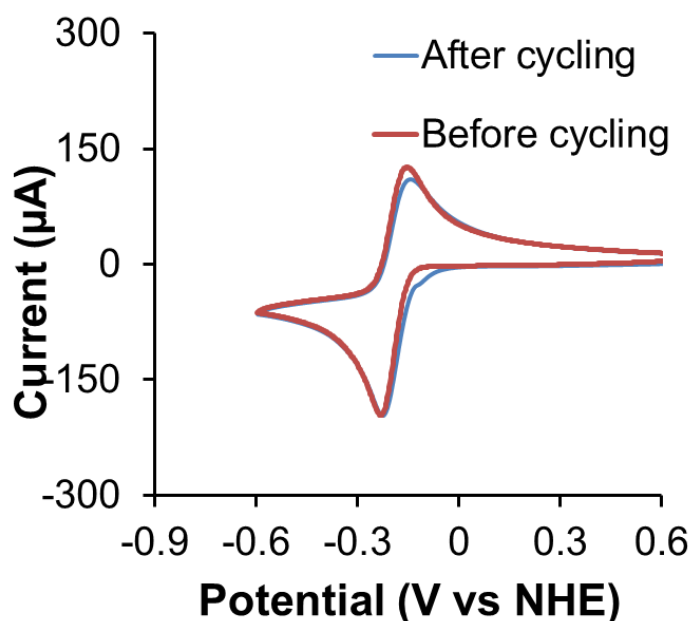


Figure 5-15. Cyclic voltammetry post analysis of the anolyte of 0.75 M $\text{AQDS}(\text{NH}_4)_2/\text{I}_2$ RFB after cycling for 300 cycles.

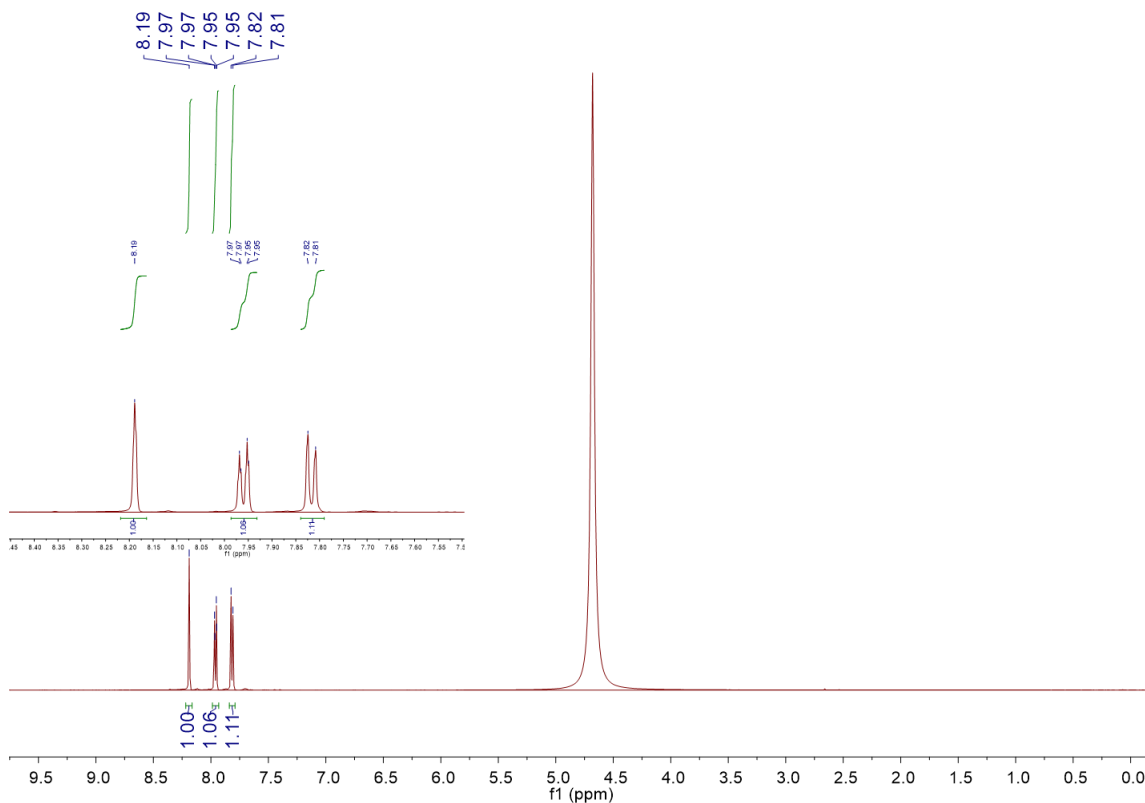


Figure 5-16. ^1H NMR post analysis of the analyte of 0.75 M $\text{AQDS}(\text{NH}_4)_2/\text{I}_2$ RFB after cycling for 300 cycles.

As shown in Figure 5-17, representative AQ based AORFBs are compared in the aspects of demonstrated energy density and normalized stability (per month). It is clear that the demonstrated pH neutral $\text{AQDS}(\text{NH}_4)_2/\text{NH}_4\text{I}$ AORFB displayed much improved performance compared to reported AQDS based AORFBs in terms of energy density and cycling stability. The acid or alkaline AQ based AORFBs suffer either low energy density or poor cycling stability, which attribute to the low solubility or poor chemical stability of active materials. As a result of the extraordinary chemical stability and solubility of $\text{AQDS}(\text{NH}_4)_2$ in the neutral supporting electrolyte, the pH neutral AORFB $\text{AQDS}(\text{NH}_4)_2/\text{NH}_4\text{I}$ system demonstrated an energy density of and the capacity retention

of ca. 100% per month, representing one of the most energy dense and stable AORFBs reported to date. Recently, a water-miscible anthraquinone (PEGAQ) molecule with 2-(2-(2-hydroxyethoxy)ethoxy)ethoxy side chains was reported, which stands for one the most water soluble anthraquinone derivatives.³³ The neutral PEGAQ/ $\text{Fe}(\text{CN})_6^{2-}$ AORFB was demonstrated with an energy density as high as 25.2 Wh/L. However, the cycling capacity retention of the battery was only 85 % per month due to the decomposition of PEGAQ.

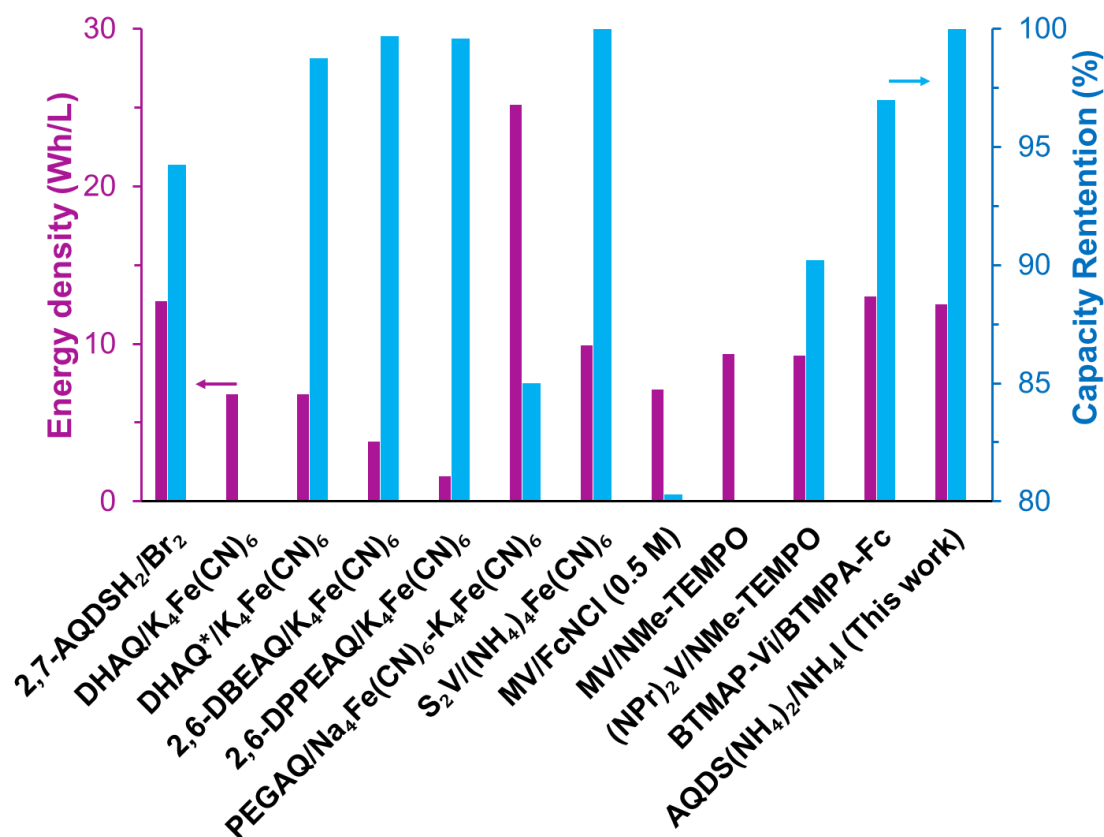


Figure 5-17. Comparison of demonstrated energy densities and capacity retention per month of the selected AQ based AORFBs (Capacity retention lower than 80 % per month was not displayed in the figure).

5-5. Conclusion

In summary, we have developed a new ammonium functionalized anthraquinone derivative (**AQDS(NH₄)₂**) as the anolyte material for pH neutral AORFB application. The synthesis of the new **AQDS(NH₄)₂** anolyte material is straightforward and convenient at ambient conditions, and scalable using common commercial precursors. In addition to its hydrophilic nature, the introduced ammonium cations form hydrogen bonds with AQDS²⁻ anion to improve the solubility of the AQDS anion. Paired with highly soluble NH₄I cathode material, the demonstrated **AQDS(NH₄)₂/NH₄I** battery stands for the most stable pH neutral, metal free anthraquinone AORFB with very high capacity and energy density. Taking account of the easy synthesis, low cost, high energy density, unbeatable stability and environmental advantage, **AQDS(NH₄)₂** can regard a highly attractive anolyte molecule in AORFBs for large scale sustainable energy storage. Moreover, the present chemistry of **AQDS(NH₄)₂** could open a new avenue to utilizing anthraquinone compounds in developing pH neutral, benign and stable cycling AORFBs to promise low cost and sustainable green energy storage.

5-6. Reference

- (1) Dunn, B.; Kamath, H.; Tarascon, J.-M. *Science*. **2011**, 334, 928.
- (2) Yang, Z.; Zhang, J.; Kintner-Meyer, M. C. W.; Lu, X.; Choi, D.; Lemmon, J. P.; Liu, J. *Chem. Rev.* **2011**, 111, 3577.
- (3) Soloveichik, G. L. *Chem. Rev.* **2015**, 115, 11533.
- (4) Wang, W.; Sprenkle, V. *Nat. Chem.* **2016**, 8, 204.

- (5) Wang, W.; Luo, Q. T.; Li, B.; Wei, X. L.; Li, L. Y.; Yang, Z. G. *Adv. Funct. Mater.* **2013**, *23*, 970.
- (6) Wei, X.; Pan, W.; Duan, W.; Hollas, A.; Yang, Z.; Li, B.; Nie, Z.; Liu, J.; Reed, D.; Wang, W.; Sprenkle, V. *ACS Energy Lett.* **2017**, *2*, 2187.
- (7) Kwabi, D. G.; Lin, K.; Ji, Y.; Kerr, E. F.; Goulet, M.-A.; De Porcellinis, D.; Tabor, D. P.; Pollack, D. A.; Aspuru-Guzik, A.; Gordon, R. G.; Aziz, M. J. *Joule*. **2018**, *2*, 1894.
- (8) Liu, T. B.; Wei, X. L.; Nie, Z. M.; Sprenkle, V.; Wang, W. *Adv. Energy Mater.* **2016**, *6*.
- (9) Hu, B.; DeBruler, C.; Rhodes, Z.; Liu, T. L. *J. Am. Chem. Soc.* **2017**, *139*, 1207.
- (10) DeBruler, C.; Hu, B.; Moss, J.; Liu, X.; Luo, J.; Sun, Y.; Liu, T. L. *Chem.* **2017**, *3*, 961.
- (11) Hu, B.; Tang, Y.; Luo, J.; Grove, G.; Guo, Y.; Liu, T. L. *Chem Commun.* **2018**, *54*, 6871.
- (12) Luo, J.; Hu, B.; Debruler, C.; Bi, Y.; Zhao, Y.; Yuan, B.; Hu, M.; Wu, W.; Liu, T. L. *Joule*. **2019**, *4*, 1.
- (13) Janoschka, T.; Martin, N.; Martin, U.; Friebe, C.; Morgenstern, S.; Hiller, H.; Hager, M. D.; Schubert, U. S. *Nature*. **2015**, *527*, 78.
- (14) Janoschka, T.; Martin, N.; Hager, M. D.; Schubert, U. S. *Angew. Chem. Int. Ed.* **2016**, *55*, 14425.
- (15) Luo, J.; Hu, B.; Debruler, C.; Liu, T. L. *Angew. Chem. Int. Ed.* **2018**, *57*, 231.
- (16) Cosimbescu, L.; Wei, X. L.; Vijayakumar, M.; Xu, W.; Helm, M. L.; Burton, S. D.; Sorensen, C. M.; Liu, J.; Sprenkle, V.; Wang, W. *Sci Rep-Uk* **2015**, *5*, 14117.

- (17) Beh, E. S.; De Porcellinis, D.; Gracia, R. L.; Xia, K. T.; Gordon, R. G.; Aziz, M. J. *ACS Energy Lett.* **2017**, 639.
- (18) Ding, Y.; Zhao, Y.; Li, Y.; Goodenough, J. B.; Yu, G. *Energy Environ. Sci.* **2017**, 10, 491.
- (19) Sevov, C. S.; Hickey, D. P.; Cook, M. E.; Robinson, S. G.; Barnett, S.; Minteer, S. D.; Sigman, M. S.; Sanford, M. S. *J. Am. Chem. Soc.* **2017**, 139, 2924.
- (20) Huskinson, B.; Marshak, M. P.; Suh, C.; Er, S.; Gerhardt, M. R.; Galvin, C. J.; Chen, X. D.; Aspuru-Guzik, A.; Gordon, R. G.; Aziz, M. J. *Nature*. **2014**, 505, 195.
- (21) Yang, B.; Hooper-Burkhardt, L.; Wang, F.; Prakash, G. K. S.; Narayanan, S. R. *J. Electrochem. Soc.* **2014**, 161, A1371.
- (22) Lin, K. X.; Chen, Q.; Gerhardt, M. R.; Tong, L. C.; Kim, S. B.; Eisenach, L.; Valle, A. W.; Hardee, D.; Gordon, R. G.; Aziz, M. J.; Marshak, M. P. *Science*. **2015**, 349, 1529.
- (23) Yang, B.; Hooper-Burkhardt, L.; Krishnamoorthy, S.; Murali, A.; Prakash, G. K. S.; Narayanan, S. R. *J. Electrochem. Soc.* **2016**, 163, A1442.
- (24) Wei, X.; Xu, W.; Vijayakumar, M.; Cosimbescu, L.; Liu, T.; Sprenkle, V.; Wang, W. *Adv. Mater.* **2014**, 26, 7649.
- (25) Lin, K.; Gómez-Bombarelli, R.; Beh, E. S.; Tong, L.; Chen, Q.; Valle, A.; Aspuru-Guzik, A.; Aziz, M. J.; Gordon, R. G. *Nat. Energy*. **2016**, 1, 16102.
- (26) Orita, A.; Verde, M. G.; Sakai, M.; Meng, Y. S. *Nat. Commun.* **2016**, 7, 13230.
- (27) Hollas, A.; Wei, X.; Murugesan, V.; Nie, Z.; Li, B.; Reed, D.; Liu, J.; Sprenkle, V.; Wang, W. *Nat. Energy*. **2018**, 3, 508.

- (28) Gerhardt, M. R.; Tong, L.; Gómez-Bombarelli, R.; Chen, Q.; Marshak, M. P.; Galvin, C. J.; Aspuru-Guzik, A.; Gordon, R. G.; Aziz, M. J. *Adv. Energy Mater.* **2017**, *7*, 1601488.
- (29) Goulet, M.-A.; Tong, L.; Pollack, D. A.; Tabor, D. P.; Odom, S. A.; Aspuru-Guzik, A.; Kwan, E. E.; Gordon, R. G.; Aziz, M. J. *J. Am. Chem. Soc.* **2019**, *141*, 8014.
- (30) Ji, Y.; Goulet, M.-A.; Pollack, D. A.; Kwabi, D. G.; Jin, S.; De Porcellinis, D.; Kerr, E. F.; Gordon, R. G.; Aziz, M. J. *Adv. Energy Mater.* **2019**, *9*, 1900039.
- (31) Luo, J.; Sam, A.; Hu, B.; DeBruler, C.; Wei, X.; Wang, W.; Liu, T. L. *Nano Energy*. **2017**, *42*, 215.
- (32) Lee, W.; Permatasari, A.; Kwon, B. W.; Kwon, Y. *Chem. Eng. J.* **2019**, *358*, 1438.
- (33) Jin, S.; Jing, Y.; Kwabi, D. G.; Ji, Y.; Tong, L.; De Porcellinis, D.; Goulet, M.-A.; Pollack, D. A.; Gordon, R. G.; Aziz, M. J. *ACS Energy Lett.* **2019**, *4*, 1342.
- (34) Carney, T. J.; Collins, S. J.; Moore, J. S.; Brushett, F. R. *Chem. Mater.* **2017**, *29*, 4801.

CHAPTER VI

HETEROGENEOUS ELECTROCATALYTIC CARBON DIOXIDE REDUCTION TO
FORMATE ON A NITROGENASE MODIFIED BIOELECTRODE ^f**6-1. Abstract**

Nitrogenases catalyze all biological dinitrogen (N_2) reduction to ammonia (NH_3) and have been shown to reduce a number of non-physiological substrates, including carbon dioxide (CO_2) to formate ($HCOO^-$) and methane (CH_4). Three versions of nitrogenase are known (Mo-, V-, and Fe-nitrogenase), with each showing different reactivity towards the array of substrates. Normally, electrons for substrate reduction are delivered by the Fe protein nitrogenase component, with energy coming from the hydrolysis of 2 ATP to 2 ADP + 2 Pi for each electron transferred. Recently, it has been demonstrated that energy and electrons can be delivered from an electrode to the catalytic nitrogenase MoFe-protein without the need for the Fe protein and ATP hydrolysis. Here, we demonstrate that both the MoFe- and FeFe-protein can be attached to an electrode in a polymer layer and electron transfer mediated by cobaltacene can drive CO_2 reduction to formate. It was found that the FeFe-protein diverts a greater percentage of electrons to CO_2 reduction versus proton reduction compared to the MoFe-protein. Quantification of electron flow and all products showed Faradaic efficiencies of CO_2 conversion to formate of 9% for MoFe protein and 32% for FeFe-protein, with the remaining electrons going to proton reduction to make H_2 .

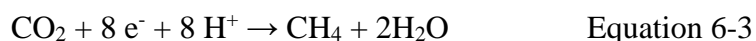
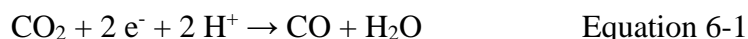
^f Adapted with permission from [Hu, B.; Harris, D.; Dean, D.; Liu, T. L.; Yang, Z.; Seefeldt L. Bioelectrochemistry. **2018**, 120, 104]. Copyright 2018 Elsevier Inc. Reproduced by permission of Elsevier Inc., <https://www.sciencedirect.com/science/article/pii/S1567539417305558?via%3Dihub>

6-2. Introduction

Nitrogenases are the enzymes that catalyze all biological N_2 reduction to NH_3 , being the major contributor of fixed N into the biogeochemical N cycle.¹ There are three known types of nitrogenase, called the Mo-dependent, the V-dependent, and the Fe-dependent nitrogenase.²⁻⁶ Each nitrogenase is coded for by distinct genes, resulting in distinct catalytic systems.^{7,8} The basic architecture for the nitrogenase proteins is similar; an electron donating Fe protein that transfers one electron at a time from its 4Fe-4S cluster into the catalytic component protein (called MoFe, VFe, and FeFe protein) which house an electron mediator 8Fe-7S cluster called P cluster and the active site metal cluster called FeMo-co, FeV-co, and FeFe-co, respectively (Figure 6-1).^{2,4,5,9} The active site metal cofactor structures for FeMo-co and FeV-co are known and are very similar with an exchange of Mo for V.¹⁰⁻¹⁵ Further, the VFe-co contains a carbonate that replaces one of bridging sulfides.¹⁰ No X-ray crystal structure for the FeFe-co is available, but spectroscopic evidence indicates that it is similar to the other two cofactors with Fe substituting for V or Mo found in the other systems.¹⁶

The catalytic cycle of nitrogenase involves the transient association of the Fe protein component with the catalytic component protein followed by the transfer of an electron from the Fe protein into the catalytic component with hydrolysis of two ATP molecules bound in the Fe protein to two ADP and two P_i .^{2,9,17,18} The oxidized and ADP containing Fe protein dissociates and the cycle must be repeated for each electron accumulated.¹⁸⁻²⁰ Thus, the energy for electron accumulation at the active site for substrate reduction comes from hydrolysis of two ATP (ΔG° 61 kJ/mol).^{9,21}

The reduction of substrates has been investigated for the Mo-dependent nitrogenase in considerable detail,^{2,9,17,18,22,23} while very little known about the mechanism of the V- and Fe-nitrogenases.^{3-5,24} For the Mo-nitrogenase, N₂ reduction requires 8 electrons and 8 protons, and thus the hydrolysis of 16 ATP ($\Delta G^\circ = 488$ kJ/mol). One H₂ is formed for each N₂ reduced as an essential part of the catalytic mechanism.^{9,17,25-29} In addition to reducing protons and N₂, Mo-nitrogenase has been shown to reduce a number of small molecules with double and triple bonds.^{2,30} Among the many molecules reduced by Mo-nitrogenase is carbon dioxide (CO₂).³¹⁻³⁶ There is considerable interest in reducing CO₂ as one way to mitigate the considerable CO₂ production from the burning of fossil fuels.³⁷⁻⁴¹ Mo-nitrogenase was shown to reduce CO₂ by two electrons and two protons to CO³¹ and formic acid³³ and by 8 electrons and 8 protons to methane^{32,34} (Equation 6-1 to 6-3).



The V-nitrogenase has also been shown to reduce CO₂ to CH₄ and C₂ and C₃ hydrocarbons.^{35,36} In vivo studies with the Fe-nitrogenase indicate that this enzyme shows the highest CO₂ reduction to CH₄ of the three nitrogenases.⁴² This study demonstrated the reduction of CO₂ to CH₄ when driven by Fe protein and ATP for both purified Fe-nitrogenase component proteins and in whole cells.

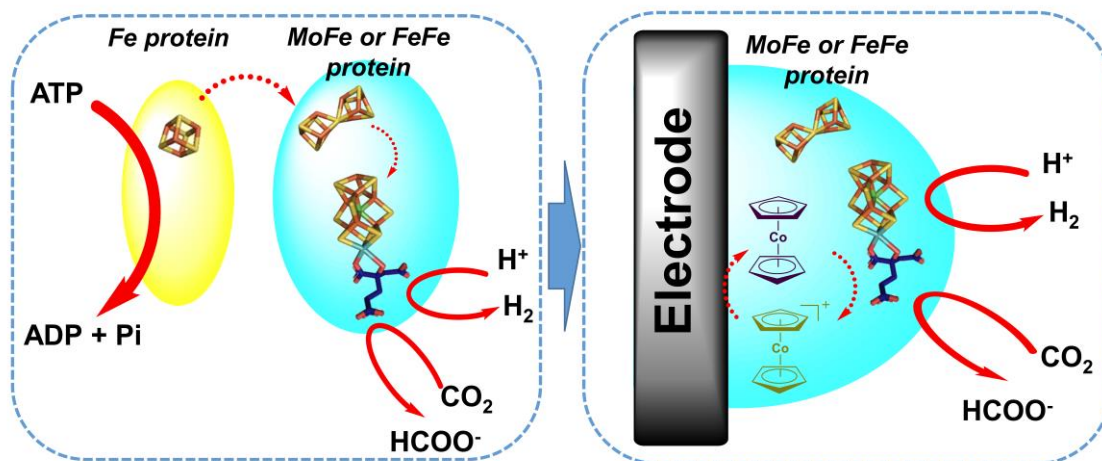


Figure 6-1. Schematic showing nitrogenase catalysis with electron transfer from the Fe protein and ATP hydrolysis (left) or from cobaltacene mediated electron catalysis (right) for the MoFe or FeFe proteins catalyzing proton and CO₂ reduction.

As a way to bypass the energy requirement of ATP hydrolysis that is needed for electron delivery by the Fe protein to the catalytic component protein, an electrochemical method has been developed to allow the MoFe-protein to be isolated in a polymer layer on a glassy carbon electrode with cobaltacene mediated electrocatalysis.⁴³ This method is a promising new approach to achieve small molecule reduction catalyzed by a nitrogenase component⁴³ and as a way to probe the mechanism of nitrogenase catalysis.⁴⁴ Using the MoFe-protein, it has been demonstrated that protons, nitrite, and azide can be reduced with the electrons and energy coming from the electrode. Here, we immobilize the MoFe- and FeFe-proteins on an electrode and show the catalytic reduction of CO₂ to formate, with the FeFe-protein showing the greatest Faradaic efficiency for CO₂ reduction.

6-3. Materials and methods

Materials

Poly(vinylamine) hydrochloride (PVA) was purchased from Polysciences, Inc (Warrington, PA). Ethylene glycol diglycidyl ether (EDGDE) was received from TCI (Portland, OR). Pyrene, cobaltocenium hexafluorophosphate and 4-(2-Hydroxyethyl)piperazine-1-ethanesulfonic acid (HEPES) were obtained from Sigma Aldrich (City, State). All chemicals were used as received without further purification. FeFe protein and MoFe protein were purified as described and were diluted to 20 mg/mL with deoxygenated HEPES buffer solution (50 mM, pH = 7.4). Deionized water and HEPES buffer solution were degassed by Argon before use. Glassy carbon electrodes were polished with 0.5 μm aluminum powder, sonicated in isopropanol and rinsed with deionized water before using.

Bacterial growth and protein purification

Fe-nitrogenase proteins were expressed in *Azotobacter vinelandii* strain DJ1255 cells grown at 30 °C in Burk N-free medium with Na_2MoO_4 omitted in a custom-built 100 L fermenter with stirring and aeration to an OD600 of 1.8-2.0 and then harvested. Mo-nitrogenase proteins were expressed in *Azotobacter vinelandii* strains DJ995 for MoFe protein and DJ884 for Fe protein and purified as previously described.⁴⁵ Crude extracts were prepared and proteins purified according to previously described methods with minor modifications. Cell extracts of DJ1255 cells were prepared by using a French pressure cell operated at 1,500 lb/in² in a degassed 50 mM Tris·HCl buffer (pH 8.0) with 2 mM sodium dithionite under Ar.⁴⁶ Protein concentrations were determined by the Biuret assay using bovine serum albumin as a standard. Protein purity was confirmed by sodium dodecyl sulfate polyacrylamide gel electrophoresis (SDS-PAGE) analysis using

Coomassie blue staining. The proteins were fully active based on proton reduction specific activities under Ar.

ATP-driven CO₂ reduction by MoFe and FeFe protein

CO₂ reduction assays were conducted in 9.4 mL serum vials containing an assay buffer consisting of an MgATP regeneration system (13.4 mM MgCl₂, 60 mM phosphocreatine, 10 mM ATP, 0.4 mg/mL creatine phosphokinase, and 1.2 mg/mL BSA) and 20 mM sodium dithionite in 100 mM HEPES buffer at pH 7.8. After solutions were made anaerobic, 0.45 atm CO₂ was added and the gas and liquid phases were allowed to equilibrate for approximately 10 minutes. FeFe or MoFe protein was then added, the vials vented to atmospheric pressure, and the reaction initiated by the addition of the appropriate Fe protein. Reactions were conducted at 30°C for 60 minutes and then quenched by the addition of 500 µL of 400 mM EDTA pH 8.0. H₂ was quantified according to published methods.⁴⁵ Formate was quantified by two methods: (1) a previously described colorimetric assay⁴⁷ with an internal formate standard was prepared by adding NaHCOO⁻ to 500 µL of sample to a final concentration of 2 mM; (2) a modified ¹H-NMR method with bis(cyclopentadienyl)cobalt(III) hexafluorophosphate as an internal standard. After the reaction 1 mL solution was transferred into a 10 mL flask. 60 µL 1 mM cobaltocenium solution (in 50 mM HEPES buffer, pH=7.4) was added. The solution was carefully dried by a rotary evaporator under vacuum. The residue was dissolved in D₂O for NMR experiments.

Electrocatalytic CO₂ reduction by MoFe and FeFe protein.

Bio-electrodes preparation: 15 µL of PVA solution (10 mg/mL in 250 mM HEPES buffer, pH 7.4) and 1 µL of pyrene solution (1 mg/mL in dimethyl formamide)

were mixed to form a homogeneous suspension. Then 2 μL of EDGDE cross linker solution (10 % volume ratio in 250 mM HEPES buffer, pH 7.4) was added followed by 20 μL protein solution (20 mg/mL in HEPES buffer). 8 μL of the suspension was dropped on the surface of a polished glassy carbon electrode and dried in an Ar filled glove box for 2 h at room temperature. All operations were conducted in an Ar filled glove box with oxygen concentration less than 1 ppm.

Electrochemical test: All electrochemical tests were performed on an Autolab potentiostat with a three electrode system. Glassy carbon electrode (or protein coated glassy carbon electrode, area 0.071 cm^2), saturated calomel electrode and platinum wire were used as working electrode, reference electrode, and counter electrode, respectively. 50 mM HEPES buffer (pH=7.4) was used as supporting electrolyte. 0.4 mM cobaltocenium hexafluorophosphate was added. Normal pulse voltammetry was applied to determine the redox potential of electron mediator. Cyclic voltammetry (CV) spectra were collected in the potential range between -1.35 V to -0.8 V (vs. SCE) at a scan rate of 2 mV/s. Bulk electrolysis was conducted by a chronoamperometry (CA) method under a set potential of -1.26 V vs. SCE for 2 hours. All the operations were conducted at room temperature in an Ar filled glove box with oxygen concentration lower than 1 ppm.

Products characterization and quantification

Hydrogen was confirmed and quantified by GC. Formate was confirmed and quantified by ^1H -NMR using cobaltocenium as the internal reference.

6-4. Results and discussion

Fe protein-ATP driven CO_2 reduction by nitrogenases.

The purified MoFe protein and FeFe protein were assayed for the ability to reduce CO₂ when provided with the appropriate Fe protein (NifH or AnfH) and ATP.⁴⁶ Both proteins were found to reduce CO₂ to formate and to reduce protons to H₂. The FeFe-protein demonstrated a greater percentage of electrons directed to CO₂ reduction to yield formate when compared to the MoFe protein, with $31.0 \pm 0.29\%$ of electrons going to CO₂ reduction in the FeFe-protein compared to $9 \pm 1.4\%$ of electrons going to CO₂ reduction in the MoFe-protein. For both systems, the remaining electron flow is used to reduce protons to produce H₂. These findings are consistent with the *in vivo* studies that previously indicated FeFe-protein is a superior catalyst for CO₂ reduction compared to the MoFe-protein.⁴²

Electrocatalytic CO₂ reduction by nitrogenases

Unlike the Fe protein/ATP driven CO₂ reduction described above, an electrocatalytic process does not require Fe protein or ATP. Electrons are provided from the electrode and are delivered through the mediator cobaltocenium to the MoFe protein or FeFe protein.⁴³ Cyclic voltammetry (CV) studies were conducted to examine the electrochemical property of the mediator on a bare glassy carbon electrode. The normal CV trace of cobaltocenium showed a pair of irreversible reduction/oxidation peaks that result from insoluble cobaltocene deposition on the surface of the working electrode (Figure 6-2 dash trace). The half wave potential $E_{1/2}$ was estimated as -1.15 V (vs. SCE), which agrees with the reported result⁴⁸ although the supporting electrolyte is different. This $E_{1/2}$, and an appropriately negative electrode potential, ensured that electrons are readily shuttled from the electrode to the active center of Mo nitrogenase. In order to validate that cobaltocenium alone has no catalytic capacity for CO₂ reduction, sodium

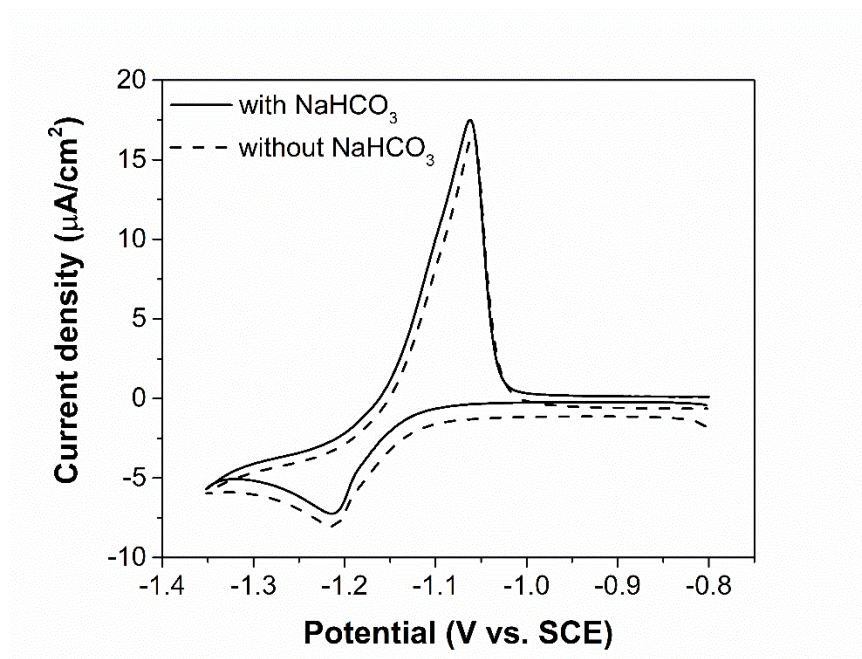


Figure 6-2. Cyclic voltammetry of Cobaltocenium (Cc^+) on glassy carbon with and without NaHCO_3 . Conditions: 0.2 mM Cc^+ in 50 mM HEPES buffer solution (PH=7.4).

bicarbonate was then added into the solution as a carbon dioxide source and the CV was run again. An almost identical CV was observed compared to the control without bicarbonate added, demonstrating that cobaltocenium shows no catalytic activity for the reduction of CO_2 under these conditions (Figure 6-2 solid trace).

In a previous electrocatalytic study of proton reduction by MoFe protein, the MoFe protein was immobilized on the electrode by mixing PVA, EDGDE and protein solutions together, followed by casting the mixture onto a glassy carbon electrode.^{43,44} The crosslink reaction resulted in insoluble film or hydrogel on the surface of the glassy carbon electrode, thus allowed the immobilization of the protein on the electrode as shown in Figure 6-3. First, we followed the same protein immobilization protocol to prepare the electrode. Then we examined the catalytic activity of FeFe-protein from Fe-

nitrogenase for CO₂ reduction. Compared with the CV of Cc⁺ on bare GC electrode, the reduction current of Cc⁺/Cc on FeoFe-protein modified electrode increased from -0.44 μ A to -2.06 μ A and the oxidation peak disappeared, which was due to the electrocatalytic reduction of proton by the catalyst (FeFe-protein). With the adding of more and more NaHCO₃, the current kept increasing. When the concentration of NaHCO₃ reached 200 mM, a well-defined “S” shape catalytic cyclic voltammogram was obtained with a catalytic current of -3.96 μ A (54 μ A/cm²) at the potential of -1.26 V vs. SCE (Figure 6-4 red trace). The obtained CV showed a mediated CO₂ reduction onset potential of -1.0 V vs. SCE (i.e. -0.759 V vs SHE), revealing an overpotential of only 72 mV when the thermodynamic potential for CO₂ reduction to formate was considered as -0.687 V vs. SHE at pH 8.3 (Equation 1-6 and Table 1-1).

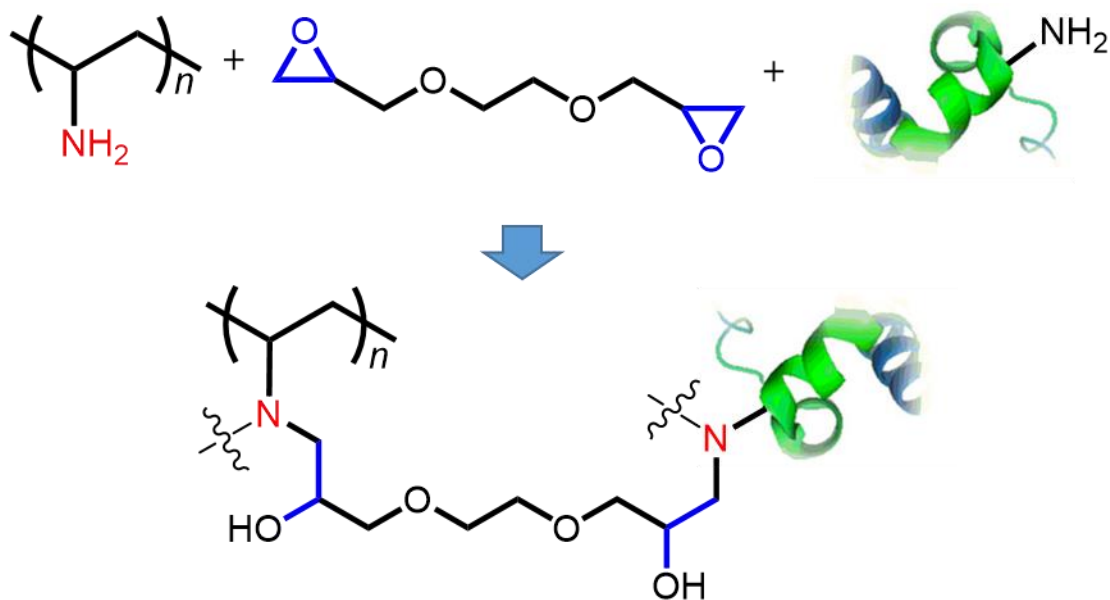


Figure 6-3. Schematic of the crosslink reaction among PVA, EDGDE and nitrogenase protein.

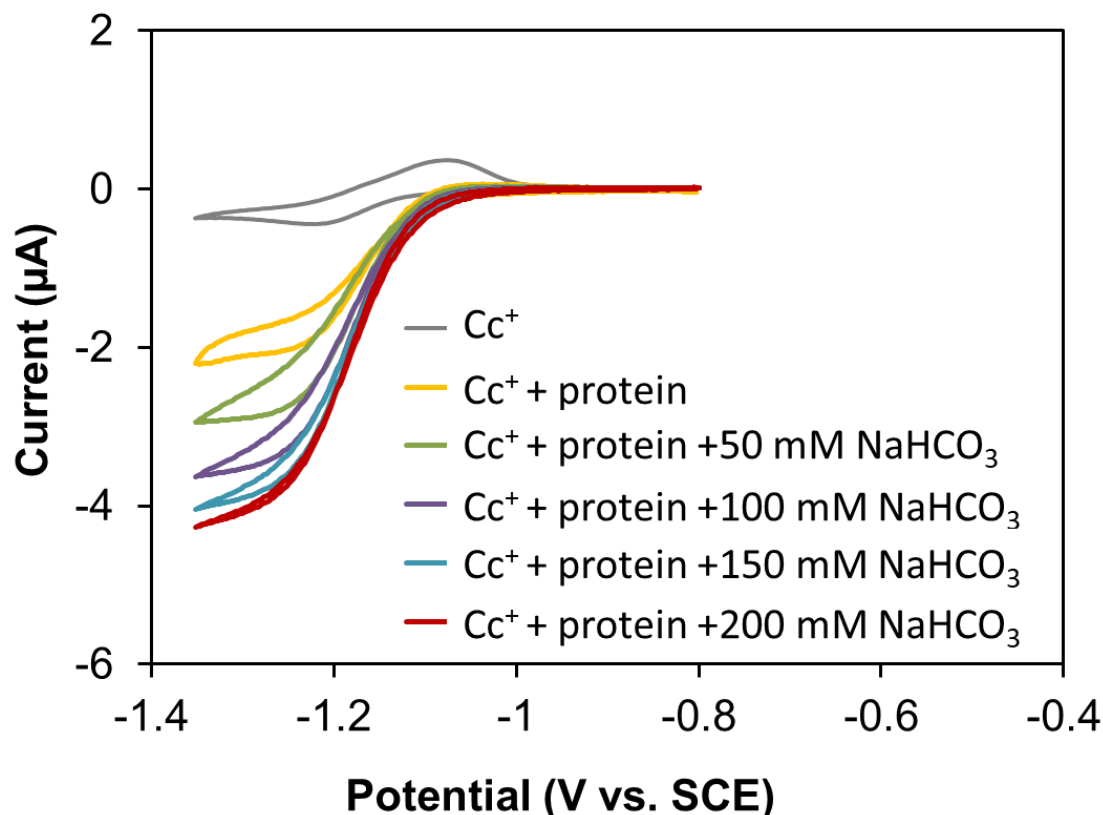


Figure 6-4. Cyclic voltammetry evaluation of the catalytic performance of Cc^+ mediated FeFe-protein bio-electrode. The gray trace is the CV of Cc^+ on bare glassy carbon electrode. Others CVs were all obtained based on the same FeFe-protein immobilized electrode with the increased $NaHCO_3$ concentration. Conditions: working electrode, MoFe protein modified glassy carbon electrode; reference electrode, saturated calomel electrode (SCE); counter electrode, Platinum wire; supporting electrolyte, 50 mM HEPES buffer (pH=7.4); Cc^+ concentration, 0.4 mM; scan rate, 5 mV/s.

However, the biofilm formed on the electrode under these conditions is unstable at times. With continuous CV scans for cycles, the film could drop off from the GC surface. In order to obtain a more stable adhesion of biofilm on the electrode, pyrene was added. Pyrene can form strong π - π interaction with glassy carbon and with the polymer matrix (e.g., the carbon chain backbone from PVA) and the protein, thus facilitating binding of the polymer immobilized protein to the electrode.⁴⁹ The CV of FeFe-protein

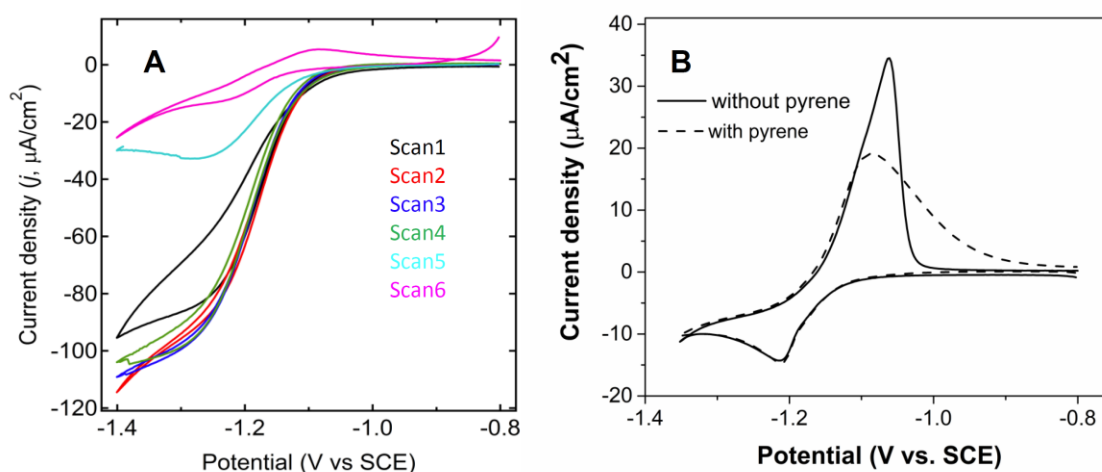
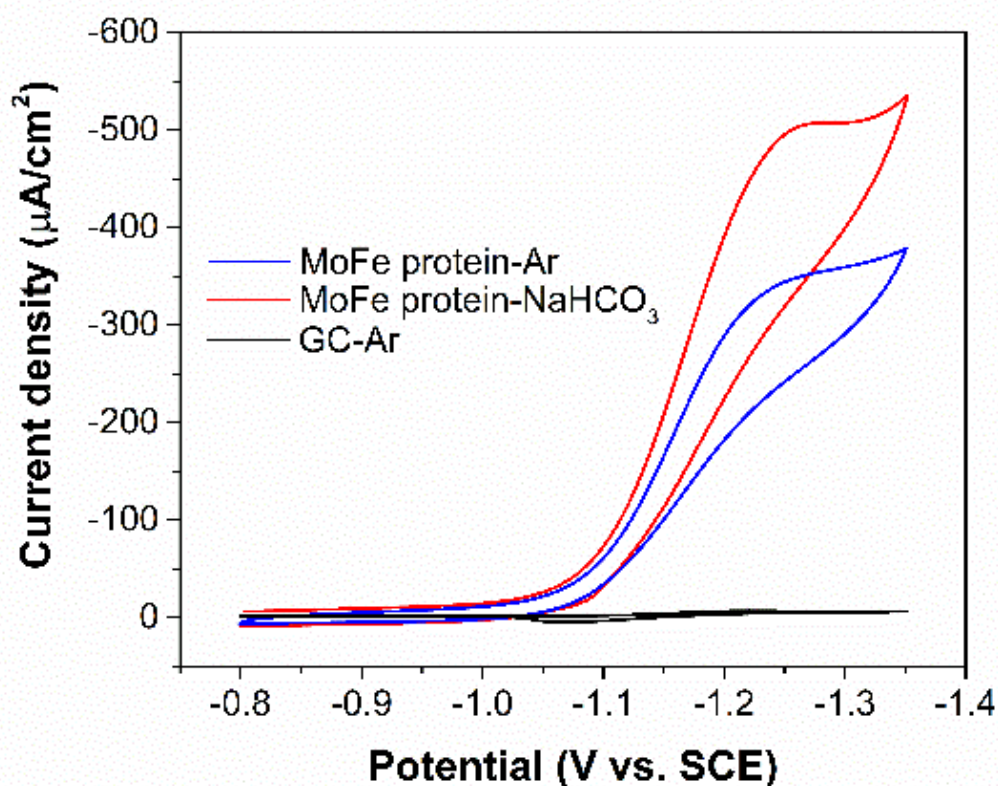


Figure 6-5. A. Continuously CV scans of pyrene modified FeFe electrode. (The 4th, 5th, 6th curves are almost overlapped.) B. Cyclic voltammetry of cobaltocenium on bare glassy carbon electrode (solid line) and pyrene modified electrode.

immobilized with the addition of pyrene in the presence of cobaltocenium (0.4 mM) showed excellent current and stability. Pyrene addition did not change the Cc^+/Cc redox potential in the CV compared to a bare glassy carbon electrode (Figure 6-5B) although the oxidation peak became boarder and current density became lower in the presence of pyrene. This phenomenon is likely due to the strong π - π interactions between pyrene and the glassy carbon electrode, and between pyrene and Cc^+/Cc that might affect the charge and mass transfer processes.

Then, the bio-electrodes were prepared using either MoFe-protein or FeFe-protein with the addition of pyrene. These bioelectrodes were used to examine catalytic activity for proton and CO_2 reduction. As shown in Figure 6-6, the CV of cobaltocenium without protein only showed a reductive current density of $5.5 \mu\text{A}/\text{cm}^2$. Reductive current densities were greatly enhanced by the addition of either MoFe- or FeFe- protein in the absence of CO_2 . The loss of the oxidative peaks indicated the consumption of

cobaltocene by proteins and the catalytic reduction of protons to make H_2 . The MoFe protein showed much higher catalytic current up to $350 \mu A/cm^2$ (Figure 6-6A) for proton reduction than FeFe protein (only $150 \mu A/cm^2$) (Figure 6-6B). After 200 mM sodium bicarbonate was added, the catalytic current increased and anodically shifted for both proteins. MoFe protein displayed a higher catalytic current density than FeFe protein for overall catalysis (both proton and CO_2 reduction). However, the current density increased only 45.7% for MoFe protein, whereas 146.7% for FeFe protein. The greater increase in current for the FeFe protein was consistent with more active CO_2 reduction compared to the MoFe protein.



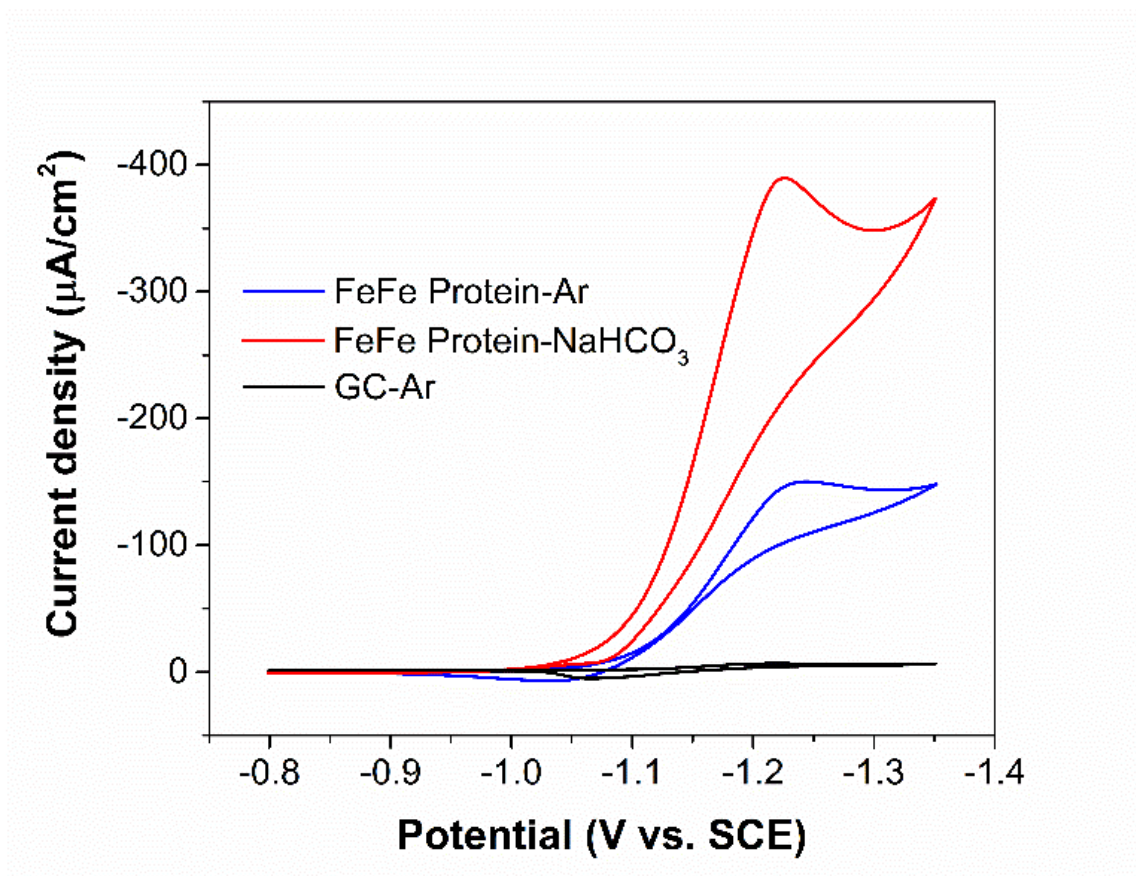


Figure 6-6. Cyclic voltammetry of cobaltocenium mediated electrocatalysis by MoFe protein (top) and FeFe protein (bottom) in the absence (blue traces) and presence of sodium bicarbonate as CO_2 source (red traces). CV traces for a bare glassy carbon electrode under Ar (GC-Ar, black traces) are shown as a control.

To validate that both proteins were actually reducing CO_2 , bulk electrolysis experiments were conducted at a potential of -1.26 V vs. SCE in 10 mL sealed vials. At this potential, the initial catalytic current densities were 502 and 367 $\mu\text{A}/\text{cm}^2$ for MoFe- and FeFe-protein bioelectrodes, respectively. Over time, the current density decreased and stabilized at 170 $\mu\text{A}/\text{cm}^2$ for the MoFe protein electrode and 130 $\mu\text{A}/\text{cm}^2$ for the FeFe protein electrode (Figure 6-7). The change in current over the first 1000 s could be caused by a number of different factors given the complexity of this system, including diffusion of substrates (protons and CO_2) and the electron mediator (cobaltocenium)

through the polymer matrix, and conversion of sodium bicarbonate to CO_2 under the pH condition used in the experiments. At the steady state, the current density of the MoFe electrode was 31% higher than the FeFe protein, consistent with currents observed in the CVs. By integrating the current versus time curves in the electrolysis experiments, the charges of the reactions were found to be 0.07545 C for the MoFe protein electrode and 0.06262 C for the FeFe protein electrode, from which the overall amount of the two-electron reduction products, H_2 plus formate, was calculated by $n = C/(n_e \cdot F)$ as 391.0 nmol for MoFe-protein bioelectrode and 324.5 nmol for the FeFe-protein bioelectrode, where n is the total amount of products, C is the overall charge, and n_e is the number of electrons assigned to either CO_2 or proton reduction reactions (both assigned as 2). F is the Faraday constant.

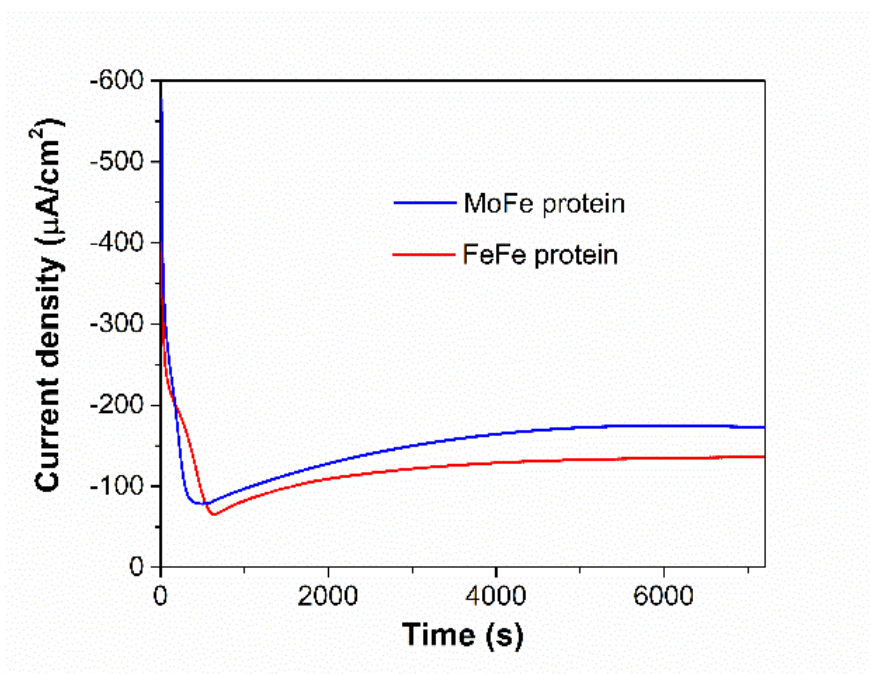


Figure 6-7. Bulk bioelectrosynthetic reduction of 200 mM NaHCO_3 in stirred 50 mM HEPES buffer solution (with 200 mM NaCl and 0.4 mM cobaltocenium) by MoFe (blue trace) and FeFe protein (red trace) bioelectrodes.

At the end of the electrolysis experiment (120 min), 200 μL was removed from the gas phase and analyzed by gas chromatography to quantify the H_2 produced. H_2 was found to be 409.8 nmol for the MoFe protein electrode and 171.0 nmol for the FeFe protein electrode. For each sample, the liquid phase was collected and dried by rotary evaporation under vacuum at 40° C. The remaining white solid was dissolved in D_2O and analyzed by ^1H -NMR (Figures 6-9 and 6-10) with a T_1 relaxation time of 40 s to allow the full relaxation of all forms of protons. Formate was confirmed by the singlet peak at a chemical shift around 8.38 ppm. Cobaltocenium (0.4 mmol) also displayed a singlet peak with a chemical shift of 5.7. By integrating the NMR peaks, the formate was quantified to

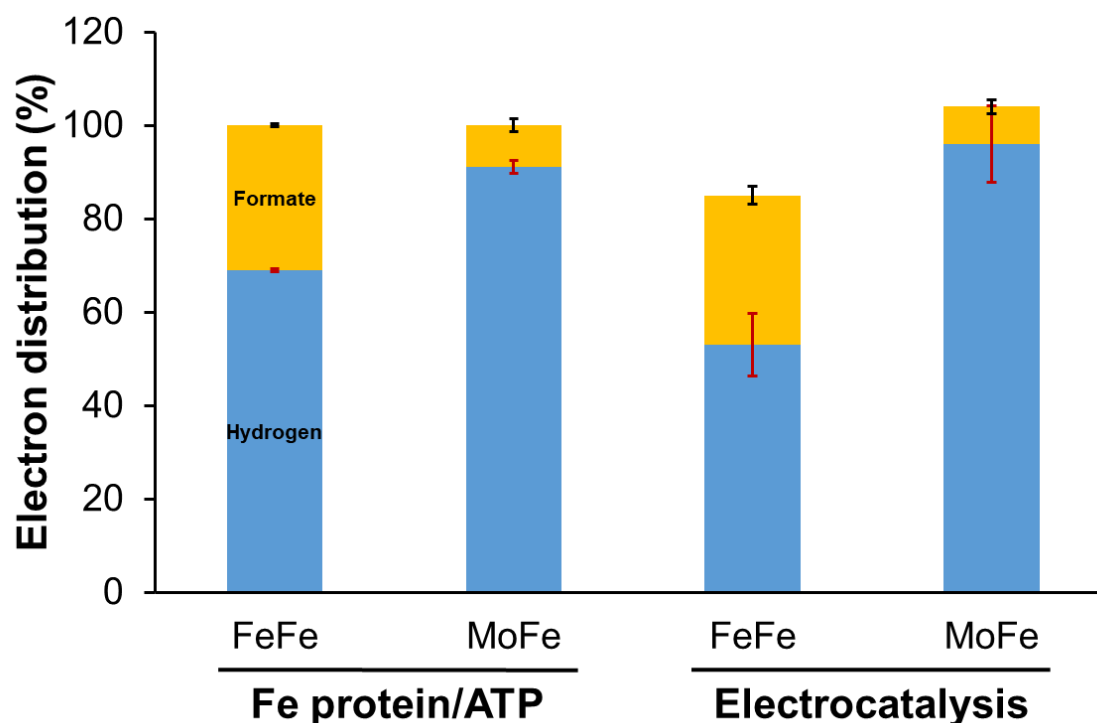


Figure 6-8. Percentage of electrons going to different products when driven by Fe protein/ATP (left) or electrocatalysis (right) for the MoFe protein (MoFe) or FeFe protein (FeFe). H_2 is shown in blue, and formate is shown in yellow.

be 35.5 nmol and 101.6 nmol for the MoFe protein and the FeFe-protein electrocatalysis experiments, respectively. From these values, the Faradaic efficiencies for H₂ and formate production by electrocatalysis were determined. The electron distribution to different products for the MoFe- and FeFe-protein when driven by the Fe protein/ATP or by the electrode are shown in Figure 6-8. The FeFe protein showed the highest distribution of electrons to CO₂ reduction to make formate under both Fe protein/ATP and electrocatalysis, with approximately $31 \pm 0.3 \%$ and $32 \pm 1.8 \%$, respectively. The MoFe protein showed lower electron flux distributed to CO₂ reduction for both Fe protein/ATP and electrocatalysis. The electrocatalytic reactions for MoFe protein showed $8.0 \pm 1.6 \%$ of electron flux going to formate formation with the rest of electron flux going to H₂, whereas the Fe protein/ATP driven reactions showed $9.0 \pm 1.4 \%$ of electrons used for formate formation. When both the FeFe protein and the MoFe protein were driven by Fe protein and ATP, a trace of CH₄ product was also observed during CO₂ reduction. However, this product was not observed during electrocatalysis. The similarity between the distribution of electrons to different products for the two proteins when driven by Fe protein or the electrode provides evidence that in both catalytic situations, the active agent is the intact protein.

6-5. Conclusion

MoFe protein and FeFe protein can be used for the electrocatalytic reduction of protons to yield H₂ and reduction of CO₂ to yield formate, with all of the energy coming from the electrode. In the future, it should be possible to connect the electrode to a photovoltaic cell, thus allowing light-driven CO₂ reduction coupled to water oxidation. In both Fe protein/ATP and electrocatalytic reactions, the FeFe-protein shows a significantly higher

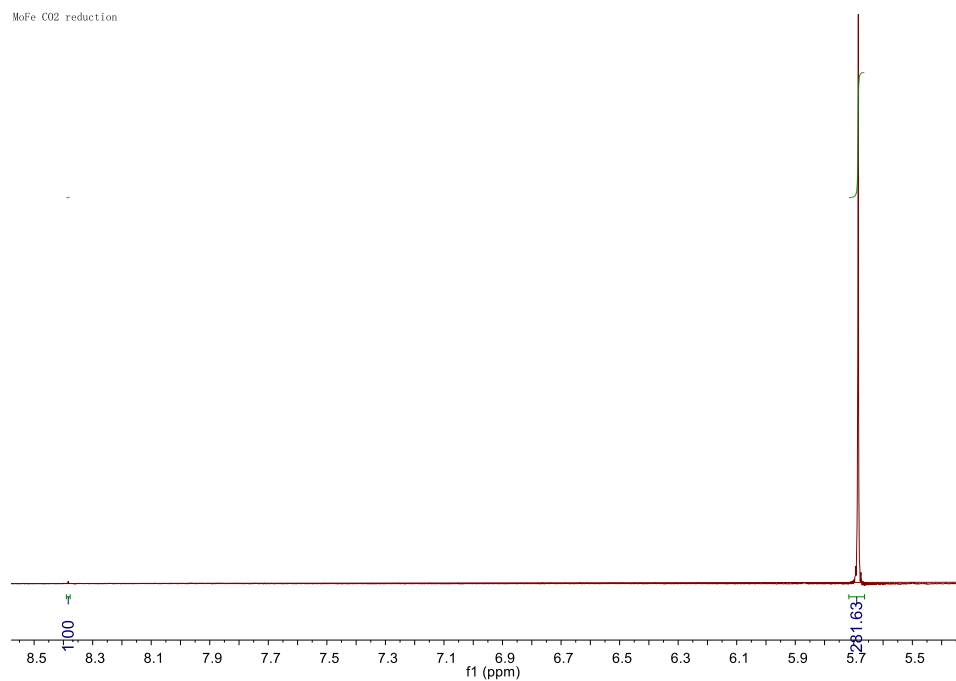


Figure 6-9. ¹H-NMR of the product of bioelectrocatalytic reduction of CO₂ by MoFe electrode

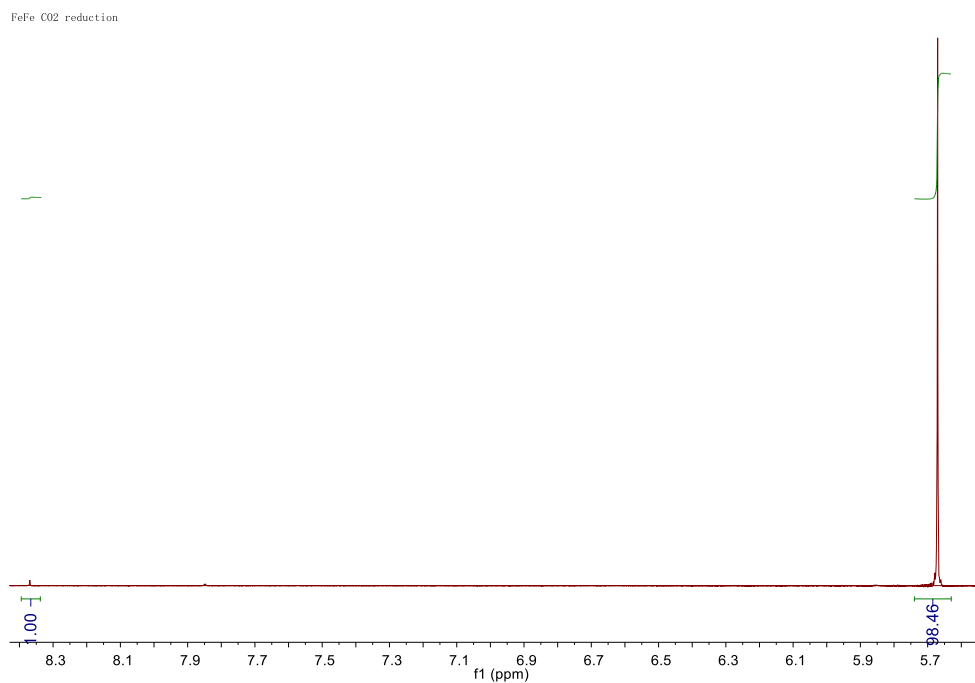


Figure 6-10. ¹H-NMR of the product of bioelectrocatalytic reduction of CO₂ by FeFe electrode.

distribution of electrons to CO₂ reduction compared to the MoFe protein. Further, the similarity in electron distribution between the Fe protein driven and electrode driven processes support the intact MoFe-protein and FeFe-protein as the catalyst. The present studies lay the foundation for work to investigate the mechanism of CO₂ reduction and the factors controlling electron distribution to different substrates in both of these nitrogenase proteins.

6-6. References

- (1) V. Smil. Enriching the earth: Fritz Haber, Carl Bosch, and the transformation of world food production, MIT Press, Cambridge, Mass, **2001**.
- (2) B.K. Burgess.; D.J. Lowe. *Chem. Rev.* **1996**, 96, 2983.
- (3) R.R. Eady. *Chem. Rev.* **1996**, 96, 3013.
- (4) R.R. Eady, *Coord. Chem. Rev.* **2003**, 237, 23.
- (5) K. Schneider.; A. Müller. Iron-only nitrogenase: exceptional catalytic, structural and spectroscopic features, in: *Catalysts for Nitrogen Fixation*, Springer, **2004**.
- (6) Y. Hu.; C.C. Lee.; M.W. Ribbe. *Dalton Trans.* **2012**, 41, 1118–1127.
- (7) Y. Hu.; M.W. Ribbe. *Ann. Rev. Biochem.* **2016**, 85.
- (8) L.M. Rubio.; P.W. Ludden. *Annu. Rev. Microbiol.* **2008**, 62, 93.
- (9) B.M. Hoffman.; D. Lukoyanov.; Z.-Y. Yang.; D.R. Dean.; L.C. Seefeldt. *Chem. Rev.* **2014**, 114, 4041.
- (10) D. Sippel.; O. Einsle. *Nat. Chem. Biol.* **2017**, 13, 2428.
- (11) J.A. Rees.; R. Bjornsson.; J.K. Kowalska.; F.A. Lima.; J. Schlesier.; D. Sippel.; T. Weyhermüller.; O. Einsle.; J.A. Kovacs.; S. DeBeer. *Dalton Trans.* **2017**, 46, 2445.

- (12) T. Spatzal.; K.A. Perez.; J.B. Howard.; D.C. Rees. *ELife Sciences*. **2015**, 4, e11620.
- (13) D.C. Rees.; F.A. Tezcan.; C.A. Haynes.; M.Y. Walton.; S. Andrade.; O. Einsle.; J.B. Howard. *Phil. Trans. R. Soc. A*. **2005**, 363, 971.
- (14) F.A. Tezcan.; J.T. Kaiser.; J.B. Howard.; D.C. Rees. *J. Am. Chem. Soc.* **2014**, 137, 146.
- (15) O. Einsle, F.A. Tezcan, S.L.A. Andrade, B. Schmid, M. Yoshida, J.B. Howard, D.C. Rees, *Science*. **2002**, 297, 1696.
- (16) E. Krahn, B. Weiss, M. Kröckel, J. Groppe, G. Henkel, S. Cramer, A. Trautwein, K. Schneider, A. Müller, *J. Biol. Inorg. Chem.* **2002**, 7, 37.
- (17) R.N.F. Thorneley, D.J. Lowe, Kinetics and mechanism of the nitrogenase enzyme, in: T.G. Spiro (Ed.), *Molybdenum Enzymes*, Wiley-Interscience Publications, New York, **1985**.
- (18) Z.-Y. Yang, R. Ledbetter, S. Shaw, N. Pence, M. Tokmina-Lukaszewska, B. Eilers, Q. Guo, N. Pokhrel, V.L. Cash, D.R. Dean, E. Antony, B. Bothner, J.W. Peters, L.C. Seefeldt, , *Biochemistry*. **2016**, 55, 3625.
- (19) R.V. Hageman, R.H. Burris, *Proc. Natl. Acad. Sci. U.S.A.* **1978**, 75, 2699.
- (20) S. Duval, K. Danyal, S. Shaw, A.K. Lytle, D.R. Dean, B.M. Hoffman, E. Antony, L.C. Seefeldt, *Proc. Natl. Acad. Sci. U. S. A.* **2013**, 110, 16414.
- (21) K.A. Brown, D.F. Harris, M.B. Wilker, A. Rasmussen, N. Khadka, H. Hamby, S. Keable, G. Dukovic, J.W. Peters, L.C. Seefeldt, P.W. King, *Science*. **2016**, 352, 448.
- (22) L.C. Seefeldt, B.M. Hoffman, D.R. Dean, Electron transfer in nitrogenase catalysis, *Curr. Opin. Chem. Biol.* **2012**, 16, 19.

- (23) B.M. Hoffman, D. Lukoyanov, D.R. Dean, L.C. Seefeldt, *Acc. Chem. Res.* **2013**, *46*, 587.
- (24) B.J. Hales. *Adv. Inorg. Biochem.* **1990**, *8*, 165.
- (25) D. Lukoyanov, N. Khadka, Z.-Y. Yang, D.R. Dean, L.C. Seefeldt, B.M. Hoffman. *J. Am. Chem. Soc.* **2016**, *138*, 1320.
- (26) D. Lukoyanov, N. Khadka, Z.-Y. Yang, D.R. Dean, L.C. Seefeldt, B.M. Hoffman. *J. Am. Chem. Soc.* **2016**, *138*, 10674.
- (27) D. Lukoyanov, Z.-Y. Yang, N. Khadka, D.R. Dean, L.C. Seefeldt, B.M. Hoffman, *J. Am. Chem. Soc.* **2015**, *137*, 3610.
- (28) Z.-Y. Yang, N. Khadka, D. Lukoyanov, B.M. Hoffman, D.R. Dean, L.C. Seefeldt. *Proc. Natl. Acad. Sci. U.S.A.* **2013**, *110*, 16327.
- (29) D. Lukoyanov, N. Khadka, D.R. Dean, S. Raugei, L.C. Seefeldt, B.M. Hoffman. *Inorg. Chem.* **2017**, *56*, 2233.
- (30) L.C. Seefeldt, Z.-Y. Yang, S. Duval, D.R. Dean. *Biochim. Biophys. Acta.* **2013**, *1827*, 1102.
- (31) L.C. Seefeldt, M.E. Rasche, S.A. Ensign. *Biochemistry.* **1995**, *34*, 5382.
- (32) Z.-Y. Yang, V.R. Moure, D.R. Dean, L.C. Seefeldt. *Proc. Natl. Acad. Sci. U.S.A.* **2012**, *109* 19644.
- (33) N. Khadka, D.R. Dean, D. Smith, B.M. Hoffman, S. Raugei, L.C. Seefeldt. *Inorg. Chem.* **2016**, *55*, 8321.
- (34) K.R. Fixen, Y. Zheng, D.F. Harris, S. Shaw, Z.-Y. Yang, D.R. Dean, L.C. Seefeldt, C.S. Harwood. *Proc. Natl. Acad. Sci. U. S. A.* **2016**, *113*, 10163.
- (35) N.S. Sickerman, Y. Hu, M.W. Ribbe. *Chem. Asian J.* **2017**, *12*, 1985.

- (36) J.G. Rebelein, Y. Hu, M.W. Ribbe, *Angew. Chem. Int. Ed.* **2014**, 53, 11543.
- (37) A. Taheri, L.A. Berben, *Chem. Commun.* **2016**, 52, 1768.
- (38) I. Ganesh. *Renew. Sustain. Energy Rev.* **2016**, 59, 1269.
- (39) N.V.D. Long, J. Lee, K.-K. Koo, P. Luis, M. Lee. *Energies.* **2017**, 10, 473.
- (40) D.J. Darensbourg. *Inorg. Chem.* **2010**, 49, 10765.
- (41) A.M. Appel, J.E. Bercaw, A.B. Bocarsly, H. Dobbek, D.L. DuBois, M. Dupuis, J.G. Ferry, E. Fujita, R. Hille, P.J.A. Kenis, C.A. Kerfeld, R.H. Morris, C.H.F. Peden, A.R. Portis, S.W. Ragsdale, T.B. Rauchfuss, J.N.H. Reek, L.C. Seefeldt, R.K. Thauer, G.L. Waldrop, , *Chem. Rev.* **2013**, 113, 6621.
- (42) Y. Zheng, D.F. Harris, Z. Yu, Y. Fu, S. Poudel, R.N. Ledbetter, K.R. Fixen, Z.-Y. Yang, E.S. Boyd, M.E. Lidstrom, L.C. Seefeldt, C.S. Harwood. *Nat. Microbiol.* **2018**, 3, 281.
- (43) R.D. Milton, S. Abdellaoui, N. Khadka, D.R. Dean, D. Leech, L.C. Seefeldt, S.D. Minteer. *Energy Environ. Sci.* **2016**, 9, 2550.
- (44) N. Khadka, R.D. Milton, S. Shaw, D. Lukoyanov, D.R. Dean, S.D. Minteer, S. Raugei, B.M. Hoffman, L.C. Seefeldt. *J. Am. Chem. Soc.* **2017**, 139, 13518.
- (45) J. Christiansen, P.J. Goodwin, W.N. Lanzilotta, L.C. Seefeldt, D.R. Dean. **1998**, 37, 12611.
- (46) D.F. Harris, D. Lukoyanov, S. Shaw, N. Khadka, P. Compton, M. Tokmina-Lukaszewska, B. Bothner, N. Kelleher, D.R. Dean, B.M. Hoffman, L.C. Seefeldt. *Biochemistry*, **2018**, 57, 701.
- (47) R. Sleat, R.A. Mah. *Appl. Environ. Microbiol.* **1984**, 47, 884.
- (48) Y. Wang, S. Mendoza, A.E. Kaifer. *Inorg. Chem.* **1998**, 37, 317.

- (49) R.D. Milton, T. Wang, K.L. Knoche, S.D. Minter. *Langmuir*. **2016**, 32, 2291.

CHAPTER VII

EVALUATING THE HETEROGENEOUS ELECTROCATALYTIC REDUCTION OF
NITROGEN TO AMMONIA BY TETRAGONAL MOLYBDENUM NITRIDE[§]**7-1. Abstract**

Electrocatalytic nitrogen reduction reaction (ENRR) has been becoming a hot topic toward energy efficient and environmentally benign approach for ammonia synthesis. Efficient and stable catalysts are indubitably the central challenge. Molybdenum nitride (Mo_2N) was considered as an efficient catalyst for ENRR from both computational and experimental evaluation. However, these studies are lack of either consideration for the chemical stability or more reliable control experiments. Therefore, the activity of Mo_2N toward N_2 reduction is still not clear. Herein, we synthesized tetragonal Mo_2N (or $\gamma\text{-Mo}_2\text{N}$) by a “glass-urea” route and conducted a careful electrochemical test on it for NRR. Instead of catalyzing the electrochemical reduction of N_2 , it was found that tetragonal Mo_2N underwent decomposition and resulted in the generation of ammonia, which was proved by $^{15}\text{N}_2$ isotope labeling experiments. In addition, we observed that the Mo_2N chemical decomposition took place most quickly in alkaline conditions, followed by acidic and neutral conditions. The present results call urgent attention to carefully evaluate the catalytic nature of nitrogen reduction reaction (NRR) by nitrogen-containing materials.

7-2. Introduction

[§] Adapted with permission from [Hu, Bo.; Hu. M.; Seefeldt L.; Liu, T. L. *ACS Energy Letters*, **2019**, 4, 1053]. Copyright 2019. ACS Publications. Reproduced by permission of ACS Publications, <https://pubs.acs.org/doi/10.1021/acsenergylett.9b00648>.

The century-old Haber-Bosch process remains to be the only industrial process to achieve large scale ammonia production more than 150 million tons per year.¹ Despite its wide application, the Haber-Bosch process is massively energy consuming (ca. 2% of the world's energy supply), heavily fossil fuel dependent (3% - 5% of the world's natural gas production), and greenhouse gas emitting (more than 400 million tons).^{2,3} Above all, under the optimal operating temperature of the Haber-Bosch process, ammonia starts to decompose, which will affect the overall N₂ conversion efficiency. Therefore, milder, more energy efficient, and CO₂-free alternative methods are of great interest for both scientific research and industrial applications.^{2,3} Electrochemical synthesis of ammonia from nitrogen (N₂) in the presence of catalysts represents a highly attractive approach. Electrochemical devices for the nitrogen reduction reaction (NRR) could be easily integrated into renewable energy systems, thus obviates the utilization of fossil fuel and the emission of CO₂.² Due to these potential benefits, electrocatalytic N₂ fixation has been under intensive exploration over last few years and has become a hot topic in catalysis. A number of heterogeneous electrocatalysts have been reported with various claimed performances for NRR, including noble metals,⁴⁻⁶ metal oxides,⁷ metal sulfides,⁸ metal nitrides,^{9,10} and metal-free catalysts^{11,12}. Homogeneous electrocatalytic NNR was also recently demonstrated.¹³ Metal nitrides have been studied both theoretically and experimentally indicating their potential capability of electrocatalytic N₂ reduction.^{9,10,14} However, the nitrogen contained nature and chemical stability problem of the nitride materials could bring in ambiguous results.¹⁵ Herein, we carefully examined the catalytic ability of tetragonal Mo₂N for NRR. It is revealed that Mo₂N could undergo fast chemical decomposition in aqueous electrolytes and showed no catalytic activity for NRR.

7-3. Materials and methods

Materials

MoCl_5 (99.9 %) was purchased from Strem Chemicals. Urea (99 %) was purchased from TCI Chemicals. Ethanol (200 proof) was received from Pharmco Chemicals. 5 % Nafion solution was purchased from Sigma Aldrich. Titanium foil (99 %) was purchased from Giant Metals. $^{15}\text{N}_2$ was purchased from Cambridge Isotopes. The doubly deionized water was obtained from a MilliporeSigma Milli-DI Water Purification System Nafion™ 212 membranes were purchased from FuelCellStore, TX. The Nafion membranes were boiled in 1 M H_2SO_4 solution for 2 hours, 30 % H_2O_2 solution for 2 hours, and then rinsed by DI water. Titanium foil was polished by 400 grit sandpaper before use.

Catalyst synthesis

Mo_2N was synthesized by a “urea glass” method as reported. In an ice bath, 5 mL cold ethanol was added into 2.05 g MoCl_5 dropwise. After that, 0.45 g Urea was added. When the urea was totally dissolved, the formed dark brown solution was subjected to a heat treatment in a ceramic crucible in nitrogen atmosphere at 800 °C for 3 hours. The product was obtained as a silvery-black powder.

Material characterization

XRD data were collected on a Rigaku X-ray diffractometer equipped with $\text{Cu K}\alpha$ radiation. SEM measurements were performed on an FEI Quanta FEG 650 field-emission scanning electron microscope with a maximum electron energy of 30 KeV. NMR experiments were conducted on a Bruker Avance III HD Ascend-500 spectrometer

(proton at 500 MHz). UV-vis spectra were collected using an Ocean Optical UV-vis spectrometer.

Electrode preparation

A slurry was prepared by mixing 1 mg Mo₂N powder, 1 mL ethanol, and 20 μ L Nafion solution followed by sonicating for 2 hours to obtain a homogeneous suspension. Ti electrodes were sonicated in ethanol for 30 min followed by acetone for another 30 min and then dried in air. The prepared slurry was dropped onto a Ti electrode (1*1cm²) and dried for 3 hours in the air before use.

Electrochemical measurements

All electrochemical measurements were conducted on a Gamry 5000E potentiostat with a three-electrodes system, where Mo₂N coated Ti electrode, Ag/AgCl electrode, and glassy carbon rod were used as working electrode, reference electrode, and counter electrode, respectively. The potential was converted to reversible hydrogen electrode (RHE) by the equation: $E_{(vs. RHE)} = E_{(vs. NHE)} + 0.059pH$. Electrolysis experiments were conducted with an H-type cell (6 mL electrolyte in each side) separated by a piece of Nafion 212 membrane. During the catalysis, N₂ gas was kept feeding into the electrolyte. For ¹⁵N₂ controlled experiments, the H-type cell was first well sealed and degassed under vacuum. 20 mL pre-purified ¹⁵N₂ gas was slowly injected into the cell every 15 min (80 mL in total).

¹⁵N₂ purification

The ¹⁵N₂ gas was pre-purified as follows. 20 mL H₂SO₄ aqueous solution (50 mM) was added into a 200 mL glass vessel (well-sealed by a pharmaceutical septum sealed) with a stir bar. Then vacuum was applied to the solution by a shrink line for 2

hours to remove the dissolved gas. Thereafter, 200 mL $^{15}\text{N}_2$ gas was added into the well-sealed vessel by slowly bubbling the gas into the solution. The solution was stirred overnight to absorb the impurities from the $^{15}\text{N}_2$ gas.

NH₃ assay

The amount of produced ammonia was determined by the indophenol-blue method as reported.¹⁶ Specifically, a 1 ml aliquot of the solution was removed from the H-type cell after electrolysis. To this solution was added 1 ml of a 1M NaOH solution containing 5% salicylic acid and 5% sodium citrate (by weight), followed by addition of 0.5 ml of 50 mM NaClO aqueous solution and 50 μL of an aqueous solution of 1% (by weight) $\text{Na}[\text{Fe}(\text{NO})(\text{CN})_5]$ (sodium nitroferricyanide). After 2 hours, the absorption spectrum was measured. A standard curve was prepared by using NH_4Cl solution with a concentration of 0.5, 1, 2, 3, 4, 5 $\mu\text{g/mL}$ in 0.1 M $\text{HCl}_{(\text{aq})}$ (see figure 7-4). The left solution was concentrated by a rotary evaporator at 40 $^\circ\text{C}$ to 0.5 mL. Then the solution was added into an NMR tube for ^1H NMR characterization with a sealed capillary tube filled with D_2O .

Faradaic efficiency (FE) calculation

FE was calculated by the following equation:

$$FE = \frac{3 * C_{\text{NH}_3} * V}{\left(\frac{Q}{F}\right)}$$

Where C_{NH_3} is the concentration of NH_3 in the electrolyte, V is the total volume (12 mL), Q is the charge consumed during electrolysis, and F is the faradaic constant.

7-4. Results and discussion

Characterization of γ -Mo₂N

Tetragonal Mo₂N was synthesized *via* the well-known “urea glass” route according to the literature.¹⁷ In Figure 7-1, X-ray diffraction (XRD) analysis revealed a pure tetragonal phase Mo₂N with a good crystallinity which was in line with the standard PDF card. The small impurity peaks around 54 degrees corresponded to carbon which might come from the pyrolysis of the carbon contained material under nitrogen. The morphology of the material was studied by scan electron microscope (SEM) displaying partially aggregated nanoparticles (30-50 nm) with a homogeneous distribution of Mo and N elements (Figure 7-2)

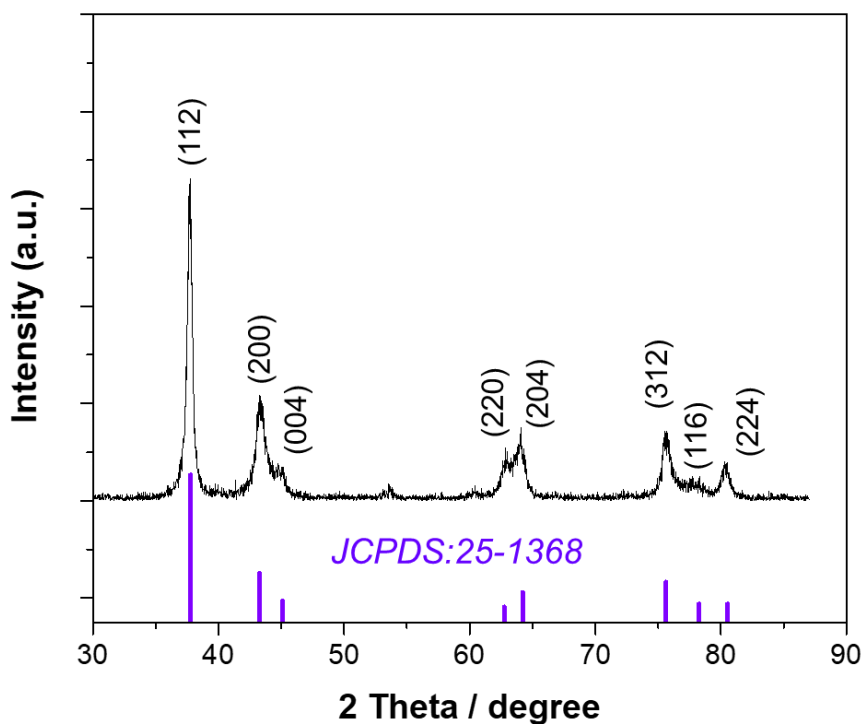


Figure 7-1. XRD pattern of the synthesized Mo₂N. The blue pattern is the standard PDF card for γ -Mo₂N.

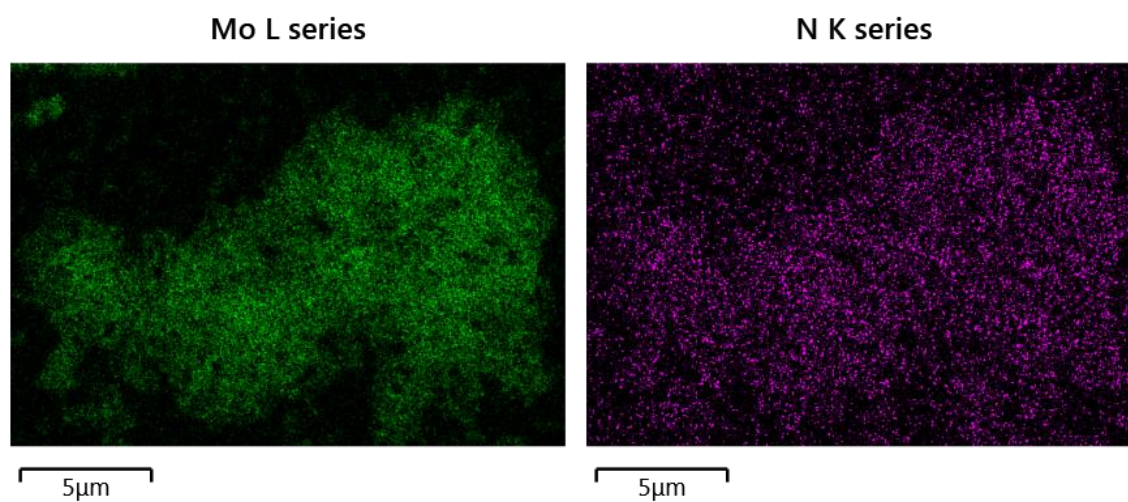
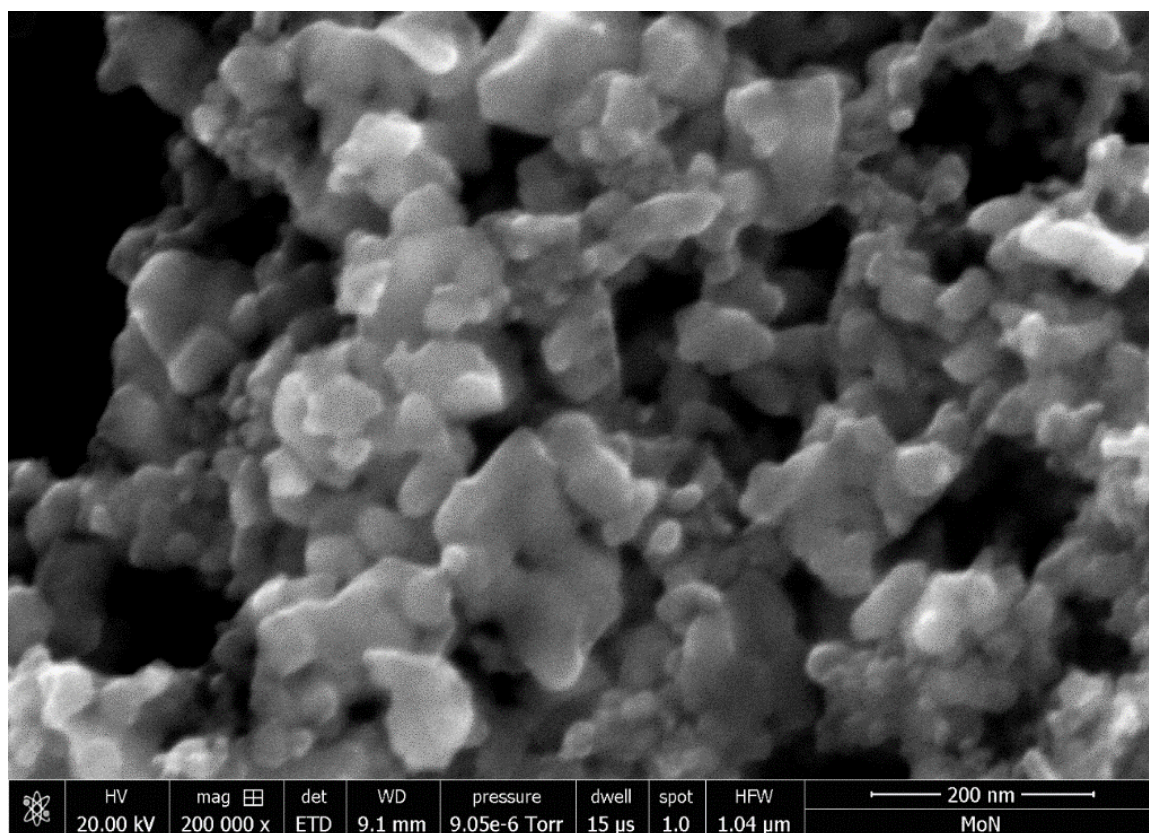


Figure 7-2. Top: SEM image elemental mapping of the synthesized γ -Mo₂N. Bottom: EDS scanning of Mo and N elements for the selected area, showing homogeneous distribution.

Electrochemical chemical studies of γ -Mo₂N the for NRR

The synthesized Mo₂N was evaluated for NRR at ambient conditions. Although carbon paper is the most common substrate for catalysts loading NRR studies, titanium was selected as the substrate in this study due to its good stability, hydrogen evolution reaction (HER) and nitrogen reduction reaction (NRR) inertness. To be in accordance with other reported metal nitride catalyzed NRR experiments, our electrochemical studies were conducted in 0.1 M HCl solution (pH = 1). Linear sweeping voltammograms (LSV) were

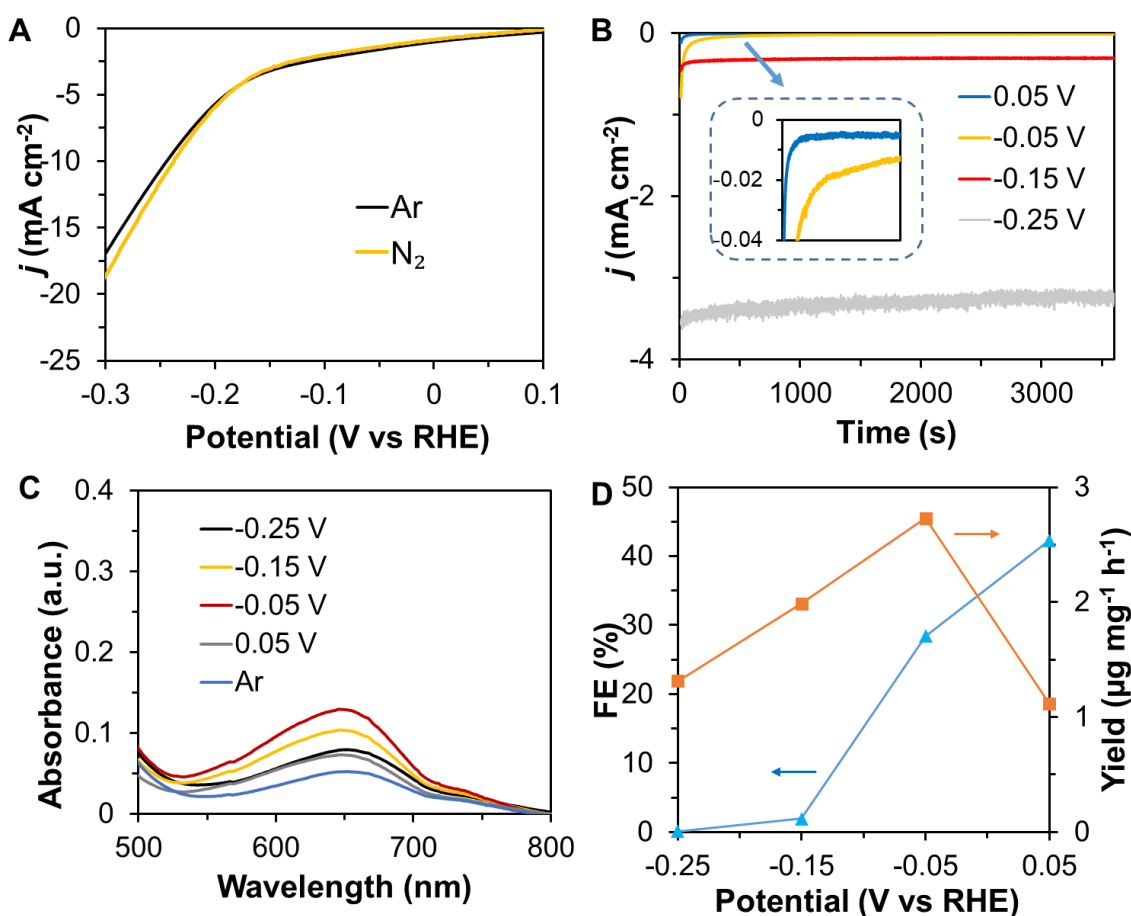


Figure 7-3. (A) LSV curves for the γ -Mo₂N@Ti electrode in N₂ and Ar saturated HCl supporting electrolyte (pH=1). Scan rate: 50 mV/s. (B) Chronoamperometric curves for the electrolysis at various controlled potentials with N₂ as the feeding gas. (C) UV-Vis tests (indophenol-blue assay) for ammonium after electrolysis at various controlled potential. (D) Faradaic efficiency and reaction rate at different potentials.

collected on a $\text{Mo}_2\text{N@Ti}$ electrode in both argon and nitrogen saturated electrolytes. As shown in Figure 7-3A, a slight current increase in the nitrogen saturated electrolyte indicated the possibility of catalytic N_2 reduction taking place at more negative potential less than - 0.22 V. When the catalyst was subjected to controlled potential electrolysis, the current density experienced dramatic change from less than $10 \mu\text{A cm}^{-2}$ at 0.05 V to 3.3 mA cm^{-2} at -0.25 V vs RHE, which was attributed to the more favorable HER. After bulk electrolysis for 1 hour at the potential from -0.25 V to 0.05 V vs RHE (Figure 7-3B), the amount of ammonia was detected by UV-vis spectroscopy using the Indophenol-blue assay. Figure 7-4 shows the standard curve for ammonia quantification. Assuming N_2 was electrocatalytically reduced to ammonia, the highest faradaic efficiency (FE) was obtained at - 0.05 V vs RHE up to 42.3% with a yield of $1.99 \mu\text{g mg}^{-1} \text{ h}^{-1}$. At 0.05 V, the reaction showed the highest yield of $2.73 \mu\text{g mg}^{-1} \text{ h}^{-1}$ with a good FE of 28.4 %. When the potential

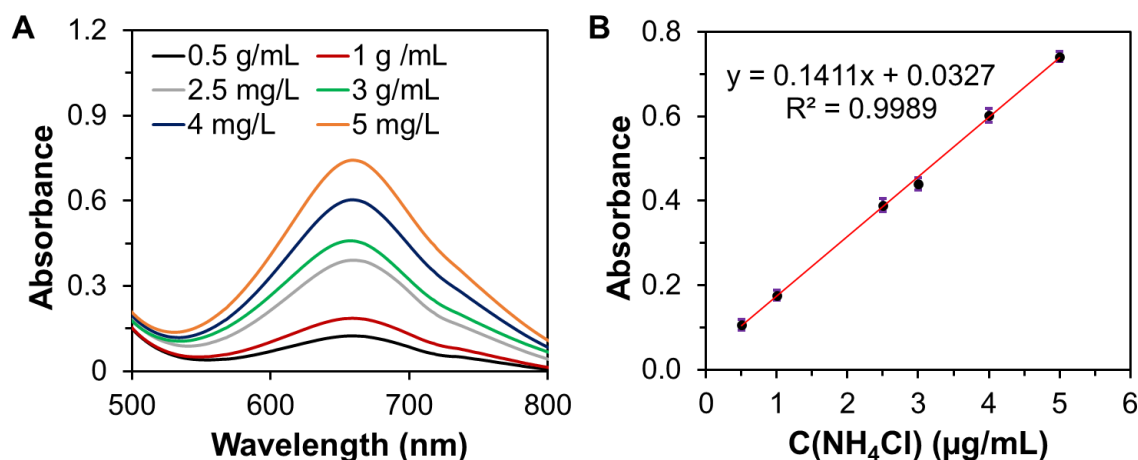


Figure 7-4. (A) UV-vis measurements of indophenol-blue standard samples with various concentrations of NH_4Cl . (B) Linear fitting for the absorbance versus NH_4Cl concentration. The final standard linear relationship was converted to concentration of ammonia as $y = 0.4431x + 0.0327$ ($R^2 = 0.9989$)

was applied to -0.15 V, faradaic efficiency dramatically dropped to 1.93 %. In all the experiments, no hydrazine product was detected.

$^{15}\text{N}_2$ isotope labeling experiments

The obtained results which appeared very exciting prompted us to conduct $^{15}\text{N}_2$ controlled experiments to confirm the catalytic nature of NRR. It is worth noting that a non-negligible amount of $^{15}\text{NH}_4^+$, $^{15}\text{NO}_2^-$, and other impurity exist in the commercialized $^{15}\text{N}_2$ gas.¹⁸ It is also noted fact that the reported $^{15}\text{N}_2$ controlled experiments seldom conducted pretreatment or showed $^{15}\text{NH}_4^+$ background, bringing in ambiguous results. Thus, before the test, the $^{15}\text{N}_2$ gas was treated by 50 mM sulfuric acid overnight to remove the impurities as much as possible. After bulk electrolysis under a $^{15}\text{N}_2$ atmosphere for 1

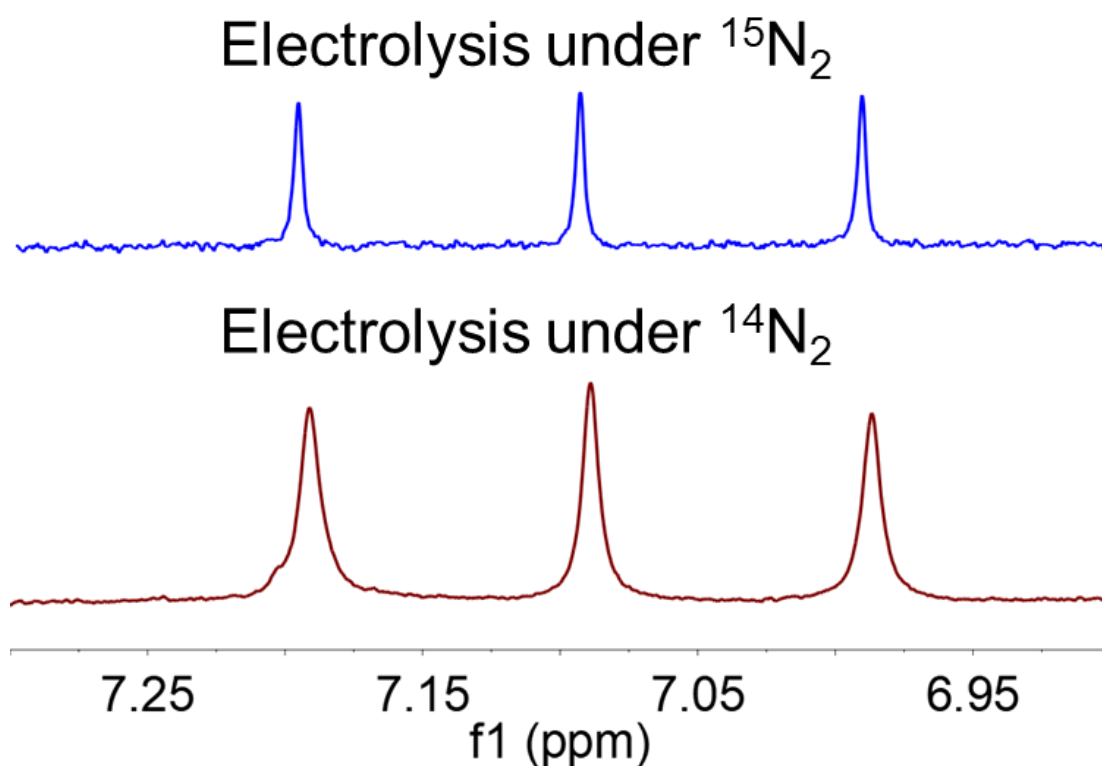


Figure 7-5. ^1H NMR spectra of ammonium in the sampled electrolytes after one hour's electrolysis in the presence of saturated $^{15}\text{N}_2$ and $^{14}\text{N}_2$, respectively

hour, ^1H -NMR experiments were carried on to verify the $^{15}\text{NH}_4^+$ formation. To our surprise, no $^{15}\text{NH}_4^+$ was detected (no doublet peaks) while a significant amount of $^{14}\text{NH}_4^+$ was observed (Figure 7-4). The finding suggested the ammonia formation could originate from a chemical decomposition process of Mo_2N other than a catalytic process.

In order to further elucidate the chemical decomposition of Mo_2N , the $\text{Mo}_2\text{N}@\text{Ti}$ electrodes were treated in 0.1 M HCl, 0.1 M NaOH, and 0.5 M NaCl solutions, respectively. After the electrodes were incubated for 1 hour, the detected ammonia for all conditions was just slightly less than the electrolysis at 0.05 V vs RHE (see Figure 7-5). We assume that

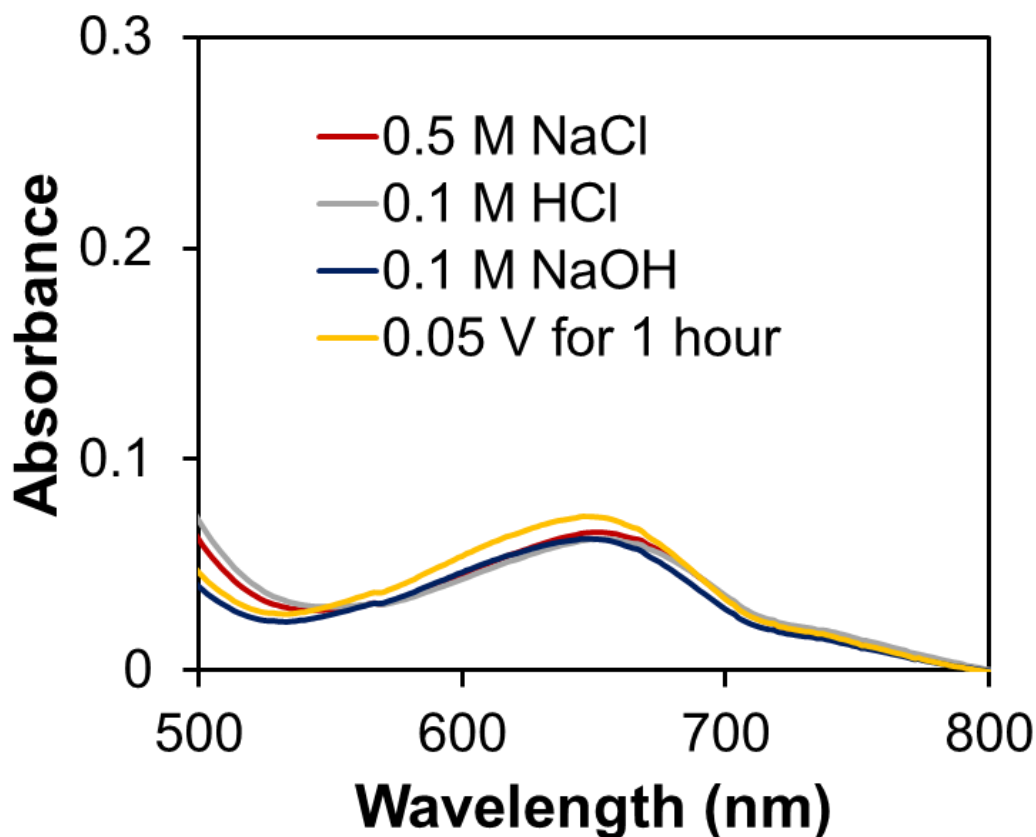


Figure 7-6. Indophenol-blue assay for ammonium after the electrodes were immersed in the different supporting electrolytes (labeled) for 1 hour.

the decomposition of Mo_2N could be accelerated under the electrochemical reduction condition. Moreover, it is found that Mo_2N displayed much poorer stability in alkaline conditions than in acidic and neutral conditions. As shown in Figure 7-6, after 96 hours' treatment, much more ammonia was detected in the NaOH solution than in the HCl and NaCl solutions. Mo_2N was even totally dissolved in NaOH solution after 1 week. Furthermore, -0.15 V vs. RHE was applied to the electrolysis with the same electrode continuously for 5 hours. The sample was taken out for UV-Vis tests after the first hour's

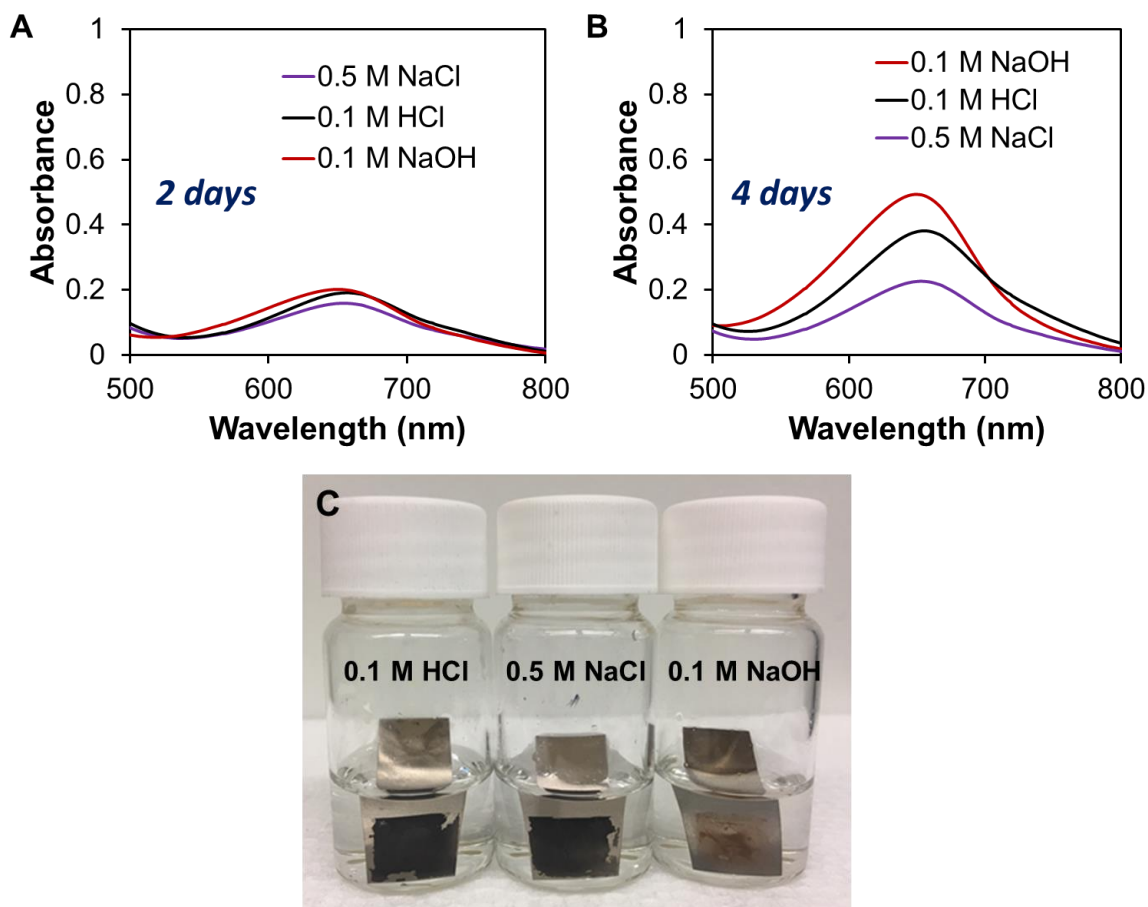


Figure 7-7. Ammonium tests after Mo_2N was treated for (A) 2 days and (B) 4 days. (C) Images of the samples treated by various electrolytes for 1 week. Note in (C): Mo_2N dissolved in 0.1M NaOH after 1 week.

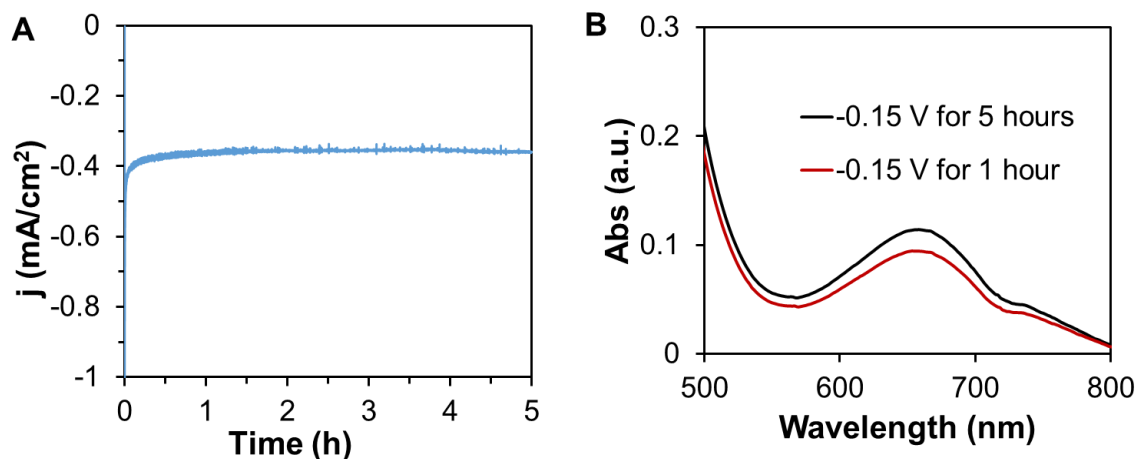


Figure 7-8. (A) The chronoamperometric curve for the electrolysis at -0.15 V vs. RHE with N_2 as the feeding gas. (B) UV-Vis tests for the product after 1 hour's and 5 hours' reaction.

bulk electrolysis and after 5 hours. As shown in Figure 7-7, compared with the first hour's reaction, 5 hours' electrolysis only showed a small increase of the amount of ammonia. The result also indicated the fast chemical decomposition of the active nitride compound on the surface of the electrode at the beginning of the electrolysis.

7-5. Conclusion

In summary, the failure of the $^{15}\text{N}_2$ isotope labeling experiment and fast chemical decomposition leads us to draw a conclusion that Mo_2N has no catalytic activity in terms of N_2 catalytic reduction. The present results raise an urgent alert to the application of other metal nitrides or even nitrogen contained materials for NRR. In addition to the decomposition of potential catalytic materials, we would like to highlight several other apparent pitfalls to avoid in claiming catalytic NRR. First, nitrogen contaminants in nitrogen gas, solvents, and other reactants need pretreatment to mitigate elusive results. Second, ^{15}N labeling experiments must be conducted to confirm the formation of ammonium from nitrogen. Third, turnover number (> 1) for a catalytic process needs to be

demonstrated, which requires carefully evaluate the loading of a catalyst and the yield of ammonium.

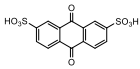
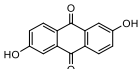
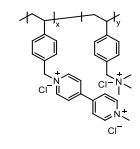
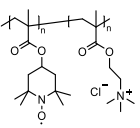
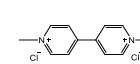
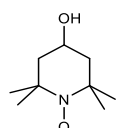
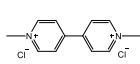
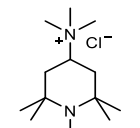
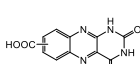
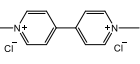

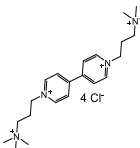
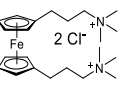
7-6. Reference

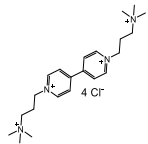
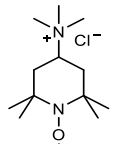
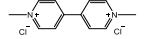
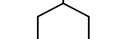
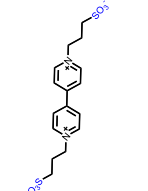
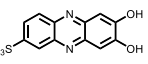
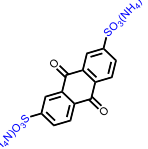
- (1) Nations., F. a. A. O. o. t. U. *World fertilizer trends and outlook to 2020*. **2017**.
- (2) Zhu, D.; Zhang, L.; Ruther, R. E.; Hamers, R. J. *Nat. Mater* **2013**, *12*, 836.
- (3) Suryanto, B. H. R.; Du, H.-L.; Wang, D.; Chen, J.; Simonov, A. N.; MacFarlane, D. *R. Nat. Catal.* **2019**.
- (4) Tao, H.; Choi, C.; Ding, L.-X.; Jiang, Z.; Han, Z.; Jia, M.; Fan, Q.; Gao, Y.; Wang, H.; Robertson, A. W.; Hong, S.; Jung, Y.; Liu, S.; Sun, Z. *Chem* **2019**, *5*, 204.
- (5) Wang, J.; Yu, L.; Hu, L.; Chen, G.; Xin, H.; Feng, X. *Nat. Commun.* **2018**, *9*, 1795.
- (6) Bao, D.; Zhang, Q.; Meng, F.-L.; Zhong, H.-X.; Shi, M.-M.; Zhang, Y.; Yan, J.-M.; Jiang, Q.; Zhang, X.-B. *Adv. Mater.* **2017**, *29*, 1604799.
- (7) Zhang, G.; Ji, Q.; Zhang, K.; Chen, Y.; Li, Z.; Liu, H.; Li, J.; Qu, J. *Nano Energy* **2019**, *59*, 10.
- (8) Zhang, L.; Ji, X.; Ren, X.; Ma, Y.; Shi, X.; Tian, Z.; Asiri, A. M.; Chen, L.; Tang, B.; Sun, X. *Adv. Mater.* **2018**, *30*, 1800191.
- (9) Ren, X.; Cui, G.; Chen, L.; Xie, F.; Wei, Q.; Tian, Z.; Sun, X. *Chem. Commun.* **2018**, *54*, 8474.
- (10) Yang, X.; Nash, J.; Anibal, J.; Dunwell, M.; Kattel, S.; Stavitski, E.; Attenkofer, K.; Chen, J. G.; Yan, Y.; Xu, B. *J. Am. Chem. Soc.* **2018**, *140*, 13387.
- (11) Song, Y.; Johnson, D.; Peng, R.; Hensley, D. K.; Bonnesen, P. V.; Liang, L.; Huang, J.; Yang, F.; Zhang, F.; Qiao, R.; Baddorf, A. P.; Tschaplinski, T. J.; Engle, N. L.;

- Hatzell, M. C.; Wu, Z.; Cullen, D. A.; Meyer, H. M.; Sumpter, B. G.; Rondinone, A. *J. Sci Adv.* **2018**, *4*, e1700336.
- (12) Qiu, W.; Xie, X.-Y.; Qiu, J.; Fang, W.-H.; Liang, R.; Ren, X.; Ji, X.; Cui, G.; Asiri, A. M.; Cui, G.; Tang, B.; Sun, X. *Nat. Commun.* **2018**, *9*, 3485.
- (13) Chalkley, M. J.; Del Castillo, T. J.; Matson, B. D.; Peters, J. C. *J. Amer. Chem. Soc.* **2018**, *140*, 6122.
- (14) Abghoui, Y.; Garden, A. L.; Howalt, J. G.; Vegge, T.; Skúlason, E. *ACS Catal.* **2016**, *6*, 635.
- (15) Du, H.-L.; Gengenbach, T. R.; Hodgetts, R.; MacFarlane, D. R.; Simonov, A. N. *ACS Sustainable Chem. Eng.* 2019.
- (16) Zhu, D.; Zhang, L.; Ruther, R. E.; Hamers, R. J. *Nat. Mater.* **2013**, *12*, 836.
- (17) Giordano, C.; Erpen, C.; Yao, W.; Antonietti, M. *Nano Lett.* **2008**, *8*, 4659.
- (18) Dabundo, R.; Lehmann, M. F.; Treibergs, L.; Tobias, C. R.; Altabet, M. A.; Moisander, P. H.; Granger, J. *PLoS One.* **2014**, *9*, e110335.

APPENDIX A. TABLES AND FIGURES

Table 1. An overview of aqueous organic RFBs to date.

Anode	Cathode	Supporting electrolyte	Concentration (M)	Cell voltage (V)	Stability (% per cycle)
	Br ₂	1 M H ₂ SO ₄	1	0.86	99.84 (750 cycles)
	K ₄ Fe(CN) ₆	1 M KOH	0.5	1.2	99.1 (100 cycles)
		2 M NaCl	0.373	1.15	~99.8 (100 cycles)
		1 M NaCl	0.5	1.25	99.89 (100 cycles)
		None	2	1.4	99.9 (100 cycle)
	K ₄ Fe(CN) ₆	1 M KOH	0.5	1.2	99.98 (400 cycles)
		2 M NaCl	0.5	1.05	99.987 (700 cycles)
		None	0.75	0.75	99.9989 (500 cycles)
		None	1.3	0.75	99.9943 (250 cycles)

		2 M NaCl	0.5	1.38	99.995 (500 cycle)
		2 M NaCl	0.5	1.4	99.982 (500 cycle)
	$\text{K}_4\text{Fe}(\text{CN})_6$	None	0.9	0.8	100 (1000 cycles)
	$\text{K}_4\text{Fe}(\text{CN})_6$	1 M NaOH	1.4	1.4	99.98 (500 cycles)
	NH_4I	0.75 M NH_4I	0.75	0.865	100 (300 cycles)

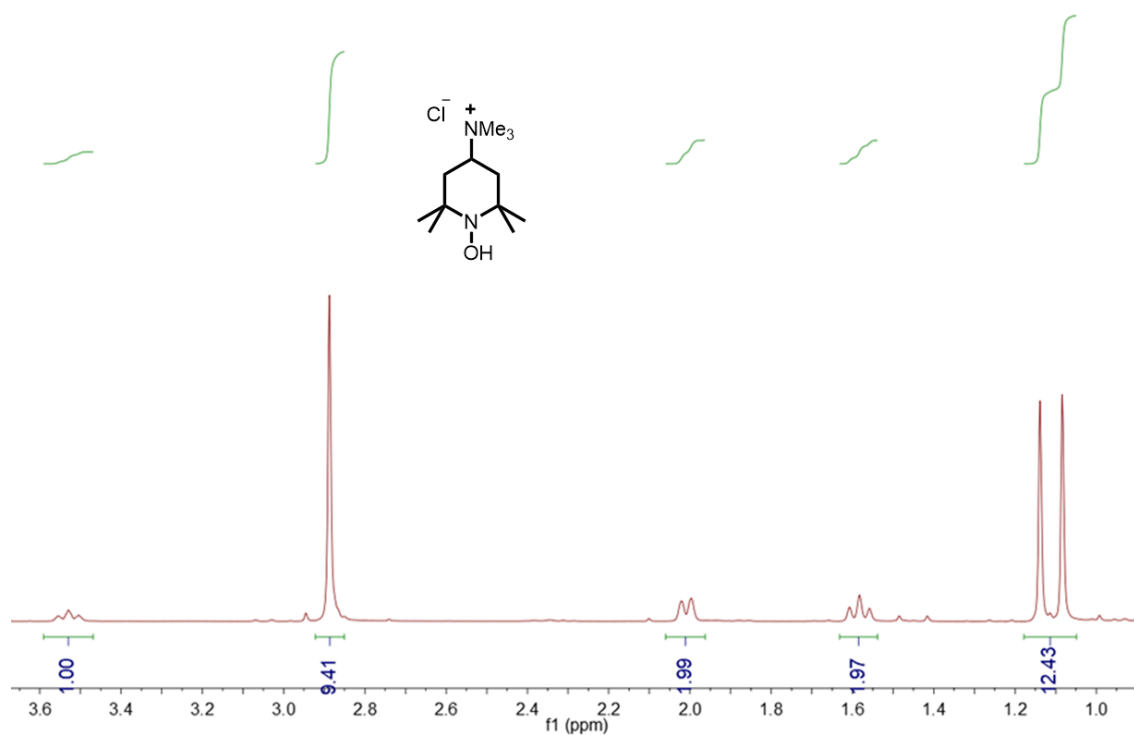


Figure 1. ^1H NMR spectrum of $\text{N}^{\text{Me}}\text{-TEMPO}$ in D_2O . (Phenol hydrazine was added to quench the radical to hydroxyamine)

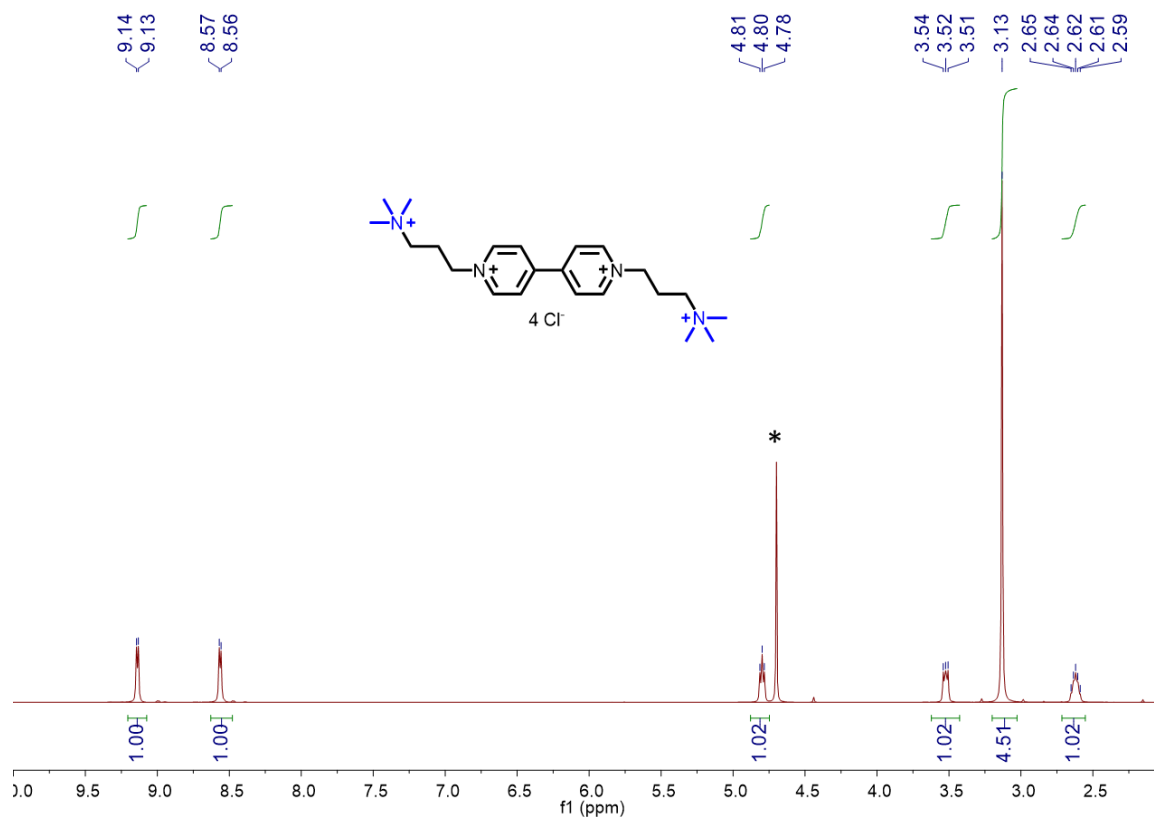


Figure 2. ^1H NMR spectrum of $(\text{NPr})_2\text{V}$ in D_2O . (* stands for solvent peak)

FcNTFSI

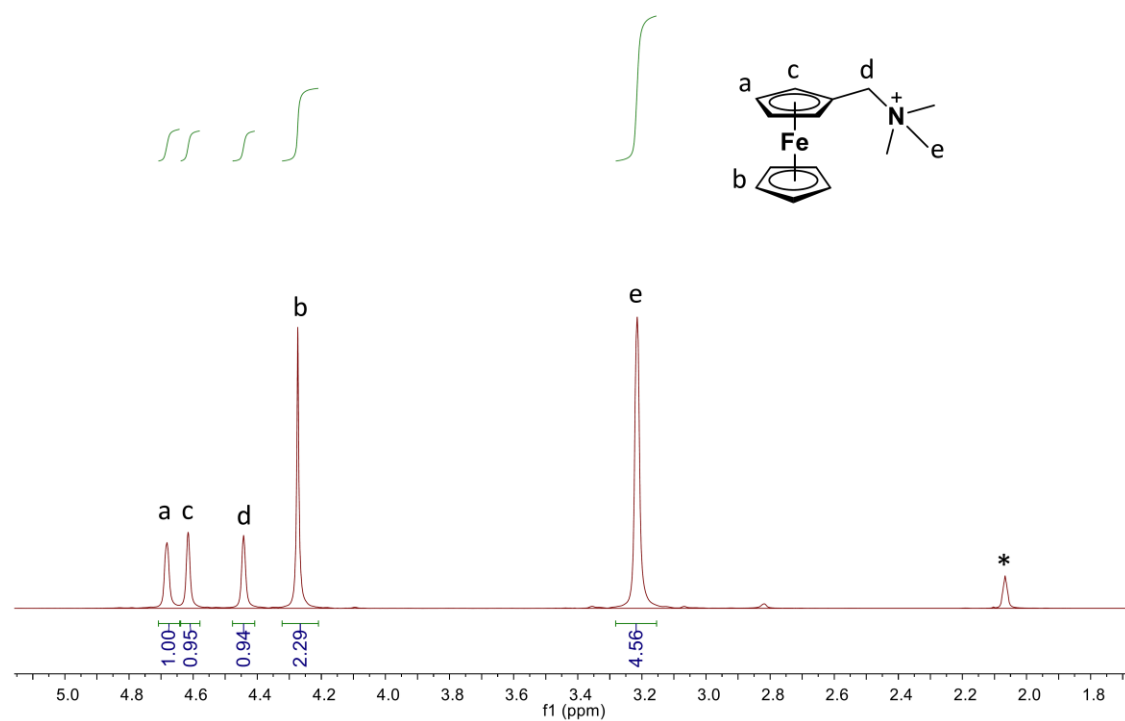


Figure 3. ^1H NMR of FcNTFSI in Acetone-d_6 . (* stands for solvent peak)

MVTFSI

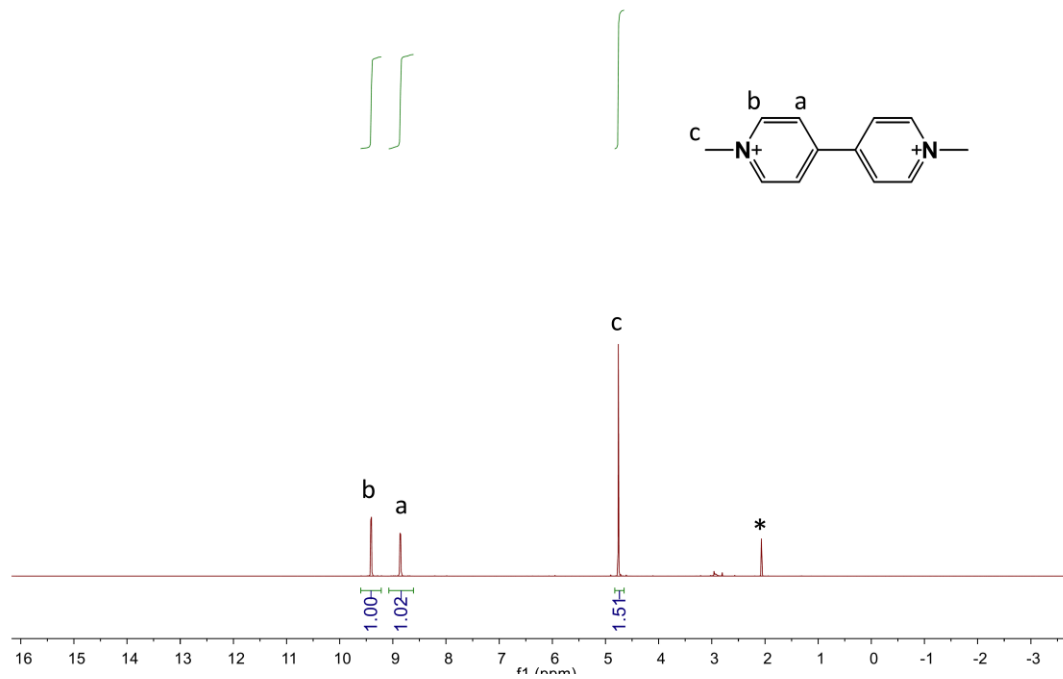


Figure 4. ^1H NMR of **MVTFSI** in Acetone-d_6 . (* stands for solvent peak)

APPENDIX B. COPYRIGHT

From: no-reply@copyright.com
Sent: Monday, November 25, 2019 9:23 AM
To: bo.hu2014@hotmail.com
Subject: RESPONSE REQUIRED for your request to John Wiley and Sons

WILEY**Accept your approved request**

Dear Mr. Bo Hu,

John Wiley and Sons has approved your recent request described below. Before you can use this content, you must accept the license fee and terms set by the publisher.

Use this [link](#) to accept (or decline) the publisher's fee and terms for this order.

Order Summary

Licensee:	Utah State University
Order Date:	Nov 22, 2019
Order Number:	501529905
Publication:	Wiley Books
Title:	Redox-Active Inorganic Materials for Redox Flow Batteries
Type of Use:	Dissertation/Thesis
Order Total:	0.00 USD

View or print complete [details](#) of your request.

Sincerely,

Copyright Clearance Center

Tel: +1-855-239-3415 / +1-978-646-2777
customer@copyright.com
<https://myaccount.copyright.com>



RightsLink

This message (including attachments) is confidential, unless marked otherwise. It is intended for the addressee(s) only. If you are not an intended recipient, please delete it without further distribution and reply to the sender that you have received the message in error.



RightsLink®



Home



Help



Email Support



Sign in



Create Account



Long-Cycling Aqueous Organic Redox Flow Battery (AORFB) toward Sustainable and Safe Energy Storage

Author: Bo Hu, Camden DeBruler, Zayn Rhodes, et al

Publication: Journal of the American Chemical Society

Publisher: American Chemical Society

Date: Jan 1, 2017

Copyright © 2017, American Chemical Society

PERMISSION/LICENSE IS GRANTED FOR YOUR ORDER AT NO CHARGE

This type of permission/license, instead of the standard Terms & Conditions, is sent to you because no fee is being charged for your order. Please note the following:

- Permission is granted for your request in both print and electronic formats, and translations.
- If figures and/or tables were requested, they may be adapted or used in part.
- Please print this page for your records and send a copy of it to your publisher/graduate school.
- Appropriate credit for the requested material should be given as follows: "Reprinted (adapted) with permission from (COMPLETE REFERENCE CITATION). Copyright (YEAR) American Chemical Society." Insert appropriate information in place of the capitalized words.
- One-time permission is granted only for the use specified in your request. No additional uses are granted (such as derivative works or other editions). For any other uses, please submit a new request.

[BACK](#)

[CLOSE WINDOW](#)

From: no-reply@copyright.com
Sent: Monday, November 25, 2019 5:53 AM
To: bo.hu2014@hotmail.com
Subject: RESPONSE REQUIRED for Your Request to Royal Society of Chemistry



Dear Mr. Bo Hu,

Royal Society of Chemistry has approved your recent request. Before you can use this content, you must accept the license fee and terms set by the publisher.

Use this [link](#) to accept (or decline) the publisher's fee and terms for this order.

Request Summary:

Submit date: 22-Nov-2019

Request ID: 600002076

Publication: Journal of materials chemistry. A, Materials for energy and sustainability

Title: Boosting the energy efficiency and power performance of neutral aqueous organic redox flow batteries Electronic supplementary information (ESI) available: Additional data as figures and tables. See DOI: Web:

10.1039/c7ta06573f

Type of Use: Republish in a thesis/dissertation

Please do not reply to this message.

To speak with a Customer Service Representative, call +1-855-239-3415 toll free or +1-978-646-2600 (24 hours a day), or email your questions and comments to support@copyright.com.

Sincerely,

Copyright Clearance Center

Tel: 1-855-239-3415 / +1-978-646-2600
support@copyright.com
[Manage Account](#)





RightsLink®



Home



Help



Live Chat



Bo Hu ▾

**Two electron utilization of methyl viologen anolyte in nonaqueous organic redox flow battery****Author:** Bo Hu, T. Leo Liu**Publication:** Journal of Energy Chemistry**Publisher:** Elsevier**Date:** September 2018

© 2018 Science Press and Dalian Institute of Chemical Physics, Chinese Academy of Sciences. Published by Elsevier B.V. and Science Press. All rights reserved.

Please note that, as the author of this Elsevier article, you retain the right to include it in a thesis or dissertation, provided it is not published commercially. Permission is not required, but please ensure that you reference the journal as the original source. For more information on this and on your other retained rights, please visit: <https://www.elsevier.com/about/our-business/policies/copyright#Author-rights>

[BACK](#)[CLOSE WINDOW](#)



RightsLink®



Home



Help



Email Support



Sign in



Create Account

**Electrocatalytic CO₂ reduction catalyzed by nitrogenase MoFe and FeFe proteins****Author:** Bo Hu, Derek F. Harris, Dennis R. Dean, T. Leo Liu, Zhi-Yong Yang, Lance C. Seefeldt**Publication:** Bioelectrochemistry**Publisher:** Elsevier**Date:** April 2018

© 2017 Elsevier B.V. All rights reserved.

Please note that, as the author of this Elsevier article, you retain the right to include it in a thesis or dissertation, provided it is not published commercially. Permission is not required, but please ensure that you reference the journal as the original source. For more information on this and on your other retained rights, please visit: <https://www.elsevier.com/about/our-business/policies/copyright#Author-rights>

BACK

CLOSE WINDOW



RightsLink®



Home



Help



Email Support



Sign in



Create Account



Electrochemical Dinitrogen Reduction to Ammonia by Mo₂N: Catalysis or Decomposition?

Author: Bo Hu, Maowei Hu, Lance Seefeldt, et al

Publication: ACS Energy Letters

Publisher: American Chemical Society

Date: May 1, 2019

Copyright © 2019, American Chemical Society

PERMISSION/LICENSE IS GRANTED FOR YOUR ORDER AT NO CHARGE

This type of permission/license, instead of the standard Terms & Conditions, is sent to you because no fee is being charged for your order. Please note the following:

- Permission is granted for your request in both print and electronic formats, and translations.
- If figures and/or tables were requested, they may be adapted or used in part.
- Please print this page for your records and send a copy of it to your publisher/graduate school.
- Appropriate credit for the requested material should be given as follows: "Reprinted (adapted) with permission from (COMPLETE REFERENCE CITATION). Copyright (YEAR) American Chemical Society." Insert appropriate information in place of the capitalized words.
- One-time permission is granted only for the use specified in your request. No additional uses are granted (such as derivative works or other editions). For any other uses, please submit a new request.

[BACK](#)

[CLOSE WINDOW](#)

CURRICULUM VITAE

Bo Hu

Email: bo.hu2014@hotmail.com

Mobile: +1 (435)554-9435

Address: 0300 Old Main Hill, Logan, UT 84322

Education

Utah State University*Ph.D. in Chemistry*

Logan, Utah, United States

Expected Spring 2020

Harbin Institute of Technology*M.S. in Inorganic Chemistry*

Harbin, China

July 2015

Nanjing University of Aeronautics and Astronautics*B.A. in Applied Chemistry*

Nanjing, China

July 2011

Language

English - Full professional proficiency**Chinese** - *Native proficiency***Research Experience**

Utah State University*Ph.D. Researcher*

Logan, Utah, United States

January 2016 - Present

- Designed and synthesized redox active materials for high performance aqueous and non-aqueous organic redox flow batteries
- Performed mechanistic studies for the materials chemical decomposition to explain the batteries' capacity fade and guide the better molecular design
- Conducted heterogeneous electrocatalytic CO₂ and N₂ reduction based on enzymatic and inorganic catalysts
- Worked on synthesizing high performance Mg electrolyte for rechargeable magnesium battery

Harbin Institute of Technology*Master's researcher*

Harbin, China

September.2013 – July.2015

- Improving the performance of CdS quantum dots synthesized TiO₂ solar cells
- Synthesized phosphate functionalized Tris(bipyridine)ruthenium complex as the photosensitizer and Co₃O₄ nanoparticles as the catalyst for photocatalytic water oxidation

Awards

2018-2019 College of Science Award (Doctoral Researcher of the Year) -Utah State University

2018-2019 Seely-Hinckley Scholarship-Utah State University (\$12,000)

2017-2018 Utah State Energy Research Triangle – student award from USTAR (\$1,5000)

2016-2019 Scholarship from aboard studying program of China Scholarship Council

Publications and Scholarly Work

1. Badalyan, A.; Yang, Z.; **Hu, B.**; Luo, J.; Hu, M.; Liu, T. L. Lance Seefeldt; "An Efficient Viologen-Based Electron Donor to Nitrogenase" *Biochemistry*, **2019**, 58, 4590.
2. Luo, J.; **Hu, B.**; Hu, M.; Liu, T. L.; "Status and Prospects of Organic Redox Flow Batteries towards Renewable Energy Storage" *ACS Energy Letters*, **2019**, 4, 2220
3. **Hu, B.**; Luo, J.; Hu, M.; Yuan, B.; Liu, T. L. "A pH Neutral, Metal Free Aqueous Organic Redox Flow Batteries Employing an Ammonium Anthraquinone Anolyte". *Angew. Chem. Int. Ed.* **2019**, 58, 2.
4. Ma, D.; **Hu, B.**; Liu, X.; Zai, J.; Shu, C.; Tsega, T. T.; Chen, L.; Qian, X.; Liu, T. L. "Highly Active Nanostructured CoS₂/CoS Heterojunction Electrocatalysts for Aqueous Polysulfide/Iodide Redox Flow Batteries". *Nat. Commun.* **2019**, 10, 3367.
5. **Hu, B.**, Hu, M., Seefeldt L.; Liu, T. L. "Electrochemical Nitrogen Reduction to Ammonia by Mo₂N: Catalysis or Decomposition?" *ACS Energy Letters*. **2019**, 4, 1053.
6. Luo, Jian; Wu, Wenda; Debruler, Camden; **Hu, Bo**; Hu, Maowei; Liu, T. Leo. "A 1.51 V pH Neutral Redox Flow Battery towards Scalable Energy Storage". *J. Mater. Chem. A*. **2019**, 7, 9136.
7. **Hu, B.**; Luo, J.; DeBruler C.; Hu, M.; Wu, W.; Liu, T. L. "Redox Active Inorganic Materials for Redox Flow Batteries". *Encyclopedia of Inorganic and Bioinorganic Chemistry: Inorganic Battery Materials*, **2019**.
8. Luo, J. (*co-1st author*); **Hu, B. (co-1st author)**; DeBruler C. Zhao, Y., Yuan B. Hu, M. Wu, W. Liu, T. L. "Unprecedented Capacity and Stability of Ammonium Ferrocyanide Catholyte in pH Neutral Aqueous Redox Flow Batteries". *Joule*. **2019**, 4, 1.
9. **Hu, B.**; Tang, Y.; Luo, J.; Grove, G.; Guo, Y.; Liu, T. L. "Improved Radical Stability of Viologen Anolytes in Aqueous Organic Redox Flow Batteries". *Chem. Commun.* **2018**, 54, 6871.
10. **Hu, B.**; Liu, T. L. "Two Electron Utilization of Methyl Viologen Anolyte in Nonaqueous Organic Redox Flow Battery". *J. Energy Chem.* **2018**, 27, 1326.
11. Li, W.; Jiang, N.; **Hu, B.**; Liu, X.; Song, F.; Han, G.; Jordan, T. J.; Hanson, T. B.; Liu, T. L.; Sun, Y. "New electrolyzer design for flexible decoupled water splitting and organic upgrading with electron reservoirs" *Chem.* **2018**, 3, 637.
12. DeBruler C.; **Hu, B.**; Moss, J.; Luo, J.; Liu, T. L. "A Sulfonate Functionalized Viologen Enabling Neutral Cation Exchange Aqueous Organic Redox Flow Batteries towards Renewable Energy Storage". *ACS Energy Letters*. **2018**, 3, 663.
13. Luo, J.; **Hu, B.**; Sam, A.; Liu, T. L. "Metal Free Electrocatalytic Aerobic Hydroxylation of Arylboronic Acids". *Org. Letters*. **2018**, 20, 361.
14. **Hu, B.**; Harris, D.; Dean, D.; Liu, T. L.; Yang, Z.; Seefeldt, C. L. "Electrocatalytic CO₂ Reduction Catalyzed by Nitrogenase MoFe and FeFe Proteins". *Bioelectrochemistry*. **2018**, 120, 104.
15. Luo, J.; **Hu, B.**; DeBruler C. Liu, T. L. "A π -Conjugation Extended Viologen as Novel Two-Electron Storage Anolyte for Total Organic Aqueous Redox Flow Battery". *Angew. Chem. Int. Ed.* **2018**, 130, 237.
16. DeBruler, C. (*co-1st author*); **Hu, B. (co-1st author)**; Moss, J.; Liu, T. L. "Designer Two Electron Storage Viologen Anode Materials for Aqueous Organic Redox Flow Batteries". *Chem.* **2018**, 3, 961.
17. Bi, Yujing.; Luo, J.; **Hu, B.**; He, S.; Nielson, K.; Liu, T. L. "Chemistry and Electrochemical Performance of Mg Electrolytes for Rechargeable Mg Batteries: A Study of Mg Powder Scavenger". *ECS Trans.* **2017**, 80, 343.
18. Luo, J.; Sam, A.; **Hu, B.**; DeBruler C. Liu, T. L. "Unraveling pH Dependent Cycling Stability of Ferricyanide/Ferrocyanide in Redox Flow Batteries". *Nano Energ.*, **2017**, 42, 215.
19. **Hu, B.**; Seefeldt, C.; DeBruler, C.; Liu, T. L. "Boost Energy Efficiency and Power performance of Neutral Aqueous Organic Redox Flow Batteries". *J. Mater. Chem. A*. **2017**, 5, 22137.
20. **Hu, B.**; DeBruler, C.; Rhodes, Z.; Liu, T. L. "Long-Cycling Aqueous Organic Redox Flow Battery

- (AORFB) toward Sustainable and Safe Energy Storage”. *J. Am. Chem. Soc.* **2017**, 139, 1207.
21. Liu, T.; Luo, J.; **Hu, B.** “Extended Viologen Molecules for Energy Storage”. filed US provisional patent, **2018**.
 22. Liu, T.; **Hu, B.**; DeBruler, C.; Luo, J. “Materials for Use in an Aqueous Organic Redox Flow Battery”. filed US non-provisional patent, US20180072669A1, **2017**.

Presentations

Oral presentations

1. “Aqueous Organic Redox Flow Batteries Based on Viologen Chemistry”, 2018 Utah Energy Symposium, UT. **2018**.
2. “Long-Cycling Ferrocene/MV Aqueous Organic Redox Flow Battery (AORFB)”, the 232nd ECS Meeting, National Harbor, MD. **2017**.
3. “Electrocatalytic carbon dioxide reduction into formate by nitrogenase”, the 4th annual Utah Inorganic/Organometallic Symposium, Provo, UT. **2017**.

Poster presentations

1. “Viologen Redox Flow Batteries for Scalable and Sustainable Energy Storage”, 2019 MRS Spring Meeting and Exhibit, Phoenix, AZ. **2019**.
2. “Chemistry and Electrochemical Performance of Inorganic Mg Electrolytes for Mg Rechargeable Batteries”, the 232nd ECS Meeting, National Harbor, MD. **2017**.
3. “Long-Cycling Aqueous Organic Redox Flow Battery (AORFB) toward Sustainable and Safe Energy Storage”, 2016 USTAR confluence, Salt Lake City, UT. **2016**.
4. “A High Performance Aqueous Organic Redox Flow Battery (AORFB) for Sustainable and Safe Renewable Energy Storage”, SELECT Annual Meeting and Technology Showcase, Logan, UT. **2016**.